

University of Windsor
Scholarship at UWindsor

[Electronic Theses and Dissertations](#)

[Theses, Dissertations, and Major Papers](#)

10-11-2024

Application of Pseudospectral Methods to Beta Decay, Two-photon Decay, and Tune-out Frequencies in Helium

Aaron Bondy
University of Windsor

Follow this and additional works at: <https://scholar.uwindsor.ca/etd>

Recommended Citation

Bondy, Aaron, "Application of Pseudospectral Methods to Beta Decay, Two-photon Decay, and Tune-out Frequencies in Helium" (2024). *Electronic Theses and Dissertations*. 9570.
<https://scholar.uwindsor.ca/etd/9570>

This online database contains the full-text of PhD dissertations and Masters' theses of University of Windsor students from 1954 forward. These documents are made available for personal study and research purposes only, in accordance with the Canadian Copyright Act and the Creative Commons license—CC BY-NC-ND (Attribution, Non-Commercial, No Derivative Works). Under this license, works must always be attributed to the copyright holder (original author), cannot be used for any commercial purposes, and may not be altered. Any other use would require the permission of the copyright holder. Students may inquire about withdrawing their dissertation and/or thesis from this database. For additional inquiries, please contact the repository administrator via email (scholarship@uwindsor.ca) or by telephone at 519-253-3000 ext. 3208.

Application of Pseudospectral Methods to Beta Decay, Two-photon Decay, and Tune-out Frequencies in Helium

By

Aaron T. Bondy

A Dissertation
Submitted to the Faculty of Graduate Studies
through the Department of Physics
in Partial Fulfillment of the Requirements for
the Degree of Doctor of Philosophy
at the University of Windsor

Windsor, Ontario, Canada

2024

©2024 Aaron T. Bondy

Application of Pseudospectral Methods to Beta Decay, Two-photon Decay, and
Tune-out Frequencies in Helium

by

Aaron T. Bondy

APPROVED BY:

M. Horbatsch, External Examiner
York University

Z. Kobti
School of Computer Science

J. Rau
Department of Physics

C. Rangan
Department of Physics

G. W. F. Drake, Advisor
Department of Physics

September 9, 2024

DECLARATION OF CO-AUTHORSHIP /

PREVIOUS PUBLICATION

I. Co-Authorship

I hereby declare that this thesis incorporates material that is result of joint research, as follows:

- Chapter 3 of the dissertation includes the outcome of a publication which has the following other co-author: G. W. F. Drake. Only my primary contributions are included in this dissertation. G.W.F.D. and I co-developed the underlying theoretical techniques and co-wrote the manuscript. I carried out the calculations.
- Chapter 4, and Appendices F and G, of the dissertation include the outcomes of two publications, shown in Sec. II, the first of which has two co-authors: D. C. Morton and G. W. F. Drake. Only my primary contributions are included in this dissertation. G.W.F.D. supervised and conceived of the work and DCM and I both carried out calculations. The manuscript was co-wrote and co-edited by the authors. The second publication has one co-author: G. W. F. Drake. G.W.F.D. and I co-developed the underlying theoretical techniques and co-wrote the manuscript.
- Chapter 5 of the dissertation includes the outcome of publications which have the following other co-authors: B. M. Henson, J. A. Ross, K. F. Thomas, C. N. Kuhn, D. K. Shin, S. S. Hodgman, Yong-Hui Zhang, Li-Yan Tang, G. W. F. Drake, A. G. Truscott, and K. G. H. Baldwin. Only my primary contributions are included in this dissertation. B.M.H., J.A.R., K.F.T., L.-Y.T., G.W.F.D., A.G.T., and K.G.H.B. conceived of the work and, along with S.S.H., co-wrote the manuscript. B.M.H., J.A.R., K.F.T., D.K.S., S.S.H., A.G.T. and K.G.H.B. carried out the experimental effort and Y.H.Z., L.Y.T., G.W.F.D., and myself carried out the theoretical calculations.

I am aware of the University of Windsor Senate Policy on Authorship and I certify that I have properly acknowledged the contribution of other researchers to my thesis, and have obtained written permission from each of the co-author(s) to include the above material(s) in my thesis.

I certify that, with the above qualification, this thesis, and the research to which it refers, is the product of my own work.

II. Previous Publication

This thesis includes four original papers that have been previously published/submitted to journals for publication, as follows:

Dissertation Chapter	Publication title/full citation	Publication status
Chapter 3	“Charge state distributions following the beta decay of ${}^6\text{He}$ to form ${}^6\text{Li}^+$ ”, A. T. Bondy and G. W. F. Drake, <i>Atoms</i> 11 , 41 (2023).	Published
Chapter 4 and Appendix F	“Two-photon decay rates in heliumlike ions: Finite-nuclear-mass effects”, A. T. Bondy, Donald C. Morton, and G. W. F. Drake, <i>Phys. Rev. A</i> 102 052807 (2020).	Published
Chapter 4 and Appendix G	“Algebraic relations from finite-nuclear-mass effects to test atomic transition rates”, A. T. Bondy and G. W. F. Drake, <i>Phys. Rev. A</i> 108 , 032807 (2023).	Published
Chapter 5	“Precision measurement of the helium ${}^2\text{S}_1 - {}^2\text{P}/{}^3\text{P}$ tune-Out frequency as a test of QED”, B. M. Henson, J. A. Ross, K. F. Thomas, C. N. Kuhn, D. K. Shin, S. S. Hodgman, Yong-Hui Zhang, Li-Yan Tang, G. W. F. Drake, A. T. Bondy, A. G. Truscott, and K. G. H. Baldwin, <i>Science</i> 376 , 199 (2022).	Published

I certify that I have obtained a written permission from the copyright owner(s) to include the above published material(s) in my thesis. I certify that the above material describes work completed during my registration as a graduate student at the University of Windsor.

III. General

I declare that, to the best of my knowledge, my thesis does not infringe upon anyone's copyright nor violate any proprietary rights and that any ideas, techniques, quotations, or any other material from the work of other people included in my thesis, published or otherwise, are fully acknowledged in accordance with the standard referencing practices. Furthermore, to the extent that I have included copyrighted material that surpasses the bounds of fair dealing within the meaning of the Canada Copyright Act, I certify that I have obtained a written permission from the copyright owner(s) to include such material(s) in my thesis. I declare that this is a true copy of my thesis, including any final revisions, as approved by my thesis committee and the Graduate Studies office, and that this thesis has not been submitted for a higher degree to any other University or Institution.

ABSTRACT

We extend the widespread use and versatility of pseudostates in the theoretical characterization of properties of two-electron atoms and ions by using them in calculations for three distinct physical processes. Atomic systems have infinitely many bound and continuum states, posing a computational challenge for calculations involving perturbation sums over intermediate states. In this work, we construct two-electron pseudostates variationally using a doubled basis set of correlated Hylleraas functions.

The first process we consider is the beta decay of ${}^6\text{He}$, an isotope of helium with a halo nucleus that lives for 0.8 s. The electron-antineutrino correlation coefficient, $a_{\beta\nu}$, is related to the kinematics following this decay and is a frequent subject of low-energy tests of the Standard Model—exotic interactions beyond vector–axial–vector would signal new physics. The Coulomb pulse resulting from the change in nuclear charge from $Z = 2$ to $Z = 3$ can shake off one or both of the atomic electrons of the ${}^6\text{Li}^+$ daughter ion. The precise charge state fractions of the daughter ion affect the kinematics of the decay, which are used to obtain $a_{\beta\nu}$. We treat the shake-up and shake-off processes in the beta decay of ${}^6\text{He}$ by developing two-electron, configuration interaction (CI) projection operators capable of distinguishing single- and double-ionization channels [A. T. Bondy and G. W. F. Drake, *Atoms* **11**, 41 (2023)]. The CI-like projection operators are formed using products of one-electron Sturmian pseudostates that have a fascinating “triangular” structure, with a wide range of nonlinear parameters, capable of spanning many distance scales and producing very-high-energy ($E > 10^{30}$ a.u.) pseudostates. We have reduced a theory-experiment discrepancy by an order of magnitude and predict the charge-state fraction of ${}^6\text{Li}^{3+}$ following this decay to be 0.35(5)% and 0.53(7)% for the $1\ 1^S_0$ and $2\ 3^S_1$ states of ${}^6\text{He}$, respectively—still much larger than the measured 0.018(15)% [T. A. Carlson *et al.*, *Phys. Rev.* **129**, 2220 (1963)] and < 0.01% [R. Hong *et al.*, *Phys. Rev. A* **96**, 053411 (2017)].

Secondly, we perform high-precision variational calculations which include finite-nuclear-mass effects for spontaneous two-photon ($2E1$) decay rates in heliumlike ions in the metastable 2^1S state, including the heavy species of muonic, pionic and antiprotonic helium [A. T. Bondy, D. C. Morton, and G. W. F. Drake, Phys. Rev. A **102**, 052807 (2020)]. This critical process helps determine population balances and serves as a temperature and pressure probe in low-particle-density regimes such as astrophysical planetary nebulae. In calculating the finite-nuclear-mass effects, mass polarization was treated as a gauge-dependent power series in μ/M , leading to novel algebraic relationships that test for gauge equivalence—for ${}^{20}\text{Ne}^{8+}$ the length and velocity gauge of the two-photon decay rates agree to 1 ppb. We generalize the algebraic relationships to test for agreement when finite-nuclear-mass effects are included between length, velocity, and acceleration gauges for any $nE1$ -photon transitions [A. T. Bondy and G. W. F. Drake, Phys. Rev. A **108**, 022807 (2023)]. These general relations are tested and verified for three cases of spontaneous decay in heliumlike ions: the $E1$ decays $2^1P - 1^1S$ and $2^3P - 2^3S$ and the $2E1$ decay $2^1S - 1^1S$. They provide a powerful new way to test the accuracy of calculations involving approximate wave functions.

Finally, the tune-out frequency near 726 THz for the 2^3S_1 state of helium, which corresponds in lowest order to a zero in the frequency-dependent polarizability, is calculated as part of a joint theoretical-experimental effort [B. Henson *et al.*, Science **376**, 199 (2022)]. This provides a novel test of QED for a physical effect other than the traditional energy level measurements, such as the Lamb shift. The problem is reformulated as a zero in the Rayleigh scattering cross section to include higher-order retardation effects. We present high-precision, variational calculations of the Rayleigh scattering cross section in helium within the framework of nonrelativistic-QED, including higher-order corrections due to relativistic, QED, and retardation effects. This theoretical-experimental comparison tests QED effects and retardation effects at the 30σ and 2σ level, respectively. The tune-out frequency is calculated to be 725 736 252(9) MHz, while the measured value is 725 736 700(260) MHz, leaving a 1.7σ discrepancy.

DEDICATION

To mom and dad, who instilled in me a strong work ethic and gave me so much love, and to Emily, who has encouraged and supported me throughout the past few years.

ACKNOWLEDGEMENTS

My supervisor, Dr. Drake, has been an incredible mentor, guiding me into the world of atomic physics. Early on, I realized the immense value of his guidance, and I am deeply grateful for his influence on my personal and academic growth. Undoubtedly, his intelligence, dedication, and hard work have inspired me and brought out the best in my abilities. Patience and encouragement were always at the forefront of his mentorship, especially when he supported my attendance at several conferences and our joint papers. He encouraged me to pursue every opportunity that would advance my career, such as conducting research abroad, teaching classes at the University of Windsor, and serving on various committees, both at Windsor and for the APS. Over time, these activities took time away from my research, and I am grateful he allowed me the flexibility to pursue them. Regardless of the challenges, he has always been kind and patient, often inviting me to events and into his home for meals and gatherings. I strive to live up to the graciousness and generosity he has consistently shown. Above all, I am thankful for the trust and freedom he has placed in me throughout this journey.

Also, I would like to acknowledge the important influence that Dr. Klaus Bartschat has had on my professional development and growth as a physicist. He hosted me twice for extended research visits where I became familiar with laser-atom interactions and attoscience, introducing me to the scattering side of atomic physics. He leads by example and has always promoted my best interest. We have collaborated outside of these visits and I have thoroughly enjoyed working with him. His generosity and graciousness are greatly appreciated.

Next, I wish to thank the Department of Physics as they have truly treated me as a family member. Overall, their contributions have been integral to my academic journey. There are no words that can express how much I appreciate the support I've received here. Long-lasting gratitude is due to Kimberly Lefebvre for our many

discussions and camaraderie over these years and for the care she has shown for me. I also want to acknowledge Nia Khuong for our discussions over the past few years and for all of her help getting me across the finish line. Kindness has always been evident in the mentorship I have received from Dr. Rangan, who served as both an academic mentor and a faculty mentor for the SAGES teaching practicum I conducted with her. Each letter she has written and every bit of advice she has given have been invaluable to me. Understanding and encouragement came also from Dr. Rehse, who I would like to thank for the wide-ranging discussions we have had over the years. Support from Dr. Rau, Dr. Hammond, and Dr. Xiao has also been integral to my development.

There are many other students over the years to whom I am grateful. Within the Drake research group: PeiPei Zhang, Dan Venn, Maha Sami, Spencer Percy, Cody McLeod, Eric Ene, Oliver Hallett, Ben Najem have all been wonderful to work with and to share ideas with, physics or otherwise. I would also like to acknowledge Griffin Howson, Sareen Sabra, and Sara Moezzi; it has been a pleasure to share an office space with the three of you. Tristhal Parasram, Nathan Drouillard, Dimitri Shinas, and Abo-Bakr Emara, it has been great to overlap with all of you as graduate students. Lamies Sati, it was a pleasure getting to know you and to work together. Evan Petrimoulx, it has been awesome working together and solving problems, you have a bright future ahead of you! Dr. Eva Schulhoff, you played a significant role in introducing me to this research group. I thank you for the many exciting discussions that we have had over coffee over the years.

Outside of Windsor, I would like to acknowledge other close collaborators with whom I had substantial contact: Dr. Donald Morton, Dr. Kathryn Hamilton, Dr. Soumyajit Saha, and Dr. Juan del Valle. I am grateful for having crossed paths with all of you and for everything that I have learned from you all and, above all, for your friendship. I would also like to acknowledge Dr. Tom Kirchner, who wonderfully taught me graduate quantum mechanics and atomic physics and has had a significant positive influence on my career.

I am very grateful for Joshua Trocchi, who has been a very supportive friend

for the past twelve years. We have spent countless hours working together and I thank you for supporting me in this journey. Our discussions about books and other subjects have been a treasure. Alex Merryfield, you have encouraged me through times thick and thin and have always been a good sounding board. I appreciate our many discussions and the great times that we have had. Thank you to all of my friends for your generosity, kindness, and humour—I can only hope to return these qualities to you.

My family has been an extreme source of support as well, especially including my Grandma Bondy, Grandma Bartlett, and Grandpa Bondy, who have passed away. Each of them played a significant role in both this academic journey and in who I am as a person. The remainder of my family have also been tremendously supportive and I am so grateful and fortunate to have them in my life. In particular, I would like to thank my Grandpa Bartlett, my Aunt Donna, Aunt Heather and Uncle Brian, and my Aunt Janice and Uncle John. All of you were there for me when my mom passed away and I am eternally thankful for your presence in my life. That goes for Lauren and Shannon, Megan, Nicole, Ally, and Ben as well. To the entirety of my family: thank you for your endless support and love. To Gudi, I appreciate your kindness and concern for me over the years, and for taking good care of my dad. To Ramón and Gaby, I look forward to many great years with you both. Your kindness, intelligence, and magnanimity are imprinted on your amazing daughter. I am eager to soon return to the beautiful Peru as a Spanish speaker.

Emily, you are a source of stability and inspiration in my life and I am eager to build a life together. You have been my rock for the past few years and have endlessly encouraged me to complete this dissertation and have always supported me. Love you!

Mom and Dad, thank you for all of your love since the day I was born. I love you both with all my heart. Thank you for always insisting that I do my best and for showing interest in whatever I was interested in. Dad, thank you for carrying on in life and always leading by example. You are the hardest working person I know. Mom, it truly does not feel that a day goes by where I do not notice your influence on my life. I still feel your love and am guided by it.

TABLE OF CONTENTS

DECLARATION OF CO-AUTHORSHIP / PREVIOUS PUBLICATION	iii
ABSTRACT	vi
DEDICATION	viii
ACKNOWLEDGEMENTS	ix
LIST OF FIGURES	xvi
LIST OF TABLES	xxi
1 Introduction	1
1.1 Background and Motivation	1
1.2 Overview of Research Projects	4
1.3 Methodology Overview	6
1.3.1 Introduction to pseudospectral methods	6
1.3.2 Examples using pseudospectra	7
1.4 Scope and Significance of Research	9
1.5 Structure of the Dissertation	11
2 Theoretical Methods	12
2.1 Overview	12
2.2 Atomic units	13
2.3 One-electron Schrödinger equation	14
2.4 Sturmian functions	17
2.4.1 The oscillation theorem	17
2.5 Two-electron Schrödinger equation	21
2.5.1 Problem statement	21
2.5.2 Spin: singlet and triplet solutions	22
2.6 Variational Principle	24
2.6.1 Rayleigh-Ritz variational method	24
2.6.2 Equivalent generalized eigenvalue problem	25
2.6.3 Extension to excited states	27
2.7 Hylleraas Trial Wave Functions	28
2.7.1 Statement of Hylleraas basis functions	28
2.7.2 Nonlinear parameters	29
2.7.3 Strategies and completeness	30
2.7.4 Comparison of Hylleraas construction to other basis sets	31

2.8	Integrals involving Hylleraas wave functions	33
2.8.1	General integral	34
2.8.2	The angular part	35
2.8.3	Radial integrals and recursion relations	36
2.8.4	Hamiltonian and overlap matrix elements	38
3	Beta Decay and Charge-state Distributions in ${}^6\text{He}$	40
3.1	Overview	40
3.2	Historical Significance	41
3.3	Motivation	44
3.3.1	The $V - A$ theory	44
3.3.2	The $\beta - \nu$ angular correlation coefficient	49
3.3.3	Uses in searches for new physics	52
3.3.4	Experimental measurements of $a_{\beta\nu}$	54
3.3.5	Advantages of light atoms	57
3.3.6	Connection to atomic physics	57
3.4	Formulation of the problem	58
3.4.1	Kinematic description	59
3.4.2	Physical assumptions	60
3.4.3	Problem statement	62
3.5	State of the art	63
3.5.1	Previous theoretical attempts	63
3.5.2	Foundation: doubled Hylleraas basis functions	66
3.6	Overestimated Double Ionization	69
3.6.1	Energy does not describe charge state	69
3.6.2	Suppression of double ionization	71
3.7	Projection Operators	73
3.7.1	Construction of projection operators	74
3.8	Results	81
3.9	Future Work	86
3.9.1	Delta function matrix elements: A potential new method for treating one- and two-channel scattering problems	87
4	Finite-nuclear-mass Effects in Two-photon Decay in Heliumlike Ions	91
4.1	Overview	91
4.2	Historical Significance	93
4.3	Motivation	95
4.3.1	Astrophysical observation	95
4.3.2	Theoretical motivation	98
4.4	Brief history of calculations and experiments	100
4.5	Theoretical Formulation	100
4.5.1	Single-photon transitions	102
4.5.2	Two-photon transitions	105
4.6	Wave functions for calculation	108
4.6.1	Reduced-mass atomic units	108

4.7	Finite-Nuclear-Mass Effects	109
4.7.1	Three sources of finite-mass effects	109
4.7.2	Constitutive relationships	110
4.8	Treating mass polarization	111
4.8.1	Algebraic relations	112
4.8.2	Generalization to higher-order transitions	113
4.9	Results	114
4.9.1	Two-photon decay rates	114
4.9.2	Testing the algebraic relationships	119
4.10	Future Work	124
4.10.1	Inclusion of relativistic effects	125
4.10.2	Extend to additional structure problems	127
4.10.3	Extension to highly charged heliumlike ions	127
5	Testing QED with the Tune-out Frequency in Helium	128
5.1	Overview	128
5.2	Motivation	129
5.3	The tune-out frequency	131
5.3.1	Suitability of the tune-out frequency for testing QED	132
5.4	Brief overview of the experiment	134
5.5	Theoretical formulation	136
5.5.1	Consequence of linear polarization of probe beam	136
5.5.2	Nonrelativistic RSCS or dynamic polarizability	137
5.5.3	NRQED formulation of the tune-out frequency	138
5.5.4	Relativistic corrections	139
5.5.5	QED corrections	140
5.5.6	Magnetic susceptibility	141
5.5.7	Retardation corrections	141
5.6	Results	143
5.7	Future work	144
6	Conclusion and Future Work	146
6.1	Overview	146
6.2	Summary of Findings	146
6.3	Synthesis of Conclusions	148
6.4	Future Work	149
6.5	Broader Implications	152
A	Methods of Solving the Generalized Eigenvalue Problem	154
A.1	Power method	155
A.2	Brute force method	156

B	Derivation of Fermi's Golden Rule and Comments on Spontaneous Decay	159
B.1	Derivation	160
B.2	Spontaneous decay	163
C	Handedness of Leptons in the SM	164
D	Assumptions in Treating Beta Decay	166
E	Derivation of Two-photon Decay Rate and Rayleigh Scattering Cross Section	170
E.1	Setting the Stage	170
E.2	Derivation	171
E.3	Rayleigh scattering formalism	175
F	Integration to Obtain the Decay Rate	178
G	Derivation of Algebraic Relations from Perturbation Theory	179
REFERENCES		182
VITA AUCTORIS		202

LIST OF FIGURES

1.3.1	Shown are the polarizabilities, calculated according to Eq. (1.2), of the ground state of hydrogen (The correct answer in the nonrelativistic limit is 4.5 a.u.). The pseudospectra used have basis functions of the form $\chi_j = \sum_{i=1}^N c_{ij} r^i e^{-\alpha r} Y_{10}$, as described in the text. The nonlinear parameter α is varied to show regions of stability. It is remarkable that, even for a two-term pseudospectrum, when $\alpha = 1$, there is already an exact representation of the complete spectrum. For a five-term pseudospectra, we see a large region of stability, where d_z is correctly calculated for the entire $\alpha \in [0.44, 1.4]$	8
1.3.2	The partial sum of the Bethe logarithm of H, $\beta(E)$, is plotted as a function of the last—also largest—energy contained in the partial sum. Created using the formulation developed by Drake and Goldman .	9
2.4.1	The principle of generating solutions to the Sturm-Liouville (SL) equation is shown. By holding E fixed to some negative number and progressively increasing λ in Eq. (2.17), we obtain more and more solutions. The spacings are not drawn to scale; the only relevant detail is that more and more states are pulled below the fixed $E = -\epsilon$. . .	19
2.5.1	An illustration of Hylleraas coordinates. The full set of independent radial ($r_1 = \mathbf{r}_1 , r_2 = \mathbf{r}_2 , r_{12} = \mathbf{r}_1 - \mathbf{r}_2 $) and angular (θ_1, ϕ_1, χ) coordinates are shown for two electrons located at \mathbf{r}_1 and \mathbf{r}_2 relative to the centre-of-mass. Here, θ_1, ϕ_1 are the polar and azimuthal angles of electron 1 and χ is the angle of rotation of the rigid triangle formed by the $\mathbf{r}_1, \mathbf{r}_2$ and \mathbf{r}_{12}	22

2.6.1	Illustration of the Hylleraas-Undheim-MacDonald theorem. For five separate calculations that solve the GEP in Eq. (2.32), each of which increases the number of basis functions N , we see that (1) the $N - 1$ old eigenvalues of the previous calculation lie between the N new eigenvalues and (2) that each trial eigenvalue is an upper bound to the corresponding exact eigenvalue.	27
3.2.1	A plot of the intensity of beta emission with a range of energies . This result of Ellis and Wooster in 1927 shows unequivocally that the intensity of beta particles, following the beta decay of radium, is shown to vary continuously with energy. This confirmed the earlier Chadwick experiments with significantly greater resolution.	44
3.3.1	The weak interaction in beta decay. The left panel shows the post- β^- -decay products with a daughter ion and an ejected beta particle e^- with an inset showing the nuclear-level products of the β^- -decay of a neutron. The Feynman diagram corresponding to this inset is shown in the right panel. Images are in the public domain.	45
3.3.2	Scott diagram showing the value of $a_{\beta\nu}$ as a function of the Fermi fraction x , which characterizes the degree of mixing in the decay. The solid red line corresponds to the $V - A$ structure of the weak interaction observed in nature.	51
3.3.3	Kinematics following the beta decay of ${}^6\text{He}$. The angle θ between the electron and antineutrino is related to the electron-antineutrino correlation coefficient – the experimental quantity of interest in connection with searches for NP.	55
3.3.4	The predicted shapes of the recoiling daughter ion's (RI) momentum are shown for the two possible Fermi interactions (vector and scalar) and the two possible Gamow-Teller interactions (axial-vector and tensor).	56
3.6.1	Energy level diagram of ${}^6\text{Li}^+$ with the charge states indicated. Notably, the $E > 0$ region contains both the single and double ionization channels.	70

3.6.2	This diagram illustrates the phase space arguments suggesting that double ionization is rare. In the case where energy/momentum are not equally shared between the two electrons, shown in panel A, one electron will fall back and become bound, creating a singly ionized state, shown in panel B.	72
3.7.1	Schematic indicating the role of the projection operators P_{++} , namely, to resolve the overlapping continua in the $E > 0$ a.u. region. The idea is to form the projection operators using two-electron basis functions $\Phi^{(++)}$ that are constructed as doubly ionized states.	73
3.7.2	Upper panel: Comparison of a one-electron pseudostate radial wave function with the corresponding exact Coulomb wave function at the same energy ($E = 0.06$ a.u.) near the threshold. In the case of double ionization, both electrons have wave functions of this form. This shows that the pseudostate representation remains accurate out to reasonably large distances. Lower panel: The two one-electron states ($E_{1s} = -4.5$ a.u. and $E_k = 4.56$ a.u.) corresponding to a near-threshold single-ionization state, demonstrating that the region nearest the nucleus is that which contributes when taking their product and forming projection operators as described in the present work. .	77
3.8.1	An example of convergence with respect to the number of partial waves ℓ (red dots) for the ${}^6\text{Li}^{3+}$ probability following the decay of ${}^6\text{He}(2\,{}^3S)$ for the case $\Omega_1 = \Omega_2 = 8$. This is the top left result (the top number) for the ${}^6\text{He}(2\,{}^3S)$ section of Table 3.8.1.	82

3.9.1	The delta function matrix element, $\langle n^{-1}P \delta(\mathbf{r}_1) n^{-1}P\rangle \equiv \langle\delta(\mathbf{r}_1)\rangle_{n^{-1}P}$, normalized to the ground state value $\langle\delta(\mathbf{r}_1)\rangle_{1^{-1}S}$ is calculated for the ${}^6\text{He}(n^{-1}P)$ pseudostates well into the doubly ionized continuum, up to $E = 120$ eV. Several basis sets are included with 104 to 446 terms. The ground-state and $2^{-1}P$ energies are shown, along with the first and second ionization thresholds. The purpose of this graph is to illustrate that the Hylleraas pseudostates lose their “1s” character before their energies even reach the second ionization threshold.	89
4.2.1	This diagram illustrates the difference between single and multiphoton ionization of an atom with ionization potential I_p and kinetic energy KE of the ejected electron. In weak intensity regimes, single-photon processes such as the photoelectric effect occur according to $\hbar\omega_1 = KE + I_p$, however, in higher intensity regimes multiphoton processes can take place where several photons (in this case 4) can make up the energy $\hbar\omega_1$. Goeppert Mayer showed that the correct equation is $N\hbar\omega = KE + I_p$, where $N > 1$ is possible in strong fields.	94
4.3.1	Energy level diagram for the $n = 2$ manifold of helium, illustrating those metastable processes that are of astrophysical interest and indicating the decay mechanism of those of interest.	96
4.3.2	Comparing the line intensities due to recombination from the $n = 2$ manifold observed in the cosmic microwave background (CMB) spectrum. Here, the $2E1$ decays in hydrogen and helium, respectively, the thicker and thin (red) dotted lines, are compared with the dominant $E1$ lines in H and He, respectively, the thick and thin solid (black) lines. Calculations from Wong, Seager, and Scott.	97
4.9.1	Plots of the two-photon emission rate $w^{(2\gamma)}({}^4\text{He})$ (black) and the difference $\Delta w^{(2\gamma)} = w^{(2\gamma)}(\mu^2-{}^4\text{He}) - w^{(2\gamma)}({}^4\text{He})$ (red) as fractions y of the unit energy range normalized to unity.	119

5.3.1 The level shifts for the 2^3S_1 state and the $2^3P/3^3P$ manifolds are shown for the cases of (left to right) no laser light, and then for light of frequency less than, equal to, and greater than the tune-out frequency. The noteworthy feature of incident light at the tune-out frequency is that the energy shift in the 2^3S_1 vanishes. 131

5.3.2 Partial energy level diagram of ${}^4\text{He}$, showing in particular the relevant transitions between the 2^3S_1 state and the $2^3P/3^3P$ manifold, between which the tune-out frequency occurs. The tune-out frequency studied in this work is very near 726 THz, below the 771 THz transition to 3^3P shown in blue. Not drawn to scale—the splittings are greatly exaggerated in this drawing. 133

5.3.3 This curve displays the dynamic polarizability as a function of the frequency of the applied laser light. The discontinuities occur when the laser is in resonance with transitions between the (from left to right) 2^3S and $n = 2, 3, 4^3P$ manifolds. Between these discontinuities, the polarizability must pass through zero—these are the so-called tune-out frequencies. For reasons that are explained in the text, it is the tune-out (f_{TO}) around 726 THz, indicated by the red arrow, that is studied presently to test QED. Each vertical line stands for the spin-orbit-split manifold and contains additional tune-outs that are not useful since their contributions are completely dominated by the states within the manifold and adhere to 1:3:5 geometric considerations. 134

5.6.1 A visual display of the material in Table 5.6.1. The difference between theory and experiment (checkered bar), along with their respective uncertainties (in crosshatch), are shown. Also depicted are the magnitudes of the theoretical contributions outlined in Table 5.6.1 are shown. 145

LIST OF TABLES

2.7.1	Comparison of the variational ground-state energy obtained using Hylleraas trial functions formed according to Eq. (2.34) containing all powers of r_1 and r_2 , but only select powers of r_{12} . It can be seen that odd powers of r_{12} contribute significantly to improving the accuracy.	30
2.7.2	Comparison between the level of accuracy that can be achieved using the Hartree-Fock method and various correlated variational wave functions. The Hylleraas basis states achieve much better accuracy than the rest	33
3.3.1	Summary of the value of the beta-neutrino angular correlation coefficient ($a_{\beta\nu}$) for pure Fermi ($x = 1$) or Gamow-Teller ($x = 0$) decays. The SM ($V - A$) predictions lie in the “Vector/Axial-Vector” column. . .	51
3.3.2	Ongoing nuclear beta decay experiments studying the correlation coefficient $a_{\beta\nu}$ are listed. Each decay is classified by its “type”: Fermi or Gamow-Teller and based on whether it is β^- or β^+ decay. See Table V in Ref. for a comprehensive list of the older experimental efforts.	54
3.5.1	Comparison of previous theory with experiment for the probabilities $P(^6\text{Li}^{k+})$ of forming the various charge states with $k = 1, 2, 3$ following beta decay of ${}^6\text{He}(1\,{}^1S_0)$ or ${}^6\text{He}(2\,{}^3S_1)$ as initial states. Ground state results in the upper panel are from Carlson <i>et al.</i> . Metastable triplet results in the lower panel are from Hong <i>et al.</i> . All quantities are expressed in percent (%).	67

3.8.1	Convergence table for ${}^6\text{Li}^{3+}$ probabilities for the initial states ${}^6\text{He}(1\ ^1S_0)$ and ${}^6\text{He}(2\ ^3S_1)$. Zeroth- and partial second-order corrections (top and bottom of each cell, respectively) from Eq. (3.53), taken in the limit of infinite partial waves as shown in Fig. 3.8.1. Results are expressed in percent(%) shown for different sizes of both the projection operator (Ω_1) and Hylleraas-type pseudostate (Ω_2) basis sets used in Eq. (3.42). The bottom entry is a partial second order correction, which, as explained in the text, ultimately cancels. The top values in the table for each state will be averaged to obtain the final ${}^6\text{Li}^{3+}$ probability. This table is continued on the following page.	84
3.8.1	Table 3.8.1 (con't): This is a continuation of Table 3.8.1 containing the convergence table for forming ${}^6\text{Li}^{3+}$ following the ${}^6\text{He}(2\ ^1S_0)$ initial state. The same description found in Table 3.8.1 and will not be reproduced.	85
3.8.2	Number of terms $N_1(\Omega_1)$ and $N_2(\Omega_2)$ in the basis sets. The factor 8 for $N_1(\Omega_1)$ accounts for the sum over partial waves up to $\ell = 7$	85
3.8.3	Previous and corrected ${}^6\text{Li}^{3+}$ charge-state fractions for each initial state following beta decay. All quantities expressed in percent (%). . . .	86
3.8.4	Corrected probabilities $p({}^6\text{Li}^{k+})$ of forming the various charge states of ${}^6\text{Li}^{k+}$, $k = 1, 2, 3$ following the beta decay of ${}^6\text{He}(1\ ^1S_0)$ or ${}^6\text{He}(2\ ^3S_1)$ as initial states. All quantities are expressed in percent (%). . . .	86
4.9.1	Convergence with respect to basis set size (N) of the ${}^4\text{He}(2\ ^1S_0)$ two-photon decay rates $w_r^{(2\gamma)}/\alpha^6$ for a finite nuclear mass $\mu/M = 1.370\,745\,62 \times 10^{-4}$. The subscripts r and p denote the length (L) and velocity (V) forms respectively. Units are atomic units. To convert to s^{-1} , multiply by $\alpha^6/\tau_e = 6242.763\,420(56) \text{ s}^{-1}$ where $\alpha = 7.297\,352\,5693(11) \times 10^{-3}$ is the fine structure constant and $\tau_e = 2.418\,884\,326\,5857(47) \times 10^{-17} \text{ s}$ is the atomic unit of time. Constants are taken from the CODATA recommendations	115

4.9.2	Extrapolated velocity (p) and length (r) two-photon decay rates $w^{(2\gamma)}/\alpha^6$ for various atoms and ions, including the heavy-helium cases with both electrons replaced by antiprotons (\bar{p}), pions (π), or muons (μ). Units are atomic units. To convert to s^{-1} , multiply by α^6/τ_x where τ_e is given in Table I, $\tau_{\bar{p}} = 1.317\,365\,60 \times 10^{-20}$ s, $\tau_{\pi} = 8.85610 \times 10^{-20}$ s, and $\tau_{\mu} = 1.169\,852\,69 \times 10^{-19}$ s for the antiprotonic, pionic, and muonic cases respectively. Numbers in parentheses () are estimated uncertainties. Not to be confused with citations, in this table the number in square brackets [] is the power of 10 that the quantity should be multiplied by.	116
4.9.3	Two-photon decay rates $w^{(2\gamma)}/\alpha^6$ for various atoms and ions, including the heavy-helium cases for both finite and infinite nuclear mass. To convert to s^{-1} multiply by α^6/τ_x —see Table 4.9.2 for this quantity and the values of $\tau_{\bar{p}}$, τ_{π} , and τ_{μ}	117
4.9.4	Maximum two-photon decay rates, energy ranges, and the wavelengths of the maximum rates. Values have converged to the figures quoted.	118
4.9.5	Final values for the two-photon decay rates, including finite nuclear mass ($\Delta w_{\mu/M}^{(2\gamma)}$) and relativistic corrections ($\Delta w_{\text{rel}}^{(2\gamma)}$) from Drake . The total $w_{\text{total}}^{(2\gamma)}$ is compared with the relativistic CI calculations of Derevianko and Johnson . Units are s^{-1} with an overall scale factor given in the last column for all the entries.	120
4.9.6	Mass-polarization parameters C_x and D_x from Eq. (4.39) are shown for the one-photon decay processes in the indicated singlet and triplet He and He-like ions, along with the accompanying algebraic relations, Eqs. (4.55) and (4.56) for $n = 1$. For the triplet transition at the bottom of the table, [†] indicates third-order contributions (E_x terms) are included in the calculation and [‡] indicates they are omitted. . .	123

4.9.7 Mass-polarization parameters C_x and D_x from Eq. (4.39) are shown for two-photon $2^1S - 1^1S$ decay in He and He-like ions, along with the accompanying algebraic relations, Eqs. (4.49) and (4.50), for the metastable singlet transition indicated.	124
5.4.1 Contributions to the measured tune-out frequency with their systematic uncertainties. The 40 MHz uncertainty in the measurement itself, however, is a statistical uncertainty. The polarization is the largest contribution to the experimental uncertainty budget.	136
5.6.1 Collection of the various theoretical contributions to the $2^3S_1 - 2^3P/3^3P$ tune-out frequency in helium near 725.7 THz. Finite-nuclear-mass effects are included in the nonrelativistic and relativistic contributions.	144

CHAPTER 1

Introduction

pseudo: being apparently rather than actually as stated; synonyms: sham, spurious

— Merriam-Webster Dictionary

His [Isaac Newton's] theory of the moon [i.e., the three-body problem] ... made his head ache, and kept him awake so often, that he would think of it no more.

— Edmond Halley, circa 1727 [1]

Physics thrives on crisis.

— Steven Weinberg, Rev. Mod. Phys. **61**, 1 (1989).

1.1 BACKGROUND AND MOTIVATION

This dissertation explores two-electron atoms, such as helium, which have played a fundamental role in developing quantum mechanics and quantum field theory. Even before these subjects were formally developed, these systems played a crucial role in nuclear physics and condensed matter physics. Helium was involved in Rutherford's gold foil experiment, which elucidated atomic structure, and Kammerlingh-Onnes' discovery of superconductivity. It is also highly relevant in astrophysics; it is the second-most abundant element in the universe. A recurrent theme in the study of helium is its simplicity. With only two electrons, a system like helium, with its theoretical simplicity and experimental accessibility, provides an ideal platform for

probing the foundations of quantum mechanics which underpin our understanding of the larger universe.

However, while atomic physics offers precise insights into certain quantum phenomena, it also brings to light broader questions that remain unresolved, particularly when we consider the universe as a whole. The Standard Model (SM) [2] is the most sophisticated and stringently tested theory but fails to describe certain critical features of the universe. The SM does not predict the existence of dark matter or dark energy, yet astrophysical observations [3] provide compelling evidence for both [4]. In fact, the SM only accounts for 4.6% of the energy-matter density of the universe. Furthermore, the SM does not predict a universe with more matter than antimatter [5], a fortunate feature of the universe for us, as we would not exist otherwise. Additional problems the SM does not address include the hierarchy problem, neutrino masses, the strong CP problem, and others such as proton decay or the cosmological constant problem.¹ This state of affairs constitutes something of a crisis in physics—our best theories do not seem able to describe much of our universe.

Building particle colliders and searching for new particles through their direct observation has been the primary means for searching for new physics (NP) that would help inform our understanding of the SM or expose its deficiencies. In these high-energy collision experiments, new particles are created and then detected. Although this effort is crucial, it is also costly. A complementary, substantially less expensive approach is to search for NP by conducting precision measurements in atomic physics and comparing the results with equally precise theoretical calculations. Finding deviations between theory and experiment is a signal for NP.

There are many examples where atomic physics as a subdiscipline contributes to this search. For example, the SM predicts that CPT (charge, parity, and time reversal) symmetry is exact.² The ALPHA-2 collaboration at CERN (European Organization for Nuclear Research) tested and confirmed this hypothesis by performing

¹Reconciling general relativity with the SM, via, e.g., string theory, does not constitute one of these problems, although it might solve one or more of these issues.

²CPT symmetry is thought to hold for all physical phenomena. Stated more precisely, any Lorentz invariant local quantum field theory with a Hermitian Hamiltonian must have CPT symmetry [6].

spectroscopy on antihydrogen [7]. Efforts within atomic physics have contributed significantly to searches for dark matter, as outlined in Ref. [8]. It is unknown what constitutes dark matter—a wide range of candidate particles have been studied, including those made from ordinary matter, such as Massive Compact Halo Objects (MACHOs) and primordial black holes, and also those involving exotic particles beyond the Standard Model, including Weakly Interacting Massive Particles (WIMPs) and axions [9]. The goal of a broad class of these efforts is to do terrestrial experiments to seek nongravitational interactions of dark matter with the particles and fields of the SM [8]. An example is the cosmic axion spin precession experiment (CASPER), which considers and tests the possibility that axion dark matter could cause the precession of nuclear spins [10].

Another incredibly active area of research involves the search for a nonzero electron electric dipole moment (eEDM) [11–13] that currently sets the upper limit on its value to $4.1 \times 10^{-30} e \text{ cm}$. A nonzero value³ would provide evidence for potential NP mechanisms leading to the baryon asymmetry. Future experiments at York University plan to place molecules in a cubic lattice of solid argon [15] or neon [16]. These experiments can now probe energies on the order of 1 PeV,⁴ much greater than those of which the Large Hadron Collider (13 TeV) [14] or its successor, the Future Circular Collider (~ 100 TeV) [19], are capable.

Further examples of atomic physics constituting NP searches include the $g - 2$ measurement in the electron [20] and the muon [21] and the so-called proton radius puzzle [22, 23].⁵ Deviations between the QED predictions for either of these quantities compared to their experimental measurement would be a signal for NP.

³The SM predicts an eEDM of approximately $10^{-38} e \text{ cm}$ [14]; the lowest measured upper limit is $4.1 \times 10^{-30} e \text{ cm}$ [13].

⁴Progressively lowering the upper limit on the eEDM probes correspondingly higher energies via ruling out new particles—expected to induce a much larger eEDM [17]—predicted at those higher energies in extensions to the SM [18].

⁵The proton radius puzzle has an exciting, recent history that began with the surprising revelation that the charge radius of the proton was 0.04 fm smaller using input data coming from spectroscopy on muonic rather than either electronic (normal) hydrogen [22] or scattering data. A very sophisticated Lamb shift measurement in 2019 confirms the 0.84 fm value [23].

1.2 OVERVIEW OF RESEARCH PROJECTS

The results of four research papers form the basis of this dissertation [24–27], which we have expanded to create three of the six chapters. These topics are briefly introduced here and are more comprehensively covered in the corresponding chapters.

Beta decay and charge-state distributions in ${}^6\text{He}$

Chapter 3 discusses the beta decay of the neutron-rich ${}^6\text{He}$ which has a lifetime of 0.8s. Beta decay is a radioactive process governed by the weak interaction where a neutron transforms into a proton, or vice-versa. Inside an atom, this implies that the daughter ion has a different nuclear charge than the parent ion and thus is a different element. This process is accompanied by the ejection of two leptons—an electron and an antineutrino, or a positron and a neutrino. The angle between these two leptons is related to the electron-antineutrino correlation coefficient, $a_{\beta\nu}$, which is actively studied in search of new physics beyond the Standard Model. This search is an example of a low-energy search for new physics, complementing the high-energy approaches taken at particle colliders such as the Large Hadron Collider at CERN [28].

The beta decay studied in this dissertation is described by the equation ${}^6\text{He} \rightarrow [{}^6\text{Li}^+] + \text{e}^- + \bar{\nu}$. The square brackets around the daughter ion indicate that “shake-up” to excited ${}^6\text{Li}^+$ states, along with “shake-off” to singly-ionized ${}^6\text{Li}^{++}$ states or doubly-ionized ${}^6\text{Li}^{3+}$ states, are possible. We are concerned with calculating the probabilities of forming each of these charge states in the daughter ion. In Chap. 3, we discuss developing and using two-electron projection operators capable of distinguishing single- and double-ionization channels. The aim is to reduce a large existing discrepancy between theory and experiment concerning the distribution over charge states of ${}^6\text{He}$ decay products, and especially the very small amount of double ionization.

Finite-nuclear-mass effects in two-photon decay in He-like ions

Astrophysical spectroscopy can be used to probe the physical conditions, such as temperature and pressure, of distant objects, including planetary nebulae and the

early universe itself. Helium constitutes 10% of the universe by number of atoms and therefore contributes significantly to the radiation observed in its study. The dominant contributions come from dipole-allowed transitions (e.g., $n^1P - n^1S$ transitions), however, dipole-forbidden transitions, such as the $2^1S - 1^1S$ spontaneous decay process studied here, are also important both in achieving high-precision and in frequency regions where the allowed emitted spectrum is relatively weak. Furthermore, forbidden rates are needed to calculate the population balance (distribution of atomic states in the atoms comprising remote astrophysical objects), a property needed to infer the aforementioned physical conditions.

In Chap. 4, we show calculations performed for two-photon decay rates, including the effect of finite nuclear mass—a small correction to the infinite nuclear mass case—for a series of heliumlike ions, including “heavy” systems such as muonic, pionic, and antiprotonic helium. One of the components of this correction is mass polarization, which corresponds to an additional term in the Hamiltonian governing the system that would otherwise be zero in the infinite-mass case. We treated this mass polarization term as a power series and demonstrated how algebraic relationships arise from this approach. These algebraic relationships test gauge equivalence between the length and velocity forms in n -photon transitions in heliumlike systems. We demonstrate their validity for the cases of $n = 1$ (single photon) and $n = 2$ (two photon) spontaneous decay. The significance of the algebraic relationships is that they provide an important new way of testing the accuracy of approximate calculations of radiative transition rates when exact wave functions are not available.

Testing QED with the tune-out frequency in helium

The tune-out frequency is the specific frequency of laser light incident upon an atom where the atom ceases to scatter that light and effectively becomes invisible to it. This situation is described as a zero in the Rayleigh scattering cross section. In lowest order, this corresponds to a zero in the dynamic polarizability, a quantity that involves a sum over a complete set of off-diagonal matrix elements of the electric dipole interaction. In this way, studying the tune-out frequency amounts to a test of QED,

involving an atomic property other than a QED energy shift such as the Lamb shift. In higher order, retardation corrections distinguish the Rayleigh scattering picture from the more usual dynamic polarizability. In Chapter 5, the tune-out frequency is calculated to high precision in the framework of nonrelativistic QED (NRQED) and the results are compared with experiment, forming the first test of QED that does not involve an energy shift. A comparison with experiment shows that there remains a 1.7σ discrepancy that requires further work.

1.3 METHODOLOGY OVERVIEW

1.3.1 Introduction to pseudospectral methods

Chapter 2 describes the general theoretical methods applicable to all projects discussed in the dissertation, while each chapter describes the particular details relevant to the project under discussion. In the present section, we discuss the common element across all studies—the use of *pseudospectra*, which are complete set of *pseudostates*. Pseudospectral methods can be defined in comparison to spectral methods, which solve differential equations, such as the Schrödinger equation

$$H\psi = E\psi, \tag{1.1}$$

with which we are concerned here, by using true eigenstates of the system’s Hamiltonian. An example of a spectral method is a complete Fourier series, where the sines and cosines are eigenfunctions (they solve the corresponding differential equation under certain boundary conditions) of some operator, e.g., in the heat equation. In pseudospectral methods, on the other hand, a finite number of pseudostates approximate the true eigenstates, as in a truncated Fourier series used in applications such as image processing. The primary use of pseudospectra in this dissertation is to carry out sums over the complete Hilbert space of the Hamiltonian—which involves an in-

finite set of bound and continuum states.⁶ Here, spectral methods would involve an infinite sum and integral and are not computationally realizable.

This section is not intended to be a rigorous description of how to obtain pseudostates or their properties, a subject discussed in Chap. 2, but instead aims to demonstrate their usefulness via two examples.

1.3.2 Examples using pseudospectra

The calculation of the polarizability of the ground state of hydrogen offers one striking example of the usefulness of pseudospectra, shown in Fig. 1.3.1. The static polarizability d_z is defined as

$$d_z = -2 \sum_{np \neq 1s} |\langle \varphi_{1s} | z | \varphi_{np} \rangle|^2 / (E_{1s} - E_{np}) = 9/2, \quad (1.2)$$

where φ_{1s} , φ_{np} are the unperturbed exact wave functions that solve Eq. (1.1) and E_{1s} , E_{np} are their energies, and the sum runs over the infinite set of $\{\varphi_{np}\}$ eigenstates which connected to φ_{1s} through the dipole operator z . This quantity has an exact value (9/2) because it can be expressed as a convergent infinite sum over both discrete and continuum states over the excited states of hydrogen that. The form of the polarizability is not especially relevant; it is only crucial to understand that its calculation involves a sum over the complete set of eigenstates of the Hamiltonian.

In Fig. 1.3.1, the exact ground state of hydrogen, φ_{1s} , was used, however, the infinite sum over $\{\varphi_{np}\}$ was replaced by a pseudospectra with basis functions of the form $\chi_j = \sum_{i=1}^N c_{ij} r^i e^{-\alpha r} Y_{10}$. Three pseudospectra are considered, with $N = 2, 3, 5$ in the plotted examples, corresponding to two, three, and five term basis sets.

Figure 1.3.1 introduces some essential concepts that will recur in this dissertation. Firstly, along the x -axis is the nonlinear parameter α —pseudospectra will be formed with both linear and nonlinear parameters that we will vary, usually to minimize energy eigenvalues. Additionally, the number of terms corresponds to enlarging the

⁶Furthermore, the exact eigenfunctions and eigenvalues for helium or any general three-body problem is impossible. Helium is the quantum mechanical version of the sun-earth-moon (three-body) problem that lamented Newton many centuries ago.

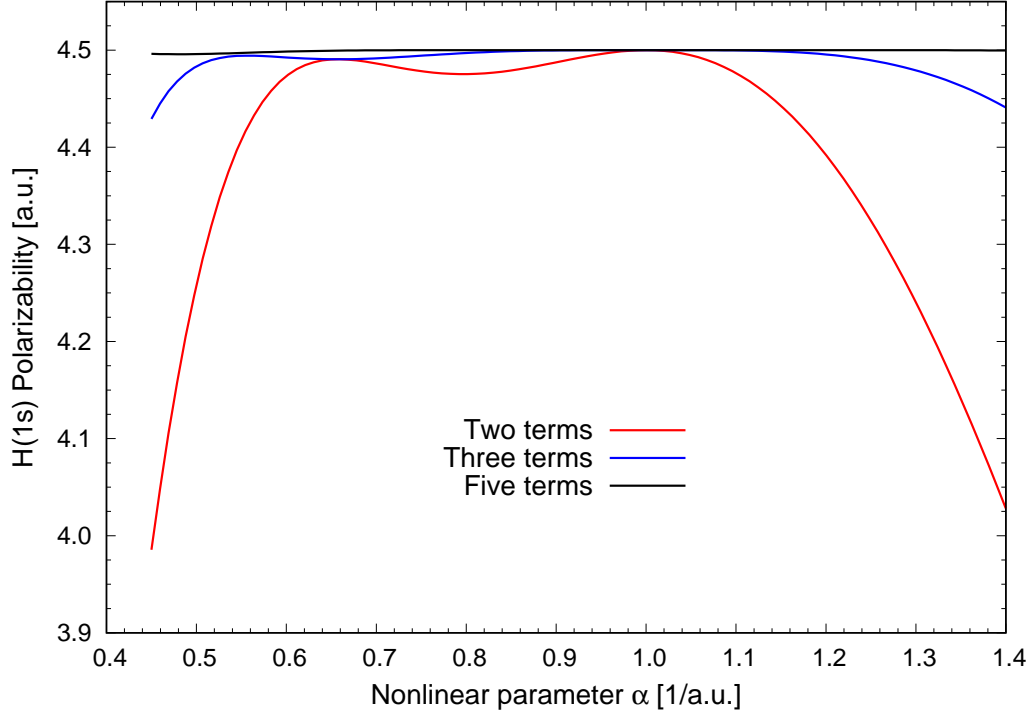


Fig. 1.3.1: Shown are the polarizabilities, calculated according to Eq. (1.2), of the ground state of hydrogen (The correct answer in the nonrelativistic limit is 4.5 a.u.). The pseudospectra used have basis functions of the form $\chi_j = \sum_{i=1}^N c_{ij} r^i e^{-\alpha r} Y_{10}$, as described in the text. The nonlinear parameter α is varied to show regions of stability. It is remarkable that, even for a two-term pseudospectrum, when $\alpha = 1$, there is already an exact representation of the complete spectrum. For a five-term pseudospectra, we see a large region of stability, where d_z is correctly calculated for the entire $\alpha \in [0.44, 1.4]$.

basis set, a method used to obtain convergence. For the polarizability, we see this convergence take place moving from $N = 2$, where only certain nonlinear parameters lead to the true polarizability, to $N = 5$ where there is a broad region of stability.

Another example demonstrating the power of pseudospectra involves the calculation of the Bethe logarithm, involving a sum over states in both the numerator and denominator,⁷ which is part of the Lamb shift and is thus an important QED contribution in atomic physics. Figure 1.3.2 shows the value of the Bethe logarithm of H as a function of the highest-energy eigenvalue included in the partial sum, using the formulation developed by Drake and Goldman [29]. We see a few things from this curve. Firstly, one must go to very high energies, about 10^8 a.u., before obtaining

⁷The partial sum is given by $\beta(E) = \mathcal{N}/\mathcal{D}$, where $\mathcal{N} = \sum_i |\langle 0|\mathbf{p}|i\rangle|^2 (E_i - E_0) \ln |E_i - E_0|$ and $\mathcal{D} = \sum_i |\langle 0|\mathbf{p}|i\rangle|^2 (E_i - E_0)$

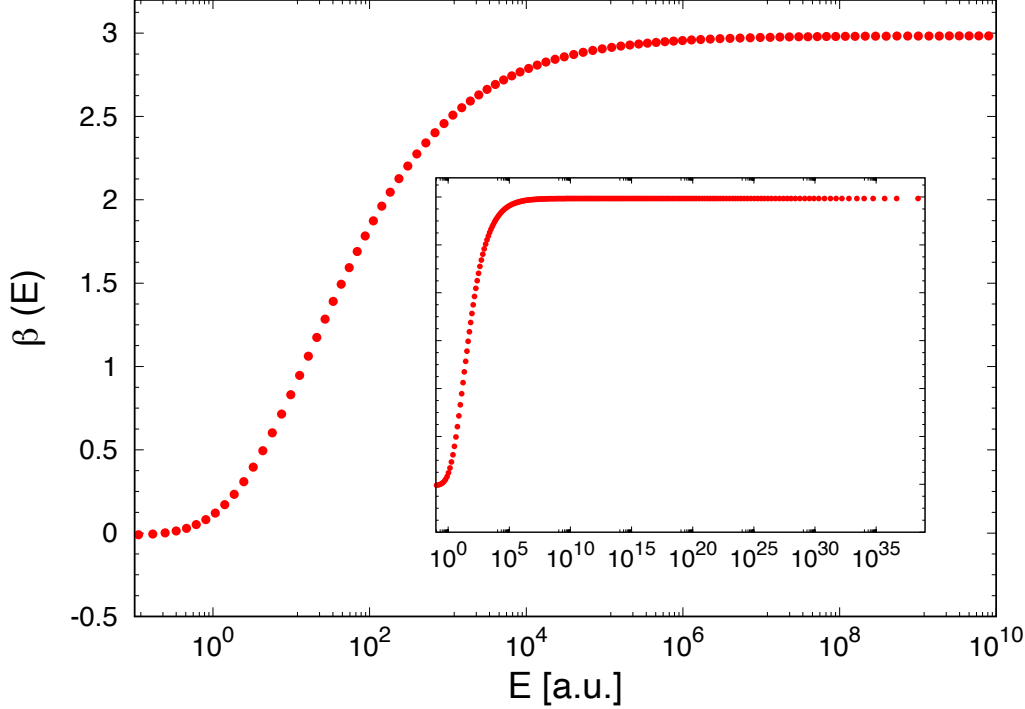


Fig. 1.3.2: The partial sum of the Bethe logarithm of H , $\beta(E)$, is plotted as a function of the last—also largest—energy contained in the partial sum. Created using the formulation developed by Drake and Goldman [29].

convergence in $\beta(E)$ and also, from the inset, that this method allows us to go to extremely high energies—almost 10^{40} a.u.

Despite the seemingly negative connotations of the term “pseudo” in general language, implying something false, this dissertation shows the invaluable role that pseudostates play in advancing our understanding of atomic systems and making possible otherwise inaccessible calculations. Through a series of projects, we will explore how pseudostates make possible profound and otherwise unattainable insights by facilitating atomic and molecular physics calculations.

1.4 SCOPE AND SIGNIFICANCE OF RESEARCH

The potential impact of this research is immense. Both the beta decay and tune-out projects seek to rectify the *crisis* that is the incompleteness of the SM by contributing directly to searches for NP. The SM makes a definite prediction about the kinematics

following beta decay and about the precise frequency at which the helium atom should become invisible to an applied laser field, i.e., the tune-out frequency. We perform calculations involving two-electron wave functions formed using Hylleraas basis states to answer whether or not the SM agrees with our collaborator’s measurements in answer to these questions. This research either confirms the SM or finds a deviation that requires more attention. This possible deviation, by itself, would not unravel the SM—to be sure, this is a physics-wide effort to probe every nook and cranny that we find plausible and possible to examine. If the discrepancy is genuine, it would pinpoint the area to explore when considering how NP might build on the existing SM.

The other two projects are related and aim to answer less extravagant but no less universal questions. In astrophysical observation, the population balance of astrophysical sources contains information about the temperature, composition, pressure, and more concerning a distant astrophysical body or, in the case of the cosmic microwave background radiation, about the early universe itself. Therefore, since helium comprises 10% of the atoms in the universe, accurate calculations of properties of two-electron atoms, such as energies and transition rates, are essential. To this end, we present calculations of the $2E1$ transition rates of helium, including the effects of a finite nuclear mass but not relativistic effects, which also contributes at an experimentally relevant level.

A central objective within this dissertation is to answer questions such as those posed above by using pseudospectral techniques described and defined in the preceding section, thereby demonstrating and exploiting their ubiquity as a computational technique in atomic physics.

1.5 STRUCTURE OF THE DISSERTATION

We synthesize four research projects in this document in three separate chapters. Each of these is self-contained in the same sense as a research paper.⁸ However, the chapters are not strict reproductions of the research papers, and they do relegate some information to the overall theory chapter or appendices when that format is more sensible as it functions in the entire document.

The main body of this dissertation consists of six chapters, of which this section concludes the first chapter: the Introduction. Chapter 2 outlines the theoretical methods underpinning the computation and analysis common to all projects studied. Chapters 3, 4, 5 contain more detailed theoretical aspects of the individual works, where the particular projects are discussed in detail. On this note, Ch. 3 contains work on the beta decay of ${}^6\text{He}$, Ch. 4 describes calculations concerning the two-photon decay of helium and also about exploring algebraic relationships that arise therein in treating mass polarization, and Ch. 5 outlines the first test of QED other than energy shifts based on the tune-out frequency of helium. Chapter 6 provides an overall conclusion of the whole dissertation and discusses future work.

Several appendices include material that was either tangential to the main discussion or too substantial to include in the relevant section of the document.

⁸The relative lengths of the chapters is indicative of the proportion of time spent on each of these projects.

CHAPTER 2

Theoretical Methods

2.1 OVERVIEW

This chapter presents an overview of the theoretical frameworks and methods common to all chapters of this dissertation. Atomic structure problems boil down to computing matrix elements, i.e., integrals, between two wave functions connected by an operator. Accordingly, the central objective in solving structure problems is to establish precisely how we obtain the wave functions and carry out these integrals.¹ Due to the nature of this dissertation—being based on four published papers [25–27], separated into chapters—we present more specialized “theoretical” material in the relevant chapters.

The contents of this chapter are as follows. After discussing atomic units in Sec. 2.2, the one-electron problem is stated and solved in Sec. 2.3, leading to the concept of Sturmian functions, discussed in Sec. 2.4. Then the two-electron problem is developed in Sec. 2.5 and is then solved throughout Secs. 2.6 and 2.7. In Sec. 2.6, the variational methods used are described, while Sec. 2.7 describes the Hylleraas wave functions employed as trial functions in this work. Finally, Sec. 2.8 outlines the analytic forms of the integrals needed in the calculations contained in this dissertation.

¹Substantial portions of the material in this chapter are heavily influenced by the collected writings and notes of G. W. F. Drake, including published works and formal and informal sets of notes and verbal correspondence. References appear where appropriate.

2.2 ATOMIC UNITS

A few comments on atomic units (a.u.)—which appear several times in the Introduction and are ubiquitous in atomic physics—are in order.² The defining property is to set the following quantities to unity:

$$m_e = \hbar = e = 4\pi\epsilon_0 = 1. \quad (2.1)$$

These assignments correspond to measuring mass in units of the mass of the electron, m_e , angular momentum in units of \hbar , charge in units of the electron charge, e , and vacuum permittivity in terms of $4\pi\epsilon_0$.

A few important scales emerge from these definitions. Carried out in SI units, the energies of the bound states of the infinite-nuclear-mass, one-electron problem have the form

$$E_n = \frac{e^2}{a_0} \left(\frac{-Z^2}{2n^2} \right), \quad (2.2)$$

where Ze is the nuclear charge, n is the principal quantum number,³ and a_0 is the *Bohr radius*, defined by

$$a_0 = \frac{4\pi\epsilon_0\hbar^2}{me^2}. \quad (2.3)$$

In atomic units, we measure energies in units of the prefactor of Eq. (2.2), which we refer to as the *Hartree energy* E_h

$$E_h = \frac{e^2}{a_0}, \quad (2.4)$$

We measure distances using the aforementioned Bohr radius. Both a_0 and E_h are 1 in atomic units.

The time-independent Schrödinger equation is stated in Sec. 2.3 in SI units and then transformed to atomic units. In Sec. 2.5.1, we further simplify, for computational purposes, to dimensionless Z -scaled atomic units where distances and energies are given by $\rho = Zr/a_0$ and $\varepsilon = Ea_0/(Ze)^2$, respectively.

²Atomic units were developed in 1928 by Hartree [30] to reduce the large number of constants that we would otherwise need to carry around in basic calculations in quantum mechanics and, therefore, atomic physics.

³Details on solving the one-electron Schrödinger equation appear in Sec. 2.3.

The idea is to perform calculations entirely in atomic units and only at the very end substitute back in the SI values of the constants used in the calculations.⁴ The current values are [31]

$$\begin{aligned} E_h &= 27.211\,386\,245\,981(30) \text{ eV} \\ &= 4.359\,744\,722\,2060(48) \times 10^{-18} \text{ J, and} \\ a_0 &= 5.291\,772\,105\,44(82) \times 10^{-11} \text{ m.} \end{aligned}$$

Finally, a comment on the dimensionless *fine-structure constant*, α , defined by [31]

$$\alpha = \frac{e^2}{4\pi\epsilon_0\hbar c} = 7.297\,352\,5643(11) \times 10^{-3}, \quad (2.5)$$

with c being the speed of light, is warranted. A consequence is that the speed of light is approximately 137 in atomic units. The fundamental measurement quantities can be expressed in terms of α , e.g.,

$$a_0 = \frac{\hbar}{\alpha mc} \quad \text{and} \quad E_h = \alpha^2 mc^2$$

High-precision atomic physics uses the fine-structure constant as an essential expansion parameter, treating relativity and QED effects as perturbations in α .

All quantities stated in this dissertation are assumed to be in atomic units unless indicated otherwise.

2.3 ONE-ELECTRON SCHRÖDINGER EQUATION

The one-electron atom or ion is a two-body problem where the electron and nucleus⁵ interact via the Coulomb interaction. We are concerned here with the nonrelativistic, time-independent case. The primary purpose of this section is to set the stage for the following section about Sturmian functions—by establishing the radial solutions

⁴The currently accepted values of these quantities are found at <https://physics.nist.gov/cuu/Constants/index.html>.

⁵Here, we treat the nucleus as a single body of mass M and charge Z .

to the one-electron Schrödinger equation. To this end, the details are kept brief. The nonrelativistic (NR) time-independent Schrödinger equation,⁶ $H\psi = E\psi$, for the one-electron problem with an infinitely heavy nucleus is:

$$H = -\frac{\hbar^2}{2m} \nabla^2 - \frac{Ze^2}{4\pi\epsilon_0 r}, \quad (2.6)$$

$$H = -\frac{1}{2} \nabla^2 - \frac{Z}{r} \quad (\text{in a.u.}), \quad (2.7)$$

where \hbar , m , Z and ϵ_0 are Planck's constant, the electron mass, the nuclear charge and the vacuum permittivity, respectively, and r , is the electron distance from the nucleus. The second line is expressed in atomic units.

This equation separates in spherical coordinates (r, θ, ϕ) according to

$$\psi(\mathbf{r}) = Y_{\ell m}(\theta, \phi) R_\ell(r) \quad (2.8)$$

with the spherical harmonics, $Y_{\ell m}(\theta, \phi)$, solving the angular part [32, pp. 19–25]. The radial equation

$$\left[-\frac{1}{2} \left(\frac{d^2}{dr^2} + \frac{2}{r} \frac{d}{dr} - \frac{\ell(\ell+1)}{r^2} \right) - \frac{Z}{r} \right] R_\ell(r) = E R_\ell(r), \quad (2.9)$$

has solutions

$$R_\ell(r) = r^\ell \exp(ikr) [A {}_1F_1(a; c; z) + BU(a, c, z)] \quad (2.10)$$

where ${}_1F_1$ and U are the regular and irregular solutions to the confluent hypergeometric functions (see, e.g. [33] for their solutions), A and B are arbitrary constants,

⁶For the structure problems in Chaps. 4 and 5, the time-independent Schrödinger equation is the appropriate starting point. In studying the time-dependent beta decay process in Chap. 3, we make the sudden approximation and therefore use the time-independent Schrödinger equation there as well.

and k, a, c, z are defined as

$$\begin{aligned} k &= \sqrt{2E}, \\ a &= \ell + 1 - ik^{-1}Z, \\ c &= 2\ell + 2, \\ z &= -2ikr. \end{aligned} \tag{2.11}$$

Eq. (2.8), using the radial function Eq. (2.10), has a complete set of solutions, including both bound states, defined by $E < 0$, and continuum states, given by $E > 0$. These are also known as Coulomb wave functions.

The bound state solutions occur when $a = -n + \ell + 1$ is a negative integer and have the form

$$R_{nl}(Zr) = \rho^\ell e^{-Zr/n} {}_1F_1(-(n - \ell - 1); 2\ell + 2; 2Zr), \tag{2.12}$$

with energies given by

$$E_n = -\frac{Z^2}{2n^2}, \tag{2.13}$$

where $n = 1, 2, 3, \dots$ is the principal quantum number and $\ell = 0, \dots, n - 1$ is the angular momentum quantum number. ${}_1F_1(a; b; z)$ is the confluent hypergeometric function of the first kind and is a finite polynomial of order $n - \ell - 1$ with $n - \ell$ terms. This form of radial powers multiplied by exponentials guides the formation of approximate two-electron wave functions in Sec. 2.7.1.

With an eye toward the prospect of performing computations on hydrogenlike atoms wherein we must sum over the complete set of eigenstates of H in Eq. (2.7), a task shown to be important in the Introduction, we can make some comments. Eq. (2.10) is the correct equation, but it contains two infinities of states: a denumerable infinity of bound states and an uncountably infinite set of continuum states. It is the latter of these that poses the much more significant obstacle. If we were summing over the bound state solutions, we could at least search for convergence as $n \rightarrow \infty$ in whatever property we study. This approach would work if it were to turn out that contributions to the sum diminished rapidly enough in this limit. This

strategy is even more difficult with the continuum, where we could seek convergence in the corresponding integral as $E \rightarrow \infty$. In general, to carry out a complete sum over states, we need to actually represent this complete set. These considerations lead us to the discussion of Sturmian functions, a topic central to the study of overlapping ionization channels in the beta decay of ${}^6\text{He}$ that is the subject of Chap. 3.

2.4 STURMIAN FUNCTIONS

Any homogeneous linear second-order differential equation⁷ can be written in the Sturm-Liouville form [34]

$$\frac{d}{dx} \left[K(x) \frac{dy}{dx} \right] - G(x)y = 0, \quad (2.14)$$

defined on the closed interval $x \in [a, b]$ and supplemented with appropriate boundary conditions. The choice $G(x) = -\lambda g(x) + l(x)$ yields an eigenvalue problem where λ can be adjusted to satisfy the boundary conditions.⁸

2.4.1 The oscillation theorem

The oscillation theorem, as described by Drake [34] and Ince [35], provides insight into the nodal properties of Sturmian eigenfunctions. The theorem is as follows.

Theorem 1 (Sturmian Oscillation Theorem). *Suppose $K(x), g(x)$, and $l(x)$ are continuous, real, positive⁹, and monotonically decreasing on $[a, b]$. Then the Sturm-Liouville problem*

$$\frac{d}{dx} \left[K(x) \frac{dy}{dx} \right] + [\lambda g(x) - l(x)]y = 0, \quad (2.15)$$

has an infinite sequence of discrete eigenvalues $\lambda_1 < \lambda_2 < \lambda_3 \dots$ with eigenvectors $y_1, y_2, y_3 \dots$ such that $y_m(x)$ has $m - 1$ zeroes on the interval $[a, b]$. The eigenvectors

⁷The radial Schrödinger equation in Eq. (2.9) is one example where $r \rightarrow x$ and $R(r) \rightarrow y$.

⁸All functions of x , namely $K(x), G(x), g(x)$, and $l(x)$, are arbitrary.

⁹The conclusion of the theorem holds in the case that g undergoes a sign change on the interval of interest, but we do not require this for the following discussion.

are orthogonal with respect to $g(x)$, and the set $\{y_m(x)\}$ forms a Sturmian basis set—which is complete.

The critical consequence of this theorem is that the Sturmian basis set, a generalized Fourier series, is complete: one can expand an arbitrary function $f(x)$ in this basis set. Notably, the eigenvalues of this basis set are discrete. Consider momentarily the formal solutions to the Schrödinger equation just discussed in the previous section. In obtaining these solutions to the radial equation in Eq. (2.9) on the interval $r \in [0, \infty]$, one effectively holds Z fixed while varying E , subject to the boundary conditions

$$\lim_{r \rightarrow 0} rR(r) = 0, \quad \lim_{r \rightarrow \infty} R(r) = 0 \quad (2.16)$$

leading to an infinite set of bound states and continuum states [34].

The Coulomb problem can be formulated as a Sturm-Liouville problem meeting the criteria outlined in Theorem 1 by writing the radial equation as

$$\left[-\frac{1}{2} \left(\frac{d^2}{dr^2} + \frac{2}{r} \frac{d}{dr} - \frac{\ell(\ell+1)}{r^2} \right) - \frac{\lambda}{r} \right] R_\ell(r) = E R_\ell(r), \quad (2.17)$$

where we regard E as fixed, along with a variable nuclear charge, denoted by λ . The procedure for generating the complete and discrete basis set is as follows. Consider a fixed negative energy $E = -\epsilon$ with $\epsilon > 0$. The horizontal line denotes this energy, E , in Fig. 2.4.1. The general strategy is to keep this energy fixed, vary the potential (λ), and look for normalizable solutions.¹⁰ The Schrödinger equation has solutions $E_n(Z) = -\frac{Z^2}{2n^2}$, meaning that a particular $E_n(Z) = -\epsilon$ can be satisfied infinitely many times via progressively increasing both λ and n . As the parameter λ increases, corresponding to increasing Z and making the potential more attractive, we pull one eigenvalue after another down through the fixed $E = -\epsilon$; these states have eigenvalues $\lambda_n = n\sqrt{2\epsilon}$. Whenever a solution to the Schrödinger equation is pulled down through $E = -\epsilon$, another solution to the Sturm-Liouville problem is obtained—a process yielding discrete eigenstates that can occur infinitely many times. Fig. 2.4.1

¹⁰We write λ instead of Z to emphasize that this is an adjustable parameter in this Sturmian formulation.

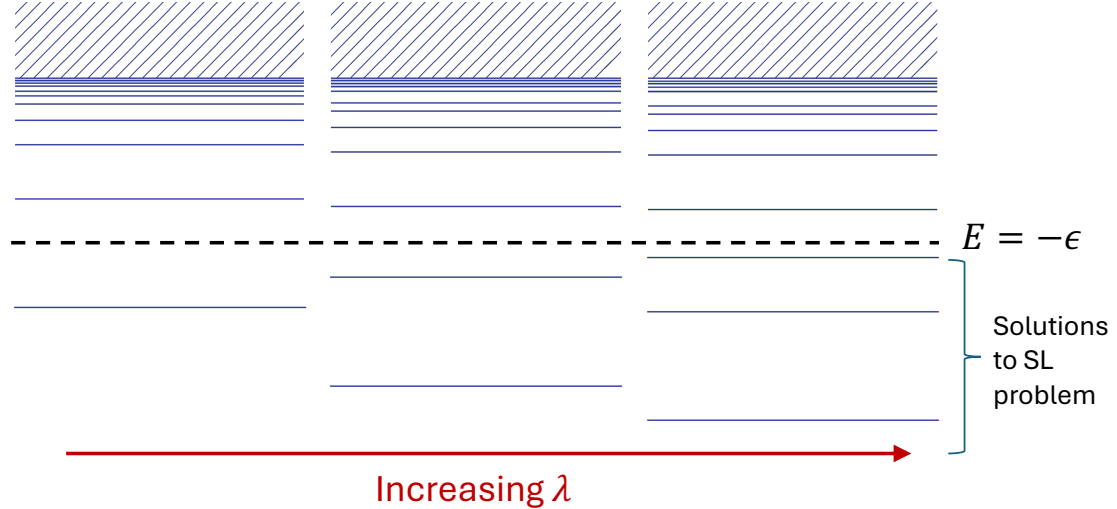


Fig. 2.4.1: The principle of generating solutions to the Sturm-Liouville (SL) equation is shown. By holding E fixed to some negative number and progressively increasing λ in Eq. (2.17), we obtain more and more solutions. The spacings are not drawn to scale; the only relevant detail is that more and more states are pulled below the fixed $E = -\epsilon$.

illustrates this procedure. The resulting set of discrete Sturmian states is complete in the limit where the number of states so obtained, N , tends to infinity [36, 37]. This set constitutes a pseudospectrum since they approximate the true eigenstates of the Hamiltonian while providing a complete basis representing bound and continuum states.

The solutions to this Sturm-Liouville radial equation are called *Sturmian functions* and have the form

$$R_{nl}(r) = \frac{1}{(2l+1)!} \left(\frac{(n+l)!}{(n-l-1)!2n} \right)^{1/2} (2\alpha)^{3/2} (2\alpha r)^l e^{-\alpha r} {}_1F_1(-n+l+1, 2l+2; 2\alpha r) \quad (2.18)$$

where $\alpha = \sqrt{2\epsilon}$ and $n \geq l+1$. Since the first argument of ${}_1F_1$ is negative, this corresponds to a finite polynomial function of r . These solutions look similar to the bound-state solutions to the radial Schrödinger equation given in Eq. (2.12), especially because both are sets of functions with discrete eigenvalues. However, Theorem 1 guarantees that, unlike the bound-state solutions, which do not include

the continuum, the set of Sturmian functions¹¹ in Eq. (2.18), in the limit where the number of states approaches infinity, does.

Another difference with the bound-state solutions lies in the critical detail that the exponent of the Sturmian functions does not depend on n . Instead, the exponential factor $-\alpha r$ is constant in Sturmian functions. Thus, Sturmian radial functions are a polynomial function multiplied by $e^{-\alpha r}$. Therefore, we can create a pseudospectra by diagonalizing the one-electron Hamiltonian in terms of basis functions with linear combinations of $\chi = r^n e^{-\alpha r}$ functions. These structure of these functions is informed by their physical relevance: they capture the appropriate near-nucleus and asymptotic behaviour of the true wave functions of the hydrogen atom. Indeed, as the introductory quote of this thesis says, the pseudostates are “false states”, i.e., they are not the exact solutions of the one-electron Hamiltonian. Even so, they are complete, and we will see that this property is even more essential and useful.

In conclusion, the preceding discussion of the Sturmian theory provides a rigorous foundation for choosing $\chi_i = c_i r^n e^{-\alpha_i r}$ type basis functions in the one-electron problem. Often, the basis functions are the sum of several such functions, $\chi = c_1 \chi_1 + c_2 \chi_2 + \dots$, where each term has a different linear parameter (coefficient) c_i and nonlinear parameter α_i . In Sec. 2.6, the minimization principles that govern the optimization of these parameters are described. We show in Sec. 2.7.3 that this property of Sturmian functions informs our choice of two-electron basis functions [38].

¹¹Additionally, according to Theorem 1, the Sturmian functions are orthogonal with respect to the potential $1/r$. In this dissertation, we orthogonalize these basis states, an operation which preserves completeness.

2.5 TWO-ELECTRON SCHRÖDINGER EQUATION

2.5.1 Problem statement

The two-electron Schrödinger equation in SI units for infinite nuclear mass¹² is [39]

$$\left[-\frac{\hbar^2}{2m}(\nabla_1^2 + \nabla_2^2) - \frac{Ze^2}{r_1} - \frac{Ze^2}{r_2} + \frac{e^2}{r_{12}} \right] \psi = E\psi \quad (2.19)$$

where \mathbf{r}_1 and \mathbf{r}_2 are the radial coordinates of the two electrons and $r_{12} = |\mathbf{r}_2 - \mathbf{r}_1|$ are Hylleraas coordinates and are defined in Fig. 2.5.1. We rewrite this in dimensionless Z -scaled units¹³ according to $\rho = Zr/a_0$ as

$$\left[-\frac{1}{2}(\nabla_{\rho_1}^2 + \nabla_{\rho_2}^2) - \frac{1}{\rho_1} - \frac{1}{\rho_2} + \frac{Z^{-1}}{\rho_{12}} \right] \psi = \varepsilon\psi, \quad (2.20)$$

with $\varepsilon = Ea_0/(Ze)^2$. Eq. (2.20) is the form of the Schrödinger equation that we solve throughout this dissertation.

Owing to the presence of the $1/\rho_{12}$ term, the two-electron problem in Eq. (2.20) cannot be separated, and it cannot be solved exactly as in the case of the one-electron problem [40, pp. 5–15]. The helium atom is the quantum mechanical three-body problem—a problem whose classical analogue is known to lack closed-form solutions for the general case.¹⁴ In practice, the fact that analytic solutions are unavailable is not a problem since numerical methods exist that are essentially exact for structure calculations in atomic physics.

¹²Chapter 4 contains work incorporating finite-nuclear-mass effects in $nE1$ transition rates in two-electron atoms. Treatment of the finite-nuclear-mass Hamiltonian is left to this chapter.

¹³This method allows the interelectron potential, $1/\rho_{12}$, to be treated as a perturbation in powers of $1/Z$.

¹⁴The prototypical example is the earth-moon-sun system that was first studied by Newton—and subsequently by the best mathematical minds for countless generations after that—in connection with the question of the stability of the solar system. Upon proving that the two-body system has closed-form solutions [41], Newton was shocked to discover that he could not solve the three-body problem—which “made his head ache, and kept him awake so often, that he would think of it no more” [1].

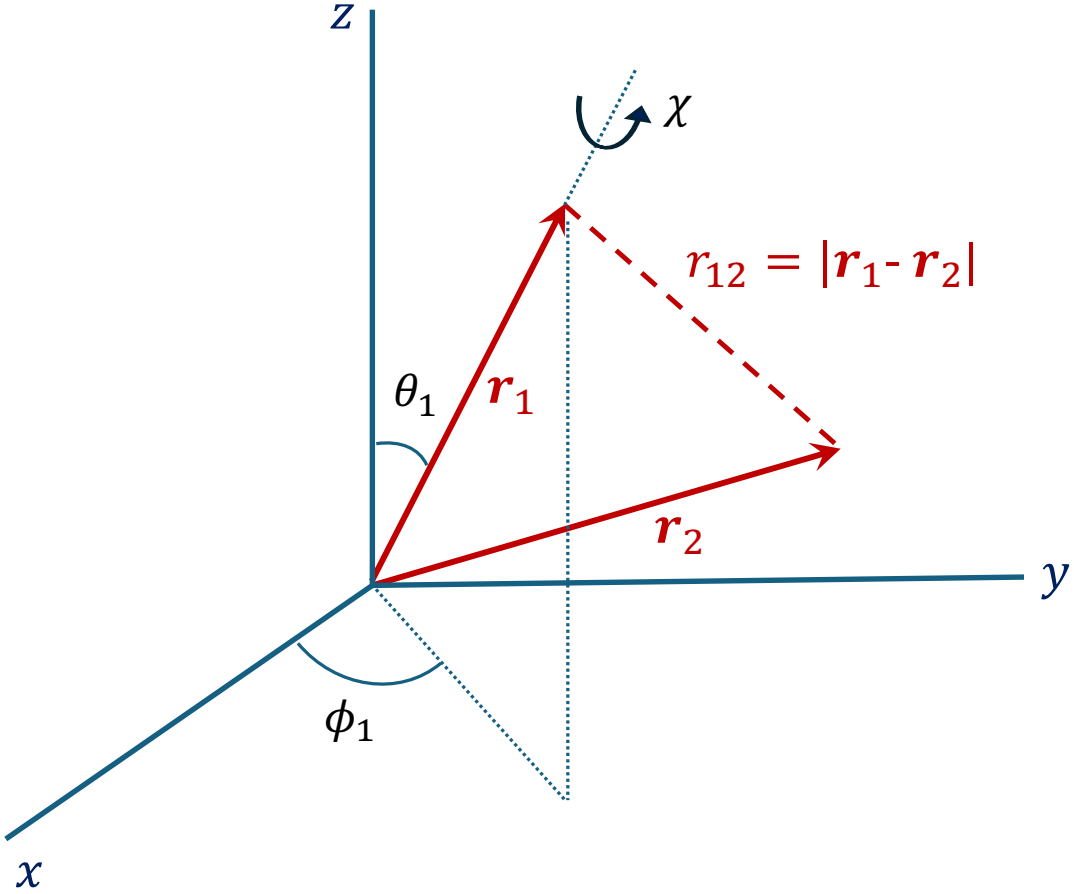


Fig. 2.5.1: An illustration of Hylleraas coordinates. The full set of independent radial ($r_1 = |\mathbf{r}_1|$, $r_2 = |\mathbf{r}_2|$, $r_{12} = |\mathbf{r}_1 - \mathbf{r}_2|$) and angular (θ_1, ϕ_1, χ) coordinates are shown for two electrons located at \mathbf{r}_1 and \mathbf{r}_2 relative to the centre-of-mass. Here, θ_1, ϕ_1 are the polar and azimuthal angles of electron 1 and χ is the angle of rotation of the rigid triangle formed by the $\mathbf{r}_1, \mathbf{r}_2$ and \mathbf{r}_{12} .

2.5.2 Spin: singlet and triplet solutions

Two separate spin configurations of two-electron systems exist: *singlet* and *triplet* states. This is a direct consequence of the fact that fermions must have a totally antisymmetric wave function. Wave functions can generally be written as a product of a spatial and spin part. This is a trivial matter in treating the one-electron Coulomb problem, and thus Eq. (2.8) only contains the spatial (r, θ, ϕ) part. The full one-electron eigenstates are a product of the spatial and spin components, $\psi\chi = RY\chi$. Since electrons are particles of spin- $\frac{1}{2}$, there are two spin states: spin up $\chi_{\uparrow} = \begin{pmatrix} 1 \\ 0 \end{pmatrix} \equiv |\frac{1}{2} \frac{1}{2}\rangle$ and spin down $\chi_{\downarrow} = \begin{pmatrix} 0 \\ 1 \end{pmatrix} \equiv |\frac{1}{2} - \frac{1}{2}\rangle$. These are written of the form $|s m_s\rangle$ where

s is the spin quantum number, and m_s is the component of spin angular momentum, which has units of \hbar . It is usual to label the one-electron spin-state with $m_s = \pm \frac{1}{2}$ alone, since $s = \frac{1}{2}$ for all electrons.

For two-electron systems, the criterion of a totally antisymmetric wave function can be expressed as [42]

$$\Psi(1, 2) = \begin{cases} \psi^S(\mathbf{r}_1, \mathbf{r}_2)\chi^A(1, 2) \\ \text{or} \\ \psi^A(\mathbf{r}_1, \mathbf{r}_2)\chi^S(1, 2), \end{cases} \quad (2.21)$$

meaning that spatial (ψ) and spin (χ) parts of the total wave function Ψ must have opposite symmetry. The symmetric/antisymmetric spatial wave functions are

$$\psi^S(\mathbf{r}_1, \mathbf{r}_2) = \frac{1}{\sqrt{2}}[\psi(\mathbf{r}_1, \mathbf{r}_2) + \psi(\mathbf{r}_2, \mathbf{r}_1)], \text{ and} \quad (2.22)$$

$$\psi^A(\mathbf{r}_1, \mathbf{r}_2) = \frac{1}{\sqrt{2}}[\psi(\mathbf{r}_1, \mathbf{r}_2) - \psi(\mathbf{r}_2, \mathbf{r}_1)]. \quad (2.23)$$

For the spin part, we now adopt the notation of $|m_{s,1} m_{s,2}\rangle$ for the coupled state $|\frac{1}{2} m_{s,1}\rangle |\frac{1}{2} m_{s,2}\rangle$. Four possibilities have a well-defined symmetry. Three of which are symmetric:

$$\chi^S = \begin{cases} |\frac{1}{2} \frac{1}{2}\rangle \\ \frac{1}{\sqrt{2}} [|\frac{1}{2} \frac{1}{2}\rangle + |\frac{1}{2} -\frac{1}{2}\rangle] \\ |\frac{1}{2} -\frac{1}{2}\rangle, \end{cases} \quad (2.24)$$

and one is antisymmetric

$$\chi^A = \frac{1}{\sqrt{2}} [|\frac{1}{2} -\frac{1}{2}\rangle - |\frac{1}{2} \frac{1}{2}\rangle]. \quad (2.25)$$

The three symmetric spin states χ^S in Eq. (2.24) form a product with the anti-symmetric spatial state ψ^A in Eq. (2.23), forming the triplet configurations. The

antisymmetric spin state χ^S combines with ψ^S , giving the singlet configuration. We solve the Schrödinger equation, Eq. (2.20), yielding the spatial part of the wave function, and thus the singlet and triplet states are ψ^S and ψ^A with the “+” and “-” signs, respectively, between the direct and exchange terms in Eqs. (2.22) and (2.23). Both singlet and triplet states are studied in this dissertation.

2.6 VARIATIONAL PRINCIPLE

Without exact solutions, we construct approximate solutions that become complete in the infinite limit obtained via progressively increasing the number of basis functions.

2.6.1 Rayleigh-Ritz variational method

For any normalizable trial function Ψ_{tr} , the quantity

$$E_{\text{tr}} = \frac{\langle \Psi_{\text{tr}} | H | \Psi_{\text{tr}} \rangle}{\langle \Psi_{\text{tr}} | \Psi_{\text{tr}} \rangle} \quad (2.26)$$

is an upper bound according to $E_{\text{tr}} \geq E_1$, where E_1 is the true ground state energy [43]. This can be shown by expanding Ψ_{tr} in the complete basis set of orthonormal eigenfunctions¹⁵ $\phi_1, \phi_2, \phi_3, \dots$ of H with eigenvalues $E_1 < E_2 < E_3 < \dots$, such that

$$\Psi_{\text{tr}} = \sum_{i=1}^{\infty} c_i \phi_i, \quad (2.27)$$

where $\{c_i\}$ are the expansion coefficients. The normalization of Ψ_{tr} ensures $\sum_{i=1}^{\infty} |c_i|^2 = 1$.

The expression for the energy of the trial wave function is then

$$E_{\text{tr}} = \langle \Psi_{\text{tr}} | H | \Psi_{\text{tr}} \rangle, \quad (2.28)$$

¹⁵Even though we do not know what these eigenfunctions are, it can be assumed that such a set, whose eigenvalues are the true energies, exists and is complete. This follows the observation that the two-electron Hamiltonian operator is self-adjoint in an appropriate Hilbert space.

and, upon expanding Ψ_{tr} in terms of the exact eigenfunctions $\{\phi_i\}$, which satisfy $\langle \phi_i | \phi_j \rangle = \delta_{i,j}$ and $\langle \phi_i | H | \phi_i \rangle = E_i \delta_{i,j}$ we have [34]

$$\begin{aligned} E_{\text{tr}} &= |c_1|^2 E_1 + |c_2|^2 E_2 + |c_3|^2 E_3 + \dots \\ &= E_1 + |c_2|^2 (E_2 - E_1) + |c_3|^2 (E_3 - E_1) + \dots \\ &\geq E_1. \end{aligned} \quad (2.29)$$

The last inequality, which establishes E_{tr} as an upper bound to the exact ground state energy, E_1 , follows from the ordering of the eigenvalues in terms of increasing energy. It is important to remember that the foundation for this technique is that the spectrum is bounded from below—the ground state forms such a bound in the spectrum of the nonrelativistic Schrödinger equation, with which we are concerned in this dissertation.¹⁶

2.6.2 Equivalent generalized eigenvalue problem

Since it is impossible to form a trial wave function whose energy is beneath the ground state by the variational principle, we thus have a license to manipulate a potential trial function in any fashion and to choose whichever results in the smallest eigenvalue. Beyond normalizability, the form of a trial function has no restrictions; however, using the one-electron solutions as an example, a trial function might look like $\Psi_{\text{tr}} = a_1 r^{a_2} e^{-a_3 r}$, with linear variational parameter a_1 and nonlinear variational parameters a_2 and a_3 .¹⁷ Minimizing the energy of this state has now become a multivariable calculus problem, where the following equations must simultaneously be satisfied:

$$\frac{\partial E_{\text{tr}}}{\partial a_p} = 0, \quad p = 1, \dots, N, \quad (2.30)$$

where, for the specific trial function mentioned above $N = 3$. Eq. (2.30) gives a set of transcendental equations that are not algebraically solvable in general. This problem is (algebraically) soluble in the special case where we only have linear variational

¹⁶Even in Chap. 5, where relativistic and QED effects are computed, we use nonrelativistic QED (NRQED) and only ever solve the NR problem, adding higher-order corrections perturbatively.

¹⁷The ensuing argument carries over directly to the two-electron case.

coefficients [34].

This linear variational eigenvalue problem can be solved by forming basis states out of the functions $\{\chi_i, i = 1, \dots, N\}$ according to

$$\Psi_{\text{tr}} = \sum_{i=1}^N a_i \chi_i, \quad (2.31)$$

where the linear coefficients $\{a_i\}$ are taken as the variational parameters. With this formulation, the minimization of the linear variational parameters expressed in Eq. (2.30) becomes identical to the equivalent generalized eigenvalue problem (GEP)

$$\mathbf{H}\mathbf{a} = \lambda \mathbf{O}\mathbf{a}, \quad (2.32)$$

where \mathbf{a} is a vector of the expansion coefficients, \mathbf{H} and \mathbf{O} are the Hamiltonian and overlap matrices, respectively, satisfying $H_{mn} = \langle \chi_m | H | \chi_n \rangle$ and $O_{mn} = \langle \chi_m | \chi_n \rangle$. The lowest of the N eigenvalues generated from this N -dimensional problem will be the upper bound to the true ground state energy. Different methods of solving this GEP depend on whether one wants a single optimized state or a complete pseudospectrum. The methods of solving this linear algebra problem are discussed in Appendix A.

Although the GEP in Eq. (2.32) is equivalent to the minimization condition expressed in Eq. (2.30), it is not equivalent to the Schrödinger equation itself: the choice of trial functions matters here. The solution obtained is only guaranteed to converge from above to the exact ground-state energy if the basis set is complete – there may be a finite gap.¹⁸ The condition that the GEP is equivalent to the Schrödinger equation is that the basis set $\{\chi_i, i = 1, \dots, N\}$ becomes complete in the limit that $N \rightarrow \infty$ [34]. The strategy to carry out these calculations is to solve the GEP for increasing values of N and then study the convergence of the corresponding quantity calculated to discern the $N \rightarrow \infty$ behaviour.

¹⁸In the two-electron problem, such a gap occurs with the Hartree-Fock method, discussed in Sec. 2.7.4. By assuming separable solutions, this method converges to too large a ground energy ($E \simeq -2.87$) compared to the exact $E = -2.903724\dots$, since it does not account for the so-called correlation energy.

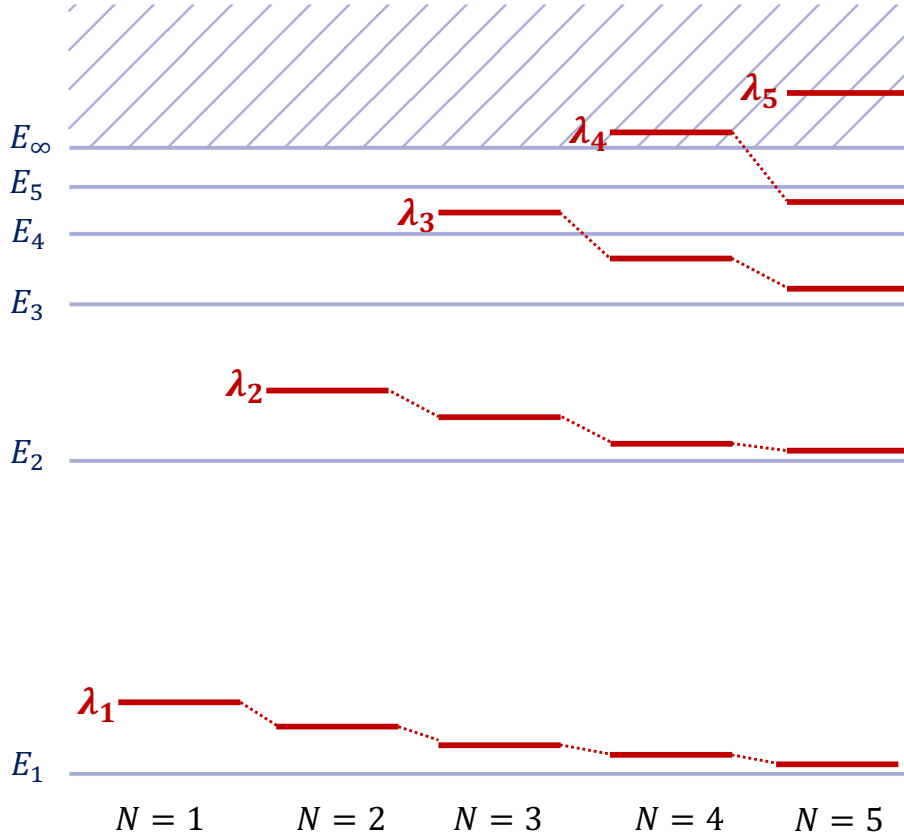


Fig. 2.6.1: Illustration of the Hylleraas-Undheim-MacDonald theorem. For five separate calculations that solve the GEP in Eq. (2.32), each of which increases the number of basis functions N , we see that (1) the $N - 1$ old eigenvalues of the previous calculation lie between the N new eigenvalues and (2) that each trial eigenvalue is an upper bound to the corresponding exact eigenvalue.

2.6.3 Extension to excited states

We have already demonstrated that the lowest eigenvalue λ_1 generated from solving the GEP is an upper bound to the exact ground state energy E_1 . The case, however, is stronger than this: the remaining λ_i for $i \geq 2$ are also upper bounds to the corresponding exact eigenvalues of the Schrödinger equation, provided that the correct number of states lies below. This is referred to as the Hylleraas-Undheim-MacDonald theorem [44, 45] and is a consequence of the matrix interleaving theorem, shown in Fig. 2.6.1. The matrix interleaving theorem states that as the dimensionality of \mathbf{H} and \mathbf{O} increases by 1, amounting to adding an extra row and column to these matrices, the old N eigenvalues must interleave the new $N + 1$ eigenvalues. This principle

is illustrated in Fig. 2.6.1 for basis sets with $N = 1$ to 5 terms. To achieve this interleaving, the eigenvalues must all move inexorably downward with each increase in N ; however, we also know that the exact spectrum is obtained as $N \rightarrow \infty$, from the assumption of completeness. This implies that each trial eigenvalue is indeed an upper bound to the corresponding exact energy, and we can strengthen the initial variational statement by including all N . Solving the GEP in Eq. 2.32 with an N -term basis set yields N eigenvalues satisfying

$$\lambda_i \geq E_i \quad \text{for } i = 1, \dots, N. \quad (2.33)$$

2.7 HYLLERAAS TRIAL WAVE FUNCTIONS

The trial functions used in this dissertation to solve the GEP in Eq. (2.32) are formed using Hylleraas basis functions; whose form we establish in this section.

2.7.1 Statement of Hylleraas basis functions

The doubled Hylleraas basis functions used in this dissertation have the form [43]

$$\Psi = \sum_{ijk}^{i+j+k \leq \Omega} \left[\underbrace{c_{ijk}^{(A)} \varphi_{ijk}(\alpha_A, \beta_A)}_{\text{A-sector}} + \underbrace{c_{ijk}^{(B)} \varphi_{ijk}(\alpha_B, \beta_B)}_{\text{B-sector}} \right], \quad (2.34)$$

where the basis functions $\varphi_{ijk}(\alpha, \beta)$ are defined by

$$\varphi_{ijk}(\alpha, \beta) = r_1^i r_2^j r_{12}^k e^{-\alpha r_1 - \beta r_2} \mathcal{Y}_{\ell_1, \ell_2, L}^M(\hat{r}_1, \hat{r}_2) \pm \text{exchange} \quad (2.35)$$

in Hylleraas coordinates. The exchange term represents the interchange of electron labels, and the $+$ and $-$ correspond to singlet and triplet states, respectively.

The quantity $\mathcal{Y}_{\ell_1, \ell_2, L}^M(\hat{r}_1, \hat{r}_2)$ represents a vector-coupled product of spherical harmonics of angular momenta ℓ_1 and ℓ_2 to form a state with total angular momentum

L and component M , according to [43]

$$\mathcal{Y}_{\ell_1\ell_2L}^M(\hat{r}_1, \hat{r}_2) = \sum_{m_1, m_2} Y_{\ell_1 m_1}(\hat{r}_1) Y_{\ell_2 m_2}(\hat{r}_2) \langle \ell_1 \ell_2 m_1 m_2 | LM \rangle, \quad (2.36)$$

where $\langle \ell_1 \ell_2 m_1 m_2 | LM \rangle$ are Clebsh-Gordan coupling coefficients [32, pp. 37–42]. The parameter $\Omega = (i + j + k)_{\max}$ controls the size of the basis set. The nominal number of terms in each sector is

$$N = \frac{1}{6}(\Omega + 1)(\Omega + 2)(\Omega + 3). \quad (2.37)$$

The Hylleraas pseudostates are a two-electron generalization of a one-electron Coulomb Sturmian basis set described in Sec. 2.4.

2.7.2 Nonlinear parameters

The basis set in Eq. (2.34) is “doubled” in the sense that different nonlinear parameters α_A , β_A and α_B , β_B are used for the asymptotic (A) and short-range (B) sectors respectively. This allows the wave functions to be modelled much more flexibly. The original Hylleraas functions were not doubled in this sense—this was a significant improvement, especially for higher-lying Rydberg states,¹⁹ initiated by Drake [48].

The nonlinear parameters are determined by calculating analytically the four derivatives $\partial E / \partial \alpha_A$, $\partial E / \partial \beta_A$, $\partial E / \partial \alpha_B$, and $\partial E / \partial \beta_B$ and finding the zeros by Newton’s method [49, 50], yielding the energy minimum on the multidimensional energy surface. In practice, one of the nonlinear parameters (usually β_1) is varied in order to optimize some quantity being calculated that depends on the wave functions. For instance, Chap. 3 of this dissertation treats the beta decay of ${}^6\text{He}$. A complete pseudospectrum of the ${}^6\text{Li}^+$ daughter ion is needed to perform this calculation. To form this pseudospectrum β_1 was optimized [51] in order to achieve variational stability for the total probability of excitation of ${}^6\text{Li}^+$, a rather complicated quantity that is the sum of several overlap integrals.

¹⁹Tripling of the Hylleraas basis sets (e.g., [46, 47]) has led to even further increases in accuracy.

Table 2.7.1: Comparison of the variational ground-state energy obtained using Hylleraas trial functions formed according to Eq. (2.34) containing all powers of r_1 and r_2 , but only select powers of r_{12} [54]. It can be seen that odd powers of r_{12} contribute significantly to improving the accuracy.

r_{12} terms	Energy (a.u.)	Error (eV)
no r_{12}	-2.879024	0.67200
r_{12}^2	-2.900503	0.08760
r_{12}^2, r_{12}^4	-2.902752	0.02640
r_{12}	-2.903496	0.00620
r_{12}, r_{12}^3	-2.903700	0.00065
all r_{12}	-2.903724	0.00000

2.7.3 Strategies and completeness

Before attempting to achieve convergence by progressively enlarging the basis sets used to solve the GEP, we must address a crucial question: Are the Hylleraas basis functions, expressed in Eq. (2.34), complete in the limit $N \rightarrow \infty$? We can guarantee they will reach the exact states and energies within this limit if they are.

Fortunately, the Hylleraas basis functions have been proven by Klahn and Bingel to be complete²⁰ in the limit $\Omega \rightarrow \infty$ [36, 53]. For S -states, completeness is ensured by two factors. The first factor is the completeness of the one-electron Sturmians, discussed in Sec. 2.4, and a complete set of angular functions [52, p. 110]. This completeness of angular functions achieved in Hylleraas basis sets results from the presence of powers of r_{12} being directly in the basis functions [54]. The powerful effect of this feature of the basis function can be seen in Table 2.7.1, which compares the energies calculated using different basis sets to the exact energy. The striking conclusion is how significant an effect the odd powers of r_{12} , starting with r_{12} itself, have on the calculation. The implications of this are most properly understood in the context of the limitations of another method of forming basis functions: the configuration interaction (CI) approach, which we now discuss.

²⁰Technically speaking, the basis set needs to become complete as $\Omega \rightarrow \infty$ in a *first Sobolev space*, which is a Hilbert space with square integrable first derivatives [52, p. 110].

2.7.4 Comparison of Hylleraas construction to other basis sets

The CI approach is another method that is complete in the limit of increasing the size of the calculation to infinity [36]. The basis functions in a CI wave functions are formed according to [38]

$$\begin{aligned}\psi(\mathbf{r}_1, \mathbf{r}_2) = & C_0 u_1^{(s)}(r_1) u_1^{(s)}(r_2) Y_{0,0,0}^0(\hat{r}_1, \hat{r}_2) + C_1 u_1^{(p)}(r_1) u_1^{(p)}(r_2) Y_{1,1,0}^0(\hat{r}_1, \hat{r}_2) \\ & + C_2 u_1^{(d)}(r_1) u_1^{(d)}(r_2) \mathcal{Y}_{2,2,0}^0(\hat{r}_1, \hat{r}_2) + \dots \pm \text{exchange},\end{aligned}\quad (2.38)$$

as an example for S state, where $u_1^{(\ell)}(r_i)$ are one-electron orbitals with angular momentum ℓ . The procedure is to couple all one-electron orbitals that can form a total $L = 0$. The comparison of the energy obtained using this method to others including the Hylleraas basis states described in Sec. 2.7.1 is shown in Table 2.7.2, along with several other techniques that can be used form the basis states. The simplest approximation to write down the two-electron wave function is via a separable product forming the the so-called Hartree-Fock method, with a radial wave function

$$\phi(\mathbf{r}_1, \mathbf{r}_2) = \frac{1}{\sqrt{2}} [u_1(r_1)u_2(r_2) \pm u_2(r_1)u_1(r_2)] \quad (2.39)$$

which, when substituted into the variational principle, Eq. (2.28), yields an energy $E \simeq -2.87$ a.u. The difference between this and the exact energy (-2.903 724 a.u.) is about 0.03 a.u. and is referred to as the correlation energy. The other methods in Table 2.7.2 account for correlation and are much more accurate than the Hartree-Fock method.

Returning now to the role of r_{12} , we begin by using the cosine law to write

$$r_{12}^2 = r_1^2 + r_2^2 - 2r_1r_2 \cos \theta_{12}. \quad (2.40)$$

The spherical harmonic addition theorem [32, p. 63]

$$P_\ell(\cos \theta_{12}) = \frac{4\pi}{2l+1} \sum_{m=-1}^1 Y_l^{m*}(\theta_1, \varphi_1) Y_l^m(\theta_2, \varphi_2), \quad (2.41)$$

$$\xrightarrow{\text{for } l=1} \cos \theta_{12} = \frac{4\pi}{3} \sum_{m=-1}^1 Y_1^{m*}(\theta_1, \varphi_1) Y_1^m(\theta_2, \varphi_2), \quad (2.42)$$

shows that powers of $\cos \theta_{12}$ correspond to correlation terms in the CI wave function. We see that r_{12}^2 , proportional to P_1 , accounts for the pp contributions in the S -state CI wave functions in Eq. (2.38). Further, the ss contributions arise from r_{12}^0 since $Y_{0,0,0}^0(\hat{r}_1, \hat{r}_2)$ is just a number. All higher $\ell\ell$ coupling can be obtained from higher even powers of r_{12} for the corresponding higher ℓ contributions of the addition theorem. In this way, including powers of r_{12}^{2n} for $n = 0, 1, 2, \dots$ systematically includes all of the coupled states of the CI method. The special role played by odd powers of r_{12} shown in Table 2.7.1 is understood by considering that if we expand the square root of the right-hand side of Eq. (2.40),

$$r_{12} \equiv \sqrt{1 + x \cos \theta_{12}} = 1 + \frac{x}{2} \cos \theta_{12} - \frac{x^2}{8} \cos^2 \theta_{12} + \dots, \quad (2.43)$$

with $x \equiv 2r_1 r_2 / (r_1^2 + r_2^2)$, we get all powers of $\cos \theta_{12}$, corresponding to *all* higher-order ll couplings via the addition theorem in Eq. (2.41). The inclusion of all possible correlations therefore happens much more quickly in Hylleraas basis sets compared to any CI methods that write down the basis functions as in Eq. (2.38).²¹ This is why the Hylleraas approach is so much more effective; even though the CI method is complete in principle, it is not computationally possible to include all couplings, whereas, with Hylleraas states, they are automatically included with the odd powers of r_{12} via the expansion shown in Eq. (2.43).

Another crucial property of the solutions containing odd powers of r_{12} is that they help satisfy²² the electron-electron cusp condition that occurs when $r_{12} = 0$, a specific

²¹These comments extend to states of higher angular momentum, with the difference being that $L \neq 0$ states can be formed by more than one coupling scheme—for $L = 0$ we only had $\ell\ell$ —which results in different sequences of basis functions Eq. (2.34).

²²The odd powers contain a square root factor and their derivative contains a cusp.

Table 2.7.2: Comparison between the level of accuracy that can be achieved using the Hartree-Fock method and various correlated variational wave functions. The Hylleraas basis states achieve much better accuracy than the rest [38].

Method	Typical Accuracy for the Energy
Basic Hartree-Fock [39]	$\sim 10^{-2}$ a.u.
Many Body Perturbation Theory [38]	$\geq 10^{-6}$ a.u.
Configuration Interaction [38]	$10^{-6} - 10^{-8}$ a.u.
Explicitly Correlated Gaussians [57]	$\sim 10^{-10}$ a.u.
Hylleraas Coordinates (He) [58–60]	$\leq 10^{-35} - 10^{-40}$ a.u.

case of the general Kato cusp condition [55],

$$\left(\frac{\partial \bar{\Psi}}{\partial r_{ij}} \right)_{r_{ij}=0} = \mu_{ij} q_i q_j \bar{\Psi}(r_{ij} = 0), \quad (2.44)$$

where $m_{i,j}$ and $q_{i,j}$ are the masses and charges of the two particles, respectively, and $\mu_{ij} = m_i m_j / (m_i + m_j)$ and $\bar{\psi}$ denotes the wave function averaged over a sphere centred at $r_{ij} = 0$ [43]. The Kato cusp condition arises because the Coulomb potential diverges when two charged particles coalesce, but the local energy must be constant. For this to be true in the case of the Schrödinger equation the diverging potential that occurs as $r_{ij} \rightarrow 0$ must cancel exactly with the “kinetic local energy,” leading to the general two-particle coalescence Kato cusp conditions in Eq. (2.44) [56].

2.8 INTEGRALS INVOLVING HYLLERAAS WAVE FUNCTIONS

The high-precision comparisons between theory and experiment in two-electron problems required to test QED (cf. Chap. 5) would be computationally infeasible if the integrals could not be evaluated in closed form. In the case of the doubled basis set of correlated Hylleraas functions, in Eq. (2.34), the procedure for analytically evaluating all integrals of interest was established by Drake in 1978 [61]. Together, Refs. [61]

and Chap. 12 of the *Springer Handbook of Atomic, Molecular, and Optical Physics, 2nd Edition* [43], also by Drake, provide the foundation for this section.²³

2.8.1 General integral

In order to solve the GEP and obtain the optimized Hylleraas pseudostates, both the Hamiltonian and overlap matrices must be established. Each element of these two matrices is itself an integral, defined in Dirac notation as $H_{mn} = \langle \chi_m | H | \chi_n \rangle$ and $O_{mn} = \langle \chi_m | \chi_n \rangle$. Once we have these pseudostates, after solving the GEP, all structure properties in atomic physics are calculated as matrix elements that are also integrals.²⁴ A preliminary step in this direction that will not be belaboured here²⁵ is to write the operators of concern, including those that comprise the Hamiltonian, in the six-dimensional Hylleraas coordinates. The six independent coordinates are shown in Fig. 2.5.1.

The most general integral between states $\chi = R\mathcal{Y}_{\ell_1\ell_2L}^M$ and $\chi' = R'\mathcal{Y}_{\ell'_1\ell'_2L'}^{M'}$ that are connected through an arbitrary operator expressed as a coupled spherical tensor $T_{k_1k_2K}^Q$ is

$$I = \iint d\mathbf{r}_1 d\mathbf{r}_2 R' \mathcal{Y}_{\ell'_1\ell'_2L'}^{M'}(\hat{r}_1, \hat{r}_2)^* T_{k_1k_2K}^Q(\mathbf{r}_1, \mathbf{r}_2) R \mathcal{Y}_{\ell_1\ell_2L}^M(\hat{r}_1, \hat{r}_2), \quad (2.45)$$

with the vector coupled spherical harmonics defined in Eq. (2.36) and likewise for the tensor operator

$$T_{k_1k_2K}^Q(\mathbf{r}_1, \mathbf{r}_2) = \sum_{q_1, q_2} \langle k_1 k_2 q_1 q_2 | KQ \rangle Y_{k_1}^{q_1}(\hat{r}_1) Y_{k_2}^{q_2}(\hat{r}_2) \quad (2.46)$$

describing the coupling of two tensor operators of rank k_1 and k_2 to form a total tensor of rank K . Thus, $T_{k_1k_2K}^Q(\mathbf{r}_1, \mathbf{r}_2)$ describes the angular part of a general operator that

²³The computer programs used in this work, which solve the GEP by evaluating the integrals contained in the section, can be found in Ref. [62]. Standard quadruple precision (about 32 decimal digits) is sufficient for the present set of calculations.

²⁴This includes diagonal matrix elements—expectation values—as in energy calculations or perturbations to energy and also off-diagonal elements such as those involved in computing the polarizability.

²⁵See references suggested at the beginning of this section for more details.

can be a function of the coordinates and derivatives of the electrons 1 and 2. The Hamiltonian and overlap are rotationally invariant operators, corresponding to rank-0 (scalar) tensors, a subset of this most general integral.

The volume element can be written as [63]

$$d\tau = r_1 dr_1 r_2 dr_2 r_{12} dr_{12} \sin \theta_1 d\theta_1 d\varphi_1 d\chi \quad (2.47)$$

corresponding to product of radial (r_1, r_2, r_{12}) and angular (θ_1, ϕ_1, χ) part, as shown in Fig. 2.5.1, yielding

$$\begin{aligned} \iint d\mathbf{r}_1 d\mathbf{r}_2 &= \overbrace{\int_0^{2\pi} d\chi \int_0^{2\pi} d\phi_1 \int_0^\pi \sin \theta_1 d\theta_1}^A \int_0^\infty r_1 dr_1 \int_0^\infty r_2 dr_2 \int_{|r_1-r_2|}^{r_1+r_2} r_{12} dr_{12} \\ &= A \times \left[\int_0^\infty r_1 dr_1 \int_{r_1}^\infty r_2 dr_2 \int_{r_2-r_1}^{r_1+r_2} r_{12} dr_{12} \right. \\ &\quad \left. + \int_0^\infty r_2 dr_2 \int_{r_2}^\infty r_1 dr_1 \int_{r_1-r_2}^{r_1+r_2} r_{12} dr_{12} \right] \end{aligned} \quad (2.48)$$

The solutions of the general integral expressed in Eq. (2.45) have the form

$$I = \sum_{\Lambda} C_{\Lambda} I_{\Lambda}(R_1 R_2) \quad (2.49)$$

where $I_{\Lambda}(R_1 R_2)$ is the radial part and the sum over Λ ensures the inclusion of all possible nonvanishing couplings—its role is seen below in the evaluation of the angular part contained in C_{Λ} .

2.8.2 The angular part

In Eq. (2.49), the remaining part, C_{Λ} , is the angular integral²⁶, which has the following general solution [61]

$$C_{\Lambda} = \sum_{\lambda_1, \lambda_2} C_{\lambda_1, \lambda_2, \Lambda}, \quad (2.50)$$

²⁶These ensuing formulae are a consequence of repeated angular couplings. Detailed derivations can be found in Ref. [61].

with the individual $C_{\lambda_1, \lambda_2, \Lambda}$ formed according to

$$C_{\lambda_1, \lambda_2, \Lambda} = (-1)^{L' - M'} \begin{pmatrix} L' & K & L \\ -M' & Q & M \end{pmatrix} X_{\lambda_1, \lambda_2, \Lambda} D_{\lambda_1, \lambda_2, \Lambda}, \quad (2.51)$$

with $X_{\lambda_1, \lambda_2, \Lambda}$ given by a prefactor multiplied by a product of four 3- j symbols

$$X_{\lambda_1 \lambda_2, \Lambda} = \frac{(-1)^{\ell'_1 + \ell'_2 + L' + \Lambda}}{8\pi} (\lambda_1, \lambda_2, \Lambda) (\ell_1, k_1, \ell'_1, \ell_2, k_2, \ell'_2, L, L', K)^{1/2} \times \begin{pmatrix} \ell_1 & k_1 & \lambda_1 \\ 0 & 0 & 0 \end{pmatrix} \begin{pmatrix} \ell'_1 & \lambda_1 & \Lambda \\ 0 & 0 & 0 \end{pmatrix} \begin{pmatrix} \ell_2 & k_2 & \lambda_2 \\ 0 & 0 & 0 \end{pmatrix} \begin{pmatrix} \ell'_2 & \lambda_2 & \Lambda \\ 0 & 0 & 0 \end{pmatrix}, \quad (2.52)$$

where $(a, b, \dots) \equiv (2a+1)(2b+1)\dots$ and $D_{\lambda_1, \lambda_2, \Lambda}$ given by a product of 6- j and 9- j symbols

$$D_{\lambda_1 \lambda_2 \Lambda} = \left\{ \begin{matrix} L' & \ell'_2 & \ell'_1 \\ \Lambda & \lambda_1 & \lambda_2 \end{matrix} \right\} \left\{ \begin{matrix} \ell_1 & \ell_2 & L \\ k_1 & k_2 & K \\ \lambda_1 & \lambda_2 & L' \end{matrix} \right\}. \quad (2.53)$$

The Wigner 3- j , 6- j and 9- j symbols that are used to form the $C_{\lambda_1, \lambda_2, \Lambda}$ are defined in Edmonds [32, pp. 45–50, 92–97, 100–108] and arise in the description of the coupling of angular momenta needed to evaluate the angular portion of the general integral.

2.8.3 Radial integrals and recursion relations

The most general statement of the radial integral I_Λ is

$$I_\Lambda(a, b, c; \alpha, \beta) = \langle f(a, b, c; \alpha, \beta) P_\Lambda(\cos \theta_{12}) \rangle_{\text{rad}}, \quad (2.54)$$

where $\langle \dots \rangle_{\text{rad}}$ corresponds to integration using the radial bounds established when defining the volume element above in Eq. (2.47) with integrand

$$f(a, b, c; \alpha, \beta) = r_1^a r_2^b r_{12}^c e^{-\alpha r_1 - \beta r_2}. \quad (2.55)$$

The $P_\Lambda(\cos \theta_{12})$ is a residual radial function from the angular integration over the set of vector coupled spherical harmonics [43], with $\cos \theta_{12} \equiv \hat{\mathbf{r}}_1 \cdot \hat{\mathbf{r}}_2$ defined in Eq. (2.40)

$$\cos \theta_{12} = \frac{r_1^2 + r_2^2 - r_{12}^2}{2r_1 r_2}. \quad (2.56)$$

Carrying out calculations in Hylleraas coordinates according to the basis functions in Eq. (2.35), the radial portion of every integrand will have the form displayed in Eq. (2.54).

The strategy used to obtain the integrals $\{I_\Lambda\}$ for the requisite $\Lambda = 0, 1, \dots$ corresponding to nonvanishing C_Λ in Eq. (2.49) is to find I_0 and I_1 first and then use the recursion relation

$$I_{\Lambda+1}(a, b, c; \alpha, \beta) = \frac{2\Lambda + 1}{c + 2} I_\Lambda(a - 1, b - 1, c + 2; \alpha, \beta) + I_{\Lambda-1}(a, b, c; \alpha, \beta), \quad (2.57)$$

when $c \neq -2$, and

$$I_{\Lambda+1}(a, b, -2; \alpha, \beta) = (2\Lambda + 1) I_\Lambda^{\log}(a - 1, b - 1, 0; \alpha, \beta) + I_{\Lambda-1}(a, b, -2; \alpha, \beta). \quad (2.58)$$

when $c = -2$ [43]. The logarithmic integrals, I_Λ^{\log} , that arise have the form

$$I_\Lambda^{\log}(a, b, c; \alpha, \beta) = \langle f(a, b, c; \alpha, \beta) \ln r_{12} P_\Lambda(\cos \theta_{12}) \rangle_{\text{rad}}, \quad (2.59)$$

with the recursion relations

$$\begin{aligned} I_{\Lambda+1}^{\log}(a, b, c; \alpha, \beta) &= \frac{(2\Lambda + 1)}{c + 2} \left[I_\Lambda^{\log}(a - 1, b - 1, c + 2; \alpha, \beta) \right. \\ &\quad \left. - \frac{1}{c + 2} I_\Lambda(a - 1, b - 1, c + 2; \alpha, \beta) \right] \\ &\quad + I_{\Lambda-1}^{\log}(a, b, c; \alpha, \beta). \end{aligned} \quad (2.60)$$

The general radial integral with $\Lambda = 0$ is $I_0(a, b, c; \alpha, \beta) = \langle r_1^a r_2^b r_{12}^c e^{-\alpha r_1 - \beta r_2} \rangle_{\text{rad}}$

has the closed-form solution

$$I_0(a, b, c; \alpha, \beta) = \frac{2}{c+2} \sum_{i=0}^{[(c+1)/2]} \binom{c+2}{2i+1} [F_{a+2i+2, b+c-2i+2}(\alpha, \beta) + F_{b+2i+2, a+c-2i+2}(\beta, \alpha)] \quad (2.61)$$

with $F_{p,q}(\alpha, \beta)$ defined by

$$F_{p,q}(\alpha, \beta) = \begin{cases} \frac{q!}{(\alpha + \beta)^{p+1} \beta^{q+1}} \sum_{j=0}^q \frac{(p+j)!}{j!} \left(\frac{\beta}{\alpha + \beta}\right)^j, & q \geq 0, p \geq 0 \\ \frac{p!}{\alpha^{p+q+2}} \sum_{j=p+q+1}^{\infty} \frac{j!}{(j-q)!} \left(\frac{\alpha}{\alpha + \beta}\right)^{j+1}, & q < 0, p \geq 0 \\ 0, & p < 0 \end{cases} \quad (2.62)$$

where $p = a + 2i + 2$, $q = b + c - 2i + 2$ and $[x]$ means “greatest integer in.”

I_1 can be written in terms of I_0 via [61]

$$I_1(a, b, c) = \frac{1}{2} [I_0(a+1, b-1, c) + I_0(a-1, b+1, c) - I_0(a-1, b-1, c+2)] \quad (2.63)$$

which, together with I_0 , provides the seeds from which all other I_Λ follow by the recursion relations given in Eqs. (2.57)–(2.60)

Any integral over Hylleraas wave functions connected by an arbitrary operator can be evaluated using the machinery developed above. One needs to write the operator in Hylleraas coordinates, which can, in practice, lead to reasonably complicated equations. Details are readily available in references contained throughout the chapter. A full table of the radial integrals I_0 and I_0^{\log} can be found in Chap. 12 of Ref. [43].

2.8.4 Hamiltonian and overlap matrix elements

As an example, we state the specialized form which the general integral in Eq. (2.45) takes for the infinite-nuclear-mass Hamiltonian and overlap matrix elements that are

input for the Eq. (2.32), the GEP. If the initial and final Hylleraas states are

$$\chi = r_1^a r_2^b r_{12}^c e^{-\alpha r_1 - \beta r_2} \mathcal{Y}_{\ell_1 \ell_2 L}^M(\hat{r}_1, \hat{r}_2) \text{ and}$$

$$\chi' = r_1^{a'} r_2^{b'} r_{12}^{c'} e^{-\alpha' r_1 - \beta' r_2} \mathcal{Y}_{\ell'_1 \ell'_2 L}^M(\hat{r}_1, \hat{r}_2),$$

then the integrals that constitute the Hamiltonian matrix elements are [43]

$$\langle \chi' | H | \chi \rangle = \frac{1}{8} \sum_{\Lambda} C_{\Lambda} \sum_{i=0}^2 \left[A_i^{(1)} I_{\Lambda}(a_+ - i, b_+, c_+; \alpha_+, \beta_+) \right. \quad (2.64)$$

$$\left. + A_i^{(2)} I_{\Lambda}(a_+, b_+ - i, c_+; \alpha_+, \beta_+) + A_i^{(3)} I_{\Lambda}(a_+, b_+, c_+ - i; \alpha_+, \beta_+) \right] \quad (2.65)$$

where $a_+ = a' \pm a$, $\alpha_+ = \alpha' \pm \alpha$, etc., and

$$\begin{aligned} A_0^{(1)} &= -\alpha_+^2 - \alpha_-^2 + 2\alpha_- \alpha_+ \left(\frac{c_-}{c_+} \right), \\ A_1^{(1)} &= 2 \left\{ \alpha_+(a_+ + 2) + \alpha_- a_- - [\alpha_+ a_- + \alpha_- (a_+ + 2)] \left(\frac{c_-}{c_+} \right) \right\} - 8Z, \\ A_2^{(1)} &= -a_+^2 - a_-^2 - 2a_+ + 2a_-(a_+ + 1) \left(\frac{c_-}{c_+} \right) + 2l_1(\ell_1 + 1) \left(1 - \frac{c_-}{c_+} \right) \\ &\quad + 2l'_1(\ell'_1 + 1) \left(1 + \frac{c_-}{c_+} \right), \\ A_0^{(3)} &= 0, \quad A_1^{(3)} = 8, \text{ and} \quad A_2^{(3)} = 2(c_+^2 - c_-^2), \end{aligned}$$

with $c_-/c_+ = 0$ for $c_+ = 0$. The $A_i^{(2)}$ differ from the $A_i^{(1)}$ only in that the replacements $a \rightarrow b$, $\alpha \rightarrow \beta$, $\ell_1 \rightarrow \ell_2$ are made.

The overlap integral, yielding overlap matrix elements, can be given in terms of the above definitions as

$$\langle \chi' | \chi \rangle = \sum_{\Lambda} C_{\Lambda} I_{\Lambda}(a_+, b_+, c_+; \alpha_+, \beta_+). \quad (2.66)$$

CHAPTER 3

Beta Decay and Charge-state Distributions in ${}^6\text{He}$

3.1 OVERVIEW

The Standard Model (SM) provides the framework for understanding the kinematics following a beta decay event in ${}^6\text{He}$, which has a lifetime of 0.8 s. Supposing this is a vector-axial semileptonic weak process, it predicts the electron-antineutrino correlation coefficient, a quantity related to the angle between the electron and antineutrino that emerges from the beta decay. Deviations from this prediction are widely postulated as signals for new physics (NP) [28]. Due to the elusive nature of neutrinos and the resulting inability to detect them experimentally, it is essential to understand what happens to the recoiling daughter ion, ${}^6\text{Li}^+$, following a decay event, to deduce the kinematics of the decay.

This chapter includes published work which attempts to resolve a significant theoretical-experimental discrepancy in the predicted amount of double ionization following this process [26]. Pseudospectra, of both the one- and two-electron variety, feature prominently in the analysis in this chapter owing to their ability to discretely represent an infinite bound and continuous spectrum.

We begin in Sec. 3.2 by giving a historical overview of this fascinating and significant problem. Section 3.3 then outlines the motivation for this work, describing how it relates to potential new physics beyond the Standard Model. This section introduces the experimental quantity of interest, the electron-antineutrino correlation

coefficient ($a_{\beta\nu}$). It is theoretically motivated, and the experiments that measure this quantity are summarized. Turning to atomic physics, Sec. 3.4 sets up the problem and describes the assumptions made. Section 3.5 describes the previous theoretical work to calculate the charge-state fractions of the ${}^6\text{Li}^+$ daughter ion following the beta decay of ${}^6\text{He}$. At this stage, previous works have significantly overestimated the amount of double ionization, i.e., formation of ${}^6\text{Li}^{3+}$, compared with experiments. Following this, Sec. 3.6 makes two theoretical arguments to support the notion that theory is indeed overestimating the amount of ${}^6\text{Li}^{3+}$ following the decay. In Sec. 3.7, an outline of the projection operators and their derivation is presented, with the results of this method being described in Sec. 3.8. Section 3.9 discusses several avenues for future work.

3.2 HISTORICAL SIGNIFICANCE

In 1959, on the heels of her major experiment studying the beta decay ${}^{60}\text{Co}$, which established nonconservation of parity in the weak interaction¹, C. S. Wu, in *Reviews of Modern Physics*, wrote [64]:

The frontier of parity study has now advanced to the field of strange particles. The atmosphere in the field of beta decay appears unusually calm and quiet after the storm. I will try to piece together the jigsaw picture and see what sorts of puzzles in beta decay have fallen into shape. Most urgent is the question of whether there are still any missing pieces and what are they if there are?

The problem of beta decay holds a significant and exciting position in the history of physics. The general equation describing beta decay² is [65]:

$${}^A_Z X_N \longrightarrow {}^A_{Z\pm 1} X'_{N\mp 1} + e^\mp + (\bar{\nu}_e \text{ or } \nu_e), \quad (3.1)$$

¹This discovery led directly to the 1957 Nobel Prize for her theoretical collaborators, C. N. Yang and T. D. Lee. Her omission from this prestigious award is indefensible, considering her crucial role. Her contributions would later be recognized with the first Wolf Prize in 1978.

²This is an atomic perspective on the problem; there are two more successively fundamental levels to consider: the nuclear and quark levels.

which describes an atomic element X with mass number A , atomic number Z , and neutron number N decaying into element X' with mass number A , atomic number $Z \pm 1$, and neutron number $N \mp 1$, along with the leptonic pairs of an electron/positron, e^\mp , and an antineutrino/neutrino ($\bar{\nu}_e / \nu_e$). This process produces energy $Q_{\beta^\mp} = [m_N(Z, A) - m_N(Z \pm 1, A) - m_e] c^2$, which is shared between the outgoing leptons and, if the decay occurs in an atom, the recoiling daughter ion (or the daughter proton in the case of bare neutron decay). In this equation, m_N is the mass of the parent or daughter nucleus (with corrections for electron binding energy), m_e is the mass of the electron, Z is the atomic number of the parent ion, and c is the speed of light. The half-life of the process is approximately 10 minutes for a bare neutron and ranges substantially in atomic systems, owing to wildly differing stability of various nuclear configurations, selection rules, and values of energy release [65].

It is worthwhile to briefly consider the historical relevance of this “storm” alluded to by Wu. We first focus on phenomena preceding quantum mechanics, leading toward the old quantum theory. In studying the phosphorescent properties of the recently discovered uranium salts in 1896, then relevant for the lighting industry, including the cathode-ray tube, Becquerel accidentally observed radioactivity for the first time [66]; he detected products of beta decay, then “uranic rays”. This work is foundational to nuclear physics and was awarded the 1903 Nobel Prize in Physics alongside Marie and Pierre Curie. By 1914, quantitative studies [67] underway³ concerning the energy of the beta rays (by 1902, it was recognized that these were *electrons*) revealed something unexpected: the energy spectrum of the beta particles was continuous. Assuming a two-body interaction, the beta particle and the leftover “daughter” nucleus, this is inconsistent with the conservation of energy and momentum. The situation, pictured in Fig. 3.2.1 was so strange that many resorted to relegating conservation of energy to a statistical law, not observed in every interaction, but observed on average [70, 71]—

³A fascinating historical episode is involved here [68]. In 1911, Meitner, Hahn, and von Baeyer measured a monoenergetic spectrum of electron emission using a photographic plate – later contradicted by two separate Chadwick measurements, one using an ionization chamber and the other with a Geiger counter. Ellis and Wooster, using yet another device, an absorption calorimeter [69], confirmed the Chadwick results. Meitner’s photographic detection method was too crude, offering insufficient resolution of the diffuse lines and preventing the conclusion that the energy spectrum was continuous.

a view advanced by even Pauli and Bohr, who renounced it in 1936 after Fermi established the theory of beta decay [72].

As a “desperate remedy” [71] to the problem of “missing” energy, Pauli proposed another subatomic particle, which he called the neutron. This particle he proposed had properties of both the actual neutron, discovered by Chadwick two years later [73], and the neutrino in Fermi’s theory of beta decay. Fermi correctly postulated that the neutrino is actually *created* during the beta decay process [74, 75] whereas others such as Pauli assumed that it was already within the nucleus. Fermi’s theory detailed a new (contact) force called the weak force and firmly restored faith in the conservation of energy law.⁴

After Fermi’s theory, physicists worked for many years to discern the Lorentz gauge the structure of the weak interaction, and understand how the weak force fits into the framework of relativity. Fermi initially predicted that the coupling structure between the outgoing leptons would have a vector character, where no spin change would happen in beta decay ($\Delta S = 0$). However, shortly after, it was shown that either an axial or tensor structure would be needed to explain the observed selection rules, which implied a spin change $\Delta S = 1$ [77]. The following section will elaborate on these points.

This work culminated in the electroweak unification led by Glashow, Salam, and Weinberg. Weinberg, in his seminal 1967 paper [78, 79], which presented the theoretical framework that unified the electromagnetic and weak forces, credited Fermi’s work on beta decay from more than 30 years prior as the first attempted unification. This unification led to correct high-energy predictions, including the W and Z bosons [80], that met with consistent experimental confirmation. The W and Z bosons were shown to mediate the weak interaction just as photons mediate the electromagnetic interaction.

As a final historical point, due to its role in stellar nucleosynthesis, beta decay influences stellar evolution, elemental abundances, and, ultimately, our understanding

⁴Fermi’s paper was rejected by *Nature* “because it contained speculations too remote from reality to be of interest to the reader” [76].

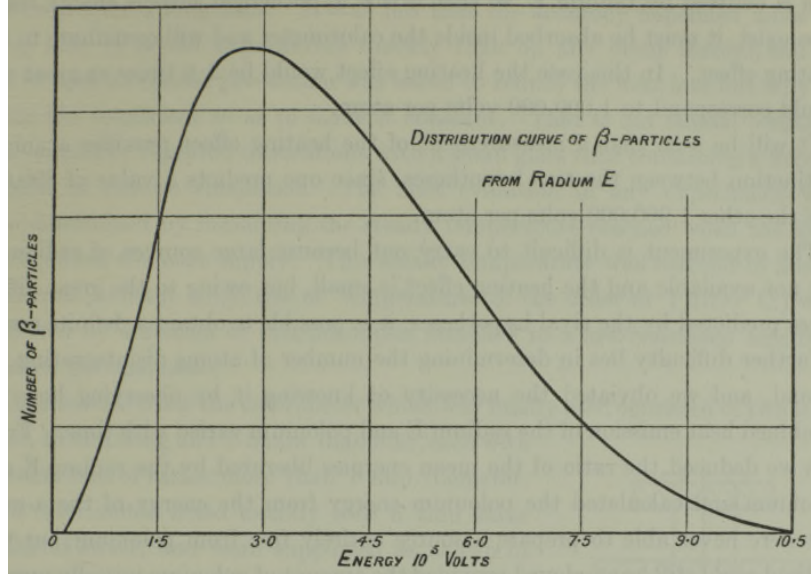


Fig. 3.2.1: A plot of the intensity of beta emission with a range of energies [69]. This result of Ellis and Wooster in 1927 shows unequivocally that the intensity of beta particles, following the beta decay of radium, is shown to vary continuously with energy. This confirmed the earlier Chadwick experiments with significantly greater resolution.

of the origins of the universe [81, 82]. Furthermore, studying beta decay in the context of neutrino physics is an essential area of active research. Work in this direction, including the study of neutrino masses and oscillations and the widely probed for neutrinoless double beta decay [83], have implications for particle physics, astrophysics and cosmology and was recognized with the 2015 Nobel Prize in Physics [84].

3.3 MOTIVATION

3.3.1 The $V - A$ theory

After a significant amount of work that led to the establishment of parity nonconservation in the weak interaction [64, 85], it was found [86–88] that the weak interaction

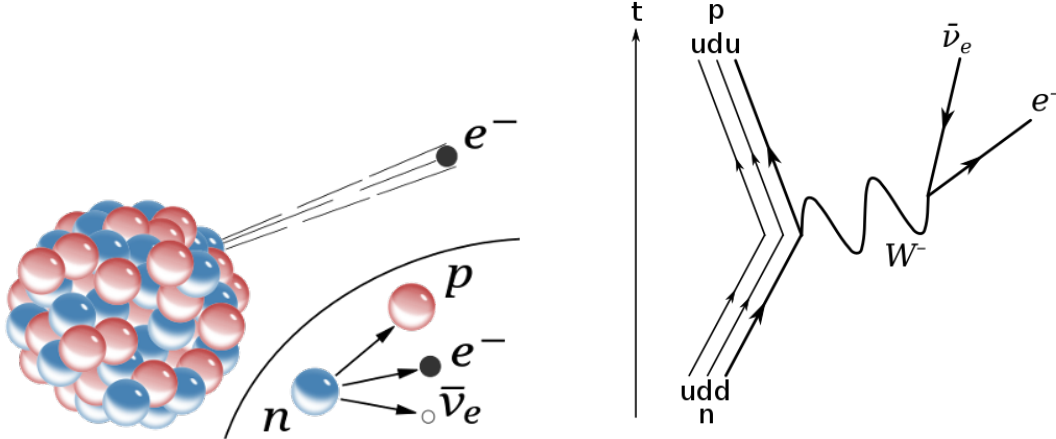


Fig. 3.3.1: The weak interaction in beta decay. The left panel shows the post- β^- -decay products with a daughter ion and an ejected beta particle e^- with an inset showing the nuclear-level products of the β^- -decay of a neutron. The Feynman diagram corresponding to this inset is shown in the right panel. Images are in the public domain.

was of the form $V - A$ ("vector minus axial-vector").⁵ Over the ensuing several years, this was confirmed by a flurry of experimental activity [91–94]. It is known now that the weak interactions are a mixture of V and A components—not necessarily strictly of the form $V - A$.

Much later, in 2009, Weinberg remarked [79] that “ $V - A$ was the key”; that the realization that this indeed was the proper form of the interaction, leading to a profound analogy between electromagnetic and weak interactions, and led to their unification.

This is the point of departure from the historical overview for our story: the elucidation of the $V - A$ theory of the weak interaction, which established its chiral nature. We begin by briefly outlining this theory and, in the following section, overview its connection to searches for new physics (NP). The question occupying the physics

⁵Even though it has been universally acknowledged (since the mid-1960s [78]) that Sudarshan and Marshak [86] have priority on the $V - A$ theory, it is still mostly referred to as the “Feynman and Gell-Mann theory,” with their work more frequently cited, possibly due to their status as Nobel laureates. In the first printing of *Surely You’re Joking, Mr. Feynman* [89], Feynman discussed beta decay and omits Sudarshan and Marshak’s contributions, claiming that understanding $V - A$ was the first and only time in his career that he truly understood something new first. Regarding the same story, Gell-Mann even threatened legal action [90] against Feynman for misrepresenting his contributions in their joint work [87]. As a result of this exchange between Feynman and Gell-Mann, subsequent printings of *Surely You’re Joking, Mr. Feynman*, if not the widespread consensus, correctly acknowledge Sudarshan and Marshak’s priority.

community after Fermi's theory was: which of the possible covariant, i.e., Lorentz invariant, expressions for the interaction Hamiltonian was correct. Covariance is an expected property of any physical theory, asserting that the laws of physics are the same in all inertial reference frames. As discussed in the Introduction, covariance is intimately related to CPT symmetry (combination of charge, parity, and time-reversal conjugation leaves the physics unchanged), perhaps the most important symmetry of the SM – and one that we have tested extensively [95] and have not yet been found to break.⁶

The form of the nuclear-level Hamiltonian⁷ governing the beta decay shown in the right panel of Fig. 3.3.1 is [96, p. 5]

$$H_F = H_n + H_p + H_e + H_{\bar{\nu}} + \sum_i g_i \int d^3x (\bar{u}_p \mathcal{O}^i u_n) (\bar{u}_e \mathcal{O}_i u_{\bar{\nu}}) \quad (3.2)$$

where $n, p, e, \bar{\nu}$ refer to the neutron, proton, electron and antineutrino along with their unperturbed Hamiltonians (H_x) and wave functions (u_x), which are solutions to the Dirac equation.⁸ There are five possible covariant interactions ($i = 1, 2, \dots, 5$) that could characterize beta decay

$$\mathcal{O}_S = 1, \quad \mathcal{O}_V = \gamma^\mu, \quad \mathcal{O}_T = \sigma^{\mu\nu}, \quad \mathcal{O}_A = \gamma^\mu \gamma_5, \quad \mathcal{O}_P = \gamma_5 = -i\gamma_0\gamma_1\gamma_2\gamma_3 \quad (3.3)$$

where S, V, T, A and P are, respectively, the scalar, vector, tensor, axial vector and pseudoscalar operators corresponding to the currents ($\bar{\psi}_p \mathcal{O}^i \psi_n$). These currents are weighted by the constants g_i . In Eq. (3.3), γ^μ are Dirac matrices and $\sigma^{\mu\nu} = \frac{i}{2}[\gamma^\mu, \gamma^\nu]$. As already mentioned, extensive experimental efforts [91–94] that continue to this

⁶In more general frameworks such as string theory, CPT symmetry violation no longer implies LI violation [6].

⁷In high-energy QCD experiments, the quark-level Hamiltonian is required [28].

⁸Eq. (3.2) can represent (pure) neutron decay or nuclear beta decay. In the former case, the wave functions are solutions to the *free* Dirac equation, whereas in the latter, the proton and neutron are bound inside of a nucleus, while the emitted beta particle exists in the Coulomb field of the atomic nucleus [96, p. 5]. Additionally, it is an open question whether or not neutrinos are Dirac or Majorana particles. If neutrinos are Dirac particles, i.e., they are fermions with distinct particles and antiparticles, then they satisfy the Dirac equation. Alternatively, if neutrinos are Majorana particles, i.e., they are their own antiparticle, then they don't satisfy the usual Dirac equation; however, they do satisfy a modified Dirac equation.

day [97, 98] have shown that it is only the vector and axial vector interactions which contribute to the interaction Hamiltonian in Eq. (3.2). The resulting Hamiltonian (from here to be referred to as the “SM prediction”)⁹

$$H_{\text{int}}(n, p, e, \nu) = \frac{G_\beta}{\sqrt{2}} \int d^3x \left[\bar{u}_p \gamma^\mu \left(1 + \frac{C_A}{C_V} \gamma_5 \right) u_n \right] \left[\bar{u}_e \gamma_\mu (1 - \gamma_5) u_\nu \right], \quad (3.4)$$

where G_β is the *Fermi constant of beta decay*, proportional to the ud -element of the Cabibbo-Kobayashi-Maskawa (CKM) matrix. It is known experimentally that $\frac{C_A}{C_V} = -1.255(6)$ [96, p. 260]. Without dwelling further on particle physics, it is important to note that current research into beta decay aims to uncover new physics by identifying additional components in decay interactions, however small. This means that the interaction term in Eq. (3.4) is rigorously tested for possibly including more than just vector and axial-vector components.

The conservation of total angular momentum of the system (nucleus and leptonic products) is

$$\mathbf{J}_i = \mathbf{J}_f + \mathbf{L}_{e\nu} + \mathbf{S}_{e\nu}, \quad (3.5)$$

where \mathbf{J}_i and \mathbf{J}_f are the initial and final total angular momenta of the nucleus and $\mathbf{L}_{e\nu}$ and $\mathbf{S}_{e\nu}$ are the total orbital and spin angular momenta of the lepton pair. Consideration of Eq. (3.5) further differentiates the types of decay events. The distinguishing feature is the alignment, or lack thereof, in the spins of the outgoing leptons. In allowed decays¹⁰ the outgoing leptons do not have orbital angular momentum ($\mathbf{L}_{e\nu} = 0$); i.e., that they are emitted as an “ s -wave” with a spherically symmetric character. The

⁹A subtle point of Eq. (3.4) is that both maximal parity violation and left-handed neutrinos are assumed in writing it this way. These are justified assumptions since they correspond to every measurement that has ever been performed. These concepts will be discussed soon. As a point of notation, we will, from now on, write e and ν for simplicity with the understanding that the leptons obey Eq. (3.1), such that one is a particle and the other an antiparticle.

¹⁰Forbidden decays, where the leptons have nonzero orbital angular momentum, are greatly suppressed and will not be discussed here.

angular momentum selection rules are [96, pp. 262–263]

$$\text{Fermi transition } (S = 0) : \quad J_f^\pi = J_i^\pi \quad (3.6)$$

$$\text{Gamow-Teller transition } (S = 1) : \quad J_f^\pi = \begin{cases} J_i^\pi, & (J_i^\pi = J_f^\pi \neq 0) \\ J_i^\pi \pm 1 & \end{cases} \quad (3.7)$$

where J_i and J_f are the initial and final total angular momenta of the nucleus and $S = |\mathbf{S}_e + \mathbf{S}_\nu|$ depicts the total spin of the lepton pair. The parity of the nucleus, π , is unchanged as a consequence of the lepton pair having $L = 0$.

The form of Eqs. (3.6) and (3.7) can be understood as follows. It can be shown by nonrelativistic reduction that the Fermi transitions proceed via vector operators, which do not cause any change in nuclear spin. Thus, in Fermi transitions, where the e^-/e^+ and $\bar{\nu}_e/\nu_e$ are *antialigned*, the total spin does not change, $\Delta S = 0$ and the total (nuclear) angular momentum remains constant. Conversely, in Gamow-Teller decays, the lepton spins are aligned and $\Delta S = 1$. It follows from Eq. (3.7) that transitions satisfying $|J_f - J_i| = 1$ are *pure* Gamow-Teller transitions. The beta decay of ${}^6\text{He}$ ($J^\pi = 0^+$) to ${}^6\text{Li}^+$ ($J^\pi = 1^+$), the subject of this chapter, is pure GT.

The most general form of the decay rate distribution, derived from Fermi's Golden Rule (cf. Appendix B), given in the beta particle (e) and (anti)neutrino (ν) directions and beta particle energy is [28, 99]

$$\begin{aligned} w(\langle \mathbf{J} \rangle | \mathbf{E}_e, \Omega_e, \Omega_\nu) dE_e d\Omega_e d\Omega_\nu &= \frac{F(\pm Z, E_e)}{(2\pi)^5} p_e E_e (E_0 - E_e)^2 dE_e d\Omega_e d\Omega_\nu \\ &\times \xi \left\{ \left[1 + a \frac{\mathbf{p}_e \cdot \mathbf{p}_\nu}{E_e E_\nu} + b \frac{m_e}{E_e} + \frac{\langle \mathbf{J} \rangle}{J} \right] \left[A \frac{\mathbf{p}_e}{E_e} + B \frac{\mathbf{p}_\nu}{E_\nu} + D \frac{\mathbf{p}_e \times \mathbf{p}_\nu}{E_e E_\nu} \right] \right\} \end{aligned} \quad (3.8)$$

where E , \mathbf{p} , Ω are the energy, momentum and solid detection angle for the two leptons; E_0 is the maximum beta particle energy, \mathbf{J} and $\langle \mathbf{J} \rangle$ are initial angular momentum and polarization of the initial (nuclear) state; $F(\pm Z, E_e)$ is the Fermi function, a correction factor accounting for the distortion felt by the beta particle, which is moving in the Coulomb field of the nucleus of charge Z [96, pp. 263–269]; and a, b, A, B, D (each multiplied ξ) are correlation coefficients depending on the form of the transition

matrix elements of the beta decay Hamiltonian in Eq. (3.2). Although all five of these coefficients are actively studied in searches for new physics (see Ref. [28] for details), we are exclusively concerned with $a_{\beta\nu}$, the $\beta-\nu$ angular correlation coefficient, in this dissertation. With this in mind, a simplified version of this equation [98, 100] where, for example, unpolarized ($\langle \mathbf{J} \rangle = 0$) nuclei can be used, will serve our purpose:

$$w(E_e, \theta) \propto C \left(1 + b \frac{m_e}{E_e} + a_{\beta\nu} \frac{p_e}{E_e} \cos \theta \right). \quad (3.9)$$

In Eq. (3.9), C describes the phase space density of such transitions [100] and depends on the momenta and energy of the outgoing leptons. The so-called Fierz term, b , remains in this equation, even though we do not explicitly consider it here, and the SM predicts it to be 0 in pure Gamow-Teller beta decays [98]. The reason for this is that measurements of $a_{\beta\nu}$, as in those of Müller *et al.*, [98], are automatically sensitive to potentially nonzero values of b which could point to new physics (NP).

3.3.2 The $\beta-\nu$ angular correlation coefficient

In order to understand the relevance of $a_{\beta\nu}$ in searches for NP, we begin by considering the SM prediction for its value. “Correlation coefficients” such as $a_{\beta\nu}$, appearing in Eqs. (3.8) and (3.9) are formed as products of nuclear matrix elements, including both the Fermi and Gamow-Teller type, and coupling constants. The full form¹¹ of $a_{\beta\nu}\xi$, for the general case of mixed decay ($0 < x < 1$) is [99]

$$a_{\beta\nu}\xi = |M_F|^2 \left\{ |C_V|^2 + |C'_V|^2 - |C_S|^2 - |C'_S|^2 \right\} - \frac{1}{3} |M_{GT}|^2 \left\{ |C_A|^2 + |C'_A|^2 - |C_T|^2 - |C'_T|^2 \right\}, \quad (3.10)$$

¹¹Terms arising from the so-called Coulomb correction have been omitted here, owing to their smallness relative to the magnitudes of interest [94]. See [99] for the full expression.

where M_F and M_{GT} are the Fermi and Gamow-Teller nuclear matrix elements.¹² ξ itself is given by

$$\xi = |M_F|^2 [|C_V|^2 + |C'_V|^2 + |C_S|^2 + |C'_S|^2] + |M_{GT}|^2 [|C_A|^2 + |C'_A|^2 + |C_T|^2 + |C'_T|^2].$$

The $\{C_i\}$ and $\{C'_i\}$, for $i = S, V, T, A$, are the Lee-Yang coupling constants, i.e., ‘‘currents’’, appropriate for characterizing the beta decay process at the level of constituent nucleons.¹³ C_i and C'_i refer to parity conserving and nonconserving components of the interaction, respectively [85].¹⁴ The implication is that the $\{C_i\}$ retain their sign under parity inversion whereas $\{C'_i\}$ undergo a sign change. In the maximal parity violation predicted by the SM, these currents satisfy $C_i = C'_i$. The $\{C_x^{(\prime)}\}$ parameters are related to the more fundamental hadronic charges and further to the Wilson coefficients at the quark level predicted by QCD [28].

In the SM [101], pure decays, where either $M_F = 0$ (in GT decays) or $M_{GT} = 0$ (in Fermi decays) can be written in terms of the coupling constants as

$$a_{\beta\nu;F} = 1 - \frac{|C_S|^2 + |C'_S|^2}{|C_V|^2} \quad (3.11)$$

$$a_{\beta\nu;GT} = -\frac{1}{3} \left[1 - \frac{|C_T|^2 + |C'_T|^2}{|C_A|^2} \right], \quad (3.12)$$

where the second term in each of these is expected to be zero based on the SM prediction. Thus, a measurement of $a_{\beta\nu}$ constitutes a measurement of the ratio of these coupling constants. This can be expressed even more simply as

$$a_{\beta\nu} = \frac{1}{3} \left(\frac{3 - \rho^2}{1 + \rho^2} \right) = \frac{1}{3} (4x - 1), \quad (3.13)$$

where ρ is the Gamow-Teller/Fermi mixing ratio,¹⁵ or expressed in terms of x the

¹² $M_F = 0$ ($M_{GT} = 0$) in GT (F) decays.

¹³Appendix C discusses the handedness of leptons in the SM, a relevant concept for the present consideration.

¹⁴These are effective couplings which relate to the more ‘fundamental’ quark-level parameters including masses and couplings of potential new particles [28].

¹⁵The mixing ratio, ρ , is the ratio of the product of the coupling constant and the nuclear matrix element for each decay type (terms to be soon discussed) so that $\rho = \frac{C_A M_{GT}}{C_V M_F}$.

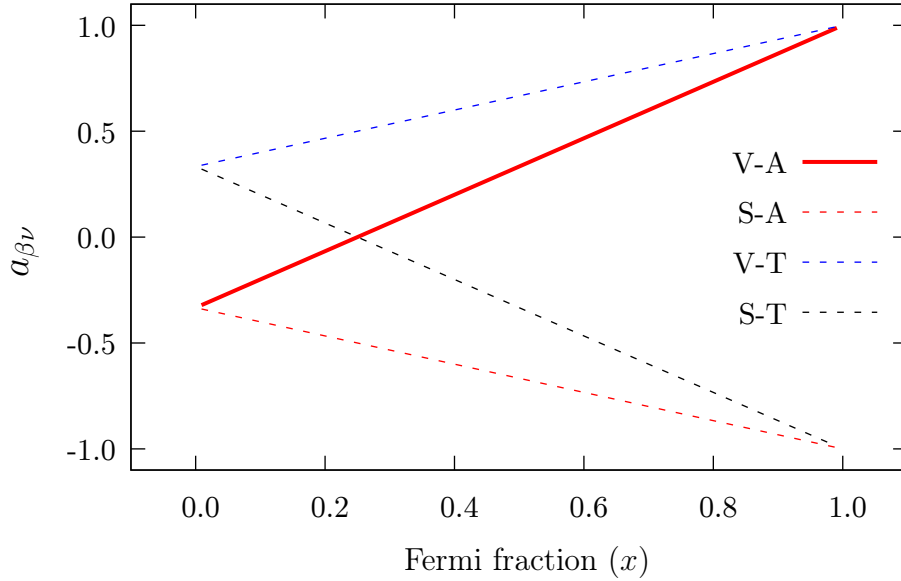


Fig. 3.3.2: Scott diagram showing the value of $a_{\beta\nu}$ as a function of the Fermi fraction x , which characterizes the degree of mixing in the decay. The solid red line corresponds to the $V - A$ structure of the weak interaction observed in nature.

Table 3.3.1: Summary of the value of the beta-neutrino angular correlation coefficient ($a_{\beta\nu}$) for pure Fermi ($x = 1$) or Gamow-Teller ($x = 0$) decays. The SM ($V - A$) predictions lie in the “Vector/Axial-Vector” column.

Transition Type	Vector/Axial-Vector	Scalar/Tensor
Pure Fermi	+1	-1
Pure Gamow-Teller	-1/3	+1/3

Fermi fraction. Pure decays ($x = 0$ for Gamow-Teller and $x = 1$ for Fermi decays) are found at the endpoints of the Scott diagram in Fig. 3.3.2.

In allowed transitions, the SM predicts that the values of $a_{\beta\nu}$ for pure scalar, vector, tensor, axial-vector interactions to be [94], respectively -1 , 1 , $\frac{1}{3}$, $-\frac{1}{3}$ (this is summarized in Table 3.3.1). Since the SM predicts the weak interaction to be V and A , we expect that $a_{\beta\nu}$ will lie along the solid red line in the Scott diagram shown in Fig. 3.3.2. Deviations from this prediction are actively sought in searches for NP.

3.3.3 Uses in searches for new physics

As described in the Introduction, despite the sweeping and significant successes of the SM, there are several critical questions for which it has no answer. Phenomena such as dark matter and baryonic asymmetry point to new physics (NP). The weak sector of the SM, and in particular the correlation coefficient $a_{\beta\nu}$ in beta decay, is a popular starting point to detect such NP directly [28]. This is the first example in this thesis that searches for NP at the *low-energy frontier* by using high-precision measurements and supporting theoretical efforts.

Many extensions¹⁶ to the SM (i.e., “beyond SM” (BSM) theories) postulate new particles that have couplings different from what we see in the SM [104]. Data from beta decay experiments competes with and complements other sources, such as the LHC [105] and astrophysical data, such as the neutrino flux from observed supernovae [106].

Although the specific modification to the weak interaction is dependent on which BSM is under consideration [107], the generic mathematical form underlying how NP would become manifest in beta decays is in changes to the quark-level transition $d \rightarrow ue^-\bar{\nu}_e$, a process that is mediated by W^\mp bosons [104, 107]. The cause of this is that the beta decay Hamiltonian predicted by the SM (Eq. (3.4)) picks up additional terms corresponding to scalar, tensor, or even pseudoscalar terms and also containing right(left)-handed (anti)leptons.

The usual way to capture this mathematically is by adding terms with NP-couplings α_i for hypothetical interactions O_i to the SM Langrangian \mathcal{L}_{SM} according to

$$\mathcal{L}_{\text{BSM}} = \mathcal{L}_{\text{SM}} + \sum_i \alpha_i O_i. \quad (3.14)$$

In addition to the new terms introduced in this fashion, new interference terms

¹⁶All have the virtue of explaining some as yet unexplained phenomena such as the *naturalness problem* or affording a BSM mechanism for CP violation believed to be required for the observed baryon asymmetry in the universe. Since CP violation [102] is required for baryon asymmetry, and CPT, tied intimately to Lorentz invariance [103], is believed to be a good symmetry [8], a specific set of theoretical efforts are focused on adding terms to the beta decay Lagrangian which violate T-reversal symmetry.

between the SM and BSM couplings can be expected to contribute to the decay rates. Generally, these additional terms correspond not only to new couplings but also to new particles and forces.

One concrete example of a BSM theory which generates an exotic, i.e., non-SM, weak interaction is the “Minimal Supersymmetric Standard Model” (MSSM) [108] wherein right-handed (RH) interactions are introduced via RH sfermions.¹⁷ These supersymmetric corrections generate scalar and tensor interactions which modify the beta decay Hamiltonian in Eq. (3.4) and the *testable* parameter $a_{\beta\nu}$, directly related to the Lee-Yang coupling constants.¹⁸ To compete with the constraints imposed from other sources, such as the LHC, beta decay measurements must take place at the $\delta a_{\beta\nu}/a_{\beta\nu} \sim 0.1\%$ level of precision to be sensitive to left-handed scalar and tensor interactions and $\delta a_{\beta\nu}/a_{\beta\nu} \sim 0.01\%$ to compete in studies of right-handed interactions [107]. While the former limit ($\sim 0.1\%$) is well within reach of many experiments (almost all of those described in Table 3.3.2), a precision of $\sim 0.01\%$ is not within the current capability of ongoing experiments.

In experimental determinations of $a_{\beta\nu}$, one searches for possible “exotic” scalar or tensor contributions that would manifest as terms quadratic in the corresponding coupling constants [28]. The quantity that is measured is not $a_{\beta\nu}$, but rather

$$\tilde{a}_{\beta\nu} = a_{\beta\nu} / \left(1 + \left\langle b \frac{m_e}{E_e} \right\rangle \right), \quad (3.15)$$

where the dependence on the Fierz term, b , manifests through the weighted average of its product with the total mass (m_e) and energy (E_e) of the beta particle [109]. In the SM, b has a nonzero value. It becomes nonzero through couplings between standard (V, A) and exotic (S, T) currents [126]. In practice, depending on which type of decay is probed, the relative contributions of $|C_T/C_A|$ (in pure Gamow-Teller decays) or $|C_S/C_V|$ (in pure Fermi decays) can be determined, both of which are expected to be 0 in the SM.

¹⁷Sfermions are the superpartners of fermions characteristic of SUSY theories.

¹⁸The C'_i can also be calculated directly from lattice QCD, yielding results in agreement with experiment. However, the theoretical errors are typically much larger than those obtained from using data from low-energy beta decay experiments.

Table 3.3.2: Ongoing nuclear beta decay experiments studying the correlation coefficient $a_{\beta\nu}$ are listed. Each decay is classified by its “type”: Fermi or Gamow-Teller and based on whether it is β^- or β^+ decay. See Table V in Ref. [109] for a comprehensive list of the older experimental efforts.

Parent	Type	Experiment	Year (Most Recent)
${}^6\text{He}^+$	GT/ β^-	LPCTrap (GANIL) [97, 110, 111]	2012
${}^{35}\text{Ar}^+$	Mixed/ β^+	LPCTrap (GANIL) [112, 113]	2018
${}^{19}\text{Ne}^+$	Mixed/ β^-	LPCTrap (GANIL) [113]	2018
${}^6\text{He}$	GT/ β^-	Oak Ridge [114]	1963
		U. Washington [98, 115]	2022
		Weizmann Inst. [116]	In Progress
		SARAF (Yavne) [117]	In Progress ^a
${}^{21}\text{Na}$	Mixed/ β^+	Berkeley [118, 119]	2008 ^b
${}^{32}\text{Ar}$	Both	ISOLDE (CERN) [101, 120, 121]	2020
${}^{38}\text{K}^m$	F/ β^+	TRIUMF [122]	2005
${}^8\text{Li}^+$	GT/ β^-	ATLAS (Argonne) [123–125]	2015 ^c

^a The SARAF experiment will also look at several isotopes of neon: ${}^{18}\text{Ne}$, ${}^{19}\text{Ne}$, ${}^{23}\text{Ne}$.

^b There is some interesting history surrounding the Berkeley experiments. The initial experiments [118] found a substantial (3.6σ) disagreement with the SM, while the latter measurement [119] showed that the original effort was compromised by unintentionally trapped ${}^{21}\text{Na}_2$ molecules.

^c In these ${}^8\text{Li}^+$ experiments, it is α - β - $\bar{\nu}$ correlations that are studied.

There are several completed, ongoing, and planned experiments which seek to measure every coefficient (a, b, A, B, D) in Eq. (3.8), which are all connected to fundamental predictions of the SM. Efforts to determine $a_{\beta\nu}$ are reviewed in the following section. A complete list of these experiments can be found in Section 3 of the Review by González-Alonso *et al.* [28]. These beta decay experiments all seek to discern and stringently test the fundamental properties of the weak interaction.

3.3.4 Experimental measurements of $a_{\beta\nu}$

Careful measurement of the the beta decay rate of unpolarized nuclei, governed by Eq. (3.9) offers one means of obtaining the quantity of interest $a_{\beta\nu}$. Since the

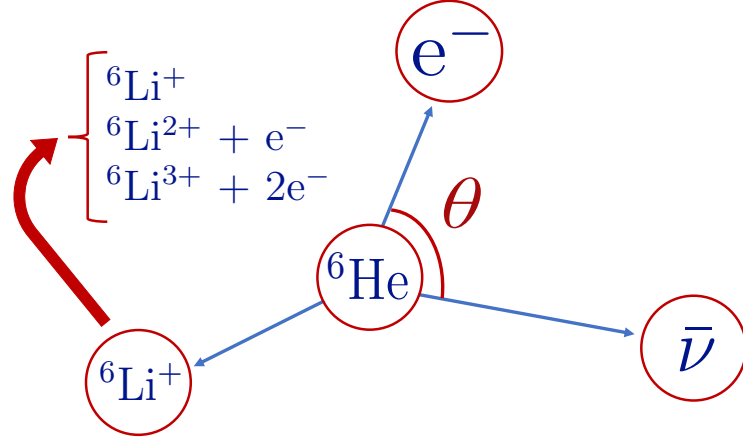


Fig. 3.3.3: Kinematics following the beta decay of ${}^6\text{He}$. The angle θ between the electron and antineutrino is related to the electron-antineutrino correlation coefficient – the experimental quantity of interest in connection with searches for NP.

(anti)neutrino cannot be detected directly in experiments, $a_{\beta\nu}$ can be deduced by observing the momentum spectra of the recoiling nucleons in coincidence with the beta particle.¹⁹ The typical situation is illustrated by considering the beta decay of ${}^6\text{He}$ shown in Fig. 3.3.3. Due to the elusive nature of neutrinos and the resulting inability to detect them experimentally, it is essential to understand what happens to the recoiling daughter ion, ${}^6\text{Li}^+$, following a decay event, to deduce the kinematics of the decay.

A summary of these experiments is given in Table 3.3.2. Early work to establish the $V-A$ theory, such as from Allen *et al.* [93], is omitted from this table. The significant advancements that have been made in the techniques of laser cooling and trapping²⁰ have facilitated a strong resurgence of interest in this problem. Well-localized atomic clouds allow decay products—importantly, the recoil ions—to emerge with minimal scattering, offering great control over associated systematic uncertainties [28]. The high intensity of radioactive source atoms and ions provided from the various sources like GANIL, ISOLDE, and CENPA at the University of Washington

¹⁹In this work, we are concerned with nuclear beta decays, that is, beta decays that occur in atoms or ions, but there is also significant activity which considers bare neutron beta decay (e.g., the *a*SPECT spectrometer at Institut Laue-Langevin [127] and the *a*CORN spectrometer at NIST [128]).

²⁰Ion (Paul or Penning) and atom (magneto-optical) traps are both extensively used to study beta decay. .

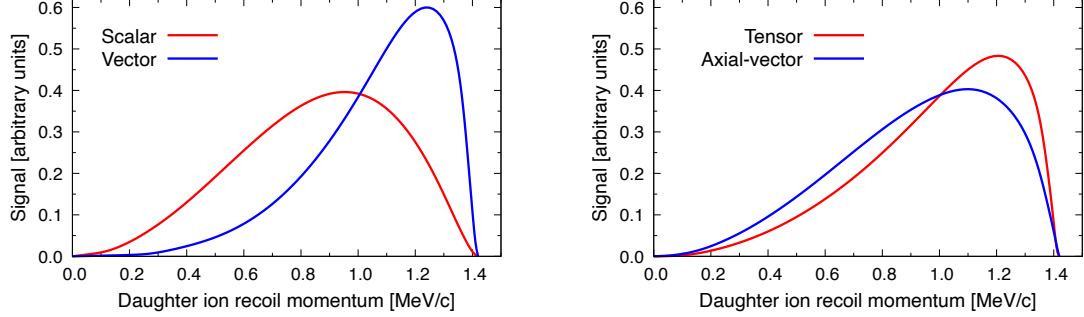


Fig. 3.3.4: The predicted shapes of the recoiling daughter ion's (RI) momentum are shown for the two possible Fermi interactions (vector and scalar) and the two possible Gamow-Teller interactions (axial-vector and tensor).

discussed in Table 3.3.2 is a critical reason contributing to the high precision that is now possible in low-energy decay experiments. The radioactive atoms are produced typically via a stripping interaction (e.g., ${}^7\text{Li}(\text{d},\text{p}){}^8\text{Li}$ at ISOLDE-CERN [125]) and are then cooled and trapped, possibly multiple times. The common objective in all experimental efforts studying nuclear beta decay is to measure in coincidence the recoiling daughter ion (RI) and the beta particle. Spatial- and energy-resolved measurements of the recoiling ion and beta particle are made possible by a microchannel plate and a telescope/scintillator, respectively. Time-of-flight (TOF) analysis allows for determining the momenta of the RI.²¹ The decay rate is thus measured as a function of the momentum of the RI. These measurements are compared with the theoretical curves [93, 94], which depend on the value of $a_{\beta\nu}$, as shown in Fig. 3.3.4. In comparing the observed spectra with those predicted theoretically with *different values of $a_{\beta\nu}$* that the data analysis proceeds. This is a difficult task, especially when considering that the results must be precise ($\delta a_{\beta\nu}/a_{\beta\nu} \sim 0.1\%$) in order to be helpful. Furthermore, to obtain the theoretical curve, very realistic simulations must be carried out [126] and in particular, the centre of the trap must be known very precisely, as it is often the leading source of systematic uncertainty [129]. Great efforts are taken to model the trapped ion cloud and the electric and magnetic fields present in order to cor-

²¹The exact mechanism of how the TOF measurement is performed is slightly different in certain experiments. For example, experiments at GANIL and University of Washington use a set of plates in an electrostatic mechanism whereby the RI is accelerated. On the other hand, the ISOLDE-CERN WITCH experiment uses a magnetic spectrometer where recoil ions spiral adiabatically from a high B field to a low B field.

rectly capture the dynamics of the field and cooling effects along with the N -body interactions present in the buffer gas [98, 129]. As in all precision experiments, the continuous development of better detection schemes and methodologies to improve measurement statistics is of chief importance.

3.3.5 Advantages of light atoms

Although, as illustrated in Table 3.3.2, many isotopes can be studied, there are certain advantages to using a “simple” atom such as ${}^6\text{He}$, or the still more straightforward one-electron system ${}^6\text{He}^+$. Firstly, this is a pure GT decay and is exclusively sensitive to potential exotic tensor currents and will serve to measure C_T/C_A . The advantage to studying a pure decay is that the Fermi fraction (x) has a known value (0 or 1) rather than a value $0 < x < 1$ that requires calculation and measurement. Furthermore, in light nuclei such as this $A = 6$ system, the high-precision few-body nuclear structure calculations needed to model the decay, in comparison with the experiment, are possible [98]. Few-nucleon systems such as ${}^6\text{He}$ facilitate the inclusion of higher-order (nuclear) contributions such as recoil order and radiative corrections that produce more accurate (nuclear) simulations. Additionally, ${}^6\text{He}$ (or ${}^6\text{He}^+$) is one of the lightest nuclei to undergo beta decay with a relatively large energy release ($Q \sim 3.5$ MeV), providing ideal conditions for the detection of the RI [130]. The relatively low energies of the beta particle and the RI make these experiments challenging. The large Q value of ${}^6\text{He}$ decay balances accurate nuclear theory calculations and sufficient experimental signal.

3.3.6 Connection to atomic physics

From the viewpoint of calculating atomic properties, ${}^6\text{He}$ is an excellent candidate parent ion for studying beta decay because this is a simple *atomic system* comprised of two electrons.²² The atomic electrons can be modelled with high-precision in these

²²The one-electron ${}^6\text{He}^+$, studied extensively at GANIL (e.g., [111]), is also excellent in this regard. Adopting a “glass is half full” sentiment; the two-electron case is valuable as it tests electron correlation and exchange effects while remaining very accurate.

systems and this feature is how atomic theory connects to these nuclear physics experiments. The excitation and ionization processes of the RI are referred to as “shake-up” and “shake-off”. Understanding these atomic effects is ultimately crucial in the experimental determination of $a_{\beta\nu}$ since the different charge states of the daughter ion can be discerned by TOF analysis. As such, the distribution between the daughter ion’s charge states must be known to experimentally realize the RI momentum spectrum of Fig. 3.3.4 and thereby determine $a_{\beta\nu}$. This can be achieved by setting thresholds on the minimum beta particle energy to restrict attention to decays that completely separate charge states based on TOF analysis (e.g., Ref. [130]). However, in simple atomic systems with one or two electrons, it should also be possible to predict the amount of shake-up and shake-off accurately. For example, in the one-electron ${}^6\text{He}^+$ system, theory [131] and experiment [111] are in perfect agreement. This behaviour of atomic electrons is also studied in more sophisticated decays, such as ${}^{19}\text{Ne}^+$ and ${}^{35}\text{Ar}^+$ [113], however, here it is noted that the ability to calculate the shake-off probabilities of these “highly” multielectron system is difficult to calculate to high accuracy. This work focuses on the two-electron system ${}^6\text{He}$, the “sweet spot” between these two extremes, where theory is still competent but where electron-electron correlation must be considered.

3.4 FORMULATION OF THE PROBLEM

Atomic calculations predict the behaviour of the two atomic electrons following beta decay. The daughter ion can become excited (in shake-up), singly, or doubly ionized (in shake-off). These three channels correspond to different charge states of the ${}^6\text{Li}^+$ daughter ion: ${}^6\text{Li}^+$, ${}^6\text{Li}^{++}$, and ${}^6\text{Li}^{3+}$. In particular, the primary objective of this work was to rectify the fact that previous theoretical efforts [131, 132] and [133, pp. 59–66] have universally overestimated the quantity of double ionization (formation of ${}^6\text{Li}^{3+}$) relative to experiments [114, 115]. This section formulates the problem to be solved by first describing the kinematics of the beta decay and then outlining the physical assumptions made. Henceforth, we will be exclusively concerned with pure

GT beta decay of ${}^6\text{He}$.²³

3.4.1 Kinematic description

We have established in this chapter that the beta decay ${}^6\text{He} \rightarrow [{}^6\text{Li}^+] + \text{e}^- + \bar{\nu}$ is studied to determine whether or not NP is present in the $a_{\beta\nu}$ coefficient. The square brackets around the daughter ${}^6\text{Li}^+$ ion are a reminder that shake-up (excitation to $({}^6\text{Li}^+)^*$) and shake-off (single or double ionization to ${}^6\text{Li}^{++}$ or ${}^6\text{Li}^{3+}$, respectively) are all possible outcomes of ${}^6\text{He}$ decay, as shown in Fig. 3.3.3. The experimental challenge is that $\bar{\nu}$ cannot be detected directly, so its momentum vector must be deduced from the overall kinematics of the decay process, including both the β particle and the recoiling ${}^6\text{Li}^+$ nucleus, together with its two atomic electrons. In Sec. 3.3.4, it was shown that interpreting correctly the recoil ion momentum spectra, needed to determine $a_{\beta\nu}$, one must consider its charge state. Otherwise, deviations due to the electronic momentum might masquerade as a signal for new physics. First, we must formulate the kinematics of the decay.

The kinematics of the process is as follows. As discussed previously [115, 132], the emitted β particle has a maximum kinetic energy of $E_{\max} = 3.51$ MeV with a broad energy distribution going down to nearly zero. However, in the experiment of Hong *et al.* [115], only those events with $E > 1$ MeV were counted to ensure separation in the TOF spectra used to disentangle the separate charge states. At these energies, the β particle is relativistic. From the relativistic energy-momentum equation $(E_{\max} + m_e c^2)^2 = c^2 P^2 + m_e^2 c^4$, the maximum recoil momentum is $P_{\text{rec}} = 1070$ a.u. In contrast, since the recoiling ${}^6\text{He}$ nucleus is much more massive ($M = 6.01523$ u), its recoil velocity of $v_{\text{rec}} = 0.0925$ a.u. is nonrelativistic. The atomic electrons acquire a corresponding momentum $K = m_e v_{\text{rec}} = 0.0925$ a.u.; however, this amount is so small that it is unimportant for the present discussion, though it was considered in [132] and [133, pp. 32–43].

²³The decay of ${}^6\text{He}^+$ (identical from a nuclear physics perspective) will also be briefly discussed.

3.4.2 Physical assumptions

The three points of discussion concerning the physical process here are the recoil of the daughter ion, the decay itself, which results in a change in nuclear charge, and the outgoing beta particle. Recall that we are interested in calculating the amount of each ${}^6\text{Li}^+$ charge state following the decay. In these three cases, we will ask what effect these have on the atomic electrons and to what (if any) extent we must accommodate them in our theoretical treatment. The future works at the end of this chapter in Sec. 3.9 addresses the possible relaxation of these assumptions.

Firstly, a perturbation is introduced by the fact that the ${}^6\text{Li}^+$ daughter ion acquires momentum due to the decay. Mathematically, this recoil is generated by the operator $e^{i\mathbf{K}\cdot(\mathbf{r}_1+\mathbf{r}_2)}$. Recoil corrections are important for analyzing experiments [132]. However, for the present study, we worked in the limit of zero recoil ($\mathbf{K} = 0$) where the operator mentioned above is 1 since the recoil effects do not materially change the charge-state distributions, which are our main focus. In particular, the probability for the formation of Li^{3+} can be written in the form [132]:

$$P(\text{Li}^{3+}) = A + K^2 B + \dots, \quad (3.16)$$

where $\hbar K = \hbar |\mathbf{K}|$ is the magnitude of the recoil momentum, with $B \simeq 0.005$ so that $K^2 B \simeq 4 \times 10^{-5}$ relative to the previously calculated value $A \simeq 0.012$ [132]. The present work, therefore, focused on the leading A term and neglected the recoil. It will be seen that the discrepancy in predicted double ionization is much larger than this.

The most significant perturbation contributing to exciting or ionizing atomic electrons is the change in nuclear charge accompanying decay.²⁴ The charge goes from $Z = 2$ to $Z = 3$, and thus, the Hamiltonian changes (from $H_{Z=2}$ to $H_{Z=3}$) in a very short time. In this work, we adopt the sudden approximation (SA), where this change in nuclear charge is modelled as taking place *instantaneously*. This simplifica-

²⁴The other process that can happen is “direct-collision”, where an orbital electron is Coulomb scattered by the emitted beta particle. This effect was shown to be of order $\approx \alpha^2(\alpha Z)^2 \approx 10^{-8}$ in helium [134], much too small for us to be concerned with here.

tion has been almost universally used in studying beta decay in light atoms such as ${}^6\text{He}$ [111, 114, 131, 132, 134]. In particular, Couratin *et al.* [111] showed agreement between theory and experiment in the one-electron ${}^6\text{He}^+$ while using the SA. The SA should work just as well in the $Z = 2$ two-electron case since the energies involved are not significantly different from the one-electron case (and, as shown in Appendix D, the argument for its use is that the beta particle being significantly greater than the binding energy of the atomic electrons. To this point, Chizma *et al.* [135] considered how the SA affects the calculated decay rates (cf. Eq. (3.8)). They show that it is for beta energies $E_\beta \lesssim 0.05Z^2$ a.u. that the SA needs to be relaxed.

The physical justification for making the SA is that the emitted β particle is relativistic and can be thought of as a spherical shell of charge expanding with (nearly) the speed of light. The SA is valid for “fast” processes that occur on time scales much shorter than the natural timescales governing the system’s dynamics. The key result is that the wave functions of the electrons do not have time to adjust to the new Hamiltonian. The initial helium wave function $\Psi({}^6\text{He})$, an eigenstate of $H_{Z=2}$, is *not* an eigenstate of $H_{Z=3}$ and (by assuming the SA) does not have time to adiabatically adjust to the new system. Thus, it must be expanded over the complete set of states $\Psi_i({}^6\text{Li}^+)$ according to

$$\Psi(\text{He}) = \sum_i c_i \Psi_i(\text{Li}^+). \quad (3.17)$$

See Appendix D for a derivation of and further comments on the SA.

The next question is whether the outgoing beta particle interacts significantly with the atomic electrons. This leads to the necessity of including exchange effects arising from the indistinguishability of the atomic electrons and the outgoing beta particle. We make the approximation that the beta particle is *distinguishable* from the atomic electrons, thereby neglecting the exchange effect.²⁵ The physical reason for adopting this approximation is that the beta particle has very high energy and is in a continuum state with minimal overlap with the (bound) two-electron wave function. Further, the relativistic beta particle will spend little time interacting with the atomic

²⁵To be clear, both exchange effects and full correlations are accounted for in the treatment of the two atomic electrons.

electrons, so any possible exchange interaction will occur on very small timescales. Cooper and Åberg [136] have considered exchange effects using a “single-step” model, which extends the SA. They derived a formula and concluded that for both shake-up and shake-off processes, the predictions of the SA are obtained in the limit $E_\beta \gg E_a$, where the beta particle has much more energy than the atomic electrons. In the beta decay of ${}^6\text{He}$, where $E_\beta \sim 10^4$ a.u. and $E_a \sim 1$ a.u., this condition is easily met.²⁶ Exchange effects between the β particle and the atomic electrons have been considered explicitly and found to be negligible at these energies [136, 137].

3.4.3 Problem statement

We are trying to solve the problem of determining the probabilities of forming daughter ions of each charge state. The first step is to calculate the individual probabilities of a transition into each final state $|\Psi_f({}^6\text{Li}^+)\rangle$. In the limit of no nuclear recoil, this becomes [132]:

$$P_{i \rightarrow f} = |\langle \Psi_i({}^6\text{He}) | \Psi_f({}^6\text{Li}^+) \rangle|^2 = A_{if}. \quad (3.18)$$

Since there are a countably infinite number of discrete bound states and an uncountably infinite number of continuous scattering states, the methods used to sum or integrate the $\{P_{i \rightarrow f}\}$ corresponding to a given charge state require careful consideration and constitute the primary challenge.

A consequence of working only with $P_{i \rightarrow f} \approx A$ is that this work is only concerned with transitions that involve no change in angular momentum ($\Delta L = 0$) and only $S - S$ transitions as we are always starting in S states. Transitions to higher angular momentum states occur only at higher orders of \mathbf{K} , with much smaller probabilities,

²⁶In higher- Z atoms, where typically E_β is smaller than in ${}^6\text{He}$ and E_a , which scales as Z^2 , exchange effects are more important, and the formalism developed in Ref. [136] can be consulted.

due to the expansion of the recoil operator

$$e^{i\mathbf{K}\cdot\mathbf{r}} = e^{iKz} = 1 + iKz - \frac{(Kz)^2}{2!} + \dots, \quad (3.19)$$

$$= 1 - \underbrace{\frac{(Kr)^2}{6}}_{S-S} + \underbrace{iKz}_{S-P} - \underbrace{\frac{(Kr)^2}{3}P_2(\cos\theta)}_{S-D} + \dots, \quad (3.20)$$

Refs. [132] and [133, pp. 32–43] treat these recoil-dependent effects, and the methodology developed here could also be turned towards recoil corrections in the future.²⁷

3.5 STATE OF THE ART

There have been several attempts to predict the probabilities of shake-up and shake-off (of as many electrons as possible) in various atomic systems, as discussed in Sec. 3.3.6. The conclusion of previous work is that in one-electron systems, theoretical predictions agree with experiment [111, 131], whereas in systems with more than one electron, theory and experiment do not agree (e.g., [113–115]). We are concerned with the two-electron system, which has been studied experimentally [114, 115] and theoretically in Refs. [131, 132, 134]. The critical problem we seek to rectify is the overestimation of double ionization, i.e., the formation of ${}^6\text{Li}^{3+}$, following the beta decay of ${}^6\text{He}$. This section critically reviews previous theoretical efforts, and problems are revealed in their formalism. In particular, the work of Schulhoff and Drake [132] serves as the foundation for the present work.

3.5.1 Previous theoretical attempts

The key problem, stated in Eq. (3.18), is to (1) calculate squared overlap matrix elements $|\langle \Psi_i({}^6\text{He}) | \Psi_f({}^6\text{Li}^+) \rangle|^2 = P_{i \rightarrow f}$ that represent the probability of transition from the initial state $\Psi_i({}^6\text{He})$, with energy E_i , to a final state $\Psi_f({}^6\text{Li}^+)$ of energy E_f ; and (2) add or integrate these probabilities according to charge state. Thus, the

²⁷That we don't obtain agreement even on the recoil-independent A probabilities, though we do find improvement on previous work, is why we have not yet taken this further step.

problem involves choosing accurate wave functions with a well-defined charge state and correctly integrating the appropriate $\{P_{i \rightarrow f}\}$ corresponding to each charge state.

A common feature of all approaches to this problem is to use a discrete pseudospectrum, a concept introduced in Sec. 2.7.1, to represent both the bound and continuum states. This allows the integral $\int_{E>0} \mathcal{P}(\mathcal{E}) dE$ over the continuum to be replaced by a computationally-tractable sum. In using a pseudospectrum, this integral can be approximated by the sum $\sum_f w_f P(E_f)$, where the weights are chosen with the understanding that each pseudostate $\Psi_f(^6\text{Li}^+)$ with energy E_f corresponds to an energy range. The goal, then, is to develop a finite set of pseudostates which capture the essential physics of the problem. At a minimum, these basis sets should be asymptotically complete and cover the energy range that is expected to be important for the problem. The following text outlines various methods to achieve this goal. Further efforts undertaken will be the main focus of the subsequent Secs. 3.6 and 3.7.

One of the first treatments of the beta decay of ${}^6\text{He}$ was by Winther in 1952 [138], where he considered only bound-bound transitions $P_{i \rightarrow f}$ where $\Psi_f = {}^6\text{Li}^+(1s n s^1 S)$ for $n = 1-4$. In this calculation, Hylleraas wavefunctions were used to represent the ground states of ${}^6\text{He}$ and ${}^6\text{Li}^+$ along with the first excited state of ${}^6\text{Li}^+$, while Hartree wave functions were used for the remaining bound states of ${}^6\text{Li}^+$. A problem with this pioneering implementation was that the bound states of ${}^6\text{Li}^+$ generated in this way were not orthonormal. Due to this, the probabilities calculated do not add exactly to 1, so even though estimates are given for transitions to the continuum, they cannot be taken too seriously. One remarkable fact about Winther's work is that using Hylleraas wave functions with a single nonlinear parameter for the ground ($1s^2 {}^1 S$) for ${}^6\text{He}$ and ${}^6\text{Li}^+$ with only 6 and 9 terms, respectively,²⁸ predicted $|\langle {}^6\text{He}(1s^2 {}^1 S) | {}^6\text{Li}^+(1s^2 {}^1 S) \rangle|^2 \approx 0.670$, when the current best value [132] is 0.7086.... This indicates the importance of electron exchange and correlation effects in the beta decay process. Hylleraas wave functions, even in their simplest and restricted form, are well-suited to tackle this problem.

²⁸In the present work, we used up to 650 terms in our Hylleraas basis functions, with two basis sectors, i.e., sets of terms in the wave function with different nonlinear parameters.

In 1968, Carlson *et al.* [139] used nonrelativistic Hartree-Fock wave functions to carry out a much more comprehensive calculation. They considered the probability P_K of creating a vacancy in the K -shell in elements in the $Z = 2$ to 92 range undergoing beta decay from the ground state. Although this calculation is sophisticated, the P_K value is insufficient to partition the charge state fractions of the daughter ion following beta decay. In ${}^6\text{He}$, they calculated $P_K = 0.269$ and the current best value is [132] $P_K = 0.291$. This difference cannot be attributed to the number of terms in the wave functions in this case; rather, the method of forming the wave functions is insufficient. Hartree-Fock wave functions do not account for correlation even in this limit of an infinite basis set size. An important finding of this work was that for $Z \gtrsim 31$, relativistic Hartree-Fock-Slater wave functions are needed.²⁹

Wauters and Vaeck used the first configuration interaction (CI) method in treating this problem [131]. In their work, two-electron wave functions are formed using configurations built on one-electron orbitals that are formed using B splines. The central property is that the wave functions are formed as linear combinations of positive piecewise polynomials (i.e., B splines) defined on a knot sequence via recursion relations [131]. The advantage of B splines is that each basis function is nonzero only over a limited range; this simplifies calculations as the interactions become local. Other basis functions, such as Slater or Gaussian orbitals, are infinite in extent. Furthermore, the one-electron basis set constructed of B splines is effectively complete, allowing for the entire spectrum of the one-electron Hamiltonian $H^{(1)}$ to be described by a finite pseudospectrum. These one-electron orbitals are combined as described in Sec. 2.7.4. and the calculated charge-state fractions using this method appear in Table 3.5.1.

Although CI methods systematically include electron correlation, Table 2.7.2 shows that they do this much less effectively than Hylleraas wave functions. Furthermore, in Table 3.5.1, we see that the probabilities for the various charge states following the beta decay of ${}^6\text{He}$ that are calculated using this method do not add

²⁹Another significant aspect of this work is that it was one of the early successes of the Hartree-Fock code written by Charlotte Froese Fischer [140]. This would later evolve into the famous multi-configurational Hartree-Fock program, using the self-consistent field method.

exactly to 100%. For these reasons, Hylleraas wave functions were deemed the appropriate starting place for this calculation.

Frolov and Ruiz [134] calculated transition shake-up probabilities in the light atoms He, Li, and Be. In the two-electron He, they used the so-called Hylleraas-CI [141, 142], a hybrid method that uses higher angular momentum states characteristic of the CI that include the interelecton coordinate r_{12} , the hallmark of the Hylleraas approach, into the basis states. These calculations yielded high-precision results for the $|\langle {}^6\text{He}(1^1S)|{}^6\text{Li}^+(n^1S)\rangle|^2$ up to $n = 7$ that was surpassed in 2015 by Schulhoff and Drake [132], who used a fully correlated and doubled Hylleraas basis set to variationally solve the two-electron problem.

3.5.2 Foundation: doubled Hylleraas basis functions

The current work builds on Ref. [132], and it therefore serves to briefly recapitulate this work. Recall that the problem we wish to answer is: What is the probability of forming ${}^6\text{Li}^+$, ${}^6\text{Li}^{++}$, and ${}^6\text{Li}^{3+}$ following the beta decay of ${}^6\text{He}$. For this purpose, we use variationally constructed Hylleraas states (cf. Sec. 2.7.1).

In Ref. [132], the ${}^6\text{Li}^+$ final states in Eq. (3.18) were partitioned by their energy range (bins) as a proxy for the charge state, according to

$$\begin{aligned} \text{Bin 1 (shake-up)} : \quad & E_g(\text{Li}^+) \leq E < E_g(\text{Li}^{++}) \\ \text{Bin 2 (single ionization)} : \quad & E_g(\text{Li}^{++}) \leq E < E_g(\text{Li}^{3+}) \\ \text{Bin 3 (double ionization)} : \quad & E_g(\text{Li}^{3+}) \leq E < \infty \end{aligned} \quad (3.21)$$

where $E_g(\text{Li}^+) = -7.2799134\dots$ is the ground-state energy of ${}^6\text{Li}^+$, $E_g(\text{Li}^{++}) = -4.5$ a.u., and $E_g(\text{Li}^{3+}) = 0$. This is shown below in Fig. 3.6.1. Bin 1 corresponds to shake-up, whereas Bins 2 and 3 are classified as shake-off. The pseudospectra were optimized by varying β_1 in the first sector of the Hylleraas basis functions, with the remaining nonlinear parameters chosen to be similar to the low-lying bound states [51]. Further, since this is a pseudospectrum, each eigenstate represents a range of energies. The method of Stieltjes imaging [143] was used to approximate the differential transition

Table 3.5.1: Comparison of previous theory with experiment for the probabilities $P(^6\text{Li}^{k+})$ of forming the various charge states with $k = 1, 2, 3$ following beta decay of ${}^6\text{He}(1\ ^1S_0)$ or ${}^6\text{He}(2\ ^3S_1)$ as initial states. Ground state results in the upper panel are from Carlson *et al.* [114]. Metastable triplet results in the lower panel are from Hong *et al.* [115]. All quantities are expressed in percent (%).

${}^6\text{He}$ state ^a	Daughter ion	Theory [132]	Theory [131]	Exp't.
$1\ ^1S_0$	${}^6\text{Li}^+$	89.03(3)	89.09	89.9(2)
	${}^6\text{Li}^{++}$	9.7(1)	10.44	10.1(2)
	${}^6\text{Li}^{3+}$	1.2(1)	0.32	0.018(15)
	Total	99.9(1)	99.85	100.0(2)
$2\ ^3S_1$	${}^6\text{Li}^+$	88.711(3)		89.9(3)(1)
	${}^6\text{Li}^{++}$	9.42(7)		10.1(3)(1)
	${}^6\text{Li}^{3+}$	1.86(7)		<0.01
	Total	99.99(7)		100.00

^a Results have also been calculated [133, pp. 67–73] and measured [115] for the ${}^6\text{He}(2\ ^3P)$ initial state. As the text mentions, P states are not featured in the present work as we are focused on resolving a simpler problem first.

probability per unit energy interval $\frac{dP(E)}{dE}$ from the initial state of ${}^6\text{He}$ to a final state of ${}^6\text{Li}^+$ with energy E in the form

$$\frac{dP(\bar{E})}{dE} \approx \frac{1}{2} \frac{P_{j+1} + P_j}{\varepsilon_{j+1} - \varepsilon_j} \quad (3.22)$$

evaluated at $\bar{E}_j = (\varepsilon_{j+1} + \varepsilon_j)/2$. Stieltjes imaging yielded increased stability in the $\frac{dP(\bar{E})}{dE}$ vs. \bar{E}_j graphs with an increasing number of terms N_2 in the variational wave functions and therefore in the calculated charge state fractions. The validity of this method was demonstrated in the problem of photoionization of hydrogen [144]. A linear smoothing method was applied for those states closest to the bin boundaries [133, pp. 51–52].

In addition to giving closure, as indicated by a total probability being equal to 100%, as shown in Table 3.5.1, in Ref. [132], several oscillator strength sum rules are shown to be satisfied for the wave functions used to describe the initial ${}^6\text{He}$ state and

the ${}^6\text{Li}^+$ pseudospectra. In particular, a generalized Thomas-Reiche-Kuhn (TRK) sum rule,³⁰ that includes the change in Coulomb potential accompanying beta decay, was derived and found to be satisfied. To account for this change, a modification to the ordinary optical oscillator strength³¹ was made according to

$$f_{i \rightarrow f} = 2[E_{\text{Li}^+(f)} - E_{\text{He}(i)}]|\langle i|z_1 + z_2|f \rangle_{\text{Li}^+}|^2. \quad (3.23)$$

The TRK sum rule then acquires an extra term due to the change in the Coulomb potential with the result

$$\sum_n f_{i \rightarrow n} = N + 2\langle i|(V_{\text{Li}^+} - V_{\text{He}})(z_1 + z_2)^2|i \rangle \quad (3.24)$$

$$= 2 - 2\langle i| \left(\frac{1}{r_1} + \frac{1}{r_2} \right) (z_1 + z_2)^2|i \rangle, \quad (3.25)$$

where $N = 2$ is the number of electrons and $|i\rangle$ denotes the ${}^6\text{He}$ initial state. For $\text{He}(1^1S) \rightarrow \text{Li}(n^1P)$, the sum rule is

$$\sum_n f_{\text{He}(1^1S) \rightarrow \text{Li}(n^1P)} = -1.9734403, \quad (3.26)$$

which is satisfied to many figures using the Hylleraas pseudostates obtained via the procedures described here. The sum rules interconnect and tightly constrain the calculated charge-state fractions and justify the completeness assumption contained in Eq. (3.17),

$$\Psi({}^6\text{He}) = \sum_i c_i \Psi_i({}^6\text{Li}^+)$$

that these fully correlated pseudostates $\Psi_i({}^6\text{Li}^+)$ on the right-hand-side contain complete information about all possible two-electron states, including single- and double-continuum states, as well as autoionizing resonances, at least in the limit of large basis sets and in the region of space near the nucleus (cf. Sec. 2.7.3).

³⁰The normal TRK sum rule is: $\sum_n f_{i,n} = N$ where N is the number of electrons [40, p. 256]. Eq. (3.25) reduces to this normal case when the initial and final state are from the same Hamiltonian.

³¹The ordinary oscillator strength looks identical to Eq. (3.23) but assumes that the initial and final states come from the same Hamiltonian.

The results for the calculated charge state fractions following decay from the ground and metastable triplet state of ${}^6\text{He}$ are shown in Table 3.5.1. Predictions from theory, namely the Hylleraas approach of Schulhoff and Drake [132], and the CI + B spline approach of Wauters and Vaeck [131] are compared with two experiments, one old [114] and one new [115]. The predictions of the Hylleraas method are superior to the CI method and will, from here on, be synonymous with “theory” since it better includes electron correlation—a feature that Wauters and Vaeck [131] explicitly demonstrated to be important in treating atomic rearrangement following beta decay. Also, the CI method does not give closure as the total probability does not add to 100% as it does with the Hylleraas method. The theory compares favourably with the experiment for all but the amount of double ionization or formation of ${}^6\text{Li}^{3+}$, where there is a disagreement by several orders of magnitude. This overestimation of Bin 3 in Eq. (3.21) is the focus of the present work.

3.6 OVERESTIMATED DOUBLE IONIZATION

This section outlines why a metric other than energy must be deployed to partition the charge states in the ${}^6\text{Li}^+$ daughter ions following beta decay. First, it is shown that the $E > 0$ region contains contributions from single and double ionization. Then, we directly confront the experimental reality that *very little* ${}^6\text{Li}^{3+}$ is measured, regardless of the charge state (cf. 3.5.1), and sketch an argument as to why this makes sense. This serves to justify the creation of projection operators, which will be described in the subsequent section.

3.6.1 Energy does not describe charge state

The primary limitation of the method employed by Schulhoff and Drake [132] is that energy is not the appropriate metric to describe the charge state of an atom. Their calculation identified the charge states by the energy bin into which the pseudostate fell, summarized in Eq. (3.21).

Bins 1 and 2 contain purely ${}^6\text{Li}^+$ and ${}^6\text{Li}^{++}$ states (Bin 2 includes doubly excited

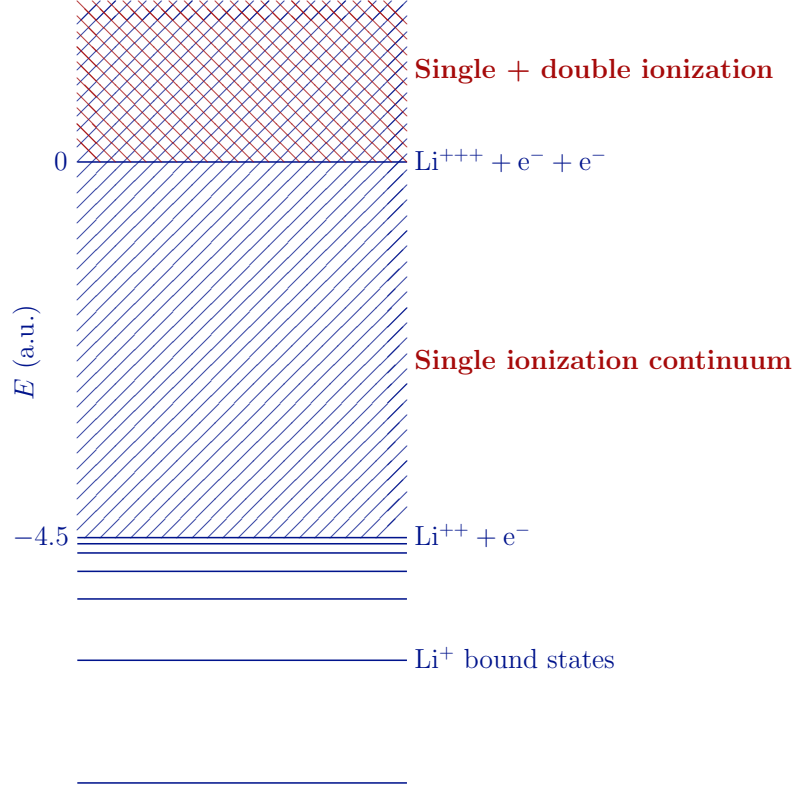


Fig. 3.6.1: Energy level diagram of ${}^6\text{Li}^+$ with the charge states indicated. Notably, the $E > 0$ region contains both the single and double ionization channels.

autoionizing states), but Bin 3 contains both ${}^6\text{Li}^{++}$ and ${}^6\text{Li}^{3+}$. It is in Bin 3, where $E > 0$ a.u. that the energy fails to represent unambiguously the charge state. This is illustrated in Fig. 3.6.1 and can be understood as follows. The argument begins with a discussion of how the ionization thresholds are calculated and an analysis of why the energy parameter in Bins 1 and 2 is an unambiguous indication of the charge state.

In the screened hydrogenic and independent particle approximations, which are sufficient for the ensuing argument, the energy is the sum of the Bohr energies:

$$E = -\frac{Z^2}{2n_1^2} - \frac{(Z-1)^2}{2n_2^2}$$

where Z , n_1 , and n_2 are the nuclear charge and the principal quantum numbers of electrons one and two, respectively. For singly excited states $n_2 \rightarrow \infty$, the first electron is in the ground state ($n_1 = 1$), giving the first ionization threshold in ${}^6\text{Li}^+$

as $E_{1st} = -4.5$ a.u.. This is the lowest possible energy that a ${}^6\text{Li}^{++}$ state can have as it is simply the binding energy of the remaining one-electron ($n = 1$) system, while the ejected electron moves away with kinetic energy that must be added to -4.5 a.u.. In doubly ionized states, both $n_1 \rightarrow \infty$ and $n_2 \rightarrow \infty$, leading to $E_{2nd} = 0$. This is the lowest possible energy that a ${}^6\text{Li}^{3+}$ state can have; the kinetic energy of the two ejected electrons must be added to 0 a.u.. Any states with $E < E_{1st}$ are bound, and it follows that bound states cannot have $E > E_{1st}$. For the same reason, since n_1 remains finite in Bin 2, no doubly ionized states can have $E < E_{2nd}$. Thus, states with energies in Bin 2, $E_{1st} < E < E_{2nd}$, are all singly ionized. These arguments set strict limits on the contents of Bins 1 and 2, but concerning Bin 3, they only tell us that ${}^6\text{Li}^+$ states cannot possibly be there.

Figure 3.6.1 shows clearly that the energy bin $E > 0$ is not exclusively composed of doubly ionized states. As mentioned above, in the single ionization channel, ${}^6\text{He}(1s^2) \rightarrow {}^6\text{Li}^{++}(1s) + e^-$, the energy is calculated (to a good approximation appropriate for this heuristic argument) according to $E_{++} = -4.5 + K_2$, where -4.5 a.u. is the ${}^6\text{Li}^{++}(1s)$ binding energy and $K_2 > 0$ is the kinetic energy of the ejected electron. In beta decay events leading to singly ionized daughter ions, there is no restriction on how much energy K_2 the ejected electrons can carry away. Since the ejected electron can carry away an arbitrarily high amount of energy – even enough to give $E_{++} > 0$, therefore the $E > 0$ region described by Bin 3 contains overlapping continua, which both contribute.

3.6.2 Suppression of double ionization

Based on the above reasoning, we would expect that the previous theoretical formulation is overestimating the amount of Li^{3+} . Here, we present an argument that outlines why very little double ionization should occur. It is known from work on the related problem of the single- and double-photoionization [145] cross sections that (1) the cross section σ becomes progressively smaller as the energy is increased, and (2) double ionization is significantly suppressed near threshold [146]. In the same way that

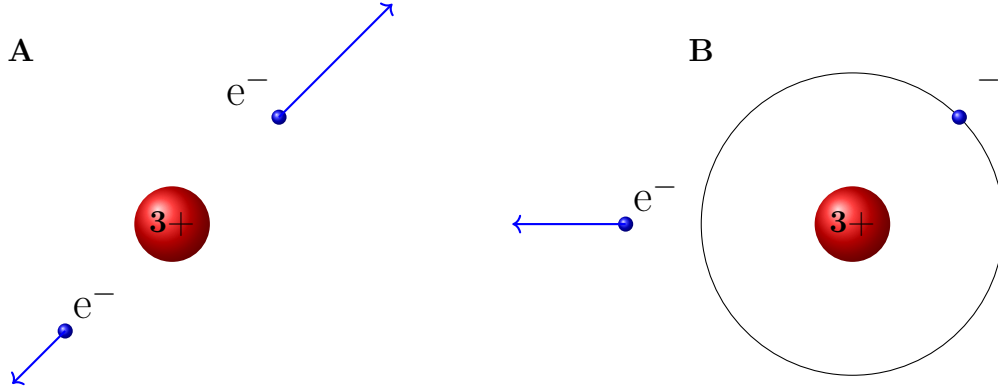


Fig. 3.6.2: This diagram illustrates the phase space arguments suggesting that double ionization is rare. In the case where energy/momentum are not equally shared between the two electrons, shown in panel A, one electron will fall back and become bound, creating a singly ionized state, shown in panel B.

$\sigma(E)$ decreases with energy, so does $P(E)$.³² It makes sense that the matrix elements became smaller and smaller as the energy difference between the states increased, as there is progressively less overlap between the corresponding wave functions. There is a vast literature in collision and laser physics concerned with cross-section calculations that are very similar in spirit to the present work. The points mentioned here are revisited in the context of contributing to this literature in the discussion of future work in Sec. 3.9.1.

Figure 3.6.2 considers the situation where the daughter atom has some $E > 0$ that is relatively small. The two possibilities are that the atom is singly ionized, with one ejected electron, or doubly ionized, with two ejected electrons. Phase space considerations support the notion that very little double ionization should occur in these “near-threshold events.” Suppose that two electrons are being ejected but with very little total energy, so they are moving slowly. For both electrons to truly be ejected, in this limiting case, the energy needs to be shared almost equally between them, or else one of them will “fall back,” leaving the atom singly ionized. This argument extends to relatively low-energy $E > 0$ states, just above threshold, suggesting that at these small energies single ionization remains dominant. Although if the energy to be

³²The photoionization cross section is proportional to squared dipole matrix elements $\sigma(E) \propto \Delta E |\langle f|z|i \rangle|^2$, as compared with beta decay probabilities, which scale according to $P(E) \propto |\langle f|i \rangle|^2$. Both $\sigma(E)$ and $P(E)$ decrease significantly with increasing energy.

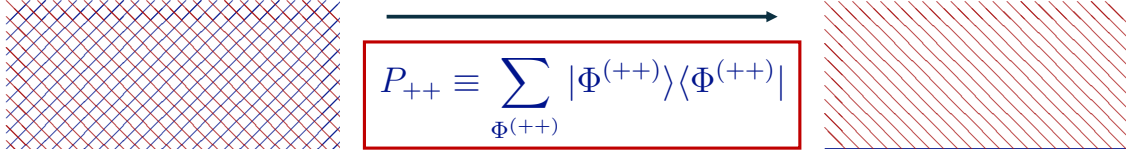


Fig. 3.7.1: Schematic indicating the role of the projection operators P_{++} , namely, to resolve the overlapping continua in the $E > 0$ a.u. region. The idea is to form the projection operators using two-electron basis functions $\Phi^{(++)}$ that are constructed as doubly ionized states.

shared is sufficiently large, this argument becomes less important, it remains true, in the related problem of photoionization of helium, that the double-to-single-ionization ratio, $\sigma(E)_{++}/\sigma(E)_+$ is very small near the double ionization threshold and never becomes much larger than 2 even at extremely high energies [146].

We have formed a complete pseudospectrum that includes electron correlation. However, since energy eigenvalues are not a good proxy for the charge state and double ionization is significantly suppressed near the threshold, we must establish a method that correctly encodes the charge state of the ${}^6\text{Li}^+$ daughter ion. To this end, we construct projection operators, as discussed in the following section.

3.7 PROJECTION OPERATORS

The overall strategy employed in this work is to build on the work of Schulhoff and Drake [132]. We retain the same optimized initial ${}^6\text{He}$ states, adding the metastable singlet ${}^6\text{He}(2\,{}^1S)$ state,³³ and also the same ${}^6\text{Li}^+$ with the same optimized nonlinear parameters that were found initially in Ref. [51]. The present work aims to develop projection operators P_{++} (hereafter denoted simply by P), illustrated in Fig. 3.7.1, that are applied to the $E > 0$ region of the ${}^6\text{Li}^+$ pseudospectra in order to *resolve* the overlapping ionization channels.

The central problem then is to construct a projection operator P and its orthogonal complement Q such that $P|\Psi_i({}^6\text{Li}^+)\rangle$ corresponds to states where both electrons have asymptotically outgoing boundary conditions (i.e., ${}^6\text{Li}^{3+}$ states) and such that

³³Optimized as in Ref. [51]

$P|\Psi_i(^6\text{Li}^+)\rangle = 0$ for states lying below the double-ionization threshold. Our strategy is to resolve each pseudostate $|\Psi_i(^6\text{Li}^+)\rangle$ lying above the double-ionization threshold at $E = 0$ into its orthogonal component parts $|c_i^{3+}|^2 = \langle\Psi_i(^6\text{Li}^+) | P | \Psi_i(^6\text{Li}^+)\rangle$ and $|c_i^{++}|^2 = \langle\Psi_i(^6\text{Li}^+) | Q | \Psi_i(^6\text{Li}^+)\rangle$, where

$$R_i^{3+} = |c_i^{3+}|^2/|c_i|^2 \quad (3.27)$$

$$R_i^{++} = |c_i^{++}|^2/|c_i|^2 \quad (3.28)$$

are the fractional probabilities for the formation of ${}^6\text{Li}^{3+}$ and ${}^6\text{Li}^{++}$, respectively. As usual, the projection operators have the properties $P + Q = 1$ and $PQ = 0$.

3.7.1 Construction of projection operators

Our approach is to construct projection operators for the correlated two-electron pseudostates $\Psi_i(\mathbf{r}_1, \mathbf{r}_2)$ in terms of the sums of the products of one-electron pseudostates $\phi_n(\mathbf{r})$. They are obtained by first orthogonalizing and then diagonalizing the unscreened hydrogenic Hamiltonian:

$$H_0 = -\frac{1}{2}\nabla^2 - Z/r \quad (3.29)$$

in a basis set of functions $\chi_{j,k}(\mathbf{r}) = r^j e^{-\alpha\lambda^k r}$ for a range of powers j and k such that a particular $\phi_{nl}(\mathbf{r})$ for angular momentum l has the form³⁴ (for example):

$$\begin{aligned} \phi_{nl}(\mathbf{r}) = & [(a_{10} + a_{11}r + a_{12}r^2 + a_{13}r^3)e^{-\alpha\lambda r} \\ & + (a_{20} + a_{21}r + a_{22}r^2)e^{-\alpha\lambda^2 r} \\ & + (a_{30} + a_{31}r)e^{-\alpha\lambda^3 r} \\ & + (a_{40})e^{-\alpha\lambda^4 r}]r^l Y_\ell^m(\theta, \phi) \end{aligned} \quad (3.30)$$

³⁴The theory of these Sturmian functions is discussed in Sec. 2.4 along with several properties that make them extremely useful, perhaps most notably the fact that Sturmian functions form a complete – and discrete – representation of the spectrum of the one-electron Hamiltonian.

for the case $\Omega_1 = 4$, where $\Omega_1 = (j+k)_{\max}$, and a_{st} are linear variational parameters. Because of their shape, we call these “triangular” basis sets, as used previously in the calculation of the Bethe logarithms for hydrogen [29]. The total number of terms is $N_1 = \Omega_1(\Omega_1 + 1)/2$ if all terms in Equation (3.30) are kept. The triangular basis sets have two important features. First, the highest eigenvalue is pushed up by many orders of magnitude beyond what is typically achieved with a single exponential term (i.e., a “linear” basis set). For our typical values of $\alpha = 0.1Z$ and $\lambda = 5.15$, the highest eigenvalue is approximately $E_{\text{high}} = 10^{0.715\Omega_1 - 3.61}$ a.u., or 2.5×10^6 a.u., although, for different constructions, this can be pushed much higher (cf. The Bethe logarithm problem in Fig. 1.3.2) The basis set, therefore, spans a huge range of (nonrelativistic) energy and distance scales. The ground state and the first several excited states are also well represented. Second, the basis set has a remarkable degree of numerical stability despite the huge range of distance scales covered. With quadruple precision, Ω can be increased to around 17 or 18. As shown previously [29], the positive eigenvalues are roughly evenly spaced on a logarithmic energy scale up to very high energies.

Assume for simplicity that $\Psi_i(\mathbf{r}_1, \mathbf{r}_2)$ is an S-state. Neglecting the $1/r_{12}$ electron-electron interaction, a zero-order approximation to the P projection operator can then be formed from a doubly-positive-energy sum over all (anti)symmetrized products of one-electron pseudostates:

$$P^{(0)} = \sum_{\ell} \sum_{n_+} | n_+, \ell \rangle \langle n_+, \ell | \quad (3.31)$$

where the sum over ℓ is a sum over two-electron partial waves coupled to form an S -state and n_+ stands for a pair of integers $\{n, n'\}$ such that both $\phi_{n,l}(\mathbf{r})$ and $\phi_{n',l}(\mathbf{r})$ lie in the positive-energy scattering continuum. $| n_+, \ell \rangle$ is then correspondingly defined by

$$| n_+, \ell \rangle = \frac{1}{\sqrt{2}} [| \phi_{n_+,l}(\mathbf{r}_1) \rangle | \phi_{n'_+,l}(\mathbf{r}_2) \rangle \mathcal{Y}_{ll0}^0(\hat{\mathbf{r}}_1, \hat{\mathbf{r}}_2) \pm \text{exchange}] \quad (3.32)$$

where $\mathcal{Y}_{\ell_1\ell_2L}^M(\hat{\mathbf{r}}_1, \hat{\mathbf{r}}_2)$ is a vector-coupled product of spherical harmonics with $L = 0$ and $M = 0$. The generalization to states of arbitrary L is straightforward. The complementary operator Q_0 is then defined by

$$Q^{(0)} = \sum_{\ell} \sum_{n_-} | n_-, l \rangle \langle n_-, l | \quad (3.33)$$

where, for brevity, n_- stands for all three combinations $\{+, -\}$, $\{-, +\}$, and $\{-, -\}$, indicating that at least one of the two electrons is in a negative-energy-bound pseudostate.

This method of calculation is similar in spirit to that of Forrey et al. [147] for double-photoionization of helium, except that the true Coulomb waves are here replaced by pseudostates at the same energy. As shown in Fig. 3.7.2, the two agree very well out to quite large distances.

The method is justified by the degree to which the final results converge with the basis set size and the sum over partial waves:

$$\begin{aligned} & \langle \Psi_i(\mathbf{r}_1, \mathbf{r}_2) | P^{(0)} + Q^{(0)} | \Psi_i(\mathbf{r}_1, \mathbf{r}_2) \rangle \\ &= \langle \Psi_i(\mathbf{r}_1, \mathbf{r}_2) | \Psi_i(\mathbf{r}_1, \mathbf{r}_2) \rangle \end{aligned} \quad (3.34)$$

is satisfied. Instead of analyzing the asymptotic form of the scattering solution, as in an R -matrix calculation, the method analyzes the correlated positive-energy pseudostate in the region near the nucleus, where the Q operator projects out that part that has the asymptotic form of a bound state for one of the two electrons. This is then identified as the amplitude for single-ionization and the orthogonal P component as the amplitude for double ionization. The contrast between the two asymptotic forms is illustrated by comparing the top and bottom panels in Fig. 3.7.2.

The method must also converge with respect to the inclusion of the electron-electron interaction $V = 1/r_{12}$ in $P^{(0)}$ as a perturbation. Up to second order, the

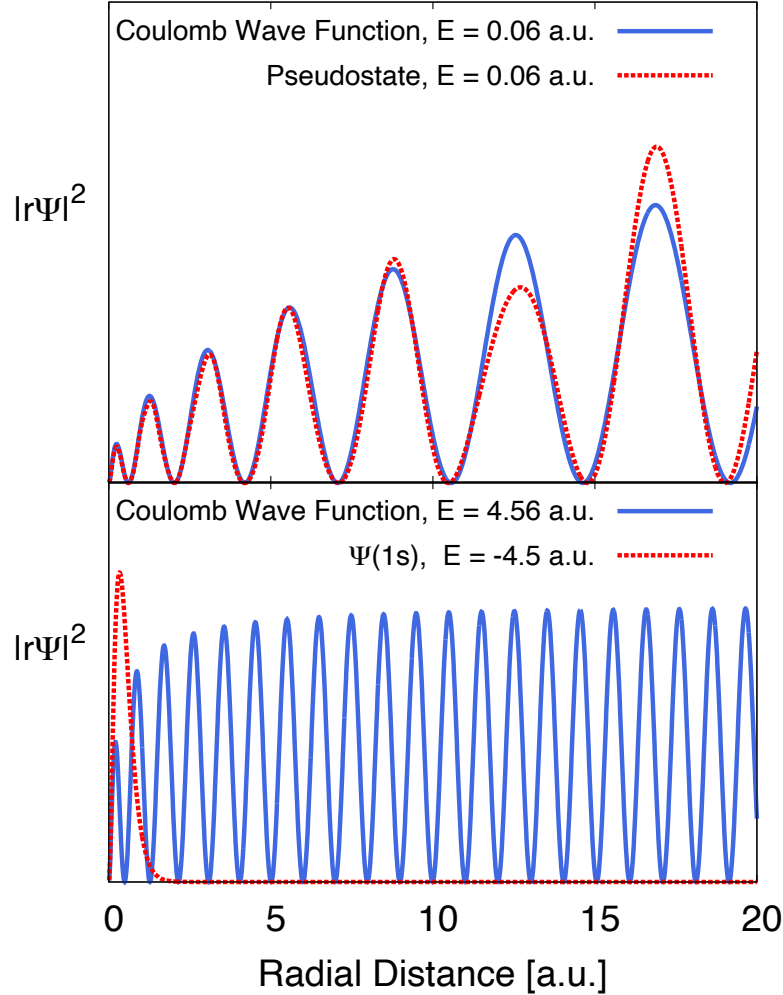


Fig. 3.7.2: Upper panel: Comparison of a one-electron pseudostate radial wave function with the corresponding exact Coulomb wave function at the same energy ($E = 0.06$ a.u.) near the threshold. In the case of double ionization, both electrons have wave functions of this form. This shows that the pseudostate representation remains accurate out to reasonably large distances. Lower panel: The two one-electron states ($E_{1s} = -4.5$ a.u. and $E_k = 4.56$ a.u.) corresponding to a near-threshold single-ionization state, demonstrating that the region nearest the nucleus is that which contributes when taking their product and forming projection operators as described in the present work.

perturbed projection operator is

$$P = P^{(0)} + P^{(1)} + P^{(2)} \quad (3.35)$$

with

$$P^{(1)} = \sum_{n_+} [|n_+\rangle^{(1)}\langle n_+| + |n_+\rangle\langle n_+|^{(1)}] \quad (3.36)$$

and

$$P^{(2)} = \sum_{n_+} [|n_+\rangle^{(2)}\langle n_+| + |n_+\rangle\langle n_+|^{(2)} + |n_+\rangle^{(1)}\langle n_+|^{(1)}] \quad (3.37)$$

where the sum over the zeroth-order two-electron states $\{n_+\}$ is understood to contain the sum over l such that the total $L = 0$ states are formed. The perturbed wave functions are (in the finite set of pseudostates $|n_+\rangle$)

$$|n_+\rangle^{(1)} = \sum_{m_+\neq n_+} |m_+\rangle \alpha_{m_+,n_+} \quad (3.38)$$

and

$$\alpha_{m,n} = \frac{V_{m,n}}{E_m - E_n} \quad (3.39)$$

with $V_{m,n} = \langle m|V|n\rangle$. The (unnormalized) second-order solutions are

$$\begin{aligned} |n_+\rangle^{(2)} &= \frac{1}{E_{n_+} - H} (V - V_{n_+,n_+}) |n_+\rangle^{(1)} \\ &= |T_{+,+}\rangle + |T_{+,-}\rangle + |T_{-,+}\rangle + |T_{-,-}\rangle \end{aligned} \quad (3.40)$$

where, for the perturbed state $|n_+\rangle^{(2)}$,

$$|T_{p,q}\rangle = \sum_{\substack{m_p \neq n_+ \\ i_q \neq n_+}} \frac{|m_p\rangle\langle m_p|(V - V_{n_+,n_+})|i_q\rangle}{E_{n_+} - E_{m_p}} \alpha_{i_q,n_+} \quad (3.41)$$

and p and q each take on the values $+$ or $-$. Only $|T_{+,+}\rangle$ and $|T_{+,-}\rangle$ contribute to the positive-energy projection operator P , with $|T_{+,-}\rangle$ corresponding to virtual transitions to negative-energy states and back again. The transition probability into the projected final state corresponding to ${}^6\text{Li}^{3+}$ then corresponds to the diagonal

matrix elements:

$$\begin{aligned} |c_i^{3+}|^2 &= \langle \Psi_i(^6\text{Li}^+) | P^{(0)} + P^{(1)} + P^{(2)} | \Psi_i(^6\text{Li}^+) \rangle \\ &\equiv |c_i^{(0)3+}|^2 + |c_i^{(1)3+}|^2 + |c_i^{(2)3+}|^2 \end{aligned} \quad (3.42)$$

The first-order correction $|c_i^{(1)3+}|^2$ given by

$$|c_i^{(1)3+}|^2 = \sum_{\substack{n_+ \\ m_+ \neq n_+}} \langle \Psi_i | m_+ \rangle \langle n_+ | \Psi_i \rangle \alpha_{m_+, n_+} \quad (3.43)$$

vanishes identically since the matrix elements are real and $\alpha_{m_+, n_+} = -\alpha_{n_+, m_+}$. The second-order correction consists of the diagonal matrix elements of the (0, 2) and the (1, 1) parts, as shown in Equation (3.37). The (0, 2) part is

$$\begin{aligned} &\sum_{n_+} [|n_+ \rangle \langle n_+ |^{(2)} + |n_+ \rangle^{(2)} \langle n_+ |] \\ &= \sum_{\substack{n_+ \\ m_+ \neq n_+}} \frac{|n_+ \rangle \langle m_+ |}{E_{n_+} - E_{m_+}} (V_{m_+, m_+} - V_{n_+, n_+}) \alpha_{m_+, n_+} \\ &+ \sum_{\substack{n_+ \\ m_+ \neq n_+}} \frac{|n_+ \rangle \langle m_+ |}{E_{n_+} - E_{m_+}} \sum_{i_+ \neq m_+, n_+} V_{m_+, i_+} \alpha_{i_+, n_+} \\ &+ \sum_{\substack{n_+ \\ m_+ \neq n_+}} \frac{|n_+ \rangle \langle m_+ |}{E_{n_+} - E_{m_+}} \sum_{i_-} V_{m_+, i_-} \alpha_{i_-, n_+} + (n_+ \leftrightarrow m_+) \end{aligned} \quad (3.44)$$

The first term vanishes because it is antisymmetric under the interchange $(n_+ \leftrightarrow m_+)$.

The second and third terms can both be rewritten by the use of the identity:

$$\frac{V_{m_+, i_\pm} \alpha_{i_\pm, n_+} - V_{n_+, i_\pm} \alpha_{i_\pm, m_+}}{E_{n_+} - E_{m_+}} = \alpha_{m_+, i_\pm} \alpha_{i_\pm, n_+} \quad (3.45)$$

to obtain the remaining diagonal part:

$$\begin{aligned}
& \sum_{n_+} [|n_+\rangle\langle n_+|^{(2)} + |n_+\rangle^{(2)}\langle n_+|] \\
= & \sum_{\substack{n_+ \\ m_+\neq n_+}} |n_+\rangle\langle m_+| \sum_{i_+\neq m_+, n_+} \alpha_{m_+, i_+} \alpha_{i_+, n_+} \\
+ & \sum_{\substack{n_+ \\ m_+\neq n_+}} |n_+\rangle\langle m_+| \sum_{i_-} \alpha_{m_+, i_-} \alpha_{i_-, n_+}
\end{aligned} \tag{3.46}$$

The remaining (1, 1) contribution from Equation (3.37) is

$$\begin{aligned}
\sum_{n_+} |n_+\rangle^{(1)}\langle n_+|^{(1)} = & \sum_{\substack{n_+ \\ m_+\neq n_+}} |m_+\rangle\langle m_+| \alpha_{m_+, n_+}^2 \\
+ & \sum_{\substack{n_+ \\ m_+\neq n_+}} \sum_{i_+\neq m_+, n_+} |m_+\rangle\langle i_+| \alpha_{m_+, n_+} \alpha_{i_+, n_+}
\end{aligned} \tag{3.47}$$

Interchanging the dummy indices n_+ and i_+ shows that the second term cancels the first term of Equation (3.46), leaving just the terms:

$$\begin{aligned}
P^{(2)} = & \sum_{\substack{n_+ \\ m_+\neq n_+}} |m_+\rangle\langle m_+| \alpha_{m_+, n_+}^2 \\
+ & \sum_{\substack{n_+ \\ m_+\neq n_+}} |n_+\rangle\langle m_+| \sum_{i_-} \alpha_{m_+, i_-} \alpha_{i_-, n_+}
\end{aligned} \tag{3.48}$$

However, this still must be corrected so that the total wave functions $|n_+\rangle + |n_+\rangle^{(1)} + |n_+\rangle^{(2)}$ are normalized to unity up to second order. The renormalization can be accomplished by subtracting a component of the unperturbed solution $|n_+\rangle$ from $|n_+\rangle^{(2)}$ to obtain

$$|\tilde{n}_+\rangle^{(2)} = |n_+\rangle^{(2)} - \frac{1}{2}|n_+\rangle \tag{3.49}$$

which still satisfies the second-order perturbation equation. This contributes an additional amount:

$$\Delta P^{(2)} = - \sum_{n_+, m_+} |m_+\rangle\langle m_+| \alpha_{m_+, n_+}^2 \tag{3.50}$$

leaving just the renormalized projection operator:

$$\tilde{P}^{(2)} = \sum_{n_+, m_+} |n_+\rangle \langle m_+| \sum_{i_-} \alpha_{m_+, i_-} \alpha_{i_-, n_+} \quad (3.51)$$

corresponding to the sum over virtual negative-energy states.

It turns out that even this contribution is cancelled if one includes the counterbalancing positive-energy part coming from the second-order perturbation of negative-energy states. Terms from $|n_-\rangle \langle n_-|^{(2)} + |n_-\rangle^{(2)} \langle n_-|$ do not contribute, but the first-order cross-terms contribute:

$$\sum_{n_-} |n_-\rangle^{(1)} \langle n_-|^{(1)} = \sum_{n_-, m_+ n_+} |m_+\rangle \langle n_+| \alpha_{n_-, m_+} \alpha_{n_-, n_+} \quad (3.52)$$

With the change of notation $n_- = i_-$, it is clear that this term cancels the one remaining term in Eq. (3.51) for $\tilde{P}^{(2)}$. Thus, the leading perturbative correction to P due to the electron-electron interaction is at most of third order. However, it is still of interest to calculate the

$$\sum_i |\tilde{c}_i^{(2)3+}|^2 = \sum_i \langle \Psi_i(^6\text{Li}^+) | \tilde{P}^{(2)} | \Psi_i(^6\text{Li}^+) \rangle \quad (3.53)$$

contribution (summed over positive-energy pseudostates) that would still remain without this final cancellation due to the positive-energy part coming from perturbed negative-energy states, as discussed in the following section. The second-order contributions from only positive-energy states, prior to cancellation, serve as an upper bound on the order at which third- or higher-order effects could contribute.

3.8 RESULTS

This section discusses the numerical results obtained for the transition probability coefficients $P(^6\text{Li}^{3+}) = \sum_n |c_n^{3+}|^2$ in Eq. (3.42). The calculations are first presented to test for the convergence of the leading coefficients $\sum_n |c_n^{(0)3+}|^2$ with respect to

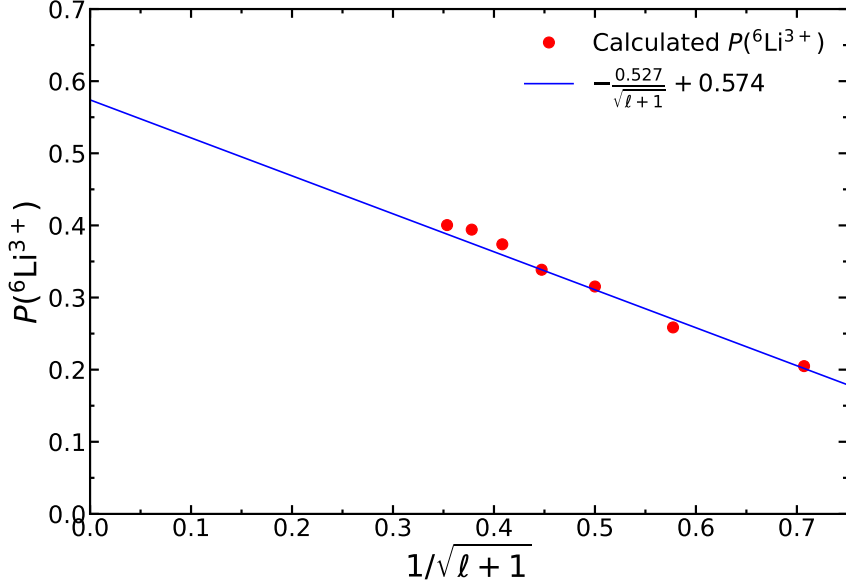


Fig. 3.8.1: An example of convergence with respect to the number of partial waves ℓ (red dots) for the ${}^6\text{Li}^3+$ probability following the decay of ${}^6\text{He}(2\ ^3S)$ for the case $\Omega_1 = \Omega_2 = 8$. This is the top left result (the top number) for the ${}^6\text{He}(2\ ^3S)$ section of Table 3.8.1.

both Ω_1 , controlling the size of the basis from which the projection operators are formed, and Ω_2 , playing the same role for the Hylleraas states used to depict the ${}^6\text{Li}^+$ pseudospectrum. In addition, we examined the convergence with respect to the sum over partial waves ℓ in Eq. (3.31) and perturbation corrections to the projection operators due to the electron-electron Coulomb interaction.

First, concerning the convergence with respect to partial waves, direct calculations were performed up to $\ell = 7$ (i.e., one-electron states with $\ell_1 = \ell_2 = \ell$ were coupled to form an S -state with $L = 0$) and an extrapolation performed up to $\ell = \infty$. The results were found to converge relatively slowly in proportion to $1/\sqrt{\ell+1}$.³⁵ As a typical example, Fig. 3.8.1 shows the convergence pattern for the ${}^6\text{He}(2\ ^3S_1)$ case with $\Omega_1 = \Omega_2 = 8$. The extrapolated value is shown by the intercept on the vertical axis.

Next, concerning the convergence with respect to Ω_1 and Ω_2 , the results are shown (as a percentage) by the top number of each pair in Table 3.8.1 and for each of the

³⁵The $1/\sqrt{\ell+1}$ form used in finding convergence was empirically found to fit the data well compared to other (negative) integral or half-integral powers of $\ell+1$ for a wider variety of (Ω_1, Ω_2) combinations for the three initial states.

three initial atomic states. The entries along the main diagonal provide a measure of the degree of convergence and their uncertainty. Since there does not appear to be a consistent trend either up or down, we took the average of all the numbers in Table 3.8.1 with the rms statistical spread as the uncertainty. The total double-ionization probability, prior to being subject to the projection operators of Equation (3.31), is the sum of overlap integrals between an optimized initial state of ${}^6\text{He}$ and a pseudospectrum representing all doubly ionized ${}^6\text{Li}^+$ states. Although this quantity can be stated with a well-defined error, as demonstrated in [132], it does not show monotonic convergence but rather oscillates around a value. The reason for this is that the nonlinear parameters in Eq. (2.34) that are used to construct the eigenvalue spectrum of pseudostates are (necessarily) not separately optimized for each state within the pseudospectrum [51]. The actual numbers of terms in the basis sets for each Ω are listed in Table 3.8.2.

Finally, concerning perturbation corrections due to the electron–electron interaction, this mixes each of the simple one-electron product pseudostates $|n_+, \ell\rangle$ with all the others, but as shown in Equation (3.43), the first-order corrections cancel in pairs when summed over the complete set of states that form the projection operator. A more lengthy calculation in Sec. 3.7.1 shows that the second-order corrections also cancel, provided that one takes into account both the renormalization of the perturbed wave functions so that $P^2 = P$ up to second order and the counterbalancing positive-energy contribution coming from the perturbed negative-energy states. It is perhaps not surprising that these perturbation corrections sum to zero because the only role of the P projection operator is to enforce doubly outgoing boundary conditions via positive energy for both electrons without further energy resolution. However, it is still interesting to see the order of magnitude of the partial-second-order contributions generated by $\tilde{P}^{(2)}$ in Equation (3.51). The results are shown by the bottom number of each pair in Table 3.8.1. Although there is no clear convergence pattern, the magnitudes are all 2% or less of the zero-order term. One can, therefore, expect third- or higher-order contributions not included in the calculation to be smaller still. The main source of uncertainty is thus the convergence uncertainty associated with

Table 3.8.1: Convergence table for ${}^6\text{Li}^{3+}$ probabilities for the initial states ${}^6\text{He}(1\ ^1S_0)$ and ${}^6\text{He}(2\ ^3S_1)$. Zeroth- and partial second-order corrections (top and bottom of each cell, respectively) from Eq. (3.53), taken in the limit of infinite partial waves as shown in Fig. 3.8.1. Results are expressed in percent(%) shown for different sizes of both the projection operator (Ω_1) and Hylleraas-type pseudostate (Ω_2) basis sets used in Eq. (3.42). The bottom entry is a partial second order correction, which, as explained in the text, ultimately cancels. The top values in the table for each state will be averaged to obtain the final ${}^6\text{Li}^{3+}$ probability. This table is continued on the following page.

${}^6\text{He}$ state	Ω_1	Ω_2			
		8	10	12	14
$1\ ^1S_0$	8	0.3663	0.3564	0.3134	0.4483
		-0.0017	-0.0011	-0.0014	-0.0009
	10	0.3142	0.3326	0.3100	0.4314
		-0.0068	-0.0057	-0.0091	-0.0011
	12	0.3123	0.3145	0.3009	0.4357
		-0.0045	-0.0027	-0.0019	-0.0066
	14	0.3145	0.3128	0.3556	0.4121
		-0.0006	-0.0001	-0.0011	-0.0008
	8	0.5740	0.4161	0.4293	0.4028
		-0.0013	-0.0004	-0.0003	-0.0003
$2\ ^3S_1$	10	0.5084	0.4947	0.5272	0.5405
		-0.0031	-0.0010	-0.0032	-0.0031
	12	0.5223	0.5281	0.5744	0.6209
		-0.0052	-0.0017	-0.0025	-0.0022
	14	0.5304	0.5314	0.6062	0.6400
		-0.0002	-0.0006	-0.0002	-0.0002

the zero-order term.

The final results are summarized in Table 3.8.3. The main conclusion is that most of the daughter ions in the energy bin with $E > 0$ are ${}^6\text{Li}^{++}$ -ions plus an energetic electron, rather than ${}^6\text{Li}^{3+}$ plus two low-energy electrons. For example, for the ${}^6\text{He}(1\ ^1S_0)$ case, of the calculated 1.2(1)% of the ${}^6\text{Li}$ -ions with $E > 0$, 0.35(5)% are ${}^6\text{Li}^{3+}$, and the remaining 0.85(10)% are ${}^6\text{Li}^{++}$. The ${}^6\text{Li}^{3+}$ fraction agrees with the 0.32% calculated by Wauters and Vaeck [131], but their total only sums to 99.85%,

Table 3.8.1 (con't): This is a continuation of Table 3.8.1 containing the convergence table for forming ${}^6\text{Li}^{3+}$ following the ${}^6\text{He}(2\,{}^1S_0)$ initial state. The same description found in Table 3.8.1 and will not be reproduced.

${}^6\text{He}$ state	Ω_1	Ω_2			
		8	10	12	14
${}^6\text{He}(2\,{}^1S_0)$	8	0.5838	0.4645	0.4829	0.5470
		-0.0041	-0.0036	-0.0027	-0.0030
	10	0.4988	0.5522	0.5611	0.6193
		-0.0284	-0.0083	-0.0196	-0.0467
	12	0.4994	0.5697	0.6046	0.6636
		-0.0023	-0.0089	-0.0012	-0.0052
	14	0.5037	0.5836	0.6196	0.6610
		-0.0027	-0.0001	-0.0034	-0.0010

Table 3.8.2: Number of terms $N_1(\Omega_1)$ and $N_2(\Omega_2)$ in the basis sets. The factor 8 for $N_1(\Omega_1)$ accounts for the sum over partial waves up to $\ell = 7$.

$\Omega_{1\text{ or }2}$	$N_1(\Omega_1)$	$N_2(\Omega_2)$		
		$1\,{}^1S_0$	$2\,{}^3S_1$	$2\,{}^1S_0$
8	81×8	181	164	182
10	196×8	295	218	301
12	400×8	442	441	457
14	729×8	624	650	652

with no uncertainty given. For the ${}^6\text{He}(2\,{}^3S_1)$ case, the fractions are 0.53(7)% for ${}^6\text{Li}^{3+}$ and 1.33(7)% for ${}^6\text{Li}^{++}$.

The redistributed charge-state fractions are shown in Table 3.8.4. However, even these reduced fractions of ${}^6\text{Li}^{3+}$ -ions are still an order of magnitude or more larger than the experimental values of 0.018(15)% for the ${}^6\text{He}(1\,{}^1S_0)$ case and $< 0.01\%$ for the ${}^6\text{He}(2\,{}^3S_1)$ case. The recalculated ${}^6\text{Li}^{++}$ fraction is now also larger than the experiment, while the ${}^6\text{Li}^+$ fraction remains lower than the experiment. The differences are much larger than the statistical uncertainties. It seems that the theoretical values for both ${}^6\text{Li}^{++}$ and ${}^6\text{Li}^{3+}$ need to be lowered by about the same amount and added

Table 3.8.3: Previous [132] and corrected ${}^6\text{Li}^{3+}$ charge-state fractions for each initial state following beta decay. All quantities expressed in percent (%).

${}^6\text{He}$ State	$p({}^6\text{Li}^{3+})$		
	Previous [132]	Present	Exp't
$1 {}^1S_0$	1.2(1)	0.35(5)	0.018(15) [114]
$2 {}^3S_1$	1.86(7)	0.53(7)	<0.01 [115]
$2 {}^1S_0$		0.56(6)	

Table 3.8.4: Corrected probabilities $p({}^6\text{Li}^{k+})$ of forming the various charge states of ${}^6\text{Li}^{k+}$, $k = 1, 2, 3$ following the beta decay of ${}^6\text{He}(1 {}^1S_0)$ or ${}^6\text{He}(2 {}^3S_1)$ as initial states. All quantities are expressed in percent (%).

${}^6\text{He}$	${}^6\text{Li}$	Theory				
		State	Ion	Present	Ref. [131]	Exp't.
$1 {}^1S_0$	${}^6\text{Li}^+$			89.03(3)	89.09	89.9(2) ^a
	${}^6\text{Li}^{++}$			10.55(10)	10.44	10.1(2)
	${}^6\text{Li}^{3+}$			0.35(5)	0.32	0.018(15)
	Total			99.9(1)	99.85	100.0(2)
$2 {}^3S_1$	${}^6\text{Li}^+$			88.711(3)		89.9(3)(1) ^b
	${}^6\text{Li}^{++}$			10.75(7)		10.1(3)(1)
	${}^6\text{Li}^{3+}$			0.53(7)		<0.01
	Total			99.99(7)		100.00

^a Carlson *et al.* [114].

^b Hong *et al.* [115].

to ${}^6\text{Li}^+$ in order to bring the theory and experiments into agreement.

3.9 FUTURE WORK

There is clearly more work to be done on the problem and good reason to believe that at least part of the outstanding discrepancies lie in the theoretical formulation of the problem. The phase space considerations alone, presented in Sec. 3.6.2, provide

a strong qualitative reasoning supporting the idea that single ionization should be significantly more probable than double ionization. One avenue for improving the calculation would be to investigate the effect of relaxing the sudden approximation, which would require solving the time-dependent Schrödinger equation. However, based on the arguments in this chapter, Ref. [134], which predicts that the SA would introduce corrections into the probabilities at the level of $3 \times 10^{-7}\%$, this is unlikely to make a difference at the level with which we are concerned. Another area of future work will be to reformulate the problem theoretically to investigate the *emitted* light resulting from the process. This would offer a complementary approach to the current experimental techniques which use methods such as time-of-flight analysis to discern the charge states of daughter ions. Yet another significantly more promising direction is to utilize the matrix elements of the delta function to diagnose whether the Hylleraas pseudostates contain an appropriate degree of $1s$ occupancy. We discuss this avenue in more detail in the ensuing section.

3.9.1 Delta function matrix elements: A potential new method for treating one- and two-channel scattering problems

The photoionization cross section $\sigma(E)$, in atomic units,³⁶ is [148, p. 148]

$$\sigma(E) = 4\pi^2\alpha\omega|\langle He(1^1S)|z_1 + z_2|He(n^1P)\rangle|^2, \quad (3.54)$$

where α is the fine-structure constant and $\hbar\omega = E(n^1P) - E(1^1S) \equiv E$, is quite similar to the beta decay transition probabilities we have been considering.

The problem of calculating the final-state fraction of ${}^6\text{Li}^{3+}$ to ${}^6\text{Li}^{++}$ is closely related to the two-electron problem of calculating the ratio of the double-to-single photoionization cross sections

$$R(E) = \sigma_{2+}(E)/\sigma_{1+}(E),$$

³⁶Assuming laser polarization in the $\hat{\mathbf{z}}$ direction.

for energies beyond the second ionization threshold $E > 0$, where the two channels compete. There is a vast and rich literature for this topic for helium, ranging from many-body perturbation theory (MBPT) [149–151], close-coupling (cc) [152], convergent close-coupling (ccc) [153], R-matrix methods [154] with a discretization of the continuum, and various distorted wave (DW) approximations for the final-state wave function [155–158]. The older literature up to 1996 was reviewed by Sadeghpour [159]. More recent work has applied these same methods to single- and double-photoionization of ${}^6\text{Li}^+$, including R-matrix calculations [160, 161], time-dependent close-coupling (TDCC) [162], ccc for the helium isoelectronic sequence [163], and B-spline methods [161, 164].

The method we propose is complementary to those mentioned above in that it uses the behaviour of the wave function as $r \rightarrow 0$ as opposed to the more common asymptotic condition as $r \rightarrow \infty$. The latter condition often relies on treating ionized states with long-range single-electron components that match the appropriate Coulomb wave functions (CWF) to large distances. In our method, as shown in Fig. 3.7.2, we operate with the assumption that a correct representation of the near-nucleus behaviour of the pseudostates should contain the same information concerning the atom’s charge state. Photoionization of $\text{He}(1s^2 {}^1S)$, shown in Eq. (3.54), describes the transition of the ground state of helium to one of two channels: (1) singly ionized $\text{He}^+(1s) + 1\text{e}^-$; (2) doubly ionized $\alpha^{++} + 2\text{e}^-$. It is known from experiment [146] that $R(E)$ is much less than 1 just above the double ionization threshold and that, even for very large energies, it never becomes larger than 4. This indicates that the two-electron wave functions used to represent this process should have a significant $1s$ component at least until the He^{++} threshold – and even a little bit beyond this. The quantity which describes the degree to which the inner electron remains bound, i.e., the amount of “ $1s$ ” character, is the delta function matrix element $\langle n \, {}^1P | \delta(\mathbf{r}_1) | n \, {}^1P \rangle \equiv \langle \delta(\mathbf{r}_1) \rangle_{n \, {}^1P}$. For bound states, this should be nearly constant as n varies, and nearly equal to that of the ground state $\langle \delta(\mathbf{r}_1) \rangle_{1 \, {}^1S}$. The singly ionized $\text{He}(n \, {}^1P)$ states should also have delta function matrix elements close to this same value. For the Hylleraas pseudospectrum $\{\Psi(n \, {}^1P)\}$ arising from the diagonalization of $H_{Z=2}$, Fig. 3.9.1 shows

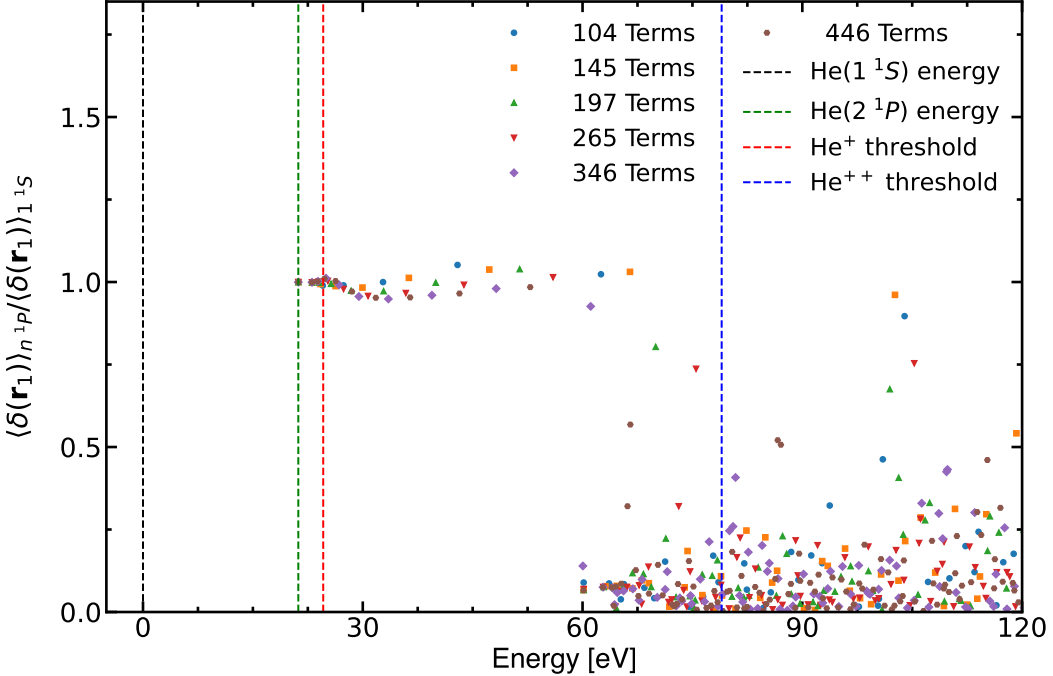


Fig. 3.9.1: The delta function matrix element, $\langle n^1P | \delta(\mathbf{r}_1) | n^1P \rangle \equiv \langle \delta(\mathbf{r}_1) \rangle_{n^1P}$, normalized to the ground state value $\langle \delta(\mathbf{r}_1) \rangle_{1^1S}$ is calculated for the ${}^6\text{He}(n^1P)$ pseudostates well into the doubly ionized continuum, up to $E = 120$ eV. Several basis sets are included with 104 to 446 terms. The ground-state and 2^1P energies are shown, along with the first and second ionization thresholds. The purpose of this graph is to illustrate that the Hylleraas pseudostates lose their “1s” character before their energies even reach the second ionization threshold.

the calculated delta function matrix elements, $\langle \delta(\mathbf{r}_1) \rangle_{n^1P}$, normalized to the ground state value. It should be noted that smoothing and averaging procedures have been employed in generating this curve to recognize that each energy truly represents a range, as found in Ref. [132] and described in Sec. 3.5.

This figure illustrates that there is an underlying problem with the $\{\Psi({}^6\text{He})\}$ pseudospectrum, namely that it does not retain its “1s” character into the double ionization continuum, as it should. This is indicated by the precipitous fall in the delta function matrix element observed even before the double ionization (He^{++}) threshold is reached. As a consequence, the photoionization cross section ratio σ_{2+}/σ_+ is too large in the region near threshold. These problems also plague the $\{{}^6\text{Li}^+\}$ pseudospectra used in this work, a variation of the same problem, and account for the difficulties encountered in actually projecting out the ${}^6\text{Li}^{++}$ from the $E > 0$ region.

The shortcoming lies not with the projection operator formalism but rather with the fact that there is little to no singly-ionized ${}^6\text{Li}^{++}$ in the Hylleraas pseudostates to begin with.

Future work³⁷ will attempt to reformulate the Hylleraas basis functions, which form the first step of solving the beta decay problem, such that they retain sufficient “1s” character into the double continuum. To this end, delta function matrix elements should be used as a diagnostic tool. The projection operators described in Sec. 3.7.1 would still be useful, to the extent that a discrete pseudospectrum would not be expected to contain complete information about the charge state. The improved Hylleraas pseudostates do not have to be perfect; they just need to have a slightly more realistic “1s” character. If successful, this approach will not only solve the beta decay problem at hand but may also be useful in the aforementioned problem of photoionization in two-electron systems. In particular, this method would offer an alternative to the theoretical methods mentioned earlier in this section that are ubiquitous in laser and collision physics.

Once the double ionization probability is correct, the methods developed here can and should be applied to the recoil-dependent probabilities and to the case of the initial state having $L \neq 0$. The projection operators could immediately be applied to the full suite of results contained in Refs. [132] and [133, pp. 59–73]. The reason for not doing this so far is that we have yet to agree with the experiment for the simpler case of initial S states.

³⁷These efforts involve altering the basis functions by (1) modifying nonlinear parameters to push the energy to which the delta function remains equal to the ground states; (2) removing the interelectron coordinate r_{12} parts of the basis set; (3) Increasing the layers of the basis set with additional customization.

CHAPTER 4

Finite-nuclear-mass Effects in Two-photon Decay in Heliumlike Ions

4.1 OVERVIEW

In Chap. 3, pseudostates were used in a scattering-type problem, namely beta decay, where the transitions take place between the initial state and an ostensibly *real* final state—the physical picture was that the change in Coulomb potential results in a redistribution of the initial ${}^6\text{He}$ state into a complete set of *real* ${}^6\text{Li}^+$ states.¹ That we needed to use a pseudospectrum was due to practical reasons in order to carry out the calculation. We now turn our attention to a conceptually distinct deployment of these pseudostates—we consider a problem within atomic structure where the “transitions” are understood to be to *virtual* states. The problem at hand in this chapter is to treat two-photon transitions, which take place by virtual interactions with the QED vacuum. That two conceptually distinct processes can be accurately treated with the same underlying paradigm is a testament to the power of forming and using pseudospectra.²

¹By *real*, we mean that these are observable states that could be physically occupied following beta decay.

²A caveat to this is that in the beta decay problem, it could be construed that we indeed were already considering transitions to virtual states since all but the lowest lying pseudostates truly do represent a *range* of energies. Nevertheless, we understand the shake-up/off processes to connect real—not virtual—states in principle.

In this chapter, we discuss the most accurate calculation to date of the finite-nuclear-mass effect for two-photon spontaneous decay rates for helium-like ions from $Z = 2$ through to $Z = 10$. This decay is relevant in astrophysical contexts where the particle density is low such as planetary nebulae, where radiative and collisional decay mechanisms compete. As part of this work, the mass polarization component of the finite-nuclear-mass effect is treated with a gauge-dependent power series.

In the theory of radiative transitions, the usual simplified gauge equivalence of the length and velocity forms applies only in the limit of infinite nuclear mass. Here, we correct this for the case of finite nuclear mass. This chapter expands the finite-nuclear-mass corrections due to mass polarization in a power series in μ/M , where μ is the reduced mass $\mu = \frac{mM}{m+M}$ and m and M are the electron and nuclear masses, respectively. New algebraic relationships connecting the length and velocity forms of the expansion coefficients are derived. These relations provide a stringent test of the accuracy of the calculation since they are only satisfied if the wave functions are exact. As a test, high-precision numerical results are presented for various transitions in helium. This chapter also generalizes the algebraic relations to arbitrary n -photon transitions. These relationships place tight constraints on the results and enable easily adjusted results in the case of slight modifications in μ , m_e , or M .

The outline of the chapter is as follows. Section 4.2 begins with a historical overview, including the relevance of multiphoton processes and spontaneous emission. In the following Sec. 4.3 the motivation for the work presented in this chapter is given, followed by a brief history of calculations in Sec. 4.4. Following this, Sec. 4.5 describes the theoretical formulation of two-photon decay and then Sec. 4.6 briefly establishes the wave functions used including a discussion of reduced-mass atomic units. Subsequently, the characterization of finite-nuclear-mass effects,³ including the establishment of general $nE1$ relationships in the length, velocity, and acceleration gauges, appear in Secs. 4.7 and 4.8. Section 4.9.1 contains a plethora of results related to calculating $2E1$ decay rates in heliumlike ions, and Sec. 4.9.2 contains results for

³The adjectives “finite-nuclear-mass” and “infinite-nuclear-mass” are abbreviated in this chapter to “finite-mass” and “infinite-mass.”

testing the corresponding algebraic relations. Lastly, Sec. 4.10 describes the horizons for future work, some of which are already underway.

4.2 HISTORICAL SIGNIFICANCE

Maria Goeppert Mayer was a student at Göttingen in the 1920s while it was a “cauldron of quantum mechanics,” where she was a student of Max Born.⁴ It was in her doctoral dissertation [166] that she established the first theoretical formulation of multiphoton processes in quantum mechanics. Following Dirac’s famous paper which developed transformation theory, establishing the equivalence between Schrödinger and Heisenberg’s formulations of quantum mechanics [167], he wrote two further papers that were to have a large influence on the work of Goeppert Mayer [168, 169].

Prior to Goeppert Mayer’s work, only single-photon processes were theoretically described, first with Einstein’s description of the photoelectric effect. Consider light shining on a metal composed of atoms. His theory says that there is a minimum frequency of light beyond which ionization will not take place. Furthermore, the intensity of the light has no effect on whether or not this process occurs; it only affects *how much* it occurs. Goeppert Mayer’s crucial contribution to this problem was to realize that, with sufficient intensity of incident light, this process could occur with more than one photon, each of which has a frequency (1) less than that needed to ionize the atom by itself and (2) that need not actually coincide with any bound states upon absorption.

This general situation is depicted in Fig. 4.2.1. The atomic system has ionization potential I_p , which must be overcome by the photon energy according to $N\hbar\omega = KE + I_p$, where ω is the laser frequency, N is the number of photons, KE the kinetic energy of the ejected electron, and I_p the ionization potential of the atomic system, representing the amount of energy needed to simply ionize the atom. In describing

⁴She was unusually well-connected: her father was not only a Professor, but she herself would go onto become the seventh straight generation of university professors on her paternal side of the family. Furthermore, David Hilbert was her immediate neighbour and a good friend of the family. Other good family friends included Max Born and James Franck, who would both significantly influence her work, the former being her Ph.D. supervisor [165].

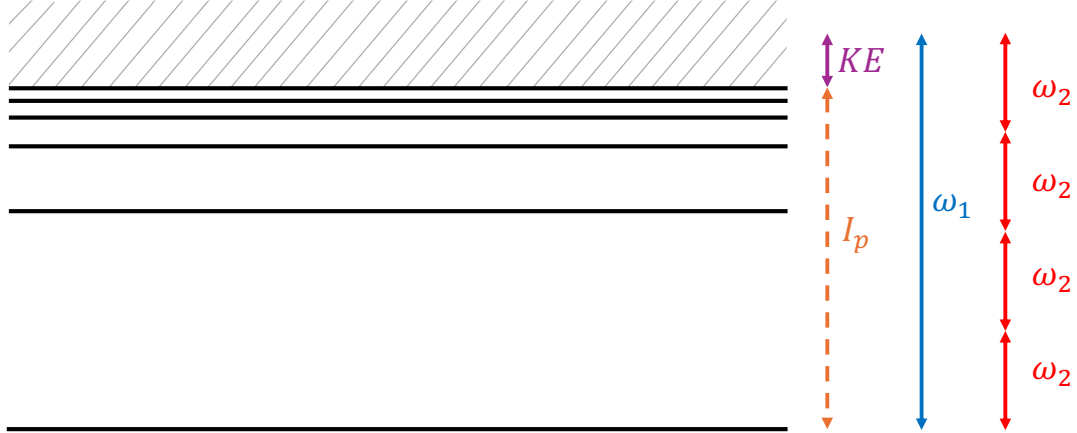


Fig. 4.2.1: This diagram illustrates the difference between single and multiphoton ionization of an atom with ionization potential I_p and kinetic energy KE of the ejected electron. In weak intensity regimes, single-photon processes such as the photoelectric effect occur according to $\hbar\omega_1 = KE + I_p$, however, in higher intensity regimes multiphoton processes can take place where several photons (in this case 4) can make up the energy $\hbar\omega_1$. Goeppert Mayer showed that the correct equation is $N\hbar\omega = KE + I_p$, where $N > 1$ is possible in strong fields.

the photoelectric effect, Einstein assumed that $N = 1$, but Goeppert Mayer showed that $N > 1$ processes are possible.⁵

It took 30 years for her theoretical predictions to be realized due to the lack of sufficient light intensities for multiphoton absorption in atoms until the advent of lasers. After Townes developed the maser in 1953, Kaiser and Garrett observed two-photon absorption in CaF_2^{2+} [176]. The crucial milestone was Maiman's invention of the laser in 1960 [177]. This rich history of laser physics underpins nonlinear optics, leading to numerous Nobel prizes, including the 2023 Nobel for attoscience. In emission, multiphoton processes are rare compared to single-photon counterparts and are typically relevant only when other decay channels are forbidden by selection rules. Continual laser improvements drive high-precision atomic physics and necessitate the theoretical calculations presented in this dissertation.

This chapter contains calculations on the *spontaneous* two-photon decay of helium. Having addressed the historical significance of “two-photon” part of the title by

⁵This chapter focuses on multiphoton processes from a structure perspective—specifically, we discuss events that involve interaction with the QED vacuum. A variety of multiphoton processes arising from laser-atom interactions are actively studied (see, for example, [170–175]).

discussing multiphoton processes and their origin, we now focus on “spontaneous” decay. Although spontaneous emission is one of the three radiative processes described by Einstein’s A and B coefficients [178], it is only postulated in his theory. Spontaneous decay occurs when an excited atom in empty space decays. While quantum mechanics provides a framework for absorption and stimulated emission, it does not offer a mechanism for spontaneous emission. The explanation lies in the nature of *empty space*, which quantum electrodynamics (QED) describes as interacting with the atom through vacuum fluctuations. These fluctuations cause spontaneous emission and phenomena like the Lamb shift [179] and Casimir effect [180].

4.3 MOTIVATION

4.3.1 Astrophysical observation

Our understanding of the composition, dynamics, and origin of the universe comes in large part from spectroscopic observations of atoms and plasmas—these data serve as a temperature and pressure probe for distant astrophysical bodies. Since helium is the second most abundant element, constituting 10% of the atoms universe, quantitative knowledge of its spectral properties is crucial to properly interpret astrophysical observations. Significant work has been conducted by Drake, Morton, and collaborators [181–183], including calculations of several structure properties for ${}^4\text{He}$ including energy levels, transition rates, lifetimes and oscillator strengths.

An important class of radiative data comes from *forbidden* transitions, from which more than half of the atoms in the universe recombined, mostly from $2E1$ processes [184]. The $2E1$ transition from $2\,{}^1S-1\,{}^1S$ in helium is shown as the thickest (and only red) line in Fig. 4.3.1, which shows all the possible decays from the $n = 2$ manifold in helium. Another crucial decay mechanism is the metastable triplet decay from the $2\,{}^3S$ state, a topic which Drake and colleagues have worked on extensively for both the $2E1$ [185, 186] and $M1$ [187] mechanisms. The long radiative lifetimes of metastable states in helium, together with collision rates, determine their population

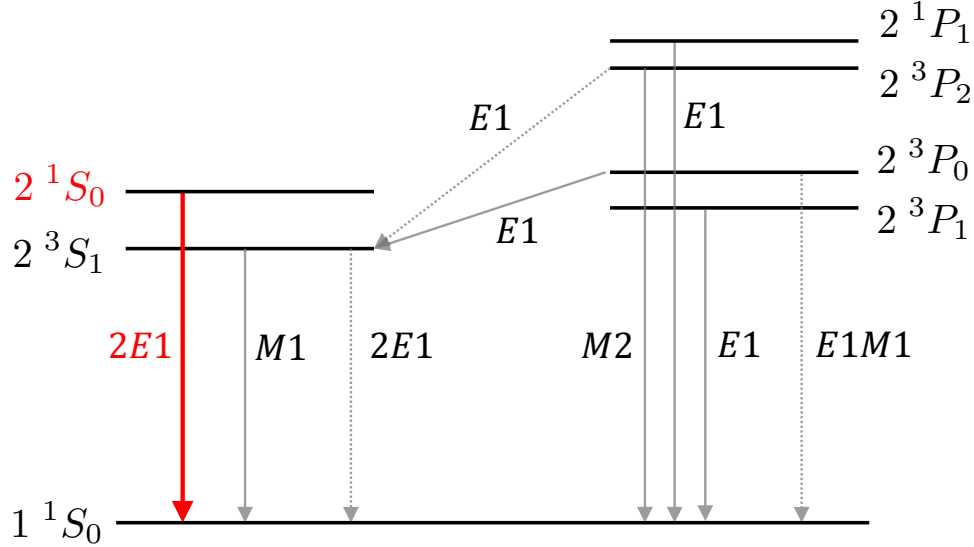


Fig. 4.3.1: Energy level diagram for the $n = 2$ manifold of helium, illustrating those metastable processes that are of astrophysical interest and indicating the decay mechanism of those of interest.

balance in astrophysical sources such as planetary nebulae. These transitions largely determine the rate of radiation loss in the early universe to form the cosmological microwave background (CMB) since there is little resonant reabsorption of radiation owing to the low particle density [188, 189].

Figure 4.3.2 illustrates this point by plotting the detailed calculations of various line intensities at the present epoch due to the recombination of hydrogen and helium [190].⁶ Both the dominant resonant processes and the forbidden two-photon processes are included. It is the plasmonic activity in the hot early universe that thermalized the radiation content, leading to the CMB. Besides this background of radiation, additional photons were generated via the recombination of certain light atoms—most importantly hydrogen, and then helium.⁷

It can be seen that, although the two-photon decay of helium is several orders

⁶The continuous and doubly-peaked spectrum of the $P - S$ recombinations is a result of several broadening mechanisms and the fact that there is a significant pre- and post-recombination contributions that occurred at different epochs are then subject to different environments [190]

⁷The redshift enlarges the originally emitted wavelength per $\lambda_{\text{observed}} = \lambda_{\text{emitted}} \times (1 + z)$. The recombination period was when the universe was about 400,000 years old, corresponding to a redshift $z = 1000$ and a wavelength observed today that is about a factor of 1000 larger. This is why the spectrum of H and He is in the μm , rather than the familiar nm range.

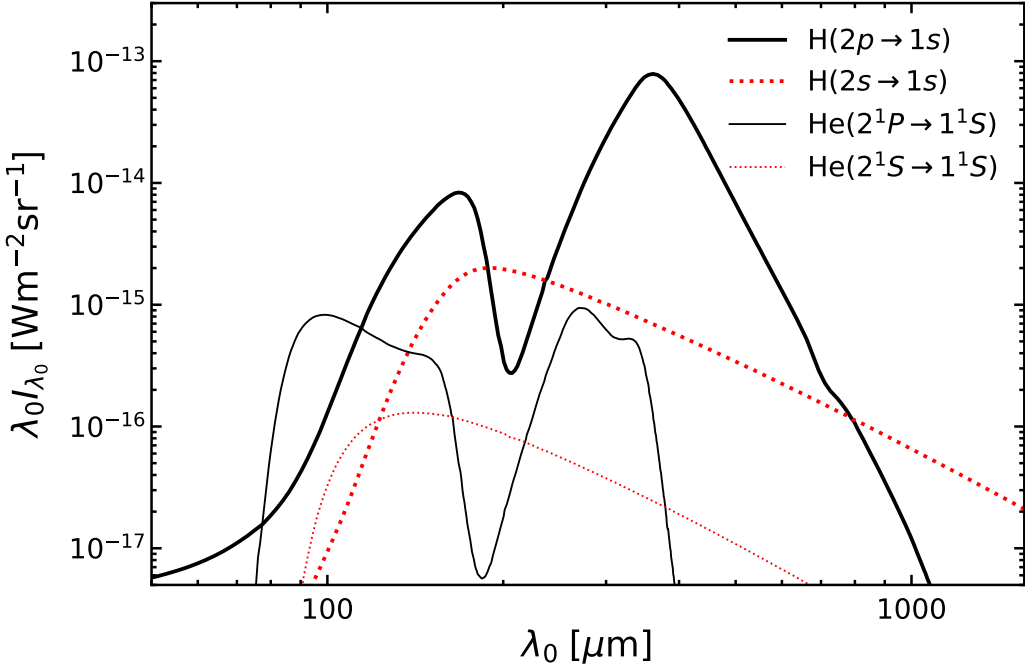


Fig. 4.3.2: Comparing the line intensities due to recombination from the $n = 2$ manifold observed in the cosmic microwave background (CMB) spectrum. Here, the $2E1$ decays in hydrogen and helium, respectively, the thicker and thin (red) dotted lines, are compared with the dominant $E1$ lines in H and He, respectively, the thick and thin solid (black) lines. Calculations from Wong, Seager, and Scott[190].

of magnitude smaller than the other components, there are indeed regions (around $200 \mu\text{m}$) where this process makes an important contribution. Including all other forbidden transitions in He from n^1S and n^1D for $n > 2$ changes the CMB anisotropy power spectrum further by about 1% [184]. Thus, an understanding of the cosmic microwave background relies on accurately accounting for the forbidden processes.

In particular, Spitzer and Greenstein [191] investigated the two-photon emission by neutral hydrogen as a source of continuum radiation from planetary nebulae and Osterbrock [192] has further elaborated its importance where particle densities are less than about 10^4 cm^{-3} . Since hydrogen has its $2p\ ^2P_{3/2}^o$ level very close to $2s\ ^2S_{1/2}$, collisions can be competitive in depopulating that level to $1s\ ^2S_{1/2}$. The hydrogen emission neglecting mass and relativity corrections has an integrated rate of 8.2294 s^{-1} [193] extending from 121.9 nm to a maximum at 243.1 nm and then decreasing through the visible and infrared spectral regions. At low densities, this two-photon emission exceeds the contributions from the recombination of ionized hydrogen and helium

from the Balmer limit at $364.6\text{ }\mu\text{m}$ to about $447.5\text{ }\mu\text{m}$ [192].

For comparison, the two-photon spectrum of neutral helium has a total rate of 50.093 s^{-1} [193] extending from $601.40\text{ }\mu\text{m}$ to a maximum at $120.28\text{ }\mu\text{m}$ decreasing to about 64% of the peak value at $364.6\text{ }\mu\text{m}$. Typically, helium is present with $1/10$ the hydrogen abundance by number of atoms [194], so the two-photon emission by helium could be an important addition to the continuum emission around $400\text{ }\mu\text{m}$ in some planetary nebulae. Similarly for helium in the early universe, two-photon emission affects the populations of the two lowest S-states.

Beyond astrophysical observations, laboratory measurements of the total decay rate have been made for He [195], and the six He-like ions with $Z = 3, 18, 28, 35, 36$, and 41 [196–201], as reviewed by Mokler and Dunford [202]. This work focuses on heavier two-electron systems where the relativistic effects become more pronounced. Each of the decay mechanisms in the Fig. 4.3.1 has been studied in detail in this regime. Recent work has focussed on the photon spectral distribution functions for heavy heliumlike ions up to $Z = 92$ using relativistic Green’s functions methods [203] in comparison with experiment [204]. For the corresponding hydrogenic case, the angular and polarization dependence of the photons in the relativistic region has been studied by Safari *et al.* [205], including hyperfine structure.

4.3.2 Theoretical motivation

A prominent aspect of this chapter in Sec. 4.9.1 involves the numerical comparison between the length and velocity forms/gauges⁸ of the calculated decay rates. Changing gauges relies on commutation relations that apply exactly when the pseudostates are exact eigenstates of the Hamiltonian. Therefore, testing gauge invariance is a crucial internal check on theoretical calculations, especially when experimental results are unavailable or theory is ahead of experiment. In radiative transitions theory, gauge equivalence of the length and velocity forms applies only in the limit of infinite nuclear mass. Here, we build on Drake’s work [193] to extend this to finite nuclear mass. A central goal is to make the relationships developed in Ref. [193] as precise

⁸These two terms are used interchangeably in this chapter.

and general as possible. In the NR limit, testing gauge invariance stringently is the primary method to assess the accuracy of both the infinite-mass pseudostates and the overall calculations of the decay rates. To facilitate this generalization for a broader range of transitions, the decay rate equations have been extended to the acceleration gauge and generalized to $nE1$ decay processes.

In extending this work to include relativistic effects,⁹ discussed in Sec. 4.10, the questions of gauge invariance and preferred gauge are very much open. Grant wrote an article titled “Gauge invariance and relativistic radiative transitions” [206] in 1974 and claimed that:

One might think that the role of gauge invariance in the study of the interaction between the electromagnetic field and the electron-positron field is a topic that is now well understood, so that it should not be necessary to write a paper with the above title.

44 years later, in 2018, in a paper calculating relativistic and radiative corrections to the dynamic Stark shift, Jentschura and Adhikari [207] say:

One might think that all conceivable questions regarding the gauge invariance of physical processes in quantum electrodynamics (QED) have already been addressed in the literature. That is not the case.

Clearly questions remain on the important topic on gauge invariance that is instrumental to internally testing theoretical results. These difficulties can arise from the treatment of negative energy states, whose contributions to the various atomic processes under consideration are not gauge invariant. This is indeed an active area of theoretical research where open questions linger.

⁹This commentary remains relevant in Chap. 5 whose topic is computing the tuneout frequency in helium as a test of QED.

4.4 BRIEF HISTORY OF CALCULATIONS AND EXPERIMENTS

Following the initial theoretical analysis by Goeppert-Mayer, Breit and Teller [208] performed the first quantitative calculations for hydrogen $2\ ^2S_{1/2} - 1\ ^2S_{1/2}$ and gave qualitative estimates for helium $2\ ^1S_0 - 1\ ^1S_0$. More quantitative estimates were obtained by Dalgarno [209] from oscillator strength sum rules and the first accurate calculations were performed by Drake *et al.* [186] for helium and the heliumlike ions up to Ne^{8+} . These calculations demonstrated the approximate Z^6 scaling of the decay rates from $51.3\ \text{s}^{-1}$ for He to $1.00 \times 10^7\ \text{s}^{-1}$ for Ne^{8+} . The accuracy was further improved by Drake [193], including an estimate of relativistic corrections derived from the one-electron case [210], and extended to all ions up to U^{90+} . The first fully relativistic calculations by were performed by Derevianko and Johnson [211], using a relativistic configuration-interaction method, and found to be in good agreement with Ref. [193]. They also confirmed previous investigations [186, 212] that the triplet-to-singlet decay rates are negligible at low atomic number, with the ratio increasing from 6.2×10^{-11} at $Z = 2$ to 2.6×10^{-6} at $Z = 16$.

4.5 THEORETICAL FORMULATION

For helium and the low- Z heliumlike ions considered in this chapter, the appropriate starting point for a discussion of finite-mass-effects is the Schrödinger equation in an inertial coordinate system. For an atom with atomic number Z and nuclear mass M located at \mathbf{R}_N and N electrons of mass m_e located at \mathbf{R}_i , the nonrelativistic Hamiltonian¹⁰ is

$$H_{\text{inert}} = \frac{\mathbf{P}_N^2}{2M} + \sum_{i=1}^N \left(\frac{\mathbf{P}_i^2}{2m_e} - \frac{Ze^2/4\pi\epsilon_0}{|\mathbf{R}_i - \mathbf{R}_N|} + \sum_{j>i}^N \frac{Ze^2/4\pi\epsilon_0}{|\mathbf{R}_j - \mathbf{R}_i|} \right) \quad (4.1)$$

¹⁰Section 4.10 outlines the inclusion of relativistic effects.

in SI units [31], where $\mathbf{P} = -i\hbar\nabla_{\mathbf{R}}$. The Schrödinger equation¹¹

$$H_{\text{inert}}|u\rangle = E_u|u\rangle \quad (4.2)$$

then determines the energy levels E_u and eigenvectors $|u\rangle$. To simplify the solution, the usual procedure is to transform to centre-of-mass (cm) plus relative coordinates defined by

$$\mathbf{R}_{\text{cm}} = \frac{M\mathbf{R}_{\text{N}} + m_{\text{e}} \sum \mathbf{R}_i}{M + Nm_{\text{e}}} \quad (4.3)$$

$$\mathbf{r}_i = \mathbf{R}_i - \mathbf{R}_{\text{N}}. \quad (4.4)$$

Transforming Eq. (4.1) to coordinates $\mathbf{r}_i = \mathbf{R}_i - \mathbf{R}_{\text{N}}$ and $\mathbf{R}_{\text{cm}} = 0$ so that

$$(M + Nm_{\text{e}})\mathbf{R}_{\text{N}} + m_{\text{e}} \sum_{i=1}^N \mathbf{r}_i = 0 \quad (4.5)$$

and taking the conserved total momentum to be zero in the absence of external forces resulting in

$$\sum_{i=1}^N \mathbf{P}_i = \sum_{i=1}^N \mathbf{p}_i \quad \text{and} \quad \mathbf{P}_{\text{N}} + \sum_{i=1}^N \mathbf{p}_i = 0$$

gives

$$\begin{aligned} H_{\text{cm}} = & \frac{1}{2\mu} \sum_{i=1}^N \mathbf{p}_i^2 + \frac{1}{M} \sum_{i=1}^N \sum_{j>i}^N \mathbf{p}_i \cdot \mathbf{p}_j + \frac{1}{2(M + Nm_{\text{e}})} \mathbf{P}_{\text{cm}}^2 \\ & - \sum_{i=1}^N \left(\frac{Ze^2/4\pi\epsilon_0}{|\mathbf{r}_i|} + \sum_{j>i}^N \frac{Ze^2/4\pi\epsilon_0}{|\mathbf{r}_j - \mathbf{r}_i|} \right). \end{aligned} \quad (4.6)$$

Here μ is the reduced electron mass $\mu = m_{\text{e}}M/(m_{\text{e}} + M)$, the term $\sum_{j>i} \mathbf{p}_i \cdot \mathbf{p}_j/M$ is the mass-polarization operator and the term involving $\mathbf{P}_{\text{cm}} = -i\hbar\nabla_{R_{\text{cm}}}$ accounts for the motion of the centre of mass relative to the inertial frame represented by the coordinates \mathbf{R}_{N} and \mathbf{R}_i .

¹¹The structure-related problem of spontaneous decay requires only the TISE as the system begins and ends in an eigenstate of the NR Hamiltonian.

We next include the interaction with the radiation field, specified by its vector potential

$$\mathbf{A}(\mathbf{R}, t) = A_0(\omega) \hat{\epsilon} e^{i\mathbf{k} \cdot \mathbf{R} - i\omega t} + \text{c.c.} \quad (4.7)$$

where

$$A_0(\omega) = c \left(\frac{\hbar}{2\epsilon_0 \omega \mathcal{V}} \right)^{1/2} \quad (4.8)$$

for a photon of frequency ω , wave vector \mathbf{k} ($|\mathbf{k}| = \omega/c$), and polarization $\hat{\epsilon} \perp \mathbf{k}$. The factor $A_0(\omega)$ normalizes the vector potential to unit photon energy $\hbar\omega$ in volume \mathcal{V} . In a semiclassical picture, the interaction Hamiltonian with the radiation field is obtained by making the minimal coupling replacements [213]

$$\mathbf{P}_N \rightarrow \mathbf{P}_N - Ze\mathbf{A}(\mathbf{R}_N) \quad (4.9)$$

$$\mathbf{P}_i \rightarrow \mathbf{P}_i + e\mathbf{A}(\mathbf{R}_i) \quad (4.10)$$

for the canonical momenta in the inertial Hamiltonian H_{inert} in Eq. (4.1). The linear coupling terms then yield

$$H_{\text{int}} = -\frac{Ze}{Mc} \mathbf{P}_N \cdot \mathbf{A}(\mathbf{R}_N) + \frac{e}{m_e c} \sum_{i=1}^N \mathbf{P}_i \cdot \mathbf{A}(\mathbf{R}_i), \quad (4.11)$$

a result valid in this work where the quadratic A^2 term can be neglected.

4.5.1 Single-photon transitions

As a point of reference, consider the well-known case of single-photon transitions for a finite nuclear mass, as first discussed by Fried and Martin [214], and extended by Yan and Drake [215] and Drake and Morton [181]. From Fermi's Golden Rule (FGR),¹² the decay rate for spontaneous emission from state i to f is

$$w_{i,f} d\Omega = \frac{2\pi}{\hbar} |\langle i | H_{\text{int}} | f \rangle|^2 \rho(\omega) d\Omega, \quad (4.12)$$

¹²See Appendix B for a sketch of how FGR arises within the framework of time-dependent perturbation theory.

where

$$\rho(\omega) = \frac{\mathcal{V}\omega^2}{(2\pi c)^3\hbar} \quad (4.13)$$

is the number of photon states with polarization $\hat{\epsilon}$ per unit energy in the normalization volume \mathcal{V} . In the long wavelength and electric dipole approximations, the factor $e^{i\mathbf{k}\cdot\mathbf{R}}$ in Eq. (4.7) is replaced by unity.

After integrating over angles $d\Omega$ and summing over polarizations $\hat{\epsilon}$, the decay rate reduces to [40, p. 248]

$$w_{i,f} = \frac{4}{3}\alpha\omega_{i,f}|\langle i|\mathbf{Q}_P|f\rangle|^2, \quad (4.14)$$

where $\omega_{i,f}$ is the transition frequency and, as follows from Eq. (4.11), \mathbf{Q}_P is the dimensionless velocity form of the transition operator

$$\mathbf{Q}_P = -\frac{Z}{Mc}\mathbf{P}_N + \frac{1}{m_e c} \sum_{i=1}^N \mathbf{P}_i \quad (4.15)$$

for the general case of N electrons. From the commutator¹³

$$[H_{\text{inert}}, \mathbf{Q}_R/\hbar\omega_{i,f}] = \mathbf{Q}_P, \quad (4.16)$$

where H_{inert} is the field-free Hamiltonian in Eq. (4.1), the equivalent length form is

$$\mathbf{Q}_R = -\frac{i}{c}\omega_{i,f} \left(Z\mathbf{R}_N - \sum_{i=1}^N \mathbf{R}_i \right). \quad (4.17)$$

Furthermore, the dipole operator in the acceleration form \mathbf{Q}_A can be obtained using the commutation relation

$$[H_{\text{inert}}, \mathbf{Q}_P/\hbar\omega_{i,f}] = \mathbf{Q}_A. \quad (4.18)$$

where

$$\mathbf{Q}_A = \frac{iZ}{m_e c \omega_{i,f}} \frac{Zm_e + M}{M} \sum_{i=1}^N \frac{(\mathbf{R}_i - \mathbf{R}_N)}{|\mathbf{R}_i - \mathbf{R}_N|^3}. \quad (4.19)$$

¹³Equations (4.16) and (4.18) follow from the basic commutation relations $[H, \mathbf{r}] = -i\hbar\mathbf{p}/m$ and $[H, \mathbf{p}] = i\hbar\partial V(r)/\partial r$, for $H = \mathbf{p}^2/2m + V(r)$. For the Coulomb potential, $V(r) = \pm Z/r$, the $[H, \mathbf{r}]$ commutator is the same, but $[H, \mathbf{p}] = \mp i\hbar Z\mathbf{r}/r^3 \equiv \mp i\hbar Z\mathbf{a}$.

All forms of the dipole operators in Eqs. (4.15), (4.17), and (4.19) are expressed in the inertial frame. Though the numerical tests in this work (as in Ref. [24]) are performed for the length and velocity forms, we present the corresponding acceleration forms throughout the chapter and extend the algebraic relations we derive to include this acceleration form.

To study mass polarization effects, \mathbf{Q}_P , \mathbf{Q}_R , and \mathbf{Q}_A must be transformed to c.m. plus relative coordinates to conform with the Hamiltonian in Eq. (4.6), with the result

$$\begin{aligned}\mathbf{Q}_p &= \frac{Z_p}{m_e c} \sum_{i=1}^N \mathbf{p}_i \\ \mathbf{Q}_r &= \frac{i\omega_{i,f}}{c} Z_r \sum_{i=1}^N \mathbf{r}_i, \\ \mathbf{Q}_a &= \frac{iZ}{m_e c \omega_{i,f}} Z_a \sum_{i=1}^N \frac{\mathbf{r}_i}{|\mathbf{r}_i|^3}\end{aligned}\quad (4.20)$$

where

$$Z_p = Z_a = \frac{Zm_e + M}{M}, \quad Z_r = \frac{Zm_e + M}{Nm_e + M},$$

and the number of electrons is $N = 2$ for heliumlike atoms. The Z_x terms account for the radiation produced by the nucleus as it moves in the c.m. frame [193]. These operators satisfy

$$\begin{aligned}[H_{cm}, \mathbf{Q}_r] &= \hbar\omega_{i,f} \mathbf{Q}_p, \text{ and} \\ [H_{cm}, \mathbf{Q}_p] &= \hbar\omega_{i,f} \mathbf{Q}_a,\end{aligned}\quad (4.21)$$

in the c.m. frame. To the extent that the nonrelativistic Schrödinger equation, Eq. (4.2), is solved exactly, the relation

$$\langle i | \mathbf{Q}_r | f \rangle = \langle i | \mathbf{Q}_p | f \rangle = \langle i | \mathbf{Q}_a | f \rangle \quad (4.22)$$

is satisfied to all orders in m_e/M . For a neutral atom, $N = Z$ and $Z_r = 1$. If,

following Ref. [181], the oscillator strength is defined by

$$f_{i,f} = \frac{2m_e c^2}{3\hbar\omega_{i,f}} \langle i | \mathbf{Q}_p \cdot \hat{\mathbf{e}} | f \rangle \langle f | \mathbf{Q}_r \cdot \hat{\mathbf{e}} | i \rangle, \quad (4.23)$$

then the Thomas-Reiche-Kuhn sum rule $\sum_f f_{i,f} = N$ is modified to read [181]

$$\sum_f f_{i,f} = N + Z^2 m_e / M \quad (4.24)$$

with emission counted as negative and absorption as positive. In this way, the sum is 2 for positronium (Ps), but 3 for Ps^- , as expected for two or three radiating particles of the same mass. The above formulas provide a smooth interpolation between the two extremes. An advantage of this definition is that the decay rate, summed over final states and averaged over initial states, has the conventional form

$$\bar{w}_{i,f} = -\frac{2\alpha\hbar\omega_{i,f}^2}{m_e c^2} \bar{f}_{i,f}, \quad (4.25)$$

where $\bar{f}_{i,f} = -(g_f/g_i) \bar{f}_{f,i}$ is the (negative) oscillator strength for photon emission from state $|i\rangle$, and g_i , g_f are the statistical weights of the states.

4.5.2 Two-photon transitions

The triply differential rate for the simultaneous emission of two photons of frequencies ω_1 and ω_2 can similarly be expressed via FGR in the form

$$dw^{(2\gamma)} d\Omega_1 d\Omega_2 = \frac{2\pi}{\hbar} |U_{i,f}^{(2)}|^2 \rho(\omega_1) \rho(\omega_2) d\Omega_1 d\Omega_2 dE_1 \quad (4.26)$$

where, in a nonrelativistic approximation, $U_{i,f}^{(2)}$ is a second-order interaction energy with the electromagnetic field given by¹⁴

$$U_{i,f}^{(2)} = - \sum_n \left[\frac{\langle f | H_{\text{int}}(\omega_1) | n \rangle \langle n | H_{\text{int}}(\omega_2) | i \rangle}{E_n - E_i + \hbar\omega_2} + \frac{\langle f | H_{\text{int}}(\omega_2) | n \rangle \langle n | H_{\text{int}}(\omega_1) | i \rangle}{E_n - E_i + \hbar\omega_1} \right] \quad (4.27)$$

summed over positive energy states, and by conservation of energy

$$E_i - E_f = \hbar\omega_1 + \hbar\omega_2. \quad (4.28)$$

The interaction energy, $U_{i,f}^{(2)}$, contains a complete sum over a set of intermediate states. Computationally, this demands a discrete pseudospectrum, just as in the final ${}^6\text{Li}^+$ spectrum in Chap. 3. As noted in the chapter overview, the strength of pseudostates—particularly their derivation through diagonalization to form a complete pseudospectrum—is fully demonstrated here. Using pseudospectra, two distinct physical processes—excitation/ionization and interaction with the QED vacuum—can be calculated.

Two-photon decay leads to a broad distribution of photon energies such that their sum is equal to the atomic energy difference. Using Eqs. (4.8) and (4.13) for A_0 and $\rho(\omega)$, and approximating $\mathbf{A} = A_0 \hat{\mathbf{\epsilon}}$, the two-photon decay rate becomes

$$dw^{(2\gamma)} d\Omega_1 d\Omega_2 = \frac{\alpha^2 \hbar \omega_1 \omega_2}{(2\pi)^3} \left| \sum_n \left[\frac{\langle f | \mathbf{Q}_p \cdot \hat{\mathbf{\epsilon}}_1 | n \rangle \langle n | \mathbf{Q}_p \cdot \hat{\mathbf{\epsilon}}_2 | i \rangle}{E_n - E_i + \hbar\omega_2} + \frac{\langle f | \mathbf{Q}_p \cdot \hat{\mathbf{\epsilon}}_2 | n \rangle \langle n | \mathbf{Q}_p \cdot \hat{\mathbf{\epsilon}}_1 | i \rangle}{E_n - E_i + \hbar\omega_1} \right] \right|^2 d\Omega_1 d\Omega_2 dE_1. \quad (4.29)$$

To treat the process in which the final polarizations are not detected, this must still be summed over two linearly independent sets of polarization vectors $\hat{\mathbf{\epsilon}}_1$ and $\hat{\mathbf{\epsilon}}_2$, and integrated over angles. For $S - S$ transitions via intermediate P -states, the matrix elements squared are proportional to $|\hat{\mathbf{\epsilon}}_1 \cdot \hat{\mathbf{\epsilon}}_2|^2$, and the sum over polarization vectors

¹⁴See Appendix E, based on Refs. [216, 217], for a sketch of how this form of the interaction energy arises by considering interaction with the QED vacuum.

yields an angular correlation factor of $1 + \cos^2 \theta_{12}$ (see Appendix F). The remaining angular integral is

$$\int_{4\pi} d\Omega_1 \int_{4\pi} d\Omega_2 (1 + \cos^2 \theta_{12}) = \frac{64\pi^2}{3} \quad (4.30)$$

The final result for the singly differential decay rate for the case of the helium 2^1S state is thus

$$\frac{dw^{(2\gamma)}}{d\omega_1} = \frac{8\alpha^2}{3\pi} |Q^{(2\gamma)}(\omega_1, \omega_2)|^2 \quad (4.31)$$

where the dimensionless quantity $Q^{(2\gamma)}$ can be expressed in velocity form (p) as

$$\begin{aligned} Q_p^{(2\gamma)}(\omega_1, \omega_2) &= -(\omega_1 \omega_2)^{1/2} \sum_n \langle 1^1S | Q_{p,z} | n^1P \rangle \langle n^1P | Q_{p,z} | 2^1S \rangle \\ &\quad \times \left(\frac{1}{\omega_n - \omega_i + \omega_2} + \frac{1}{\omega_n - \omega_i + \omega_1} \right). \end{aligned} \quad (4.32)$$

where $\omega_i = E_i/\hbar$ and $Q'_{p,z}$ is the z -component of the vector \mathbf{Q}'_p , defined in Eq. (4.33). Exactly the same expression applies for the length and acceleration forms $Q_r^{(2\gamma)}(\omega_1, \omega_2)$ and $Q_a^{(2\gamma)}(\omega_1, \omega_2)$ by replacing the $Q'_{p,z}$ with $Q'_{r,z}$ or $Q'_{a,z}$. These dimensionless dipole operators in the velocity, length, and acceleration forms are given by:

$$\mathbf{Q}'_p = \frac{1}{m_e c} Z_p \sum_{i=1}^N \mathbf{p}_i, \quad (4.33)$$

$$\mathbf{Q}'_r = \frac{i(\omega_1 \omega_2)^{1/2}}{c} Z_r \sum_{i=1}^N \mathbf{r}_i, \quad (4.34)$$

$$\mathbf{Q}'_a = \frac{iZ}{m_e c (\omega_1 \omega_2)^{1/2}} Z_p \sum_{i=1}^N \frac{\mathbf{r}_i}{r_i^3} \quad (4.35)$$

The equivalence of the three forms can also be regarded as a gauge transformation, as discussed in general by Goldman and Drake [210]. A numerical comparison of the two provides a check on the accuracy of the calculations since it is valid only if the wave functions are exact, and the sum over intermediate states is complete.

Comparing Eqs. (4.33)–(4.35) with the one-photon version summarized in Eq. (4.20), we note that the overall frequency ω and Z terms, along with the momentum \mathbf{p} and

position \mathbf{r} operators occur with the same power for the corresponding gauge. The only difference is that the frequency in the prefactor reads $(\omega_1\omega_2)^{1/2}$ for the two-photon dipole operator in the length and acceleration gauge, but just $\omega_{i,f}$ in the corresponding single-photon operator. This correspondence will be used in generalizing the conclusions drawn from one- and two-photon transition rates to the general case of $nE1$ transitions in Sec. 4.8.2.

Finally, the integrated two-photon decay rate is

$$\begin{aligned} w^{(2\gamma)} &= \frac{1}{2} \int_0^\Delta \frac{dw^{(2\gamma)}}{d\omega_1} d\omega_1 \\ &= \frac{4\alpha^2\Delta}{3\pi} \int_0^1 |Q^{(2\gamma)}(y)|^2 dy, \end{aligned} \quad (4.36)$$

where $y = \omega_1/\Delta$, $\Delta = (E_i - E_f)/\hbar$ and the factor of $1/2$ is included because each pair of photons should be counted only once.

4.6 WAVE FUNCTIONS FOR CALCULATION

In order to obtain any numerical decay rates, the first step is to choose appropriate basis sets to diagonalize the finite- and infinite-mass Hamiltonian in Eq. (4.6), generating both the initial and final helium states, and a third basis set to form the pseudospectra needed to carry out the complete sum involved in the decay rate. The same Hylleraas basis sets, developed in Sec. 2.7.1, and used in Chap. 3, are used for this purpose.

4.6.1 Reduced-mass atomic units

For the purpose of calculations, it is convenient to transform to reduced-mass atomic units of distance, time, momentum and energy, respectively, defined by

$$\begin{aligned} \rho &= \frac{\mu}{m_e} \frac{a_0}{\hbar}, & \tau &= \frac{\mu}{m_e} \frac{a_0}{\alpha c} t, \\ i\nabla &= -\frac{m_e}{\mu} \frac{a_0}{\hbar} \mathbf{p}, & \epsilon &= \left(\frac{m_e}{\mu} \right) \frac{E}{\alpha^2 m_e c^2}, \end{aligned} \quad (4.37)$$

so that the Schrödinger equation assumes the dimensionless form for two electrons

$$\left[-\frac{1}{2}(\nabla_{\rho_1}^2 + \nabla_{\rho_2}^2) - \frac{\mu}{M} \nabla_{\rho_1} \cdot \nabla_{\rho_2} + V(\rho_1, \rho_2) \right] \Psi = \epsilon \Psi \quad (4.38)$$

where $V(\rho_1, \rho_2) = -\frac{Z}{\rho_1} - \frac{Z}{\rho_2} + \frac{1}{|\rho_1 - \rho_2|}$.

The two-electron wave functions for the initial and final S -states, and the intermediate P -states are all calculated variationally as described in Chap. 2.

4.7 FINITE-NUCLEAR-MASS EFFECTS

Both finite- and infinite-mass decay rates were calculated using Eq. (4.36), using the pseudospectra with the appropriate Hamiltonian (i.e., $\mu/M \rightarrow 0$ for the infinite-mass case) to evaluate the sum over states arising in Eq. (4.32). The results are summarized in Table 4.9.3. A primary focus of this work, however, was to study the relationship between the finite- and infinite-mass cases and to discern how finite-mass effects arise. The motivation for doing this is ultimately to extend the derivation of gauge equivalence, usually given in the infinite-mass limit, to the case of finite nuclear mass. This section and the next both deal with this topic. Within this section, Sec. 4.7.1 enumerates the sources of the finite-mass effect and then Sec. 4.7.2 collects the results in the form of constitutive relationships between the finite- and infinite-mass decay rates.

4.7.1 Three sources of finite-mass effects

Finite-mass corrections to $w_{x,\infty}$ come from three sources and are first discussed with respect to $2E1$ transitions. The first is due to radiation emitted by the nucleus moving in the c.m. frame and can be expressed as a power of Z_x in Eqs. (4.33)–(4.35). In the two-photon case this is taken into account by powers four Z_x^4 in all three forms $x = p, r, a$. The second source of finite-mass-effects, analogous to the normal isotope shift, is due to the mass scaling of the energies, transition frequencies and matrix elements as calculated from wave functions expressed in reduced mass atomic units

according to Eq. (4.37). This mass scaling is expressed as powers of μ/m_e . Since the Q' terms in Eqs. (4.33)–(4.35) occur, via Eq. (4.32), with the fourth power in the integral in Eq. (4.36), along with the frequency factor Δ , the factors to transform the reduced atomic units to physical ones are $(\mu/m_e)^5$ for both $w_p^{(2\gamma)}$ and $w_a^{(2\gamma)}$, and (μ/m_e) for $w_r^{(2\gamma)}$.

The third correction comes from the direct effect of the mass polarization term $-\frac{\mu}{M} \nabla_{\rho_1} \cdot \nabla_{\rho_2}$ in Eq. (4.38) on the wave functions, energies and matrix elements, analogous to the specific isotope shift. The result can be expressed as a correction factor $F(\mu/M)$ to the two-photon decay rate for infinite nuclear mass $w_\infty^{(2\gamma)}$. For small μ/M , it is useful to expand $F(\mu/M)$ in the form

$$F_x(\mu/M) = 1 + (\mu/M)C_x + (\mu/M)^2D_x + (\mu/M)^3E_x + \dots \quad (4.39)$$

where C_x , D_x , and E_x correspond to first-, second-, and third-order mass polarization corrections for the three forms. For helium and the heliumlike ions, $\mu/M \sim 10^{-4}$, and so terms beyond D_x are negligible. The coefficients C_x and D_x could be calculated by perturbation theory,¹⁵ but we have adopted the simple expedient of calculating $F_x(\mu/M)$ for an arbitrary pair of values of μ/M and solving for C_x and D_x .

4.7.2 Constitutive relationships

These three sources of finite-mass effects are summarized as follows. We write down these relationships for the case of spontaneous emission but emphasize that the ensuing algebra is the same for other transition rates involving the same number of photons and leads to the same algebraic relationships. For single-photon decay, the

¹⁵This procedure is outlined in Appendix G.

three factors enter in the form

$$w_r^{(1\gamma)} = Z_r^2 \left(\frac{\mu}{m_e} \right) F_r(\mu/M) w_{r,\infty}^{(1\gamma)}, \quad (4.40)$$

$$w_p^{(1\gamma)} = Z_p^2 \left(\frac{\mu}{m_e} \right)^3 F_p(\mu/M) w_{p,\infty}^{(1\gamma)}, \quad (4.41)$$

$$w_a^{(1\gamma)} = Z_p^2 \left(\frac{\mu}{m_e} \right)^3 F_p(\mu/M) w_{a,\infty}^{(1\gamma)}, \quad (4.42)$$

and for two-photon decay, they enter in the form

$$w_r^{(2\gamma)} = Z_r^4 \left(\frac{\mu}{m_e} \right) F_r(\mu/M) w_{r,\infty}^{(2\gamma)}, \quad (4.43)$$

$$w_p^{(2\gamma)} = Z_p^4 \left(\frac{\mu}{m_e} \right)^5 F_p(\mu/M) w_{p,\infty}^{(2\gamma)}, \quad (4.44)$$

$$w_a^{(2\gamma)} = Z_p^4 \left(\frac{\mu}{m_e} \right)^5 F_p(\mu/M) w_{a,\infty}^{(2\gamma)}. \quad (4.45)$$

It is noteworthy, though coincidental,¹⁶ that the constitutive relationship between the finite- and infinite-mass decay rate expressions is identical in the velocity and acceleration cases—labelled as Z_p and F_p in both gauges.

4.8 TREATING MASS POLARIZATION

The first two effects, radiation emitted in the c.m. frame and mass scaling, are a direct consequence of the form the decay rate and the form of the corresponding dipole operators are easily handled. Mass polarization, on the other hand, requires a more detailed calculation. We have treated mass polarization as an additional third factor, $F_x(\mu/M)$, defined by a power series as shown in Eq. (4.39). In Appendix G, the equivalence of this approach with simple perturbation theory is shown.

¹⁶Following the gauge transformation between the velocity and acceleration forms, which is performed via the commutation relation in Eq. (4.21), the same Z term, characterizing the nuclear motion in the c.o.m. frame, and the same power of μ/m_e appear in the decay rate expression.

4.8.1 Algebraic relations

If the wave functions and sums over intermediate states are exact¹⁷, then for an $nE1$ -photon transition it should be true that $w_p^{(n\gamma)} = w_r^{(n\gamma)} = w_a^{(n\gamma)}$, or in terms of ratios

$$\frac{w_p^{(n\gamma)}}{w_{p,\infty}^{(n\gamma)}} = \frac{w_r^{(n\gamma)}}{w_{r,\infty}^{(n\gamma)}} = \frac{w_a^{(n\gamma)}}{w_{a,\infty}^{(n\gamma)}}. \quad (4.46)$$

By expanding the prefactors in the rate equations in powers of μ/M using the relations

$$\mu/m_e = 1 - \mu/M \quad (4.47)$$

$$m_e/M = \mu/M + (\mu/M)^2 + (\mu/M)^3 + \dots \quad (4.48)$$

and collecting coefficients of equal powers of μ/M up to $(\mu/M)^3$, one can derive algebraic relations connecting the coefficients C_x , D_x , E_x , \dots in Eq. (4.39). As an example, for two-photon transition rates, the relationship between these expansion coefficients are

order

$$(\mu/M) : \quad C_p - C_r = -4, \quad (4.49)$$

$$C_p = C_a,$$

$$(\mu/M)^2 : \quad 4C_p + D_p - D_r = -6, \quad (4.50)$$

$$D_p = D_a,$$

$$(\mu/M)^3 : \quad 6C_p + 4D_p + E_p - E_r = 4, \quad (4.51)$$

$$E_p = E_a,$$

where the length/acceleration relationships (not displayed) are the same as the length/velocity relationships.

The degree to which these equations are satisfied tests how well the length and velocity gauges agree for a given calculation. For example, Table 4.9.2 demonstrates

¹⁷The exactness of the wave functions ensures the exact satisfaction of the commutators in Sec. 4.5 underlying the particular gauge transformations.

agreement to 1 part in 10^8 between the length and velocity gauges for the two-photon decay rates of heliumlike ions.

4.8.2 Generalization to higher-order transitions

The preceding analysis can be extended to the general n -photon transition rate ($nE1$) problem. The constitutive relations between the two gauges can be obtained by accounting for the additional sets of intermediate states needed to accommodate higher-order transitions, leading to generalized versions of dipole operators given in Eqs. (4.33)–(4.35) for the case of two-photon transitions. This involves tracking additional powers of Z_x and μ/m_e that come from more virtual dipole matrix elements. In the general case, these relationships are

$$w_p^{(n\gamma)} = Z_p^{2n} \left(\frac{\mu}{m_e} \right)^{2n+1} F_p(\mu/M) w_{p,\infty}^{(n\gamma)}, \quad (4.52)$$

$$w_r^{(n\gamma)} = Z_r^{2n} \left(\frac{\mu}{m_e} \right) F_r(\mu/M) w_{r,\infty}^{(n\gamma)}, \text{ and} \quad (4.53)$$

$$w_a^{(n\gamma)} = Z_p^{2n} \left(\frac{\mu}{m_e} \right)^{2n+1} F_p(\mu/M) w_{a,\infty}^{(n\gamma)}. \quad (4.54)$$

In the same fashion as described in Sec. 4.8.1, this leads to the generalized algebraic relations

order

$$(\mu/M) : \quad C_p - C_r = -2n, \quad (4.55)$$

$$C_p = C_a,$$

$$(\mu/M)^2 : \quad 2nC_p + D_p - D_r = -n(2n-1), \quad (4.56)$$

$$D_p = D_a,$$

$$\begin{aligned} (\mu/M)^3 : \quad & n(2n-1)C_p + 2nD_p + E_p - E_r, \\ & = \frac{2}{3}n(n+1)(5-2n), \end{aligned} \quad (4.57)$$

$$E_p = E_a.$$

Eqs. (4.55)–(4.57) can be used to compare length and velocity $nE1$ transition rates up to order $(\mu/M)^3$. Eq. (4.57) was not tested since we are only able to achieve agreement in the finite-mass decay rates between the gauges to 1 part per billion at most, whereas, in helium, the third-order corrections contribute at the parts per trillion level. Extending this set of algebraic relations to higher-order terms in the power series is straightforward and follows the procedure described in this section.

4.9 RESULTS

In Sec. 4.9.1, high-precision two-photon decay rates in heliumlike ions are presented for both the finite- and infinite-mass case and for both the length and velocity forms. In Sec. 4.9.2, the algebraic relations from Eqs. (4.55)–(4.57) are confirmed in the cases of one- and two-photon decay for a set of heliumlike ions.

4.9.1 Two-photon decay rates

We have investigated 14 heliumlike systems, specifically ${}^4\text{He}$ and its isotope ${}^3\text{He}$, ${}^7\text{Li}$ and its isotope ${}^6\text{Li}$, along with the most abundant forms for the rest of the isoelectronic sequence to ${}^{10}\text{Ne}$. For all of these, μ/M is sufficiently small that a power series expansion in powers of μ/M is useful, and so they provide an opportunity to check the algebraic relationships by relating the coefficients. In addition, we studied three heavy helium species $\bar{p}^2\text{-}{}^4\text{He}$, $\pi^2\text{-}{}^4\text{He}$ and $\mu^2\text{-}{}^4\text{He}$ in which the two electrons are replaced by antiprotons, pions and muons respectively. Although these would be difficult to observe experimentally, the values of μ/M are so large (0.2011... for \bar{p}^2) that many terms contribute to the expansion in powers of μ/M , and so the comparison of the length and velocity forms provides a check that the mass dependence is correct to all orders in μ/M .

Table 4.9.1 shows as a typical example the convergence of the velocity and length rates¹⁸ with increasing the basis set size Ω for ${}^4\text{He}$. (The basis sets for 1S are a

¹⁸We have not investigated the acceleration form and have only present detailed calculations for $2E1$ decay—the case of chief experimental interest.

Table 4.9.1: Convergence with respect to basis set size (N) of the ${}^4\text{He}(2\,{}^1S_0)$ two-photon decay rates $w_r^{(2\gamma)}/\alpha^6$ for a finite nuclear mass $\mu/M = 1.370\,745\,62 \times 10^{-4}$. The subscripts r and p denote the length (L) and velocity (V) forms respectively. Units are atomic units. To convert to s^{-1} , multiply by $\alpha^6/\tau_e = 6242.763\,420(56) \text{ s}^{-1}$ where $\alpha = 7.297\,352\,5693(11) \times 10^{-3}$ is the fine structure constant and $\tau_e = 2.418\,884\,326\,5857(47) \times 10^{-17} \text{ s}$ is the atomic unit of time. Constants are taken from the CODATA recommendations [31].

Ω	$N(2\,{}^1S)$	$N(2\,{}^1P)$	$w_p^{(2\gamma)}/\alpha^6$	$w_r^{(2\gamma)}/\alpha^6$
4	44	104	$8.169\,161\,866\,046 \times 10^{-3}$	$8.182\,145\,206\,238 \times 10^{-3}$
5	67	145	$8.170\,301\,592\,330 \times 10^{-3}$	$8.174\,691\,464\,231 \times 10^{-3}$
6	98	197	$8.170\,633\,057\,717 \times 10^{-3}$	$8.171\,830\,051\,527 \times 10^{-3}$
7	135	265	$8.170\,667\,222\,361 \times 10^{-3}$	$8.171\,125\,033\,845 \times 10^{-3}$
8	182	346	$8.170\,684\,766\,627 \times 10^{-3}$	$8.170\,855\,798\,069 \times 10^{-3}$
9	236	446	$8.170\,690\,486\,882 \times 10^{-3}$	$8.170\,747\,017\,232 \times 10^{-3}$
10	301	559	$8.170\,691\,869\,889 \times 10^{-3}$	$8.170\,730\,900\,210 \times 10^{-3}$
11	373	692	$8.170\,692\,739\,038 \times 10^{-3}$	$8.170\,701\,468\,677 \times 10^{-3}$
12	457	836	$8.170\,692\,912\,027 \times 10^{-3}$	$8.170\,697\,771\,291 \times 10^{-3}$
13	548	1000	$8.170\,692\,965\,787 \times 10^{-3}$	$8.170\,695\,029\,079 \times 10^{-3}$
14	652	1173	$8.170\,692\,999\,658 \times 10^{-3}$	$8.170\,693\,953\,023 \times 10^{-3}$
15	763	1366	$8.170\,693\,014\,043 \times 10^{-3}$	$8.170\,693\,367\,924 \times 10^{-3}$
16	888	1566	$8.170\,693\,019\,245 \times 10^{-3}$	$8.170\,693\,193\,226 \times 10^{-3}$
Extrap.			$8.170\,693\,021\,30(21) \times 10^{-3}$	$8.170\,693\,117(8) \times 10^{-3}$

little larger than those for 2^1S .) The rates are tabulated in atomic units and divided by α^6 so that the accuracies are not limited by the uncertainty in the fine structure constant $\alpha = 7.297\,352\,5643(11) \times 10^{-3}$ [31]. The velocity rates increase while the length rates decrease in larger steps to the same final value within 2 parts in 10^8 for $\Omega = 16$ and 1 part in 10^8 for the extrapolated values. This is typical for all the systems studied with slightly poorer convergence for larger μ/M and better for the more higher Z ions reaching 6 parts in 10^9 for ${}^{20}\text{Ne}^{8+}$ with $\Omega = 16$, and 6 parts in 10^{10} for the extrapolated values, altogether providing confidence in the reliability of our wave functions. These extrapolated rates, with their uncertainty, appear in Table 4.9.2 for the $Z = 2$ to 10 heliumlike sequence, including some exotic systems. Since

Table 4.9.2: Extrapolated velocity (p) and length (r) two-photon decay rates $w^{(2\gamma)}/\alpha^6$ for various atoms and ions, including the heavy-helium cases with both electrons replaced by antiprotons (\bar{p}), pions (π), or muons (μ). Units are atomic units. To convert to s^{-1} , multiply by α^6/τ_x where τ_e is given in Table I, $\tau_{\bar{p}} = 1.317\,365\,60 \times 10^{-20}$ s, $\tau_{\pi} = 8.85610 \times 10^{-20}$ s, and $\tau_{\mu} = 1.169\,852\,69 \times 10^{-19}$ s for the antiprotonic, pionic, and muonic cases respectively. Numbers in parentheses () are estimated uncertainties. Not to be confused with citations, in this table the number in square brackets [] is the power of 10 that the quantity should be multiplied by.

Ion	Z	μ/M	$w_p^{(2\gamma)}/\alpha^6$	$w_r^{(2\gamma)}/\alpha^6$
$\bar{p}^2\text{-}{}^4\text{He}$	2	2.011 020 52[-1]	5.205 617 685 79(17)[-3]	5.205 617 713 1(13)[-3]
$\pi^2\text{-}{}^4\text{He}$	2	3.609 30 [2]	7.543 045 464 90(31)[-3]	7.543 045 560(8)[-3]
$\mu^2\text{-}{}^4\text{He}$	2	2.756 517 98[2]	7.686 982 264 6(4)[-3]	7.686 982 309 7(11)[-3]
${}^3\text{He}$	2	1.819 212 06[-4]	8.169 874 733 147(22)[-3]	8.169 874 826(8)[-3]
${}^4\text{He}$	2	1.370 745 62[-4]	8.170 693 021 30(21)[-3]	8.170 693 117(8)[-3]
${}^6\text{Li}^+$	3	9.121 675 6[-5]	3.109 011 875 468(10)[-1]	3.109 011 8852(11)[-1]
${}^7\text{Li}^+$	3	7.820 195 0[-5]	3.108 946 571 280(10)[-1]	3.108 946 5812(11)[-1]
${}^9\text{Be}^{++}$	4	6.088 199[-5]	2.911 617 478 8637(14)	2.911 617 4840(7)
${}^{11}\text{B}^{3+}$	5	4.983 870[-5]	1.476 948 014 809 15(15)[1]	1.476 948 017 98(15)[1]
${}^{12}\text{C}^{4+}$	6	4.572 544[-5]	5.292 996 164 0483(35)[1]	5.292 996 174 30(21)[1]
${}^{14}\text{N}^{5+}$	7	3.918 481[-5]	1.515 442 208 159 97(13)[2]	1.515 442 2110(6)[2]
${}^{16}\text{O}^{6+}$	8	3.430 541[-5]	3.707 994 488 493 01(25)[2]	3.707 994 492 78(16)[2]
${}^{19}\text{F}^{7+}$	9	2.888 173[-5]	8.077 050 937 463 53(4)[2]	8.077 050 9445(23)[2]
${}^{20}\text{Ne}^{8+}$	10	2.744 620[-5]	1.608 981 338 934 41(5)[3]	1.608 981 339 8859(33)[3]

the velocity rates are more rapidly convergent, we have quoted extrapolated velocity values in Tables 4.9.3 and 4.9.4.

Table 4.9.2 compares the length and velocity forms for all 14 systems. It is clear that the length and velocity forms agree to within the convergence uncertainty of about one part in 10^8 or better over the entire range of μ/M , including the three heavy-helium species. The results verify that the combined mass dependence from all three sources—mass scaling, mass polarization and nuclear motion—have been correctly calculated, and all three must be included to bring the L and V forms into agreement.

Table 4.9.3: Two-photon decay rates $w^{(2\gamma)} / \alpha^6$ for various atoms and ions, including the heavy-helium cases for both finite and infinite nuclear mass. To convert to s^{-1} multiply by α^6 / τ_x —see Table 4.9.2 for this quantity and the values of $\tau_{\bar{p}}$, τ_π , and τ_μ .

Ion	Z	$w^{(2\gamma)} / \alpha^6$	$w_\infty^{(2\gamma)} / \alpha^6$	$w^{(2\gamma)} / w_\infty^{(2\gamma)}$
$\bar{p}^{2-4}\text{He}$	2	$5.205\,617\,685\,79(17) \times 10^{-3}$	$8.173\,194\,7151(20) \times 10^{-3}$	0.636 913 455 17(28)
$\pi^{2-4}\text{He}^+$	2	$7.543\,045\,464\,90(31) \times 10^{-3}$	$8.173\,194\,7151(20) \times 10^{-3}$	0.922 900 497 0(4)
$\mu^{2-4}\text{He}$	2	$7.686\,982\,264\,6(4) \times 10^{-3}$	$8.173\,194\,7151(20) \times 10^{-3}$	0.940 511 334 0(5)
^3He	2	$8.169\,874\,733\,147(22) \times 10^{-3}$	$8.173\,194\,7151(20) \times 10^{-3}$	0.999 593 796 30(36)
^4He	2	$8.170\,693\,021\,30(21) \times 10^{-3}$	$8.173\,194\,7151(20) \times 10^{-3}$	0.999 693 914 82(35)
$^6\text{Li}^+$	3	$3.109\,011\,875\,468(10) \times 10^{-1}$	$3.108\,554\,078\,983(7) \times 10^{-1}$	1.000 147 269 91(4)
$^7\text{Li}^+$	3	$3.108\,946\,571\,280(10) \times 10^{-1}$	$3.108\,554\,078\,983(7) \times 10^{-1}$	1.000 126 262 01(4)
$^9\text{Be}^{++}$	4	2.911 617 478 8637(14)	2.910 640 612 6215(16)	1.000 335 618 983(8)
$^{11}\text{B}^{3+}$	5	$1.476\,948\,014\,809\,15(15) \times 10^1$	$1.476\,253\,238\,3922(19) \times 10^1$	1.000 470 634 9825(16)
$^{12}\text{C}^{4+}$	6	$5.292\,996\,164\,0483(35) \times 10^1$	$5.289\,756\,826\,1109(23) \times 10^1$	1.000 612 379 367(7)
$^{14}\text{N}^{5+}$	7	$1.515\,442\,208\,159\,97(13) \times 10^2$	$1.514\,412\,420\,070\,65(13) \times 10^2$	1.000 679 991 8406(12)
$^{16}\text{O}^{6+}$	8	$3.707\,994\,488\,493\,01(25) \times 10^2$	$3.705\,284\,196\,490\,4(9) \times 10^2$	1.000 731 466 6998(24)
$^{19}\text{F}^{7+}$	9	$8.077\,050\,937\,463\,53(4) \times 10^2$	$8.071\,154\,172\,585\,4(4) \times 10^2$	1.000 730 597 4775(5)
$^{20}\text{Ne}^{8+}$	10	$1.608\,981\,338\,934\,41(5) \times 10^3$	$1.607\,689\,583\,705\,86(3) \times 10^3$	1.000 803 485 4745(4)

In Table 4.9.3, successive columns list the name, atomic number, the finite- and infinite-mass decay rates, and the ratio $w^{(2\gamma)} / w_\infty^{(2\gamma)}$. The rates increase approximately as Z^6 while the ratio $w^{(2\gamma)} / w_\infty^{(2\gamma)}$ increases gradually, being less than unity for ^4He and a little larger than unity for the higher- Z nuclei. There is clearly a cross-over point between $Z = 2$ and $Z = 3$ where the finite nuclear mass effects exactly cancel.

The spectral distribution as a function of energy is symmetric about the midpoint at $\hbar\omega = \frac{1}{2}(E_i - E_f)$. In Table 4.9.4 we list the peak emission rate in s^{-1} , the energy difference in wave numbers and the wavelength of the peak in nm units. As noted in Sec. 4.3.1, two-photon emission from ^4He is relevant in the determination of population balance astrophysical settings with low particle density, as in the characterization of planetary nebulae. References [186, 193] give the helium rates over half the spectrum, but exclude the factor of 1/2 due to double counting. Figure 4.9.1 compares the profiles for ^4He and $\mu^{2-4}\text{He}$, both normalized to unit integrated emission rate. The difference curve (red) across the middle shows that the effect of finite mass is to

Table 4.9.4: Maximum two-photon decay rates, energy ranges, and the wavelengths of the maximum rates. Values have converged to the figures quoted.

Ion	w_{\max} (s ⁻¹)	$\Delta = \omega_i - \omega_f$ (cm ⁻¹)	Peak λ (nm)
$\bar{p}^2\text{-}{}^4\text{He}$	$8.919\,855\,00 \times 10^4$	$2.984\,309 \times 10^8$	$6.701\,720 \times 10^{-2}$
$\pi^2\text{-}{}^4\text{He}$	1.8469×10^4	4.5126×10^7	4.4320×10^{-1}
$\mu^2\text{-}{}^4\text{He}$	$1.421\,736 \times 10^4$	$3.421\,138 \times 10^7$	$5.846\,008 \times 10^{-1}$
${}^3\text{He}$	$7.255\,592\,87 \times 10^1$	$1.663\,010 \times 10^5$	$1.202\,639 \times 10^2$
${}^4\text{He}$	$7.256\,232\,28 \times 10^1$	$1.663\,025 \times 10^5$	$1.202\,628 \times 10^2$
${}^6\text{Li}^+$	$2.694\,285\,13 \times 10^3$	$4.914\,063 \times 10^5$	$4.069\,952 \times 10^1$
${}^7\text{Li}^+$	$2.694\,212\,72 \times 10^3$	$4.914\,072 \times 10^5$	$4.069\,944 \times 10^1$
${}^9\text{Be}^{++}$	$2.490\,892\,44 \times 10^4$	$9.811\,005 \times 10^5$	$2.038\,527 \times 10^1$
${}^{11}\text{B}^{3+}$	$1.252\,656\,20 \times 10^5$	$1.635\,617 \times 10^6$	$1.222\,780 \times 10^1$
${}^{12}\text{C}^{4+}$	$4.461\,029\,08 \times 10^5$	$2.454\,648 \times 10^6$	$8.147\,807$
${}^{14}\text{N}^{5+}$	$1.271\,097\,75 \times 10^6$	$3.438\,289 \times 10^6$	$5.816\,846$
${}^{16}\text{O}^{6+}$	$3.098\,265\,41 \times 10^6$	$4.586\,539 \times 10^6$	$4.360\,586$
${}^{19}\text{F}^{7+}$	$6.727\,920\,98 \times 10^6$	$5.899\,395 \times 10^6$	$3.390\,178$
${}^{20}\text{Ne}^{8+}$	$1.336\,772\,61 \times 10^7$	$7.376\,858 \times 10^6$	$2.711\,181$

make the distribution curve higher and narrower.

Table 4.9.5 presents the final results for the two-photon decay rates, including an estimate of the relativistic correction $\Delta w_{\text{rel}}^{(2\gamma)}$ [193]. The relativistic contribution becomes more important with increasing Z and is larger in magnitude than the mass correction in all cases, but of opposite sign, except for $Z = 2$, where they both lower the infinite nuclear mass decay rate. To quote estimates due to relativistic effects, absent a rigorous calculation, we followed Ref. [193] assuming the effect for a two-electron system is bounded by the unscreened and fully-screened shifts for a single-electron ion and applied the mean to the $w^{(2\gamma)}$ values. Our best estimates of the net rates are in the last column with the uncertainties indicated in parentheses representing the full single-electron range. Our final numbers are essentially the same as those of Derevianko and Johnson [211], who found this procedure in [193] for infinite-mass nuclei consistent with their relativistic calculations for the low- Z

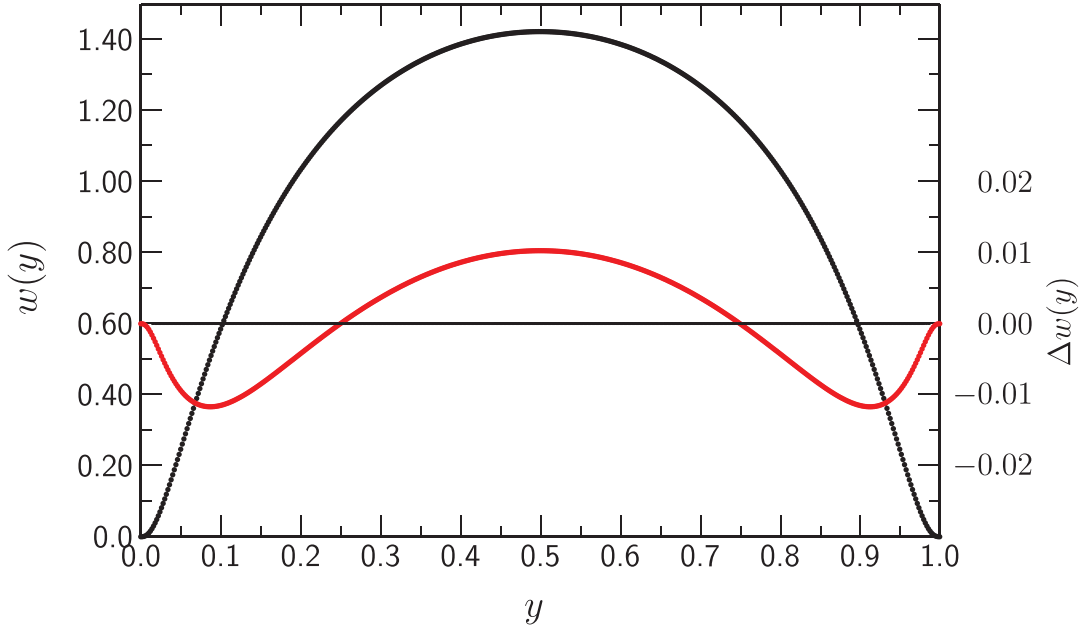


Fig. 4.9.1: Plots of the two-photon emission rate $w^{(2\gamma)}(^4\text{He})$ (black) and the difference $\Delta w^{(2\gamma)} = w^{(2\gamma)}(\mu^2-{}^4\text{He}) - w^{(2\gamma)}(^4\text{He})$ (red) as fractions y of the unit energy range normalized to unity.

ions. However, for neutral helium, where relativistic effects are small and electron correlation effects are large, there is a marginal disagreement of $0.09 \pm 0.07 \text{ s}^{-1}$.

Experimental lifetimes of $5.03(26) \times 10^{-4} \text{ s}$ for both ${}^4\text{He}$ and ${}^3\text{He}$ [195] and $1.97(10) \times 10^{-2} \text{ s}$ for ${}^7\text{Li}^+$ [196] are entirely consistent with our respective calculations of $5.178(45) \times 10^{-4}$ and $1.9634(28) \times 10^{-2}$.

4.9.2 Testing the algebraic relationships

The algebraic relations given in Sec. 4.8.1 have been tested and verified in numerical calculations involving one- and two-photon decay rates, which, as mentioned previously, give rise to identical algebraic relationships as other transitions involving the same number of photons. The algebraic coefficients, along with the satisfaction of the corresponding algebraic relations, are presented in Tables 4.9.6 and 4.9.7.

The constitutive relations between the finite- and infinite-mass decay rates in Eqs.

Table 4.9.5: Final values for the two-photon decay rates, including finite nuclear mass ($\Delta w_{\mu/M}^{(2\gamma)}$) and relativistic corrections ($\Delta w_{\text{rel}}^{(2\gamma)}$) from Drake [193]. The total $w_{\text{total}}^{(2\gamma)}$ is compared with the relativistic CI calculations of Derevianko and Johnson [211]. Units are s^{-1} with an overall scale factor given in the last column for all the entries.

Ion	$w_{\infty}^{(2\gamma)}$	$\Delta w_{\mu/M}^{(2\gamma)}$	$\Delta w_{\text{rel}}^{(2\gamma)}$	$w_{\text{total}}^{(2\gamma)}$	Ref. [211]	Difference	Scale
$\bar{p}^2\text{-}{}^4\text{He}$	9.368 660 56(8)	-3.401 634 59(3)	-0.014(13)	5.953(13)			$\times 10^4$
$\pi^2\text{-}{}^4\text{He}$	1.393 610 183(13)	-0.107 446 652	-0.0021(19)	1.284 1(19)			$\times 10^4$
$\mu^2\text{-}{}^4\text{He}$	1.055 000 450(9)	-0.062 760 569	-0.0016(15)	0.990 7(15)			$\times 10^4$
${}^3\text{He}$	5.102 332 10(5)	-0.002 072 586	-0.008(7)	5.093(7)	5.102	-0.009(7)	$\times 10^1$
${}^4\text{He}$	5.102 332 10(5)	-0.001 561 748	-0.008(7)	5.093(7)	5.102	-0.009(7)	$\times 10^1$
${}^6\text{Li}^+$	1.940 596 769(17)	0.000 285 792	-0.0020(17)	1.938 8(17)	1.940	-0.0012(17)	$\times 10^3$
${}^7\text{Li}^+$	1.940 596 769(17)	0.000 245 024	-0.0020(17)	1.938 8(17)	1.940	-0.0012(17)	$\times 10^3$
${}^9\text{Be}^{++}$	1.817 044 074(16)	0.000 609 834	-0.0022(16)	1.815 4(16)	1.816	-0.0006(16)	$\times 10^4$
${}^{11}\text{B}^{3+}$	9.215 899 72(8)	0.004 337 325	-0.014(8)	9.206(8)	9.211	-0.005(8)	$\times 10^4$
${}^{12}\text{C}^{4+}$	3.302 270 041(30)	0.002 022 242	-0.0063(33)	3.297 9(33)	3.300	-0.0021(33)	$\times 10^5$
${}^{14}\text{N}^{5+}$	9.454 118 46(9)	0.006 428 723	-0.023(10)	9.438(10)	9.444	-0.006(10)	$\times 10^5$
${}^{16}\text{O}^{6+}$	2.313 121 264(21)	0.001 691 971	-0.0068(29)	2.308 0(29)	2.310	-0.0020(29)	$\times 10^6$
${}^{19}\text{F}^{7+}$	5.038 630 60(5)	0.003 681 211	-0.018(6)	5.024(6)	5.029	-0.005(6)	$\times 10^6$
${}^{20}\text{Ne}^{8+}$	1.003 642 572(9)	0.000 806 412	-0.0044(14)	1.000 1(14)	1.001	-0.0009(14)	$\times 10^7$

(4.43) and (4.44), in terms of the expansion parameter μ/M , are

$$G_x(\mu/M) = (\mu/M)C_x + (\mu/M)^2D_x + (\mu/M)^3E_x + \dots, \quad (4.58)$$

where $G_x(\mu/M)$ is a gauge-dependent function of the finite- and infinite-mass decay rates, the radiation emitted by the nucleus in the c.m. frame, and mass scaling. Next, three values of μ/M were used: μ/M itself, along with $10(\mu/M)$ and $20(\mu/M)$, to establish three equations for Eq. (4.58).

In what follows, although the analysis of the one- and two-photon decay cases are treated somewhat differently, both methods are sufficient to obtain the coefficients needed to test the algebraic relations. The acceleration gauge is not tested in this work.

One-photon decay

In the case of one-photon decay, a system of three linear equations, defined by writing out Eq. (4.58) for the three values of μ/M mentioned above, yielding a 3×3 system, was explicitly solved in order to include finite-mass effects up to order $(\mu/M)^3$ in the mass polarization power series. This procedure is carried out for successively larger basis sets according to Eq. (2.34) up to $\Omega = (i + j + k)_{\max} = 17$. These corrections contribute to the extent that the decay rates between the length and velocity gauges agree beyond the $(\mu/M)^2$ order or better than 1 part in 10^8 . The third-order coefficients are not displayed in Table 4.9.6, nor is the third-order algebraic equation, Eq. (4.57), tested (the decay rates do not presently agree well enough to warrant such a comparison); however, nonnegligible third-order contributions to lower-order coefficients C_x and D_x are explicitly considered by solving the 3×3 system defined by Eq. (4.58),

$$\begin{bmatrix} y & y^2 & y^3 \\ 10y & 10y^2 & 10y^3 \\ 20y & 20y^2 & 20y^3 \end{bmatrix} \begin{bmatrix} C_x \\ D_x \\ E_x \end{bmatrix} = \begin{bmatrix} G_x(y) \\ G_x(10y) \\ G_x(20y) \end{bmatrix}, \quad (4.59)$$

where $y = \mu/M$ and $x = p, r$ for the two gauges.¹⁹ The first- and second-order mass polarization power series coefficients that arise in treating one-photon decay in heliumlike ions are presented in Table 4.9.6. The results are calculated by averaging the largest basis sets and the standard deviation of these was taken to be the uncertainty. The coefficients of the mass polarization power series do converge with increasing basis set sizes, but not in a monotonic fashion as in the decay rates. Thus, the stated results and errors presented in Table 4.9.6 correspond to an average and standard deviation of the calculations from the several largest basis sets. The coefficients are shown to obey the algebraic relations in Eqs. (4.49) and (4.50).

The inclusion of third-order corrections made little difference for the singlet case;

¹⁹Solving the upper 2×2 system instead of the full 3×3 form in Eq. (4.59) leads to slightly different values for C_x and D_x , even though the uncertainty in E_x itself is very large and the $(\mu/M)^3$ relationship cannot be satisfied.

a larger difference was observed in the case of triplet decay, where it was necessary to include the E_x coefficients to satisfy the $(\mu/M)^2$ algebraic relation. This point is illustrated in the last two rows of Table 4.9.6 and is a consequence of the Pauli principle: for triplet states, the electron-electron correlation plays a smaller role and more accurate wave functions are obtained. Therefore, in the triplet case of one-photon decay, the coefficients, particularly $\{D_x\}$, are sensitive to the $(\mu/M)^3$ contributions.

Two-photon decay

The algebraic relations were derived for the first time and numerically tested for the case of two-photon decay $2\ ^1S - 1\ ^1S$ in heliumlike ions ($Z = 2 - 10$), along with the heavier μ -He, π -He, and \bar{p} -He. These results are reproduced in Table 4.9.7. Instead of solving the linear system described by Eq. (4.58), as in the one-photon case, iterative linear regressions are performed on this set of equations to obtain the mass polarization coefficients C_x and D_x . On the initial iteration, the C_x values are obtained by a linear regression assuming no $(\mu/M)^2$ contributions (i.e., $D_x = 0$). Then, using these C_x values, an updated equation is subject to linear regression to get the D_x coefficients. These updated D_x values are then used for a second regression to find C_x , and the process is repeated once more to update the D_x coefficients. This procedure is carried out for successively larger basis sets according to Eq. (2.34) up to $\Omega = (i + j + k)_{\max} = 17$. The slight disagreement in the $(\mu/M)^2$ relation for $Z = 2$ and 3 indicates that the rates between the gauges don't quite agree to order $(\mu/M)^2$. This is because $\mu/M \propto 1/Z$ and $Z = 2$ and 3 are the largest μ/M values considered.

We have both derived and numerically tested general algebraic relations that quantify the agreement between the length and velocity gauge for the general n -photon ($nE1$) finite-mass transition rate equations and tested them for heliumlike ions. The corresponding relationships between the length/velocity and acceleration gauge have also been derived. These relations are built on the postulate, initially put forward in Ref. [24], that the mass polarization component of the finite mass effect can be treated with a power series in μ/M . Eqs. (4.52–4.54) provide constitutive relations that can be used to account for finite-mass effects for $nE1$ transition rates. The

Table 4.9.6: Mass-polarization parameters C_x and D_x from Eq. (4.39) are shown for the one-photon decay processes in the indicated singlet and triplet He and He-like ions, along with the accompanying algebraic relations, Eqs. (4.55) and (4.56) for $n = 1$. For the triplet transition at the bottom of the table, $[\dagger]$ indicates third-order contributions (E_x terms) are included in the calculation and $[\ddagger]$ indicates they are omitted.

Ion	C_p	C_r	$C_p - C_r$	D_p	D_r	$2C_p + D_p - D_r$
$2^1P - 1^1S$						
^4He	-3.572719(1)	-1.57271(3)	-2.00000(3)	8.888(1)	2.73(2)	-0.99(2)
$^7\text{Li}^+$	-3.299929(3)	-1.299919(7)	-2.00001(1)	6.6723(8)	1.067(4)	-0.995(5)
$^9\text{Be}^{++}$	-3.061260(8)	-1.0612(2)	-2.0005(1)	5.3580(3)	0.232(6)	-0.997(6)
$^{11}\text{B}^{3+}$	-2.896567(5)	-0.89655(3)	-2.00002(4)	4.5986(4)	-0.194(5)	-1.000(6)
$^{12}\text{C}^{4+}$	-2.780462(2)	-0.78047(3)	-1.99999(3)	4.1215(2)	-0.439(2)	-0.999(2)
$^{14}\text{N}^{5+}$	-2.6952538(3)	-0.695250(4)	-2.000003(4)	3.800(1)	-0.61(2)	-0.98(2)
$^{16}\text{O}^{6+}$	-2.6304056(1)	-0.630403(2)	-2.000002(2)	3.5687(6)	-0.702(9)	-0.99(1)
$^{19}\text{F}^{7+}$	-2.579540(1)	-0.57953(1)	-2.000006(14)	3.3959(4)	-0.762(1)	-1.001(1)
$^{20}\text{Ne}^{8+}$	-2.5386356(1)	-0.538638(6)	-1.999996(6)	3.2618(8)	-0.812(4)	-1.002(5)
$2^3P - 2^3S$						
$^4\text{He} [\dagger]$	-7.609183(1)	-5.60918375(4)	-1.999999(1)	12.9523(2)	-1.266053(8)	-1.0000(2)
$^4\text{He} [\ddagger]$	-7.609191(1)	-5.60920948(3)	-1.999982(1)	12.9703(1)	-1.206957(4)	-1.0411(1)

prefactors in these equations can be used to convert infinite-mass transition rates calculated in any theoretical/computational framework to the corresponding finite-mass rates. Eqs. (4.55-4.57) are the corresponding algebraic relationships that test for gauge agreement to ensure that mass polarization effects are included correctly to a desired order in μ/M . These relations place tight constraints on theoretical calculations of finite-mass effects in $nE1$ transition processes, as demonstrated in the case of the spontaneous emission of heliumlike ions. They also test the leading infinite-mass term since an error here would carry through to the higher-order terms in μ/M .

Another approach to obtaining the coefficients $F_x(\mu/M)$ contained in Eqs. (4.52-4.54) is to treat the mass polarization term, $\nabla_{\rho_1} \cdot \nabla_{\rho_2}$, in Eq. (4.38) perturbatively in the parameter μ/M . This would provide a more direct, but also more computationally intensive, method for calculating the coefficients C_x, D_x, E_x, \dots of the successive powers of μ/M . Appendix G explores this approach; however, it is worth noting that the coefficients (C_x, D_x) , already calculated in Tables 4.9.6 and 4.9.7, satisfy the

Table 4.9.7: Mass-polarization parameters C_x and D_x from Eq. (4.39) are shown for two-photon $2\,{}^1S - 1\,{}^1S$ decay in He and He-like ions, along with the accompanying algebraic relations, Eqs. (4.49) and (4.50), for the metastable singlet transition indicated.

Ion	C_p	C_r	$C_p - C_r$	D_p	D_r	$4C_p + D_p - D_r$
${}^4\text{He}$	-5.2333588(30)	-1.23336(8)	-4.0000(8)	16.4344(10)	1.607(26)	-6.106(27)
${}^7\text{Li}^+$	-5.385078(8)	-1.385078(12)	-4.000000(17)	17.124(27)	1.95(32)	-6.37(35)
${}^9\text{Be}^{++}$	-5.487355(9)	-1.4871(5)	-4.0002(5)	17.799(7)	1.74(35)	-5.89(36)
${}^{11}\text{B}^{3+}$	-5.557584(1)	-1.5575(1)	-4.00008(13)	18.3518(12)	2.09(12)	-5.97(12)
${}^{12}\text{C}^{4+}$	-5.6094000(16)	-1.60943(13)	-3.99996(13)	18.8227(18)	2.47(14)	-6.08(14)
${}^{14}\text{N}^{5+}$	-5.64973214(24)	-1.649718(24)	-4.000014(24)	19.24196(29)	2.661(28)	-6.018(28)
${}^{16}\text{O}^{6+}$	-5.68233816(7)	-1.682327(12)	-4.000010(12)	19.61265(9)	2.903(16)	-6.020(16)
${}^{19}\text{F}^{7+}$	-5.7094498(5)	-1.70942(6)	-4.000025(61)	19.9487(8)	3.099(99)	-5.99(10)
${}^{20}\text{Ne}^{8+}$	-5.73247255(30)	-1.73249(3)	-3.99998(3)	20.2487(10)	3.40(10)	-6.08(10)

given algebraic relations up to order $(\mu/M)^2 \approx 10^{-8}$. A further improvement could be a more judicious selection of values for μ/M used to demonstrate numerically the algebraic relations. Currently, the actual μ/M value is used, along with both $10\times$ and $20\times$ this value; however, there is nothing particular about these choices and there is no need to use μ/M itself. Exploring the space of possibilities here would likely lead to a more convincing demonstration of the algebraic relations.

4.10 FUTURE WORK

The two most immediate extensions of this work, already mentioned at points during this chapter, would be to: (1) calculate relativistic²⁰ effects to the $2E1$ decay rate in Eq. (4.36); and (2) to apply the method of characterizing mass polarization to treat finite mass effects to other atomic processes. A third and more involved extension would be to extend the applicability of the methods and calculations developed herein to higher- Z atoms using the unified method of Drake [218].

²⁰Work on a manuscript on this topic is underway.

4.10.1 Inclusion of relativistic effects

For precision QED calculations [25, 219] to be compared with experiments, finite-mass effects are needed and the method in this chapter provides a systematic method for their inclusion. In the particular problem of two-photon decay, accurate comparison with experimental results [202] also requires a correct relativistic treatment—the finite-mass effects $\propto \mu/M$ and relativistic effects $\propto Z^2\alpha^2$, respectively, which are comparable ($\sim 10^{-4}$) in helium. This has been done previously, in Refs. [193] and [211], but a novel addition would be to add relativistic effects to the finite-mass effects discussed in this chapter, using Hylleraas basis sets, by a highly accurate perturbation calculation.

An obstacle in calculating relativistic corrections to the $2E1$ decay process is that the interaction with the QED vacuum contained in FGR contains negative energy states (cf. Appendix E). The success of variational techniques that use finite basis sets, such as those in this dissertation, rely on the variational minimum principle that ensures that we find the lowest upper bounds to the true NR energies (cf. section 2.6).²¹ There are two primary ways to proceed: (1) include relativistic effects from the start and add electron correlation as a perturbation; or conversely (2) include electron correlation from the start and then add relativistic and other higher-order effects perturbatively. In the first case, the Dirac equation is solved and then the electron correlation is taken as the perturbation. Ref. [211] used a relativistic configuration interaction (RCI) approach to the two-photon decay problem and their results are in Table 4.9.5.²²

In the latter case, known as nonrelativistic-QED (NRQED), the time-independent Schrödinger equation is solved using highly accurate Hylleraas basis functions that fully include electron correlation and relativistic and higher-order QED effects are added perturbatively.²³ It is only in the special case of few-electron ($N \leq 3$) systems

²¹In practice, these problems can be overcome by a few several approaches, summarized in Ref. [220].

²²Several additional methods have seen wide use over the years such as Dirac-Hartree-Fock, multiconfigurational-Dirac-Hartree-Fock, relativistic random-phase approximation.

²³See Chap. 5, which discusses the precise calculation tune-out frequency, for more details.

that an accurate NR calculation is even possible. Since the NR calculations are essentially exact for all practical purposes, as long as the operators needed to calculate these various higher-order effects are known, as is the case with the Breit operators which capture relativistic effects [40, p. 181], this method often outperforms the variational Dirac approaches in low- Z two- or three-electron systems.

What ultimately determines the choice between the two methods is which method will have a more precise value for a given Z . Generally, a “crossing point” occurs around $Z = 27$ —values below which the NRQED method is more precise and above which methods like RCI that start with the Dirac equation will be more precise [221]. As such, the set of $Z \leq 10$ studied here are excellent candidates for the NRQED approach and will yield more accurate decay rates than that of the RCI approach of Derevianko and Johnson [211].

Goldman and Drake developed a relativistic Sturmian formulation [222] and soon thereafter demonstrated [210] that in the relativistic contributions to the one-electron $2E1$ decay rate vanish to order $(\alpha Z)^2$ in the *length gauge*. More importantly, the dipole matrix elements that comprise the calculation are given with an adjustable, continuous gauge parameter G , with the choices $G = 0$ and $G = \sqrt{2}$ yielding the velocity and length gauges, respectively, in the nonrelativistic limit [206].

Since the interaction energy form $U^{(2)}$ is the same for the two-electron case, the strategy is to derive the relativistically perturbed interaction energy, similar to Ref. [25], but to use the equivalent nonrelativistic operators chosen such that their contribution from negative energy states vanishes at the order of relativistic corrections. Work is in progress on the problem of establishing an equivalent one-electron nonrelativistic $E1$ operator²⁴ in the length gauge, where we reduced a general formula [224] to a specific form for the one-electron case and were able to show equivalence to the one-electron Dirac Sturmian result of Ref. [210]. This has been done in the velocity gauge by Sami [225], where additional spin-dependent corrections arise. Once the relationship is established for the $\text{He}^+(2s)$ decay, the methodology can be carried

²⁴The Breit-Pauli corrections to the Hamiltonian and wave functions are well-understood; however, relativistic corrections to the dipole operator itself that arise from the Foldy-Woutheyson transformation [223] must also be accounted for.

over to the two-electron case.

4.10.2 Extend to additional structure problems

The formalism developed here for treating the mass polarization component of the finite-mass effect in the calculation of $nE1$ transition rates in heliumlike ions could be extended to other atomic processes, which are in general proportional to matrix elements and energy differences raised to some power. The form of the resulting algebraic relations would be different from those presented here for other $nE1$ processes, depending on the form of the quantity being calculated; however, they would still serve as a theoretical check between calculations in the velocity and length gauges and would be derived in the same way as presented here and in Ref. [24]. In calculations of stimulated emission, absorption, and photoionization [219, 226], the same algebraic relations would apply as for spontaneous emission, but the numerical values of the C_x , D_x etc. coefficients would be different. One possible application would be to the study of Feshbach resonances [226].

4.10.3 Extension to highly charged heliumlike ions

Finite-mass effects diminish with the higher atomic number Z but nevertheless must be accurately accounted for in precise comparisons between experiment and theory [202]. The dominant coupling scheme for two-electron systems shifts from LS to jj around $Z \approx 26$, requiring different methods to be deployed in calculating relativistic contributions. The nonrelativistic approach described in this chapter addresses the low- Z region, and relativistic effects can be added perturbatively, while methods like RCI [211] are typically used to provide accurate decay rates at high- Z . These methods can be unified for general $nE1$ decay processes using the method developed by Drake [218], successfully applied to heliumlike sequences up to $Z = 100$ [227].

CHAPTER 5

Testing QED with the Tune-out Frequency in Helium

5.1 OVERVIEW

This chapter details a joint theoretical-experimental effort¹ to test QED by comparing measurements and calculations of the ~ 726 THz tune-out frequency of the 2^3S_1 state of helium. The tune-out frequency is the frequency at which an atom ceases to interact with an incident laser light. The tune-out frequency is a completely independent test of QED than the traditional experiments which measure atomic energy levels. In our work, we have reformulated the problem as a zero in the coherent Rayleigh scattering cross section, allowing for the calculation of retardation effects that arise due to the finite velocity of light. This is the first calculation of the tune-out frequency that is sensitive to these effects, building off of Pachucki and Puchalski's [228] calculation of the dynamic polarizability of helium. We are able to resolve QED effects at the 30σ level and retardation effects at the 2σ level.

In Appendix E, the problem of coherent Rayleigh scattering (RSCS), the topic of this chapter, was observed to be very similar to that of two-photon transitions, which were discussed in Chap. 4. This is yet another of a growing list of atomic physics problems where pseudospectral methods are used to represent a complete set of states. In this chapter, we use pseudospectra to treat perturbations in second

¹While essential for completeness and thematic development, this material represents a smaller portion of my research contributions. Thus, this chapter is shorter, reflecting the scope of my involvement in this project.

order, capturing QED transitions with the vacuum, and we also use them in first-order perturbation theory to treat relativistic and QED corrections.

The content of the chapter is as follows. Section 5.2 provides the background for the tune-out frequency as a test of QED. Then, Sec. 5.3 defines the tune-out frequency and explains why we specifically chose the ~ 726 THz tune-out in 2^3S_1 . Section 5.4 then briefly explains the experiment and discusses the largest sources of uncertainty. The theoretical formulation is then expounded in Sec. 5.5, following which the overall results are presented and discussed in Sec. 5.6. Lastly, future work is mentioned in Sec. 5.7.

5.2 MOTIVATION

As outlined in the Introduction and investigated in Chap. 3, a major theme of present-day physics, including atomic physics, is the search for new physics (NP) beyond the Standard Model (SM). One sector under intense scrutiny is QED [8, 229] due to continual improvements in high-precision experiments and theory. Advances in laser spectroscopy now resolve QED contributions, and in two-electron systems, improvements in variational techniques [229] and QED operators [230–233] enable precise theory/experiment comparisons. As discussed in the Introduction, many QED tests rely on precise energy measurements from spectroscopy, including the proton radius puzzle and other Lamb shift measurements. Discrepancies between theoretical QED values and observations signal NP. Precise QED calculations also determine physical quantities like the nuclear radius of helium isotopes with halo nuclei [234–237], such as ${}^6\text{He}$ discussed in Chap. 3.

Common to all of the aforementioned examples is that they compare energy measurements and calculations to probe QED. Energies are expectation values, i.e., diagonal matrix elements of the Hamiltonian matrix. Comparison of quantities other than energies, such as lifetimes and transition rates, are generally much less accurate than energy measurements. For instance, in Ref. [238], the transition rate ${}^3P_1 - {}^1S_0$ was measured to only 4.5% accuracy. Measurements such as this test off-diagonal matrix

elements. The dynamic polarizability $\alpha_d(\omega)$, a quantity proportional to the energy shift² an atom experiences in an optical field of frequency ω with $\hat{\mathbf{z}}$ polarization, is defined in the nonrelativistic limit to be [148, p. 256]

$$\alpha_d(\omega) = \sum_n |\langle i | z | n \rangle|^2 \left(\frac{1}{\Delta E_n + \hbar\omega} + \frac{1}{\Delta E_n - \hbar\omega} \right), \quad (5.1)$$

with matrix elements between the state in question, $|i\rangle$, and all other states, $\{|n\rangle\}$, must be computed.

These tests, therefore, offer not only an alternative, completely independent approach to testing QED, but are much more constrained in that the line strength of every transition in the atomic spectrum, bound and continuum, contributes to this quantity. In fact, the polarizability—both the dynamic case shown above and the static case—have been of significant interest in the determination of several standards and constants, including the pressure [239] and temperature [240] standards, which can be written in terms of the index of refraction [241]. The index of refraction, in turn, can be calculated using very precise values of the dipole polarizability [242]. In fact, in recently calculating the index of refraction, Pachucki and Puchalski demonstrated that the dipole polarizability formulation does not account for retardation effects [228]. The index of refraction ultimately considers how plane waves of light propagate through disordered media, and the slowing effect is due to scattering. The process that should be considered is not polarizability but rather the Rayleigh forward scattering amplitude—the photon nature of light is relevant to this process [228]. We turn our attention towards the frequencies at which these quantities vanish: the tune-out frequencies, i.e., zeroes in the Rayleigh scattering cross section.

²The energy shift ΔE that an atom experiences in an optical field with electric field strength F , is related to the dynamic polarizability via $\Delta E \approx -\frac{1}{2}\alpha_d(\omega)F^2$. The relation is approximate as there are higher-order polarizabilities that contribute as well in the exact relation.

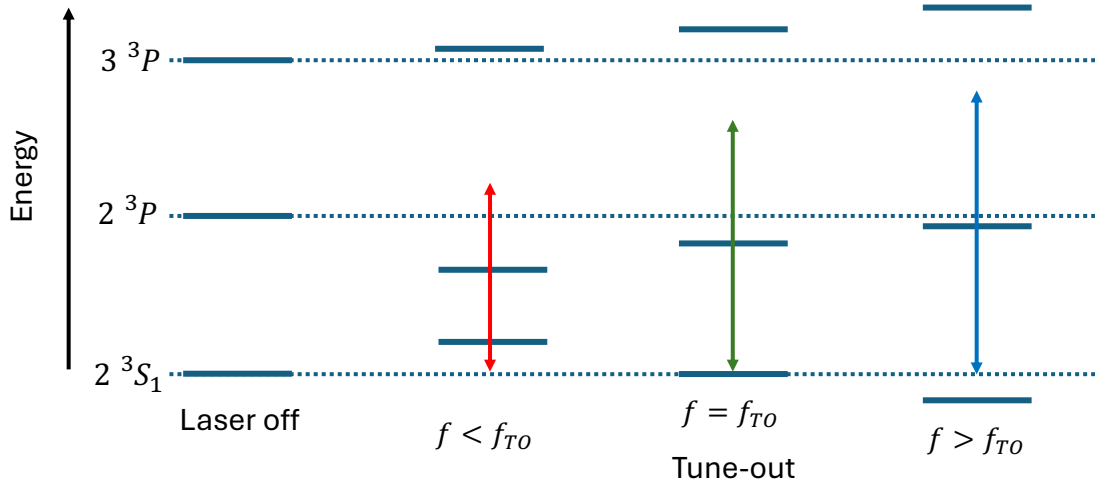


Fig. 5.3.1: The level shifts for the 2^3S_1 state and the $2^3P / 3^3P$ manifolds are shown for the cases of (left to right) no laser light, and then for light of frequency less than, equal to, and greater than the tune-out frequency. The noteworthy feature of incident light at the tune-out frequency is that the energy shift in the 2^3S_1 vanishes.

5.3 THE TUNE-OUT FREQUENCY

The tune-out frequency, or equivalently, the tune-out wavelength, is essentially the frequency/wavelength of an optical field incident upon a system (an atomic system in our discussion) where the system ceases to *interact* with the applied field. Figure 5.3.1 demonstrates the situation for a helium atom prepared in its metastable 2^3S state. At the tune-out frequency, f_{TO} , the energy level shift cancels—a remarkable zero since it is the result of the sum of an infinite number of terms.

As mentioned above, there are two alternative physical interpretations³ of this phenomenon that are equivalent in lowest order but lead to different higher-order corrections. The experimental conditions determine which of these pictures is correct. This was discussed by Drake *et al.* [217] for the case of the tune-out frequency of helium prepared in its metastable 2^3S state—the configuration with which we are concerned in this chapter.

The first formulation of the tune-out frequency arose in the context of creating optical lattices to selectively trap one type of atom in ultracold experiments involving

³The mathematical details of the two interpretations will be addressed in the following section discussing the NRQED formalism.

multiple atomic species.⁴ Here, LeBlanc and Thywissen developed a scheme⁵ where the trapping wavelength of the optical trap was chosen to lie between two manifolds of one of the two atomic species, such that the induced dipole moment in that species, and thus the level shift, is zero. This situation is illustrated in Figs. 5.3.2 and 5.3.3 for the case of He(2^3S). The effect of this is that this species is no longer trapped, i.e., they achieved species selective trapping. Within an optical lattice, the appropriate formalism is to consider the dynamic polarizability, since the potential is fixed in space and oscillates in time and the atom's position relative to the nodes of this potential determines the interaction [217].

The tune-out experiment consists of a magnetically trapped Bose-Einstein condensate of metastable He(2^3S_1) atoms subjected to a probe beam that is a travelling transverse plane wave. In this second formulation, the photon nature of the interaction must be considered for higher-order effects, including retardation effects. Due to this, the proper physical picture for this *interaction* is the point at which the atom ceases to scatter light: the frequency at which the Rayleigh scattering cross section (RSCS) vanishes [217].

5.3.1 Suitability of the tune-out frequency for testing QED

The tune-out frequency is an excellent nonenergy candidate for studying QED that was first pointed out by Mitroy and Tang in 2013 [244]. Experimentally, it is advantageous because it constitutes a null measurement that does not require careful calibration of light intensity or beam profile. Furthermore, unlike other experiments that test QED, measuring excitation probabilities is not required here.⁶

The metastable state of helium has an exceptionally long lifetime (approximately 8000s) relative to typical atomic transition timescales ($\sim 10^{-9}$ s), making it ideal for trapping and probing. It is also well-situated with respect to the energy level scheme of

⁴A landmark dual-species result involved observing the Fermi pressure in a fermion-boson $^6\text{Li}/^7\text{Li}$ mixture [243].

⁵This experiment focused on binary mixtures ultracold alkali-metal atoms such as Li-Cs, K-RB, etc.

⁶Measuring direct transitions, such as the 2^3S_1 – 3^3S_1 transition in helium [245], or lifetimes, require measurement of excited state populations [246].

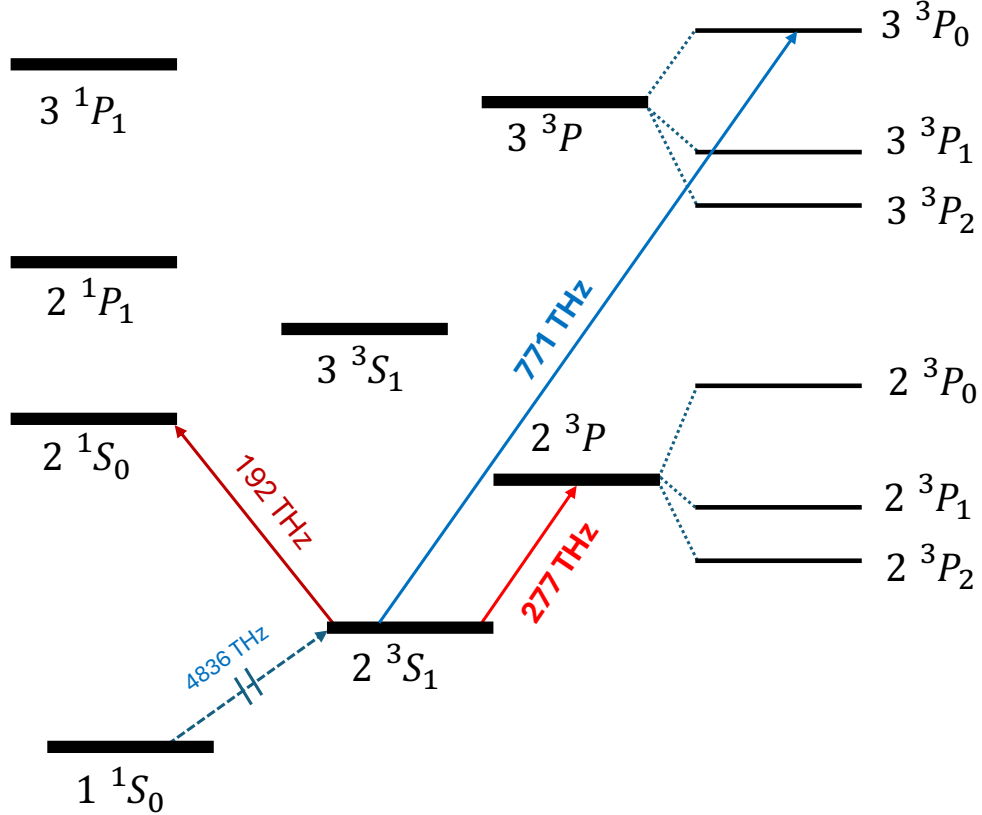


Fig. 5.3.2: Partial energy level diagram of ${}^4\text{He}$, showing in particular the relevant transitions between the 2^3S_1 state and the $2^3P/3^3P$ manifold, between which the tune-out frequency occurs. The tune-out frequency studied in this work is very near 726 THz, below the 771 THz transition to 3^3P shown in blue. Not drawn to scale—the splittings are greatly exaggerated in this drawing.

helium for measuring the tune-out property. Of the infinite set of tune-out frequencies for the $\text{He}(2^3S_1)$ atom, the $f_{\text{TO}} \approx 726$ THz is the best choice. As shown in Fig. 5.3.3, the $f_{\text{TO}} \approx 726$ THz is well separated from resonances, making it possible to actually measure it without having the signal partially masqueraded by the sharp effects seen near the resonances. Further, the gradient of the induced energy shift with respect to the applied frequency, $\frac{d\alpha}{df}$, is very small here compared to alternative decays [244]. This is a result of the fact that the two closest transitions (2^3S_1 – 2^3P and 2^3S_1 – 3^3P) are separated by more than a factor of two in frequency. Therefore, for this tune-out, the negative contributions to the RSCS due to 2^3S_1 – 2^3P transitions are mostly balanced by the positive 2^3S_1 – 3^3P contributions.⁷

⁷The higher 2^3S_1 – n^3P with $n > 3$ contributions are also positive, but relatively small.

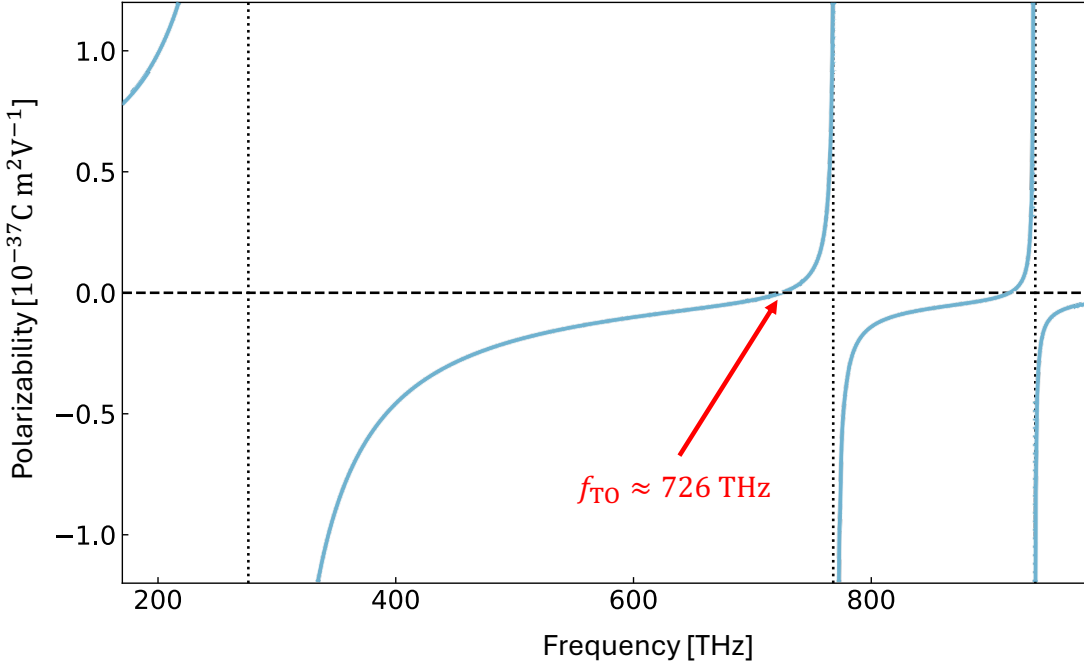


Fig. 5.3.3: This curve displays the dynamic polarizability as a function of the frequency of the applied laser light. The discontinuities occur when the laser is in resonance with transitions between the (from left to right) $2\ ^3S$ and $n = 2, 3, 4\ ^3P$ manifolds. Between these discontinuities, the polarizability must pass through zero—these are the so-called tune-out frequencies. For reasons that are explained in the text, it is the tune-out (f_{TO}) around 726 THz, indicated by the red arrow, that is studied presently to test QED. Each vertical line stands for the spin-orbit-split manifold and contains additional tune-outs that are not useful since their contributions are completely dominated by the states within the manifold and adhere to 1:3:5 geometric considerations [244].

In summary, the tune-out frequency is an ideal property to test QED independent of energy shifts. Clearly, the $2\ ^3S_1$ state of helium has excellent properties that make this a candidate for precise and reliable measurement and calculations—which will now be discussed in turn.

5.4 BRIEF OVERVIEW OF THE EXPERIMENT

The experiment was carried out by the He* BEC group at the Australian National University; here, we touch on the most salient details. This section thus contains a brief overview of the experiment itself and also a commentary on the most significant sources of systematic error. Complete information can be found in the manuscript

and accompanying supplementary materials that this chapter is based on [25], or in even more detail in Ref. [247].

The central idea is to subject helium atoms, prepared in the $2^3S_1(M_J = 1)$ state, to a freely propagating, frequency-tunable pulsed laser beam and determine the point at which they cease to scatter photons—in this experiment, we measured the frequency at which the optical dipole potential vanished. The mechanism for performing the tune-out measurement was the trap oscillation method. The magnetic trap forms a sinusoidal oscillation with a trapping frequency of Ω_{trap} . Then, the probe laser interacts with the trapped BEC with frequency f . Its Gaussian optical potential, approximately harmonic, results in a response frequency Ω_{probe} . Atoms are outcoupled and their net oscillation frequency, Ω_{net} , corresponding to $\Omega_{\text{net}}^2 = \Omega_{\text{probe}}^2 + \Omega_{\text{trap}}^2$ is measured by plotting their velocities. Upon measuring Ω_{trap} separately, the above formula gives an expression for Ω_{probe}^2 , which itself is a function of the frequency of the probe laser frequency f . It turns out that Ω_{probe}^2 is proportional to the RSCS according to $\Omega_{\text{probe}}^2 \propto \alpha(f)I$, with I the intensity of the probe beam, and thus it is zeroes in the Ω_{probe}^2 vs. f graph that yield $f = f_{\text{TO}}$.

Table 5.4.1 shows the different contributions to the measured tune-out frequency, including systematic effects and their uncertainties. We discuss only the largest of these: beam polarization. This experiment requires accurate measurement of the beam polarization when it interacts with the helium atoms. This is not possible, however, since this interaction takes place inside the vacuum system where the beam polarization is not measured. The beam polarization was measured immediately before it enters and after it exits the chamber, though it could have slightly changed during its passing through the vacuum. The birefringence of the vacuum windows and the non-uniformity of the beam polarization across the beam are the effects that carry the largest uncertainty budget associated with this.

Table 5.4.1: Contributions to the measured tune-out frequency with their systematic uncertainties. The 40 MHz uncertainty in the measurement itself, however, is a statistical uncertainty. The polarization is the largest contribution to the experimental uncertainty budget.

Term	Estimate (MHz)	Uncertainty (MHz)
Measured Value	725 736 810	40
Polarization		
- Birefringence	-100	200
- Beam Anisotropy	0	150
Method Linearity	24	30
Hyperpolarizability	-30	50
Broadband Light	0	30
DC Electric field	0	$\ll 1$
Wave-meter	0	4
Mean-Field	0	$\ll 1$
Total	725 736 700	260

5.5 THEORETICAL FORMULATION

5.5.1 Consequence of linear polarization of probe beam

Before unravelling the details of the calculation, it must be clear exactly what we have calculated. In principle, the tune-out frequency, f_{TO} , corresponds to a zero in the multicomponent field RSCS, $\alpha(f_{TO}) = 0$. The RSCS is a multicomponent field that contains scalar, vector and tensor components that depend on the degree of linear and circular polarization of the probe beam in the atom's reference frame. With arbitrary polarization, for the $2^3S_1(M_J = 1)$ state, this results in a tune-out frequency with scalar (S), vector (V), and tensor (T) components defined by:

$$f_{TO}(\mathcal{Q}_A, \mathcal{V}) = f_{TO}^S + \frac{1}{2}\beta^V \cos(\theta_k) \mathcal{V} - \frac{1}{2}\beta^T \left[3 \sin^2(\theta_k) \left(\frac{1}{2} + \frac{\mathcal{Q}_A(\mathcal{Q}_L, \theta_L)}{2} \right) - 1 \right], \quad (5.2)$$

where \mathcal{Q}_A and \mathcal{V} are the second and fourth Stokes parameters, respectively, and θ_k is the angle between the laser propagation direction and the magnetic field vector; β^V and β^T are the vector and tensor polarizabilities divided by the gradient of the scalar

RSCS at the tune-out frequency. $\mathcal{Q}_{\mathcal{L}}$ and $\theta_{\mathcal{L}}$, are the laboratory measured second Stokes parameter and the angle between the lab and atomic frames, respectively.

If the laser has a linear polarization that is perpendicular to the laser propagation and the magnetic field, then $f_{TO}(\mathcal{Q}_{\mathcal{A}}, \mathcal{V})$ simplifies to $f_{TO}(-1, 0)$, corresponding to a RSCS

$$\alpha(f) = \alpha^S(f) - \frac{1}{2}\alpha^T(f). \quad (5.3)$$

It is this quantity which is interrogated in the comparison between experiment and theory.⁸

5.5.2 Nonrelativistic RSCS or dynamic polarizability

For a system defined in NR-order by $H_0|\psi\rangle = E_0|\psi\rangle$, with H_0 the field-free Hamiltonian, subject to an optical field of frequency $\omega = 2\pi f$, and in initial state ψ_0 , the resolvent operator is

$$\mathcal{R}(\omega) = Q(H_0 - E_0 + \hbar\omega)^{-1}Q, \quad (5.4)$$

with projection operator $Q = 1 - |\psi_0\rangle\langle\psi_0|$. With these definitions, the frequency-dependent dipole polarizability can be written as

$$\bar{\alpha}_d(\omega) = \frac{1}{2}[\alpha_d(\omega) + \alpha_d(-\omega)] \quad (5.5)$$

where $\alpha_d(\pm\omega)$ given by

$$\alpha_d(\pm\omega) = 2\langle\psi_0|\hat{\mathbf{e}} \cdot \mathbf{r}\mathcal{R}(\pm\omega)\hat{\mathbf{e}} \cdot \mathbf{r}|\psi_0\rangle \quad (5.6)$$

where $\hat{\mathbf{e}}$ is the polarization of the incident field and $\mathbf{r} = \mathbf{r}_2 + \mathbf{r}_2$.

A complete set of discrete pseudostates, via Q in the resolvent operator in Eq. (5.4),

⁸The experiment actually measured $f_{TO}(\mathcal{Q}_{\mathcal{A}}, \mathcal{V})$ for many polarizations and probe frequencies and performed interpolations to obtain $f_{TO}(-1, 0)$, using only the sign of β^T from theory. The rationale for not using Eq. (5.2) is simply that the direction of the magnetic field—a quantity needed on the theory side if Eq. (5.2) is used—could not be measured to sufficient precision. $f_{TO}(-1, 0)$ is independent of this quantity.

can be inserted to evaluate Eq. (5.6):

$$\bar{\alpha}_d(\omega) = e^2 \sum_n |\langle \psi_0 | \hat{e} \cdot \mathbf{r} | \psi_n \rangle|^2 \left(\frac{1}{E_n - E_0 + \hbar\omega} + \frac{1}{E_n - E_0 - \hbar\omega} \right). \quad (5.7)$$

Thus, any time the resolvent operator $\mathcal{R}(\omega)$ appears in the expression, a pseudospectrum is used to represent the complete set of states. In our calculation, summarized in the following section in Table 5.6.1, the finite-nuclear-mass effects are included by using the appropriate Hamiltonian H_0 where M remains finite.

5.5.3 NRQED formulation of the tune-out frequency

In order to test QED, higher-order effects, beginning with relativistic effects, must be systematically included in the calculation. Our approach is similar to that of Refs. [219, 241, 242]. Higher-order relativistic and QED effects are added perturbatively to Eq. (5.6), yielding (2+1)-order corrections according to

$$\delta\alpha_d^{\hat{X}}(\omega) = 2\langle \psi_0 | [2\hat{e} \cdot \mathbf{r} \mathcal{R}(\omega) \hat{e} \cdot \mathbf{r} \mathcal{R}(\omega) \hat{X} + \hat{e} \cdot \mathbf{r} \mathcal{R}(\omega) (\hat{X} - \langle \hat{X} \rangle) \mathcal{R}(\omega) \hat{e} \cdot \mathbf{r}] | \psi_0 \rangle, \quad (5.8)$$

where, \hat{X} stands for each relativistic or QED perturbation operator, and $\langle \hat{X} \rangle$ is its expectation value. The polarizability/RSCS expression is already a second-order perturbation and is further perturbed with respect to the effects in question. In two-electron problems, this method is a great choice [229] since Hylleraas pseudostates can be used to generate extremely accurate NR wave functions;⁹ for example, Petrimoulx *et al.* recently calculated the NR ground state energy and wave functions of H^- to 27 and 14 figures, respectively [47].

The tune-out frequency for S -states, which are considered here, is the zero of the

⁹Manalo showed [248] that the NRQED method with Hylleraas basis states used here agrees, up to relativistic order, for the calculation of the frequency-dependent polarizability with earlier calculations [242] that used “Slater germinals” comprised of all-exponential basis functions.

total polarizability/RSCS whence all of these corrections are added in [228]:

$$|\mathbf{E}|^2 \left[\bar{\alpha}_d(\omega) + \sum_{\hat{X}} \delta \bar{\alpha}_d^{\hat{X}}(\omega) + \delta \bar{\alpha}_d^{\partial \varepsilon \ln k_0}(\omega) + \delta \bar{\alpha}_{d,\text{ret}}(\omega) \right] + |\mathbf{B}|^2 [\chi + \delta \chi_{\text{ret}}(\omega)] = 0, \quad (5.9)$$

where \mathbf{E} and \mathbf{B} are the fields of the laser, χ is the magnetic susceptibility, and $\delta \bar{\alpha}_d^{\partial \varepsilon \ln k_0}(\omega)$ is a further QED effect arising from the second-order perturbation of the Bethe logarithm due to the electric field of the laser; $\delta \alpha_{d,\text{ret}}$ and $\delta \chi_{\text{ret}}$ are retardation corrections.

5.5.4 Relativistic corrections

The nonzero¹⁰ relativistic corrections arise from the nonrelativistic reduction of the Dirac equation, and the Pauli form of the Breit interaction at order α^2 are given (in SI units) by [40, p. 181]

$$H_1 = -\frac{(p_1^4 + p_2^4)}{8m^3c^2} \quad (5.10)$$

$$H_2 = -\frac{e^2}{2(mc)^2 r_{12}} \left[\mathbf{p}_1 \cdot \mathbf{p}_2 + \frac{\mathbf{r}_{12} \cdot (\mathbf{r}_{12} \cdot \mathbf{p}_1) \mathbf{p}_2}{r_{12}^2} \right] \quad (5.11)$$

$$H_4 = \pi(\alpha e a_0)^2 [Z \delta^3(\mathbf{r}_1) - \delta^3(\mathbf{r}_{12})] \quad (5.12)$$

$$H_5 = \frac{4\mu_0^2}{r_{12}^3} \left[\mathbf{s}_1 \cdot \mathbf{s}_2 - \frac{3(\mathbf{s}_1 \cdot \mathbf{r}_{12})(\mathbf{s}_2 \cdot \mathbf{r}_{12})}{r_{12}^2} \right] \quad (5.13)$$

where $\mu_0 = \frac{e\hbar}{2mc} (1 + \frac{\alpha}{2\pi} + \dots)$ is the Bohr magneton and $\alpha \simeq 1/137.03599906$ is the value used fine structure constant. The relativistic kinetic energy (H_1), the orbit-orbit interaction (H_2), and the Darwin term (H_4) are spin-independent terms, while the spin-spin term (H_5) is spin-dependent and itself accounts entirely for the tensor component $\alpha^T(f)$ in Eq. (5.3).

¹⁰The spin-orbit and spin-other-orbit terms of the Breit interaction vanish when summed over the fine-structure splittings of the intermediate P -states—if they are regarded as degenerate, which they can be in this limit. Also, the portion of the spin-spin term, H_5 , proportional to $\delta(r_{12})$, vanishes due to the Pauli exclusion principle—since these are triplet states.

5.5.5 QED corrections

The leading QED operators (in atomic units) are [249]

$$\hat{X}_{\text{QED}}^{(3)} = \alpha^3 \left\{ \frac{4Z}{3} \left(\frac{19}{30} - \ln \alpha^2 - \ln k_0 \right) [\delta^3(\mathbf{r}_1) + \delta^3(\mathbf{r}_2)] - \frac{7}{6\pi} \left(\frac{1}{r_{12}^3} \right)_{\text{P.V.}} \right\} \quad (5.14)$$

and

$$\begin{aligned} \hat{X}_{\text{QED}}^{(4)} = \alpha^4 \pi & \left[\left(\frac{427}{96} - 2 \ln 2 \right) Z^2 + \left(-\frac{9\zeta(3)}{4\pi^2} - \frac{2179}{648\pi^2} + \frac{3 \ln 2}{2} - \frac{10}{27} \right) Z \right] \\ & \times [\delta^3(\mathbf{r}_1) + \delta^3(\mathbf{r}_2)], \end{aligned} \quad (5.15)$$

where $\ln k_0$ is the Bethe logarithm, $\left(\frac{1}{r_{12}^3} \right)_{\text{P.V.}}$ is the principal value of the divergent integral given by

$$\left(\frac{1}{r_{12}^3} \right)_{\text{P.V.}} = \lim_{\epsilon \rightarrow 0} r_{12}^{-3}(\epsilon) + 4\pi(\gamma + \ln \epsilon)\delta(\mathbf{r}_{12}), \quad (5.16)$$

with ϵ the radius of a small sphere about $r_{12} = 0$ that is omitted from the range of integration and γ is Euler's constant. $\zeta(z)$ is the Riemann zeta function. The third-order QED contribution listed above contains Araki-Sucher terms, while the fourth-order term contains radiative contributions [250, 251].

The remaining nonradiative contributions were taken as the dominant source of theoretical uncertainty (cf. Table 5.6.1)—these were estimated to be 6 MHz, i.e., about 5% of the magnitude of the radiative terms [232, 241]. This is, in fact, the dominant source of uncertainty, not only for the QED part but for the entire theoretical calculation.

Another very small QED contribution comes from the second-order electric field perturbation to the Bethe logarithm—the term in the tune-out condition expressed in Eq. (5.9). This correction is equal to

$$\delta\bar{\alpha}_d^{\partial_{\mathcal{E}}^2 \ln k_0}(\omega) = \frac{8}{3} \alpha^3 \partial_{\mathcal{E}}^2 \ln k_0 \langle \psi | \delta^3(\mathbf{r}_1) + \delta^3(\mathbf{r}_2) | \psi \rangle, \quad (5.17)$$

and $\partial_{\varepsilon}^2 \ln k_0 = 0.048\,557\,2(14)a_0^3$ was calculated in Ref. [219]. Drake and Yan [252] argued that this value comes entirely from the inner $1s$ electron and can thus be taken to be the value for any excited or singly ionized state of He to an accuracy of about 1%. For $\omega \lesssim 1$ this correction will not differ significantly from the static case calculated in Ref. [219].¹¹ The value used for $\partial_{\varepsilon}^2 \ln k_0$ in the present work is $0.049(1)a_0^3$, which contributes at the negligible level of $\delta\bar{\alpha}_d^{\partial_{\varepsilon}^2 \ln k_0} \approx 0.18 \times 10^{-6}$ a.u. to the RSCS corresponding to a correction $\delta\omega_{\text{TO}} \simeq 0.124(3)$ MHz to the tune-out frequency.

5.5.6 Magnetic susceptibility

The magnetic susceptibility is a frequency-independent quantity defined by [253, 254]

$$\chi = -\frac{\alpha^2 a_0}{4} \left\langle \sum_{i=1}^2 (\mathbf{r}_i \times \hat{\mathbf{B}})^2 \right\rangle = -\frac{\alpha^2 a_0}{6} \left\langle \sum_{i=1}^2 r_i^2 \right\rangle, \text{ for S-states,} \quad (5.18)$$

where $\hat{\mathbf{B}}$ denotes a unit vector. The expectation value $\langle r_1^2 + r_2^2 \rangle$ is $22.928644a_0^2$ for the 2^3S_1 state of helium, yielding a correction of 188 MHz.

5.5.7 Retardation corrections

Retardation corrections were recently derived by Pachucki and Puchalski [228] for the first time in treating the interaction of laser light incident upon a medium of helium atoms as part of an investigation of the refractive index of helium gas. Prior to their work, for instance, in Ref. [242], this problem was treated as a zero in the dynamic polarizability—a strategy that must be reformulated in order to properly account for retardation corrections. It is in these corrections that the difference in the physical circumstances makes a difference in the calculation. For an atom in the presence of a freely propagating laser beam, we expect retardation corrections that arise from finite wavelength properties of light. For this, the correct theoretical formulation of the vanishing interaction is as a zero in the RSCS, not the dynamic polarizability. This introduced by Drake *et al.* [217] for the tune-out problem and is explained in

¹¹The calculation in Ref. [219] used $\langle \psi | \delta^3(\mathbf{r}_1) + \delta^3(\mathbf{r}_2) | \psi \rangle = 3.620\,858\,63(1)$.

Appendix E.

Ref. [228] defines the generalized polarizabilities (all in units of a_0^5 except α_0 which is in units of a_0^3) as

$$\alpha_0(\omega) = \frac{e^2}{3} \sum_{a,b} \langle r_a^k \mathcal{R}(\omega) r_b^k \rangle \quad (5.19)$$

$$\alpha_1(\omega) = \frac{e^2}{3} \sum_{a,b} \langle (r_a^k r_a^l)^{(2)} \mathcal{R}(\omega) (r_b^k r_b^l)^{(2)} \rangle \quad (5.20)$$

$$\alpha_2(\omega) = \frac{e^2}{3} \sum_{a,b} \langle r_a^k \mathcal{R}(\omega) r_b^k r_b^2 \rangle \quad (5.21)$$

$$\alpha_3(\omega) = \frac{2i\hbar e^2}{3m} \sum_{a,b} \langle r_a^k \mathcal{R}(\omega) \mathcal{R}(\omega) i(\mathbf{L}_b \times \mathbf{r}_b - \mathbf{r}_b \times \mathbf{L}_b)^k \rangle \quad (5.22)$$

$$\alpha_4(\omega) = \frac{e^2}{3} \sum_{a,b} \langle r_a^2 \mathcal{R}(\omega) r_b^2 \rangle, \quad (5.23)$$

where the a and b sums are over the electronic coordinates 1 and 2, and a sum over the repeated Cartesian vector components k and l is assumed. Also, $(r^k r^l)_a^{(2)} \equiv r^k r^l - \delta_{kl} r^2/3$ is the quadrupole moment operator.

The above definitions differ by a factor of 2/3 from those in Ref. [228] so that here $\alpha_0(\omega) \equiv \alpha_d(\omega)$, and $\alpha_1(\omega)$ corresponds to the standard definition of the quadrupole polarizability [255]. Further, $\alpha_2(\omega)$ corresponds to finite-wavelength corrections, $\alpha_3(\omega)$ contains relativistic corrections to the dipole transition operator [224], and the $\alpha_4(\omega)$ term is magnetic in origin which cancels in the final analysis. For each term, the above bar notation applies: $\bar{\alpha}_i(\omega) = \frac{1}{2}[\alpha_i(\omega) + \alpha_i(-\omega)]$. The retardation corrections to the polarizability α_0 and diamagnetic coupling χ are then

$$\bar{\alpha}_{\text{ret}}(\omega) = \frac{3k^2}{2} \left(\frac{\bar{\alpha}_1(\omega)}{15} - \frac{2\bar{\alpha}_2(\omega)}{15} + \frac{\bar{\alpha}_4(\omega)}{18} \right), \quad (5.24)$$

$$\bar{\chi}_{\text{ret}}(\omega) = \frac{3k^2}{2} \left(\frac{\bar{\alpha}_1(\omega)}{60} + \frac{4\bar{\alpha}_2(\omega)}{45} + \frac{\bar{\alpha}_3(\omega)}{9} - \frac{\bar{\alpha}_4(\omega)}{18} \right), \quad (5.25)$$

where $k = \omega/c$. This yields a total retardation correction of

$$\bar{\alpha}_{\text{ret}}(\omega) + \bar{\chi}_{\text{ret}}(\omega) = \frac{3k^2}{2} \left(\frac{\bar{\alpha}_1(\omega)}{20} - \frac{2\bar{\alpha}_2(\omega)}{45} + \frac{\bar{\alpha}_3(\omega)}{9} \right) \quad (5.26)$$

contributing a total retardation correction of -477 MHz. These contributions include relativistic—but not QED—corrections to the dipole transition operator.

The smallest correction was to account for finite nuclear size. In Ref. [256], the operator $\frac{4\pi}{3}r_{^4\text{He}}^2[\delta^3(\mathbf{r}_1) + \delta^3(\mathbf{r}_2)]$ was evaluated, using $r_{^4\text{He}} = 1.6755$ fm [257], yielding a finite-nuclear-size correction of 2.75 fm.

5.6 RESULTS

The various matrix elements that contribute to calculating the RSCS were calculated using the doubled Hylleraas basis sets (cf. Sec. 2.7.1). For the 2^3S_1 state, an optimized calculation is performed, whereas for all pseudospectra—coinciding with the presence of the $\mathcal{R}(\omega)$ —a complete diagonalization of the Hamiltonian matrix is performed.

Table 5.6.1 lists all of the theoretical contributions for the categories described in the previous section. Since, according to Eq. (5.8), the individual perturbations are frequency-dependent, the tune-out frequency changes as each is added, and so the total must be iterated to convergence.¹² Finite-mass effects are included in the values quoted for the NR and relativistic contributions in Table 5.6.1. As mentioned in Sec. 5.5.5, the dominant source of uncertainty is the nonradiative terms of order α^4 , estimated ± 6 MHz.

Overall, the final theoretical result of $725\ 736\ 252(9)$ MHz differs from the experimental result by -448 ± 260 MHz, 1.7 the measurement uncertainty σ . This is shown graphically in Fig. 5.6.1, from which it is clear that this theoretical-experimental comparison is able to discern QED contributions to the tune-out frequency f_{TO} at the $\sim 30\sigma$ level retardation effects at the $\sim 2\sigma$ level. This is the first calculation of f_{TO} that includes retardation corrections, which could be tested much more stringently if the experimental precision were increased.

¹²This procedure was relaxed, beginning at QED-order, for the terms of order α^3 or smaller as they are small enough to be added into Eq. (5.9) linearly.

Table 5.6.1: Collection of the various theoretical contributions to the $2^3S_1 - 2^3P/3^3P$ tune-out frequency in helium near 725.7 THz. Finite-nuclear-mass effects are included in the nonrelativistic and relativistic contributions.

Quantity	Value (MHz)	Uncertainty (MHz)
Nonrelativistic (NR)	725 645 115	2
Relativistic scalar (α^S) ^a	97 101	6
Relativistic tensor ($-\frac{1}{2}\alpha^T$)	1 744	6
Total non-QED	725 743 960	6
QED α^3	-7 297	2
QED α^4	-127	6
Total QED	-7 424	6
Retardation	-477	2
Nuclear size ^b	5	6
Magnetic polarizability	188	3
Theory (Total)	725 736 252	9
Experiment	725 736 700	260
Difference	-448	260

^a Obtained using $R_\infty c = 3.2898419602508(64) \times 10^9$ MHz.

^b This value was converted from data 2.75 fm in Ref. [256].

5.7 FUTURE WORK

Looking at the experimental uncertainties listed in Table 5.4.1, it is clear that experimental improvements should be concerned with improving our ability to measure the polarization—ideally even within the vacuum itself. Further, pursuant to the discussion in Sec. 5.5.1, if the angle between the laser and the magnetic field were able to be measured more precisely, this would allow independent testing of the scalar, vector, and tensor parts of Eq. 5.2—an altogether stricter test of QED. The method could be used to treat other tune-out frequencies in helium, and furthermore, it could help to determine the charge radius of helium if the precision can be increased to the MHz level.

On the theoretical side, higher-order retardation corrections due to the finite speed

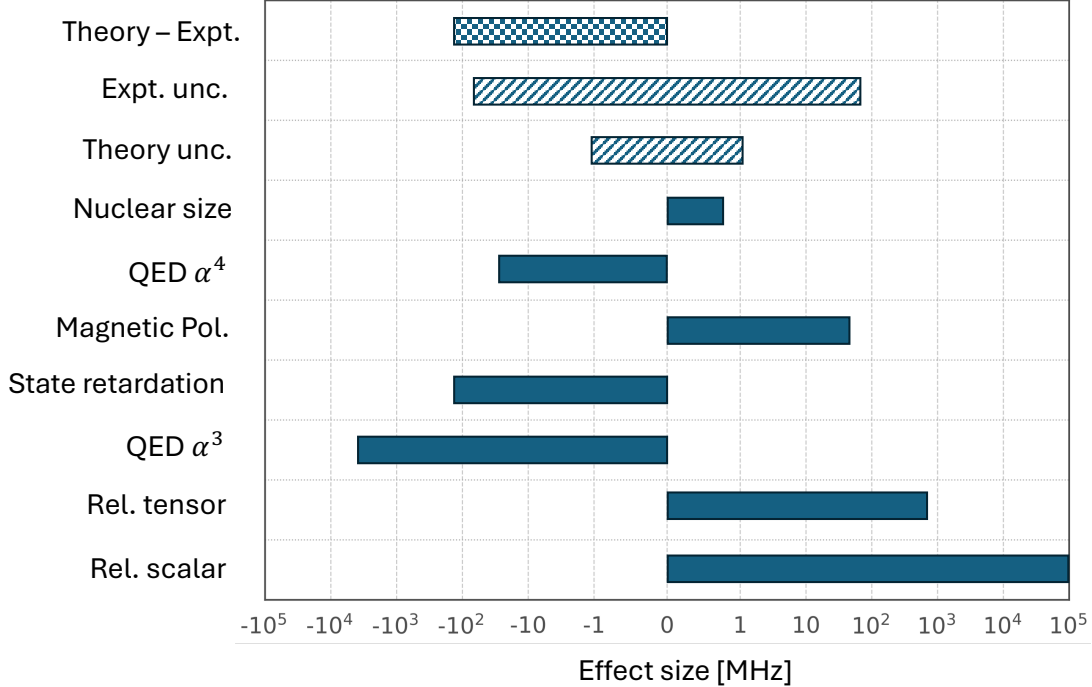


Fig. 5.6.1: A visual display of the material in Table 5.6.1. The difference between theory and experiment (checkered bar), along with their respective uncertainties (in crosshatch), are shown. Also depicted are the magnitudes of the theoretical contributions outlined in Table 5.6.1 are shown.

of light can be calculated, which will contribute if the experiment reduces its uncertainty by an order of magnitude. This calculation can be used to measure the molar mass constant (M_u), a quantity related to the index of refraction of helium gas [219, 242], which is no longer exactly $M_u = 1$ g/mol with the SI unit redefinitions in 2019 [258] that made Avogadro's number exact.

Additional theoretical extensions of this work include making small QED corrections more precise. Firstly, the electric field perturbation to the Bethe logarithm could be explicitly calculated for the 2^3S_1 state, along with finite-mass corrections. Also, the omitted nonradiative contributions [232] of order α^4 Ry could be explicitly calculated for this state.

CHAPTER 6

Conclusion and Future Work

6.1 OVERVIEW

This chapter begins in Sec. 6.2 with concluding remarks on each topic addressed in this dissertation, highlighting the significance of each result obtained. The findings are then synthesized in Sec. 6.3. They strongly support the theme that pseudospectra, with their broad utility, can significantly enhance our understanding and applications in atomic physics. Future work is discussed in Sec. 6.4, beginning with a recapitulation of the most significant extensions suggested and then a suggestive example of where one could apply the methodologies developed beyond the selection of projects in this dissertation. Lastly, in Sec. 6.5, the significance of this work in terms of its implications for ongoing activities in atomic physics is considered.

6.2 SUMMARY OF FINDINGS

The first project considered in this dissertation, in Chap. 3, was the beta decay of ${}^6\text{He}$. The problem addressed in this work was that previous theoretical attempts to quantify the amount of double ionization following this decay consistently overestimated the measured amount—by several orders of magnitude. This quantity is related to the electron-antineutrino correlation coefficient, $a_{\beta\nu}$, which is widely studied in low-energy searches for new physics through potential non-Standard Model contributions to the $V - A$ theory of beta decay. We developed two-electron projection operators formed of products of one-electron Sturmian functions to partition the overlapping single

and double ionization continua. As a result of these efforts, we have reduced the discrepancy between theory and experiment by an order of magnitude, although a disagreement that requires further attention remains.

In the next project, contained within Chap. 4, the two-photon decay rates of metastable 2^1S heliumlike ions were calculated. Two-photon decay of the metastable 2^1S_0 competes with collisional deactivation under low density and temperature conditions in astrophysical sources. So, the population balance provides a probe of temperature and density [259, 260]. In this work, we obtained accurate values for the effects of finite nuclear mass on this process. In characterizing these finite-mass effects, we developed a technique for treating the mass polarization using a gauge-dependent power series. We extended the notion of gauge equivalence beyond the usual context of infinite nuclear mass. In doing so, we derived algebraic relations for $nE1$ -photon transitions in heliumlike systems. They were used to successfully demonstrate gauge equivalence in the $2E1$ decay of the 2^1S state along with the $E1$ decay of both the 2^1P and 2^3P states. These relationships were used in our work to provide a very stringent test of the calculation’s accuracy, as they are only satisfied to the extent that the wave functions are exact.

Chap. 5 focuses on a joint theory-experiment effort to test QED by comparing calculations and measurements of the tune-out frequency of $\text{He}(2^3S_1)$. This novel test of QED is independent of the traditional measurements of energy shifts, such as the Lamb shift. A genuine discrepancy in the resulting comparison would be a signal for new physics. On the theoretical side, we carried out a high-precision calculation that was able to resolve both QED and retardation corrections to 30σ and 2σ , respectively, where σ is the measurement uncertainty. Building on the work of Drake *et al.* [217], these retardation corrections have been included for the first time in the present calculation. This amounts to reformulating the problem as a zero in the coherent Rayleigh scattering cross section instead of a zero in the dynamic polarizability, as previously assumed [244]. The result of this project was that there was a 1.7σ disagreement between theory and experiment.

6.3 SYNTHESIS OF CONCLUSIONS

The unifying theme connecting the distinct physical processes studied in this dissertation lies within the methods used to carry out the calculations. In the epigraph of this dissertation, we saw that “pseudo” means to be “false, deceptive, or having the appearance of something it is not.” Indeed, at least for the two-electron problem, pseudostates are not exact eigenstates. However, using variational methods, they can become arbitrarily close to eigenstates and, more importantly, the *pseudospectra* formed by solving the appropriate generalized eigenvalue problem tend to completeness in the limit of large basis sets. The resulting computationally realizable discrete sum, which replaces the infinite bound sum and continuum integral, demonstrates that the prefix “pseudo” applies in name only. These powerful objects enable an entire class of calculations that would otherwise be more difficult.

In this dissertation, we make repeated use of pseudospectra. In the beta decay work, the foundation of our work was to expand an initial ${}^6\text{He}$ state in terms of a complete set of final ${}^6\text{Li}^+$ states, including single and double ionization channels. The physics of the instantaneous change in nuclear charge following this event makes possible electronic rearrangement to *any* final state of ${}^6\text{Li}^+$. Therefore, the $\{{}^6\text{Li}^+\}$ pseudospectra, which includes ${}^6\text{Li}^{++}$ and ${}^6\text{Li}^{3+}$ states, represents actual states where transitions from the initial ${}^6\text{He}$ state occur.¹ Beyond this, in forming the projection operators to apply to each of these pseudostates, one-electron pseudospectra were formed using Sturmian functions, taking advantage of their well-defined charge state and ability to mimic the exact Coulomb wave functions over the region of interest.

This conceptualization of the complete set of states as actual states, in the sense described in Footnote 1, contrasts with the use of pseudospectra that arise in deriving the two-photon decay rate and the Rayleigh scattering cross section. In the latter case, the sums enter the calculation to treat the interaction with the QED vacuum, and we interpret these as sums over virtual rather than actual states. We also made

¹Strictly speaking, via Stieltjes imaging, pseudostates represent a block of the continuum, and therefore, the transitions described are from the initial state to a set of continuum states within an energy range.

this interpretation when using perturbation theory to treat the relativistic and QED corrections. This diversity of use is a testament to the versatility of pseudospectra. The resolvent operators $(H - E_m)^{-1}$ that arise in perturbation theory can be formally evaluated by inserting the identity operator $\sum_n |\phi_n\rangle\langle\phi_n| = 1$ and so any problem in this class makes use of pseudospectra. The pseudospectral techniques developed and used in this dissertation offer a common approach to both classes of problems.

6.4 FUTURE WORK

Each of Chapters 3, 4, and 5 concludes with a section outlining extensions and potential next steps for the respective project. This section highlights the most exciting and relevant extension from each chapter, followed by a project that was not mentioned but is an example of one of the many calculations that can be carried out using the techniques developed in this work.

The most promising avenue to address the remaining discrepancy in the beta decay of ${}^6\text{He}$ is to reformulate the ${}^6\text{Li}^+$ basis functions that comprise the pseudospectra to which the projection operators were applied. One can accomplish this by studying the delta function expectation value of these wave functions—a quantity that should remain equal to its ground state, $\langle 1\,{}^1S|\delta(\mathbf{r}_1)|1\,{}^1S\rangle$ value, for energies near the double ionization continuum. The wave functions used in Ref. [132] did not satisfy this condition. By manipulating the Hylleraas pseudostates introduced in Chap. 2, with the benefit of the variational principle, we aim to create wave functions whose delta function matrix elements are close to the ground state value, and we postulate that this will remove much of the remaining discrepancy between theory and experiment.

Concerning the two-photon decay rates that were the subject of Chap. 4, there is a very straightforward but necessary subsequent step: evaluating relativistic effects. Once completed, the data will be the most accurate two-photon decay rates for astrophysical applications, replacing Ref. [211]. To compare with experiment, finite-mass corrections of order μ/M must be accompanied by $(\alpha Z)^2$ relativistic corrections, since these are both of relative order 10^{-4} in ${}^4\text{He}$ —the isotope of astrophysical interest. We

perform this calculation by deriving a set of corrections via “2+1” order perturbation theory, as in the Breit corrections in the tune-out project, except here the two-photon emission interaction energy has a slightly different form than the Rayleigh scattering cross section. Another extension of the work in Chap. 4 would be to calculate the algebraic expansion coefficients by performing a perturbation expansion in the parameter μ/M , as indicated in Appendix G. Additionally, the algebraic relations could be derived and used to characterize other processes in atomic physics, including absorption, photoionization, and Feshbach resonances.

As mentioned above, in the tune-out frequency study, there is a 1.7σ discrepancy between theory and experiment. The source of this disagreement is currently unknown. Still, suppose we assume that the theoretical calculations are correct. In that case, the next step will be to include higher-order retardation effects, which will become relevant if the measurement uncertainty improves by an order of magnitude—a possibility that will likely require in-vacuum optics to reduce the systematic uncertainty associated with the laser polarization. This work could contribute to determining the molar mass constant, which no longer equals 1 after the last SI redefinitions in 2019.

The discussion above is primarily concerned with direct extensions of the projects addressed in this work. There is a lot of practical and valuable work to be done in these directions; however, the methods developed can be applied to many more problems beyond those mentioned here, including the broad class of perturbation calculations, such as adding relativistic and QED corrections to the determination of the ground state energy of H^- , and the equally broad class of scattering problems, such as the double photoionization of helium.

One particular project we will pursue is calculating the Lamb shift for high- L Rydberg states in helium. The most difficult part of this calculation—briefly referenced in the Introduction—is calculating the two-electron Bethe logarithm (BL).² The two-electron BL component of the Lamb shift is the most difficult to calculate. For initial

²Despite significant recent work on the higher-order effects on the helium Lamb shift in low-lying states, little attention has been paid to the Rydberg series.

state $|0\rangle$, it has the form

$$\beta(nLS) = \frac{\sum_i |\langle 0|\mathbf{p}|i\rangle|^2 (E_i - E_0) \ln |E_i - E_0|}{\sum_i |\langle 0|\mathbf{p}|i\rangle|^2 (E_i - E_0)} \quad (6.1)$$

where E_0 is the NR energy of the state in question, $\mathbf{p} = \mathbf{p}_1 + \mathbf{p}_2$ is the momentum operator, and $\{|i\rangle, i = 1, \dots, N\}$ is a complete set of states. The denominator is $2\pi\langle\delta(\mathbf{r}_1) + \delta(\mathbf{r}_2)\rangle_0$ via the sum rule [261]; however, due to the logarithmic term the numerator does not have a simple sum rule and needs to be evaluated by carrying out the summation. Another difficulty is that this sum contains contributions from very high-energy states (cf. Fig. 1.3.2 from the Introduction).

In low-lying states of helium, variational approaches have calculated the Lamb shift, including the BL, with sufficient accuracy [29, 262], but this is more difficult for high- L Rydberg states.³ To overcome these difficulties, Goldman and Drake [261] developed a global formula for the asymptotic expansion for the Lamb shifts in helium that calculates the perturbation of the electric field due to the Rydberg electron on the inner $\text{He}^+(1s)$ Lamb shift. The two-electron BL of $\beta(1snl)$ with large l is [261]

$$\beta(1snl) \approx \beta(1s) + \frac{1}{n^3} \left(\frac{Z-1}{Z} \right)^4 \beta(nl) + c_2 F^2 + O(F^4) \quad (6.2)$$

where $\beta(nl)$ denotes the one-electron BL and F describes the magnitude of the electric field of the Rydberg electron at the location of the inner $1s$ electron and is $F^2 = \langle r^{-4} \rangle_{nL}$ where r is the position of the Rydberg electron. c_2 is calculated perturbatively and currently [43] has the value $c_2 = 0.316\,205(6)Z^{-6}$. Each of $\beta(1s)$, $\beta(nl)$, and c_2 can now be calculated with higher precision than Ref. [263, 264] since larger basis sets can be formed. Calculating $\beta(1s)$ and $\beta(nl)$ involves evaluating the one-electron BL⁴ for the $1s$ and nl states and perturbing it with an electric field to obtain the c_2 coefficient. To this end, we use the same one-electron, triangular Stur-

³Apart from the BL, the remaining contributions to the Lamb shift are proportional to the delta function matrix elements. For the high- L Rydberg states, highly accurate calculations of delta function matrix elements become computationally difficult and limiting in terms of an overall calculation of the Lamb shift.

⁴The one-electron form of the BL is the same as the two-electron form shown in Eq. (6.1).

mian functions developed in Chap. 3 [29]. The Bethe logarithm calculations can then be used with the asymptotic expansions of the delta functions [263] to accurately calculate the Lamb shift of Rydberg states of two-electron atomic systems.

6.5 BROADER IMPLICATIONS

Physics is an experimental discipline guided and supported by robust theoretical efforts. The theoretical work presented here involves active collaboration with experimental physicists across various disciplines, including nuclear, particle, and atomic physics and astrophysical applications. Atoms have long been studied alongside quantum mechanics due to their accessibility, simplicity, and ubiquity. These traits contribute to a continuously evolving field that remains rooted in its foundational principles. Atomic physics can be defined by the endeavours of atomic physicists, a representative sample of which is showcased in this thesis.

The search for new physics (NP) beyond the Standard Model (SM) is a significant discipline-wide effort to which atomic physicists contribute. From gravitational lensing experiments indicative of dark matter to the apparent observation of baryonic asymmetry via our universe's matter content, it is clear that the SM (along with general relativity) likely represents only part of the story. Atomic physicists are engaged in numerous projects aimed at this goal, including studies of the electron electric dipole moment (eEDM), muon $g - 2$ measurements, and various dark matter searches mentioned in the Introduction.

The beta decay and tune-out frequency projects in this dissertation align with this larger effort. The tune-out frequency project exemplifies the advancements made possible by improvements in experimental capabilities. As laser power and precision continue to improve, increasingly accurate measurements in AMO physics will become feasible. These advancements necessitate that the theoretical AMO physics community calculate the corresponding quantities with sufficient accuracy. Although the NP sought in the study of beta decay pertains to nuclear physics, given that most beta decay events occur within an atom, the motion of atomic electrons is relevant and

must be accurately known. Both projects thus underscore the integral role of atomic physics in advancing our understanding of fundamental processes and highlight the necessity of precise theoretical and experimental collaboration in the field.

APPENDIX A

Methods of Solving the Generalized Eigenvalue Problem

In Chap. 2, we show that, although the nonrelativistic two-electron Schrödinger equation does not have exact solutions, it can be solved to essentially arbitrary accuracy using the Rayleigh-Ritz variational method.¹ It was shown that if the trial functions forming the basis set are written with *linear* variational coefficients $\Psi_{tr} = \sum_{i=1}^N a_i \chi_i$, then solving the minimization problem

$$\frac{\partial E_{tr}}{\partial a_p} = 0, \quad p = 1, \dots, N, \quad (\text{A.1})$$

is identical to the generalized eigenvalue problem (GEP)

$$\mathbf{H}\mathbf{a} = \lambda \mathbf{O}\mathbf{a}, \quad (\text{A.2})$$

where \mathbf{a} is a vector of the expansion coefficients, \mathbf{H} and \mathbf{O} are the Hamiltonian and overlap matrices, respectively, satisfying $H_{mn} = \langle \chi_m | H | \chi_n \rangle$ and $O_{mn} = \langle \chi_m | \chi_n \rangle$. This appendix discusses how Eq. (A.2) is solved. Standard quadruple precision (approximately 32 decimal digits) is sufficient for the calculations in this dissertation.

We use two separate methods—the power method and the brute force method—to “solve” Eq. (A.2), depending on our objective.² The power method is used in this

¹This technique guarantees that the N eigenvalues found by diagonalization in any N -dimensional basis set will be upper bounds to the N exact—though unknown—eigenvalues.

²The primary reference for this appendix is the “Notes on solving the Schrödinger equation in Hylleraas coordinates for heliumlike atoms” by Drake [39].

dissertation when a single, optimized state is needed (e.g., the initial $\text{He}(2\ ^1S)$ state in the two-photon decay studied in Chap. 4 and the beta decay in Chap. 3). The brute force method is used when the entire pseudospectrum of the Hamiltonian is needed due to sum(s) over state(s) appearing in the equations of interest—a necessity that arises in every project considered in this dissertation and forms the common theme.

A.1 POWER METHOD

The power method applies for a diagonalizable $N \times N$ matrix \mathbf{H} that has eigenvalues $\lambda_1, \lambda_2, \dots, \lambda_N$ corresponding to eigenvectors $\Psi^{(1)}, \Psi^{(2)}, \dots$ and has one eigenvalue, λ_M , that is much larger than the others.

If $\chi = \begin{pmatrix} a_1 \\ \vdots \\ a_n \end{pmatrix}$ is an arbitrary vector in this space, it is always possible to expand it in terms of the exact eigenvectors that diagonalize \mathbf{H} , according to $\chi = \sum_{q=1}^N x_q \Psi^{(q)}$. This corresponds to the members of the basis set of the trial Hylleraas wave function. If χ is acted upon n times by \mathbf{H} according to

$$(\mathbf{H})^n \chi = \sum_{q=1}^N x_q \lambda_q^n \Psi^{(q)} \longrightarrow x_M \lambda_M^n \Psi^{(M)}, \quad (\text{A.3})$$

the RHS tends to only a single term, containing the largest eigenvalue and its eigenvector, provided $x_M \neq 0$.

This method can find any eigenvalue of \mathbf{H} by manipulating the GEP into an inverse problem. We begin by subtracting $\lambda_q \mathbf{O}\Psi$ from both sides

$$\mathbf{H}\Psi = \lambda \mathbf{O}\Psi \quad (\text{A.4})$$

$$(\mathbf{H} - \lambda_q \mathbf{O})\Psi = (\lambda - \lambda_q) \mathbf{O}\Psi, \quad (\text{A.5})$$

leading to the related eigenvalue problem

$$\mathbf{G}\Psi = \frac{1}{\lambda - \lambda_q} \Psi \quad (\text{A.6})$$

where $\mathbf{G} = (\mathbf{H} - \lambda_q \mathbf{O})^{-1} \mathbf{O}$ with eigenvalues $(\lambda_n - \lambda_q)^{-1}$.

Supposing we are ultimately interested in the eigenvalue λ_J , the strategy is then to make the eigenvalue $(\lambda_J - \lambda_q)^{-1}$ much larger than the rest by choosing λ_q to be very close to the desired λ_J . The procedure, as above, is to act repeatedly on χ via $(\mathbf{G})^n \chi$ as

$$\begin{aligned}\chi_1 &= \mathbf{G}\chi \\ \chi_2 &= \mathbf{G}\chi_1 \\ \chi_3 &= \mathbf{G}\chi_2 \\ &\vdots \\ \chi_n &= \mathbf{G}\chi_{n-1}\end{aligned}$$

until the ratios of components in χ_n stop changing.

It is possible to avoid the matrix inversion and multiplication necessary to compute \mathbf{G} by instead solving the equivalent linear system

$$\mathbf{F}\chi_n = \mathbf{O}\chi_{n-1} \tag{A.7}$$

where $\mathbf{F} = \mathbf{H} - \lambda_q \mathbf{O}$. To find χ_n , we solve the $N \times N$ system using the square root method [265]. This leads to the computation of λ_J by

$$\lambda_J = \frac{\langle \chi_n | \mathbf{H} | \chi_n \rangle}{\langle \chi_n | \chi_n \rangle}. \tag{A.8}$$

A.2 BRUTE FORCE METHOD

This method is used when all N eigenvectors and eigenvalues of \mathbf{H} in the GEP are required. This is a full diagonalization, so it is considerably slower than the power method described above.

The first step is to orthonormalize the basis set, which is accomplished by forming

linear combinations of the original basis set $\{\varphi_n\}$ per

$$\Phi_m = \sum_{n=1}^N \varphi_n R_{nm}, \quad (\text{A.9})$$

so that $\langle \Phi_m | \Phi_n \rangle = \delta_{m,n}$. This is computationally achieved by finding an orthogonal transformation matrix \mathbf{T} such that the overlap matrix \mathbf{O} , with elements $O_{mn} = \langle \varphi_m | \varphi_n \rangle$, is made diagonal³

$$\mathbf{T}^\top \mathbf{O} \mathbf{T} = \mathbf{I} = \begin{pmatrix} I_1 & 0 & 0 & \cdots & 0 \\ 0 & I_2 & 0 & \cdots & 0 \\ 0 & 0 & I_3 & \cdots & 0 \\ \vdots & \vdots & \vdots & \ddots & \vdots \\ 0 & 0 & 0 & \cdots & I_N \end{pmatrix}; \quad (\text{A.10})$$

Following this, a scale-change matrix \mathbf{S}

$$\mathbf{S} = \begin{pmatrix} \frac{1}{I_1^{1/2}} & 0 & 0 & \cdots & 0 \\ 0 & \frac{1}{I_2^{1/2}} & 0 & \cdots & 0 \\ 0 & 0 & \frac{1}{I_3^{1/2}} & \cdots & 0 \\ \vdots & \vdots & \vdots & \ddots & \vdots \\ 0 & 0 & 0 & \cdots & \frac{1}{I_N^{1/2}} \end{pmatrix} = \mathbf{S}^\top \quad (\text{A.11})$$

is applied so that the diagonalized matrix is the identity matrix

$$\mathbf{S}^\top \mathbf{T}^\top \mathbf{O} \mathbf{T} \mathbf{S} = \mathbf{I}. \quad (\text{A.12})$$

Thus, we have the sought after matrix $\mathbf{R} = \mathbf{TS}$ that transforms \mathbf{O} by $\mathbf{R}^\top \mathbf{O} \mathbf{R} = \mathbf{I}$.

Now we transform \mathbf{H} , with $H_{mn} = \langle \phi_m | H | \phi_n \rangle$ to the orthonormal basis set by

³The matrices \mathbf{T} and \mathbf{W} , defined below, are obtained by diagonalizing \mathbf{O} and \mathbf{H}' , respectively. The two interchangeable computational methods we used at different points in this dissertation are 1) the Jacobi method [266], and 2) the tridiagonalization + QL algorithm [267, 268].

applying \mathbf{R}

$$\mathbf{H}' = \mathbf{R}^\top \mathbf{H} \mathbf{R}. \quad (\text{A.13})$$

\mathbf{H}' is then diagonalized by

$$\mathbf{W}^\top \mathbf{H}' \mathbf{W} = \lambda = \begin{pmatrix} \lambda_1 & 0 & \cdots & 0 \\ 0 & \lambda_2 & \cdots & 0 \\ \vdots & \vdots & \ddots & \vdots \\ 0 & 0 & \cdots & \lambda_N, \end{pmatrix} \quad (\text{A.14})$$

with the appropriate orthogonal transformation matrix \mathbf{W} . The diagonal elements of λ are the eigenvalues and the q^{th} eigenvector is given by

$$\Psi^{(q)} = \sum_{n=1}^N \Phi_n W_{n,q} = \sum_{n,n'} \varphi'_n R_{n',n} W_{n,q}. \quad (\text{A.15})$$

APPENDIX B

Derivation of Fermi's Golden Rule and Comments on Spontaneous Decay

Fermi's Golden Rule, as it is commonly known¹, describes the *transition rate* between an initial eigenstate with energy E_i of a system to a final group of states within a small energy range dE about energy E_f . It reads [148, p. 135]

$$w_{i \rightarrow f} \equiv \frac{p_{i \rightarrow f}}{t} = \frac{2\pi}{\hbar} \left| \langle \phi_f | \hat{W} | \phi_i \rangle \right|^2 \rho(E_f) \equiv \frac{2\pi}{\hbar} W_{if}^2 \rho(E_f), \quad (\text{B.1})$$

where $W_{if} = \langle \phi_f | \hat{W} | \phi_i \rangle$ is the matrix element connecting the initial and final states of the system by an operator that is representative of a weak perturbation, described by operator \hat{W} , and $\rho(E_f)$ is the density of states at energy E_f —the number of continuum states divided by dE at E_f . In bound-bound transitions, assuming a single-photon transition for simplicity $\rho(E_f)$ becomes a conservation of energy-enforcing delta function because the final state is discrete.

The derivation of Eq. (B.1) follows in Sec. B.1. Since this dissertation is concerned explicitly with spontaneous decay in Chap. 4, the ensuing Sec. B.2 discusses this process regarding its connection to QED.

¹The content of the equation was almost developed many years early by Dirac [168] in the same paper that served as a significant inspiration to Maria Goeppert Mayer in her doctoral work on two-photon processes [166].

B.1 DERIVATION

This derivation is a condensed version of those found in Friedrich's *Theoretical Atomic Physics* [148, pp. 132–135] and the *Atomic and Molecular Physics Lecture Notes* of Kirchner [269]. The bulk of the derivation will assume bound-bound transitions—this will be generalized to a continuum of final states at the end.

Suppose that an atom, governed by H_0 , is contained in physical system \mathcal{S} is described by the Hamiltonian

$$H = H_0 + W \quad (\text{B.2})$$

where W is a general form of a perturbation leading to transitions in the atomic system. The time-dependent solutions to H can be expanded, in terms of the unperturbed energies E_n and eigenstates ϕ_n as

$$\psi(t) = \sum_n c_n(t) \phi_n \exp\left(-\frac{i}{\hbar} E_n t\right), \quad (\text{B.3})$$

Assuming that we are in an eigenstate of H_0 —express this as $c_n(t=0) = \delta_{n,i}$, then the ensuing dynamics are given by the coupled-channel equations

$$i\hbar \frac{dc_m}{dt} = \sum_n W_{mn} c_n \exp\left[\frac{i}{\hbar} (E_m - E_n) t\right], \quad (\text{B.4})$$

an exact set of equations in the limit that the basis is complete. The time-dependence of the coefficients can be obtained via integration:

$$c_m(t) = c_m(0) + \frac{1}{i\hbar} \int_0^t dt' \sum_n W_{mn} \exp\left[\frac{i}{\hbar} (E_m - E_n) t'\right] c_n(t') \quad (\text{B.5})$$

$$\begin{aligned} &= c_m(0) + \frac{1}{i\hbar} \int_0^t dt' \sum_n W_{mn} \exp\left[\frac{i}{\hbar} (E_m - E_n) t'\right] c_n(0) \\ &\quad + \frac{1}{(i\hbar)^2} \int_0^t dt' \sum_n W_{mn} \exp\left[\frac{i}{\hbar} (E_m - E_n) t'\right] \\ &\quad \times \int_0^{t'} dt'' \sum_l W_{nl} \exp\left[\frac{i}{\hbar} (E_n - E_l) t''\right] c_l(t''), \end{aligned} \quad (\text{B.6})$$

where the second equation is obtained by plugging in the first result, found in Eq. (B.5). This expression has been carried out to second order; higher-order terms are obtained by plugging in the most recent $c_m(t)$ where the primed $c_m(t')$ occurs in the first equation.

To first order in W , the coefficients $c_{n \neq i}(t)$ are given by the first line of Eq. (B.6)

$$c_f(t) = \frac{1}{i\hbar} \int_0^t dt' W_{fi} \exp \left[\frac{i}{\hbar} (E_f - E_i) t' \right] \quad (\text{B.7})$$

To make this general result more specific, we can assume that the perturbation is periodic in time, as in how we treat the radiation field in Chap. 4, where $\alpha \approx 1/137$ is the perturbation parameter. This time-dependent perturbation has the form:

$$W(t) = \begin{cases} 0 & t \leq t_0 = 0 \\ Be^{i\omega t} + B^\dagger e^{-i\omega t} & t > t_0 \end{cases} \quad (\text{B.8})$$

Inserting this form of $W(t)$ into the first-order Eq. (B.7)

$$c_f(t) = \frac{1}{i\hbar} \int_0^t e^{i\omega_{fi} t'} W_{fi}(t') dt' \quad (\text{B.9})$$

$$= -\frac{1}{\hbar} \left\{ \frac{\langle \varphi_f | \hat{B} | \varphi_i \rangle}{\omega_{fi} + \omega} (e^{i(\omega_{fi} + \omega)t} - 1) + \frac{\langle \varphi_f | \hat{B}^\dagger | \varphi_i \rangle}{\omega_{fi} - \omega} (e^{i(\omega_{fi} - \omega)t} - 1) \right\} \quad (\text{B.10})$$

The probability of a transition is $p_{i \rightarrow f} = |c_f(t)|^2$; upon squaring we have²

$$p_{i \rightarrow f}(t) = |B_{fi}|^2 \{ f(t, \omega_{fi} + \omega) + f(t, \omega_{fi} - \omega) \} \quad (\text{B.11})$$

$$\xrightarrow{t \rightarrow \infty} \frac{2\pi t}{\hbar} |B_{fi}|^2 \{ \delta(\omega_f - \omega_i + \omega) + \delta(\omega_f - \omega_i - \omega) \} \quad (\text{B.12})$$

²The integrals reduce to $f(t, \omega_{fi} \pm \omega) = \frac{\sin^2[(\Delta E_\pm)t/(2\hbar)]}{[(\Delta E_\pm)/2]^2}$, where $\Delta E_\pm = \hbar(\omega_f - \omega_i \pm \omega)$. As $t \rightarrow \infty$, $f(t, \omega_{fi} \pm \omega) \rightarrow \frac{2\pi}{\hbar} \delta(\Delta_\pm)$.

In this limit, the transition *decay*³ rate is

$$w_{i \rightarrow f} = p_{i \rightarrow f}/t = \frac{2\pi}{\hbar} |W_{fi}|^2 \delta(\omega_f - \omega_i - \omega) \quad (\text{B.13})$$

Eq. (B.13) shows that transitions are only possible for “resonances”—where a photon of energy $E = \hbar\omega$ is donated to the field with an energy equal to the difference between the states involved, i.e., $E = \hbar(\omega_f - \omega_i)$.⁴

The final step is to extend Eq. (B.13) to transition to a final state in a continuum. There are two physical circumstances in which this applies. The first is when looking at the transition of an atom to the actual continuum—where the eigenstates of an atomic system form a continuous spectrum. This notably applies to the beta decay problem of Chap. 3,⁵ where, due to the sudden change in nuclear potential, shake-off to the continuous single or double continuum can occur.

If we refer to the resonance bound-bound transition rate in Eq. B.13 as $w_{i \rightarrow f}^R$, then emissions to the continuum to a state $E_f = E_i - \hbar\omega$ are obtained by taking the limit of an integral about E_f as follows

$$w_{i \rightarrow f} = \lim_{\epsilon \rightarrow 0} \int_{E_f - \epsilon}^{E_f + \epsilon} w_{i \rightarrow f}^R \rho(E_f) dE_f \quad (\text{B.14})$$

$$= \lim_{\epsilon \rightarrow 0} \int_{E_f - \epsilon}^{E_f + \epsilon} \frac{2\pi}{\hbar} |W_{fi}|^2 \delta(\omega_f - \omega_i - \omega) \rho(E_f) dE_f \quad (\text{B.15})$$

$$= \frac{2\pi}{\hbar} |W_{if}|^2 \rho(E_f). \quad (\text{B.16})$$

In the above set of equations, the *density of states* $\rho(E_f)$ is included since we must be able count the states in the region $[E_f - \epsilon, E_f + \epsilon]$ in order to integrate over them. In the limit $\epsilon \rightarrow 0$, the delta function is collapsed, and the transition rate takes its value with $E_f = E_i - \hbar\omega$. This completes the derivation of Fermi’s Golden Rule.

³In decay, we have $\omega = \omega_f - \omega_i$ and the first delta function vanishes. Decay is chosen to simplify the situation and to correspond with the two-photon decay that is the subject of Chap. 4.

⁴In practice, this can be a multiphoton process where $E = n\hbar\omega$ for $n \geq 2$. These processes are less and less likely by order since they require higher powers of the perturbing operator.

⁵In studying beta decay, we were concerned with a time-independent perturbation and also with the probability as opposed to the rate, but the arguments about the density of states apply.

B.2 SPONTANEOUS DECAY

Atomic transitions are well-described by the “semiclassical theory,” which treats the atomic system quantum mechanically and the EM field classically, often using the dipole, weak field, and rotating wave approximations. This method is used in Chap. 4 to address spontaneous two-photon decay. However, spontaneous emission processes are not conceptually described by the semiclassical method, as it assumes an external classical EM field.

For example, a hydrogen atom in the $2p$ state will decay to the ground state in about 2.13 ns, regardless of an external field. An elementary semiclassical calculation can yield this Lyman- α $2p - 1s$ lifetime using Einstein coefficients [178], but it doesn’t explain how a photon is emitted without interacting with an external field. As Einstein postulated, the semiclassical theory produces correct spontaneous decay rates in an *ad hoc* manner when combined with the Planck radiation law. This approach works well conceptually for stimulated emission and absorption, corresponding to Einstein’s B_{12} and B_{21} coefficients, but not for spontaneous emission.

A complete Hamiltonian must account for both the atomic degrees of freedom and the quantized EM field. This is done by treating the EM field as quantized harmonic oscillators that define modes. The field amplitudes are creation and annihilation operators that correspond to emission and absorption in an atomic context. The vacuum comprises Fock states, specifying the number of photons in states of any frequency. Spontaneous decay processes, as discussed in Chap. 4, occur due to vacuum fluctuations, where a photon is donated to the vacuum, increasing the number of photons in the corresponding Fock state.

APPENDIX C

Handedness of Leptons in the SM

A signature feature of the weak interaction is that it is a *chiral* interaction where, unlike the other known forces, left- and right-handed (LH and RH) particles are treated differently.¹ Only LH leptons (and RH antileptons) couple to the W^\mp bosons, the mediators of beta decay. Nonconservation of parity is a direct consequence of this fact. Examining these properties supplements the discussion of $a_{\beta\nu}$ contained in Sec. 3.3.2.

That our universe is such that the weak interaction is chiral is a direct consequence of the $\frac{1}{2}(1-\gamma^5)$ (cf. the leptonic portion of Eq. (3.4)) structure of the Lorentz invariant Lagrangian that emerges when constrained to experimental data [96, pp. 16–18]. However, we do not have any explanation for why only LH (rather than RH) leptons participate in the weak interaction, when theoretically, the opposite could have been the case. This constitutes yet another unexplained aspect of the Standard Model (SM) that physicists are actively seeking new physics (NP) to explain and which is frequently linked to the problem of baryonic asymmetry [104]. Amongst other things, RH neutrinos² are also postulated as potential mechanisms in beyond-standard-model (BSM) theories for how neutrinos acquire mass. That neutrinos are massive was only established about 25 years ago by the Super-Kamiokande collaboration in Japan [270] and the Sudbury Neutrino Observatory (SNO) collaboration in Canada [271]; these efforts were recognized with the 2015 Nobel Prize in Physics. It is still unclear as

¹In the SM, leptons (and quarks) are mathematically described as Dirac (spinor) fields with well-defined chirality with two parity eigenstates (± 1) for RH/LH particles.

²In BSM theories, these are sometimes called *sterile neutrinos* because the weak interaction still only couples to LH particles and RH antiparticles. It was initially thought that only LH neutrinos exist.

to how their mass arises. The relevance of neutrino mass is that, when they were assumed massless, only LH neutrinos could exist – neutrino mass directly offers the possibility of RH chiral states [272].

Referring to the Lee-Yang coupling coefficients that appear in Eqs. (3.11) and (3.12), the condition $|C_x| = |C'_x|$ corresponds to maximal parity violation, with $C_x = +C'_x$ corresponding to LH neutrinos and $C_x = -C'_x$ to RH neutrinos [28]. In the SM $C_i = 0$ for $i \neq V, A$, but in BSM theories involving the possibility of new forces mediated by new bosons, this constraint can be removed in the case that scalar or tensor fields emerge from interactions that do not discriminate based on chirality as the current weak force does [28]. Experiments offer different constraints on these parameters depending on whether or not one allows the possibility of RH neutrinos. What can be measured is the ratios $\frac{C_T}{C_A}$ and $\frac{C_S}{C_V}$ for Gamow-Teller (GT) and Fermi type decays, respectively. For example, in studying the pure GT beta decay of ${}^6\text{He}$, Johnson *et al.* [94] set an early experimental limit on this ratio as

$$\frac{|C_T|^2 + |C'_T|^2}{|C_A|^2 + |C'_A|^2} \leq 0.4\%,$$

a result which has been revisited since [98, 110]. This experimental method allows for the explicit consideration of BSM ($C_T \neq 0$) interactions comprised of either purely LH neutrinos or the possibility of RH neutrinos ($C_T = -C'_T$). To date, all experiments have found results consistent with the SM.

APPENDIX D

Assumptions in Treating Beta Decay

This appendix considers the time-dependence of the Coulomb potential $V(t)$ due to the change in the nuclear charge from $Z = 2$ to $Z = 3$ in the beta decay ${}^6\text{He} \rightarrow {}^6\text{Li}^+ + \text{e}^- + \bar{\nu}$. Let this occur at $t = 0$. The sudden approximation (SA), whose adoption is the topic of Sec. 3.4.2, thus results in an instantaneous change in the Hamiltonian at $t = 0$, via the potential energy term.

It is shown that this approximation is valid in the beta decay process. This permits the expansion of the initial $\psi({}^6\text{He})$ state in terms of the complete set of $\{\psi({}^6\text{Li}^+)\}$ states since the initial state is not an eigenstate of the $t > 0$ Hamiltonian. Using the SA removes the time dependence, permitting the calculation to be carried out using solutions the time-independent Schrödinger equation for both the initial ${}^6\text{He}$ state and the complete set of ${}^6\text{Li}^+$ states.

The physical condition for the SA to hold is that the system's wave function does not change appreciably during the perturbation. We study the TDSE to establish the criterion for the SA. The unitary time evolution operator¹, $U(t, t_0)$ evolves a system in time according to

$$\Psi(\mathbf{r}, t) = U(t, t_0)\Psi(\mathbf{r}, t_0) \quad (\text{D.1})$$

$U(t, t_0)$ also satisfies its own TDSE

$$i\hbar \frac{\partial}{\partial t} U(t, t_0) = HU(t, t_0), \quad (\text{D.2})$$

¹The following content is referenced from Chapters 2 and 5 of *Modern Quantum Mechanics* by Sakurai and Napolitano [273].

a form that can be rewritten as

$$i \frac{\partial}{\partial s} U(t, t_0) = \frac{H}{\hbar/T} U(t, t_0), \quad (\text{D.3})$$

where $t = sT$ for dimensionless s and a timescale T over which the perturbation is applied. In the SA, $T \rightarrow 0$ and thus $T \ll \hbar/\Delta E$, where ΔE depicts the characteristic energy scale of H . Thus, the right-hand side of Eq. (D.3) goes to 0, implying that $U(t, t_0)$ is a constant, which we can take² to be 1:

$$U(t, t_0) \rightarrow 1 \quad \text{as} \quad T \rightarrow 0 \quad (\text{D.4})$$

In this case, according to Eq. (D.1), the system is in the same state during and immediately after the decay at $t = 0^+$ as it was before the decay, at $t_0 = 0^-$.

We can now state the SA:

Sudden Approximation Criterion: Suppose a perturbation occurs at $t = 0$ on the timescale T in a system whose energy scale is denoted by ΔE . If $T \ll \frac{\hbar}{\Delta E}$, then the system's state is the same immediately after the perturbation as before the perturbation. As an equation, the SA says:

$$\text{If } T \ll \frac{\hbar}{\Delta E}, \quad \text{then } \Psi(\mathbf{r}, t = 0^+) = \Psi(\mathbf{r}, t = 0^-) \quad (\text{D.5})$$

Satisfaction of the sudden approximation in the decay of ${}^6\text{He}$

The purpose of this section is to unpack the quantities T and ΔE in Eq. (D.5) within the framework of the beta decay of ${}^6\text{He}$ considered in this dissertation using the parameters used in the experimental work in Refs. [114, 115] and the theoretical works [26, 132].

In order to establish the characteristic time, T , we must consider physically how the Coulomb potential changes. The nuclear process $n \rightarrow p + e^- + \bar{\nu}_e$ (corresponding

²This amounts to adding an arbitrary constant to H in a way that would only add an overall phase that would not affect the dynamics or probabilities in a measurable way. Note that H (and ΔE) still have time dependence, but the characteristic scale is dwarfed by \hbar/T .

to $d \xrightarrow{W^-} u + e^- + \bar{\nu}_e$ in the quark picture) in the nucleus truly happens instantaneously for our purposes. The mediator of the process, the W^- boson has a half-life of about $3 \times 10^{-25} \text{ s} \approx 1.2 \times 10^{-8} \text{ a.u.}$ What is relevant is over what timescale the Coulomb potential, as seen by the atomic electrons, changes from $Z = 2$ to $Z = 3$. This happens as the beta particle passes through the electron cloud defined by the atomic electrons. As before, we consider the beta particle to be a spherical shell of a radially outward moving charge. Assuming that $r_2 > r_1$, it is thus the time that it takes the beta particle to pass through a distance $r_2 - r_1$ that defines the characteristic time. There are calculations [43] of the expectation values of $r_{12} = |\mathbf{r}_2 - \mathbf{r}_1|$, which is a different quantity, and sets an upper limit on $r_2 - r_1$ in the (doubtful) case that the electrons lie on the same side of a parallel line that goes through the nucleus. Nonetheless, as an example in ${}^6\text{He}$ the expectation value $\langle r_{12} \rangle \sim 1.4 \text{ a.u.}$, which can be used to make the extreme case for the ground state of helium. The minimum energy of beta particles considered in the measurement of the beta decay of ${}^6\text{He}$ in Ref. [115] is 1 MeV $\approx 3.7 \times 10^4 \text{ a.u.}$ giving³ $v_\beta \approx 129 \text{ a.u.}$ Thus, the characteristic time for the beta particle is $T \approx \langle r_{12} \rangle / v_\beta = 1.4 / 129 = 0.01 \text{ a.u.}$

The characteristic energy scale, ΔE , is the relative spacing between the relevant energy eigenvalues in solutions to a Hamiltonian. In atomic systems, this can, at first glance, have a slightly ambiguous meaning because transitions can, in principle, take place between states of arbitrarily high energy differences owing to the infinite continuum. However, in treating the SA in beta decay, we consider bound-state energies in helium⁴ and therefore we can set $\Delta E \sim 1 \text{ a.u.}$ Thus we have $\hbar / \Delta E \approx 1 / 1 = 1$ and (along with $T \sim 0.01$), we have established⁵ that If $T \ll \frac{\hbar}{\Delta E}$ holds for the beta decay of the ground state of ${}^6\text{He}$. Similar results hold for the $n = 2$ metastable states that have also been studied.

To be careful, in the preceding discussion, T and ΔE have been overestimated (perhaps significantly) and underestimated, respectively. So the case for the SA is

³For this relativistic electron, a kinetic energy of 1 MeV equates to a velocity of about 0.941c.

⁴With a ground state and first ionization energy of -2.903... and -2, in a.u., respectively.

⁵A cruder approach that leads to the same conclusion would be to observe that the characteristic time $T = a_0/c = \alpha \tau_a \approx 0.007 \ll \hbar / \Delta E = 1$, where τ_a is the atomic unit of time (= 1 in a.u.).

even stronger than what is presented here. Nevertheless, we can likely expect that lifting the SA will be necessary at some level of precision. As shown in Chap. 3, this is expected to be at a much smaller level of precision than we can theoretically achieve.

APPENDIX E

Derivation of Two-photon Decay Rate and Rayleigh Scattering Cross Section

E.1 SETTING THE STAGE

In this dissertation, the interaction with the QED vacuum is used in two places, in distinct but related fashions. Firstly, it is used in Chap. 4 to derive the interaction energy that appears in Fermi’s Golden Rule for the doubly differential decay rate. The other example is in Chap. 5, where the tuneout frequency is reformulated as a zero in the Rayleigh scattering cross section. The bulk of the machinery will be built up for the first of these examples.

In Chap. 4, we wrote the two-photon decay rate in terms of Fermi’s Golden Rule in the form

$$dw^{(2\gamma)} d\Omega_1 d\Omega_2 = \frac{2\pi}{\hbar} |U_{i,f}^{(2)}|^2 \rho(\omega_1) \rho(\omega_2) d\Omega_1 d\Omega_2 dE_1. \quad (\text{E.1})$$

The purpose of this appendix is to provide a more rigorous foundation for the interaction energy, $U_{i,f}^{(2)}$, in this equation. Several equations from Chap. 4 will be listed again for convenience. This derivation follows Refs. [216, 217]

In a nonrelativistic approximation, $U_{i,f}^{(2)}$ is a second-order interaction energy with

the electromagnetic field given by

$$U_{i,f}^{(2)} = - \sum_{n^+} \left[\frac{\langle f | H_{\text{int}}(\omega_1) | n \rangle \langle n | H_{\text{int}}(\omega_2) | i \rangle}{E_n - E_i + \hbar\omega_2} + \frac{\langle f | H_{\text{int}}(\omega_2) | n \rangle \langle n | H_{\text{int}}(\omega_1) | i \rangle}{E_n - E_i + \hbar\omega_1} \right] \quad (\text{E.2})$$

summed over positive energy states, and by conservation of energy $E_i - E_f = \hbar\omega_1 + \hbar\omega_2$. The n^+ under the summation sign indicates that this interaction only includes a sum over the positive energy states. This is the key piece of the interaction energy that requires justification. We have performed the calculation within the nonrelativistic (NR) framework, so it is clear that negative energy states are not included. However, the form of Eq. (E.2) needs to be justified.

For this derivation, we recall from Sec. 4.5 that $H_{\text{int}} \propto \mathbf{p} \cdot \mathbf{A}_m$ for the two photons ω_m with $m = 1, 2$. The structure of Eq. (E.2) varies depending on the gauge used and the choice of coordinate system. Therefore, we will establish this relationship without meticulously including every factor. So, we aim to show

$$U_{i,f}^{(2)} = C \sum_{n^+} \left[\frac{\langle f | \mathbf{p} \cdot \mathbf{A}_1 | n \rangle \langle n | \mathbf{p} \cdot \mathbf{A}_2 | i \rangle}{E_n - E_i + \hbar\omega_2} + \frac{\langle f | \mathbf{p} \cdot \mathbf{A}_2 | n \rangle \langle n | \mathbf{p} \cdot \mathbf{A}_1 | i \rangle}{E_n - E_i + \hbar\omega_1} \right], \quad (\text{E.3})$$

for some overall constant C .

E.2 DERIVATION

Free electrons have no structure and thus cannot emit or absorb photons—the simplest electron-photon interactions, such as the two-photon decay, are second-order processes described by the second-order scattering matrix

$$S^{(2)} = e^2 N \int \bar{\psi}(x_2) \hat{A}(x_2) S_c^{(e)}(x_1, x_2) \hat{A}(x_1) \psi(x_1) d^4 x_1 d^4 x_2, \quad (\text{E.4})$$

where ψ corresponds to the electron wave functions and A the potentials of the photon states, and $S_c^{(e)}$ describes the pairing between the electron operators.¹ The N ensures normal ordering² The integration occurs in 4 dimensional spacetime ($x_0 = ict, x_1, x_2, x_3$). Upon integrating over the time and frequency variables, we obtain:

$$S_{i \rightarrow f}^{(2)} = -2\pi i U_{i \rightarrow f}^{(2)} \delta(E_i - \omega_1 - E_f - \omega_2), \quad (\text{E.5})$$

where $U_{i \rightarrow f}^{(2)}$ is the interaction energy, corresponding to the on-shell component of the S -matrix.

$$U_{i \rightarrow f} = \frac{2\pi\hbar c^2 e^2}{\mathcal{V}\sqrt{\omega_1\omega_2}} \sum_{n^\pm} \left(\frac{\langle f | \hat{\mathbf{e}}_2 e^{-i\mathbf{k}_2 \cdot \mathbf{r}} | n \rangle \langle n | \hat{\mathbf{e}}_1 e^{i\mathbf{k}_1 \cdot \mathbf{r}} | i \rangle}{E_n - E_i - \hbar\omega_1} + \frac{\langle f | \hat{\mathbf{e}}_1 e^{i\mathbf{k}_1 \cdot \mathbf{r}} | n \rangle \langle n | \hat{\mathbf{e}}_2 e^{-i\mathbf{k}_2 \cdot \mathbf{r}} | i \rangle}{E_n - E_i - \hbar\omega_2} \right) \quad (\text{E.6})$$

This is of the form used in Chap. 4, where the normalization constant has already been imposed. In Eq. (E.6), $\hat{\mathbf{e}}_f = \gamma_\mu e_\mu$, a product of the Dirac γ -matrices and \mathbf{e} the polarization vector satisfying $\mathbf{k} \cdot \mathbf{e} = 0$. In our work, we will sum over the independent polarizations. So far, this looks identical to Eq. (E.2), with the important exception that this includes a sum over positive *and negative* energy states, whereas Eq. (E.2) is only over the positive energy states. Also, since we are working in the nonrelativistic limit, the relativistic operators will be replaced by their NR counterparts obtained by expanding the lower spinor in the expansion parameter $1/c$.

The next objective is to evaluate the sum over negative energy states and remove it from the sum in Eq. (E.6). Several approximations are now made with the ultimate consequence that each denominator in Eq. (E.6) can be replaced by the constant $-2mc^2$. The assumptions that determine this are:

1. Photon energies are small compared to the rest mass of the electron: $\omega_{1,2} \ll mc^2$; this can also be expressed as $|E_{i,f} - mc^2| \ll mc^2$.

¹The pairing operator $S_c^{(e)}$ is a Green's function for a Dirac equation for the electron in an external field, which involves a frequency integral over all of frequency space—positive and negative.

²The normal operator N ensures annihilation operators are placed to the left of creation operators.

2. Only NR intermediate states $|n\rangle$ are important in the process, which can be quantified as $||E_n| - mc^2| \ll mc^2$.

Now, under these approximations, the interaction energy, restricted to a sum over negative energy states, $U_{i \rightarrow f}^{(-)}$, reads

$$U_{i \rightarrow f}^{(-)} = C \sum_{n^{(-)}} \left[\langle f | \hat{\mathbf{e}}_2 e^{-i\mathbf{k}_2 \cdot \mathbf{r}} | n \rangle \langle n | \hat{\mathbf{e}}_1 e^{i\mathbf{k}_1 \cdot \mathbf{r}} | i \rangle + \langle f | \hat{\mathbf{e}}_1 e^{i\mathbf{k}_1 \cdot \mathbf{r}} | n \rangle \langle n | \hat{\mathbf{e}}_2 e^{-i\mathbf{k}_2 \cdot \mathbf{r}} | i \rangle \right], \quad (\text{E.7})$$

where $C = -\pi\hbar e^2 m / (\mathcal{V} \sqrt{\omega_1 \omega_2})$ is the prefactor, whose form is irrelevant to the ensuing discussion.

The next step is to transform the sum in Eq. (E.7) to include positive energy states by introducing negative energy projection operators to complete the sum by closure to obtain a result for the sum. This can be achieved by introducing the projection operator $\hat{\mathcal{P}}^{(-)}$:

$$\hat{\mathcal{P}}^{(-)} = \frac{mc^2 - \gamma_4}{mc^2 - E_n^{(-)}} \approx \frac{mc^2 - \gamma_4 mc^2}{2mc^2} = \frac{1 - \gamma_4}{2}, \quad (\text{E.8})$$

$$\text{satisfying } \gamma_4 |n^{(\pm)}\rangle = \pm mc^2 |n^{(\pm)}\rangle \quad (\text{E.9})$$

The effect of $\hat{\mathcal{P}}^{(-)}$, in the limit of the NR approximations mentioned above, expressed in the rightmost expression in Eq. (E.8), and in consideration of the eigenvalue problem of γ_4 , given in Eq. (E.9) is to leave the negative energy states alone and to annihilate the positive energy states:

$$\hat{\mathcal{P}}^{(-)} |n^{(\pm)}\rangle = \begin{cases} |n^{(-)}\rangle, & \text{if } E_n < 0 \\ 0, & \text{if } E_n > 0. \end{cases} \quad (\text{E.10})$$

Thus, if we make the following replacement $|n^{(\pm)}\rangle \rightarrow \hat{\mathcal{P}}^{(-)} |n^{(\pm)}\rangle$, we can extend the sum in Eq. (E.7) to positive energy states³

³This only needs to be done once for each factor in each of the terms in the expression in Eq. (E.11) since it of course is that same state $|n\rangle$ involved in both factors

$$U_{i \rightarrow f}^{(-)} = C \sum_{n^\pm} \left[\langle f | \hat{\mathbf{e}}_2 \frac{1 - \gamma_4}{2} e^{-i\mathbf{k}_2 \cdot \mathbf{r}} | n \rangle \langle n | \hat{\mathbf{e}}_1 e^{i\mathbf{k}_1 \cdot \mathbf{r}} | i \rangle \right. \\ \left. + \langle f | \hat{\mathbf{e}}_1 \frac{1 - \gamma_4}{2} e^{i\mathbf{k}_1 \cdot \mathbf{r}} | n \rangle \langle n | \hat{\mathbf{e}}_2 e^{-i\mathbf{k}_2 \cdot \mathbf{r}} | i \rangle \right], \quad (\text{E.11})$$

after which can complete the sum via closure, $\sum_{n^\pm} |n\rangle\langle n| = 1$.

$$U_{i \rightarrow f}^{(-)} = -\frac{C}{2} \left[\langle f | \hat{\mathbf{e}}_2 (\gamma^4 - 1) e^{-i(\mathbf{k}_2 - \mathbf{k}_1) \cdot \mathbf{r}} \hat{\mathbf{e}}_1 | i \rangle \right. \\ \left. + \langle f | \hat{\mathbf{e}}_1 (\gamma^4 - 1) e^{-i(\mathbf{k}_2 - \mathbf{k}_1) \cdot \mathbf{r}} \hat{\mathbf{e}}_2 | i \rangle \right] \\ = \dots = C \mathbf{e}_1 \cdot \mathbf{e}_2 \langle f | e^{-i(\mathbf{k}_2 - \mathbf{k}_1) \cdot \mathbf{r}} | i \rangle \quad (\text{E.12})$$

The last simplification is achieved using $\gamma_4 e = -e\gamma_4$ and $\hat{\mathbf{e}}_f \hat{\mathbf{e}}_i + \hat{\mathbf{e}}_i \hat{\mathbf{e}}_f = 2\mathbf{e}_i \mathbf{e}_i$ and further that $\gamma_4 |n\rangle \sim |n\rangle$. In the dipole approximation, which is used in calculating the the two-photon decay rates in Chap. 4, this term vanishes, since the operator goes to unity and the atomic states, $|i\rangle = \text{He}(2 \ ^1S)$ and $|f\rangle = \text{He}(1 \ ^1S)$ are orthogonal. Corrections from $U_{i \rightarrow f}^{(-)}$ come into play at relative order $\alpha^2 Z^2$ and need to be included in a relativistic calculation.

In the NR and dipole approximation, we can now return to the full interaction energy in Eq. (E.5) and remove the sum over negative states. The only remaining thing to do is to replace $\hat{\mathbf{e}}_f = \gamma_\mu e_\mu$ with the corresponding NR operators. Using the definition of the γ matrices, we can rewrite operator: $\gamma_\mu e_\mu = -i\beta \boldsymbol{\alpha} \cdot \mathbf{e}_m$ where $\mathbf{e}_m = 1, 2$ the polarization of the two photons. The anticommutator $\{\alpha_i, \beta\} = 0$ can be repeatedly applied in Eq. (E.5) to make the replacement

$$\hat{\mathbf{e}}_m e^{-i\mathbf{k}_m \cdot \mathbf{r}} \longrightarrow \boldsymbol{\alpha} \cdot \mathbf{A}_m, \quad (\text{E.13})$$

where the complex conjugate \mathbf{A}_m^* replaces \mathbf{A}_m where appropriate. Furthermore, the

operator replacement, which uses the dipole approximation, is given by⁴

$$\boldsymbol{\alpha} \cdot \mathbf{A} \rightarrow \frac{\mathbf{p} \cdot \mathbf{A}}{mc} + \boldsymbol{\mu} \times \mathbf{A}, \quad (\text{E.14})$$

For this application, the spin-dependent second term can be ignored for the two-photon problem and is included in the relativistic Breit corrections applied in our study of the tuneout frequency. The combination of Eqs. (E.12) and (E.13) allows the replacement of the operators in Eq. (E.5) by operators $\mathbf{p} \cdot \mathbf{A} \propto H_{int}$ —with the sum restricted to positive energy states, and the operators shown to be of the form this completes our goal in the derivation.

E.3 RAYLEIGH SCATTERING FORMALISM

This derivation closely follows Drake *et al.* [217], and begins with Eqs. (E.2) and (E.3), but with the simplification to the case of coherent Rayleigh scattering, defined by $E_i = E_f$, $\mathbf{k}_1 = \mathbf{k}_2$, and $\omega_1 = \omega_2$. The aim is not to reproduce this result in full, but will quote the crucial results, which are necessary inclusions in calculations that account for retardation—finite wavelength—correction. As shown in Ref. [25], the subject of Chap. 5 of this dissertation, this formalism is very important as it results in different corrections than using a seemingly appropriate and similar picture of the dynamic polarizability.

Beginning with Eq. (E.6), as in the two-photon decay, the Rayleigh scattering criterion, lead to the same numerators in both terms, lead to the following form⁵ of the total interaction energy:

$$U = \frac{2\pi c^2 e^2 \hbar}{\omega \mathcal{V}} \sum_{n\pm} |\langle i | \alpha_x e^{ikz} | n \rangle|^2 \left(\frac{1}{\Delta E_n + \bar{\omega}} + \frac{1}{\Delta E_n - \bar{\omega}} \right), \quad (\text{E.15})$$

⁴This result follows from the Foldy-Woutheyson transformation, which is applicable in the limit mentioned above in deriving $U^{(-)}$, $|E_n - mc^2| < mc^2$.

⁵For simplicity, this assumes propagation along \hat{z} and polarization along \hat{x} and $\bar{\omega} \equiv \hbar\omega$.

where $e^{ikz} = 1 + ikz - (kz)^2/2 + \dots$ is the retardation expansion. In calculating the contribution from negative energy states, in the same way as above one finds a result proportional to the matrix element $\mathbf{e}_1 \cdot \mathbf{e}_2 \langle f | e^{-i(\mathbf{k}_2 - \mathbf{k}_1) \cdot \mathbf{r}} | i \rangle$. This is equal to $N\delta_{if}$ for coherent scattering. Making the same approximations leading up to Eq. (E.14), except that the photon energy is retained, though small, in the denominator. This leads to

$$U^- = -\frac{2N\pi c^2 e^2 \hbar}{\omega \mathcal{V}} \left(\frac{1}{2mc^2 + \bar{\omega}} + \frac{1}{2mc^2 - \bar{\omega}} \right) \quad (\text{E.16})$$

$$\simeq -\frac{2N\pi e^2 \hbar}{m\omega \mathcal{V}} \left[1 + \left(\frac{\bar{\omega}}{2mc^2} \right)^2 + \dots \right]. \quad (\text{E.17})$$

Inserting this into Eq. (E.15) and making the long wavelength ($e^{i\mathbf{k} \cdot \mathbf{r}} \approx 1$) approximation and further using the NP operators and neglecting the second term in $U^{(-)}$ yields

$$U = \frac{2\pi e^2 \hbar}{\omega m \mathcal{V}} \left\{ \frac{1}{m} \sum_{n+} |\langle i | p_x | n \rangle|^2 \left(\frac{1}{\Delta E_n + \bar{\omega}} + \frac{1}{\Delta E_n - \bar{\omega}} \right) - N \right\} \quad (\text{E.18})$$

giving the velocity form of the interaction. The length form is the typical gauge for the calculation, so we will consider the length gauge via $[H, x] = i\hbar p_x/m$. It turns out that the first term in Eq. (E.18), after expanding the energy denominators, actually equals N in the limit $\omega \rightarrow 0$:

$$\frac{1}{\Delta E_n + \bar{\omega}} + \frac{1}{\Delta E_n - \bar{\omega}} = \frac{2}{\Delta E_n} \left(1 + \frac{\bar{\omega}^2}{\Delta E_n^2} + \dots \right) \quad (\text{E.19})$$

The first term in Eq. (E.18) is now equal to N by the TRK sum rule:

$$\frac{2}{m\Delta E_n} \sum_{n+} |\langle i | p_x | n \rangle|^2 = N$$

Accordingly, only the second term in Eq. (E.19) contributes to the limit $\omega \rightarrow 0$. Upon

switching to the length gauge the following form is obtained⁶

$$U = \frac{2\pi e^2 \bar{\omega}}{\mathcal{V}} \sum_{n+} \langle i|x|n\rangle \langle n|x|i\rangle \left(\frac{1}{\Delta E_n + \bar{\omega}} + \frac{1}{\Delta E_n - \bar{\omega}} \right) \quad (\text{E.20})$$

$$= \frac{2\pi \bar{\omega}}{\mathcal{V}} \alpha_d(\omega), \quad (\text{E.21})$$

which can be directly compared to the dynamic polarizability, as shown in Eq. (E.20). The zeroes in the coherent Rayleigh scattering cross section, $U(\omega)$, clearly match those in the dynamic polarizability, $\alpha_d(\omega)$, when the long wavelength approximation $kz \ll 1$ is made, interpreting the tuneout frequency equivalent in this limit.

If retardation—finite wavelength—corrections are considered, however, then the higher order terms enter into Eq. (E.15) and this is no longer the case. In this limit, the zeroes of the Rayleigh scattering cross section do not coincide with the dynamic polarizability, as shown explicitly in Ref. [217] in the velocity gauge.

⁶This involves pulling out a factor of $\frac{\bar{\omega}^2}{\Delta E_n^2}$ and subsequently resumming to infinity.

APPENDIX F

Integration to Obtain the Decay Rate

The purpose of this Appendix is to give a simple way to sum over the two independent polarization vectors $\hat{\epsilon}_1$ and $\hat{\epsilon}_2$ perpendicular to \mathbf{k}_1 and \mathbf{k}_2 in order to obtain the angular correlation function $(1 + \cos^2 \theta_{12})$.

Let \mathbf{k}_1 and \mathbf{k}_2 define the xy -plane (the collision plane). Then two possible independent choices for $|\hat{\epsilon}_1 \cdot \hat{\epsilon}_2|^2$ are first, choose $\hat{\epsilon}_1 = \hat{\mathbf{e}}_z$, $\hat{\epsilon}_2 = \hat{\mathbf{e}}_z$ perpendicular to the xy -plane. Then $|\hat{\epsilon}_1 \cdot \hat{\epsilon}_2|^2 = 1$. Second, choose $\hat{\epsilon}_1 = \hat{\mathbf{k}}_1 \times \hat{\mathbf{e}}_z$, $\hat{\epsilon}_2 = \hat{\mathbf{k}}_2 \times \hat{\mathbf{e}}_z$ so that they both lie in the xy -plane. Then, since by assumption $\hat{\mathbf{k}}_i \cdot \hat{\mathbf{e}}_z = 0$,

$$\begin{aligned} |\hat{\epsilon}_1 \cdot \hat{\epsilon}_2|^2 &= |(\hat{\mathbf{k}}_1 \times \hat{\mathbf{e}}_z) \cdot (\hat{\mathbf{k}}_2 \times \hat{\mathbf{e}}_z)|^2 \\ &= |\hat{\mathbf{k}}_1 \cdot \hat{\mathbf{k}}_2|^2 \\ &= \cos^2 \theta_{12} \end{aligned}$$

The sum of both polarization contributions is thus a factor of $1 + \cos^2 \theta_{12}$.

Similarly for the case of single-photon transitions, we need to integrate $|\hat{\epsilon} \cdot \mathbf{Q}|^2$ over solid angles $d\Omega$ for the direction of emission \mathbf{k} . For purposes of the integration, assume that \mathbf{Q} points in the z -direction. Then two possible independent choices for $\hat{\epsilon}$ are first, choose $\hat{\epsilon}_1$ to point in the $\hat{\mathbf{k}} \times \hat{\mathbf{Q}}$ direction. In this case, $\hat{\epsilon}_1 \cdot \mathbf{Q} = 0$, and so it does not contribute. Second, choose $\hat{\epsilon}_2$ to lie in the (\mathbf{k}, \mathbf{Q}) plane orthogonal to $\hat{\epsilon}_1$. Then if $\hat{\mathbf{k}} \cdot \hat{\mathbf{e}}_z = \cos \theta$, $\hat{\epsilon}_2 \cdot \hat{\mathbf{e}}_z = \sin \theta$, and the angular integral is

$$\begin{aligned} \int_{4\pi} |\hat{\epsilon}_2 \cdot \mathbf{Q}|^2 d\Omega &= |\mathbf{Q}|^2 \int_{4\pi} \sin^2 \theta d\Omega \\ &= \frac{8\pi}{3} |\mathbf{Q}|^2 \end{aligned} \tag{F.1}$$

APPENDIX G

Derivation of Algebraic Relations from Perturbation Theory

This Appendix will demonstrate that perturbation theory can be used to obtain the algebraic relations that are the subject of this Chap. 4. We will consider explicitly the relationship for the first-order mass polarization coefficients between the length and velocity forms of single-photon transitions (cf. Sec. 4.8.2), given by

$$C_p - C_r = -2. \quad (\text{A1})$$

The single-photon decay rate, given in Eq. (4.14), is

$$w_{i,f} = \frac{4}{3} \alpha \omega_{i,f} |\langle i | \mathbf{Q}_x | f \rangle|^2.$$

We will work in centre-of-mass coordinates, using reduced-mass atomic units, given in Eq. (4.37), such that the length and velocity operators are $\boldsymbol{\rho} \equiv \boldsymbol{\rho}_1 + \boldsymbol{\rho}_2$ and $\boldsymbol{\nabla} \equiv \boldsymbol{\nabla}_1 + \boldsymbol{\nabla}_2$, respectively. The condition that the length and velocity gauge should be equal with all finite-mass effects included is

$$\begin{aligned} Z_p^2 \left(\frac{\mu}{m_e} \right)^3 \Delta E |\langle i | \boldsymbol{\nabla} | f \rangle|^2 &= Z_r^2 \left(\frac{\mu}{m_e} \right) \Delta E^3 |\langle i | \boldsymbol{\rho} | f \rangle|^2 \\ |\langle i | \boldsymbol{\nabla} | f \rangle|^2 &= \left(\frac{Z_r}{Z_p} \right)^2 \left(\frac{\mu}{m_e} \right)^{-2} \Delta E^2 |\langle i | \boldsymbol{\rho} | f \rangle|^2, \end{aligned} \quad (\text{A2})$$

where we have used that $\omega_{i,f} = \Delta E_{i,f} \equiv \Delta E$ in atomic units and all finite-mass dependence besides mass polarization has been factored out. From the definitions of Z_r, Z_p (cf. Sec. 4.5.1) and μ , it follows that

$$\left(\frac{Z_r}{Z_p}\right)^2 \left(\frac{\mu}{m_e}\right)^{-2} = 1 - 2\mu/M + \dots$$

The fundamental perturbation equations

$$\begin{aligned} & \left(H_0 + \frac{\mu}{M} \nabla_{\rho_1} \cdot \nabla_{\rho_2}\right) \left(|\Psi\rangle^{(0)} + \frac{\mu}{M} |\Psi\rangle^{(1)} + \dots\right) \\ &= \left(E^{(0)} + \frac{\mu}{M} E^{(1)} + \dots\right) \left(|\Psi\rangle^{(0)} + \frac{\mu}{M} |\Psi\rangle^{(1)} + \dots\right) \end{aligned}$$

can then be solved to write ΔE and the squared dipole matrix elements $|\langle i|\rho|f\rangle|^2$ and $|\langle i|\nabla|f\rangle|^2$ as expansions in μ/M . These are

$$\begin{aligned} (\Delta E)^2 &= \left[\Delta E^{(0)} + \frac{\mu}{M} \Delta E^{(1)} + \dots\right]^2 \\ &= [\Delta E^{(0)}]^2 + 2\frac{\mu}{M} \Delta E^{(0)} \Delta E^{(1)} + \dots, \\ |\langle i|\nabla|f\rangle|^2 &= \left[\langle i|\nabla|f\rangle^{(0)} + \frac{\mu}{M} \langle i|\nabla|f\rangle^{(1)} + \dots\right]^2 \\ &= |\langle i|\nabla|f\rangle^{(0)}|^2 + 2\frac{\mu}{M} |\langle i|\nabla|f\rangle^{(1)}|^2 + \dots, \quad \text{and} \\ |\langle i|\rho|f\rangle|^2 &= \left[\langle i|\rho|f\rangle^{(0)} + \frac{\mu}{M} \langle i|\rho|f\rangle^{(1)} + \dots\right]^2 \\ &= |\langle i|\rho|f\rangle^{(0)}|^2 + 2\frac{\mu}{M} |\langle i|\rho|f\rangle^{(1)}|^2 + \dots. \end{aligned}$$

The first-order dipole matrix element terms $\langle i|\nabla|f\rangle^{(1)}$ and $\langle i|\rho|f\rangle^{(1)}$ each contain two terms, arising from first-order corrections to both the initial and final state wave functions. Finally, putting these expansions back into Eq. (A1) gives

$$\begin{aligned} & (1 - 2\mu/M + \dots) \left((\Delta E^{(0)})^2 + 2\frac{\mu}{M} \Delta E^{(0)} \Delta E^{(1)} + \dots\right) \\ & \times \left((R^{(0)})^2 + 2\frac{\mu}{M} (R^{(1)})^2 + \dots\right) \\ &= (P^{(0)})^2 + 2\frac{\mu}{M} (P^{(1)})^2 + \dots, \end{aligned}$$

where the perturbation coefficients for the length and velocity dipole matrix elements are written in a slightly abbreviated notation using $R^{(n)} \equiv |\langle i | \rho | f \rangle^{(n)}|$ and $P^{(n)} \equiv |\langle i | \nabla | f \rangle^{(n)}|$, respectively. Solving these perturbation equations yields

$$(\Delta E^{(0)} R^{(0)})^2 = (P^{(0)})^2$$

in zeroth-order, successfully recovering the commutator identity. In first-order, we obtain

$$\Delta E^{(0)} \Delta E^{(1)} (R^{(0)})^2 + (\Delta E^{(0)} R^{(1)})^2 - (\Delta E^{(0)} R^{(1)})^2 = (P^{(1)})^2.$$

Rearranging and using the zeroth-order identity gives

$$2 \left(\frac{P^{(1)}}{P^{(0)}} \right)^2 - 2 \frac{\Delta E^{(0)} \Delta E^{(1)} (R^{(0)})^2 + (\Delta E^{(0)} R^{(1)})^2}{(\Delta E^{(0)} R^{(0)})^2} = -2.$$

By identifying

$$C_p \equiv 2 \left(\frac{P^{(1)}}{P^{(0)}} \right)^2 \quad \text{and} \quad (A3)$$

$$C_r \equiv 2 \frac{\Delta E^{(0)} \Delta E^{(1)} (R^{(0)})^2 + (\Delta E^{(0)} R^{(1)})^2}{(\Delta E^{(0)} R^{(0)})^2}, \quad (A4)$$

we have recovered the desired algebraic relation in Eq. (A1), connecting the first-order length and velocity mass polarization coefficients that arise in transition rates in single-photon transitions using perturbation theory.

REFERENCES

- [1] D. Brewster, *Memoirs of the Life, Writings, and Discoveries of Sir Isaac Newton*, Vol. 2 (Thomas Constable and Co., Edinburgh, 1855) p. 158.
- [2] C. Patrignani and others (Particle Data Group), Chin. Phys. C (2016).
- [3] R. Adam and others (Planck Collaboration), Astron. Astrophys. **594**, A1 (2016).
- [4] P. J. E. Peebles and B. Ratra, Rev. Mod. Phys. **75**, 559 (2003).
- [5] M. Dine and A. Kusenko, Rev. Mod. Phys. **76**, 1 (2003).
- [6] O. W. Greenberg, Phys. Rev. Lett. **89**, 231602 (2002).
- [7] M. Ahmadi *et al.*, Nature (London) **541**, 506 (2017).
- [8] M. Safronova, D. Budker, D. DeMille, D. F. J. Kimball, A. Derevianko, and C. W. Clark, Rev. Mod. Phys. **90**, 025008 (2018).
- [9] P. Scott, *Searches for Particle Dark Matter: Dark Stars, Dark Galaxies, Dark Halos and Global Supersymmetric Fits*, Ph.D. thesis, Department of Physics, Stockholm University, (2010) pp. 15–24.
- [10] D. Budker, P. W. Graham, M. Ledbetter, S. Rajendran, and A. O. Sushkov, Phys. Rev. X **4**, 021030 (2014).
- [11] J. J. Hudson, D. M. Kara, I. Smallman, B. E. Sauer, M. R. Tarbutt, and E. A. Hinds, Nature (London) **473**, 493 (2011).

- [12] ACME Collaboration, *Nature (London)* **562**, 355 (2018).
- [13] T. S. Roussy, L. Caldwell, T. Wright, W. B. Cairncross, Y. Shagam, K. B. Ng, N. Schlossberger, S. Y. Park, A. Wang, J. Ye, and E. A. Cornell, *Science* **381**, 46 (2023).
- [14] T. Ibrahim, A. Itani, and P. Nath, *Phys. Rev. D* **90**, 055006 (2014).
- [15] A. Vutha, M. Horbatsch, and E. Hessels, *Atoms* **6**, 3 (2018).
- [16] R. Lambo, G. Koyanagi, M. Horbatsch, R. Fournier, and E. Hessels, *Mol. Phys.* **121**, e2232051 (2023).
- [17] Y. Nakai and M. Reece, *J. High Energy Phys.* **2017** (8), 1.
- [18] J. D. Wells, *Phys. Rev. D* **71**, 015013 (2005).
- [19] M. Benedikt, A. Blondel, P. Janot, M. Mangano, and F. Zimmermann, *Nat. Phys.* **16**, 402 (2020).
- [20] X. Fan, T. Myers, B. Sukra, and G. Gabrielse, *Phys. Rev. Lett.* **130**, 071801 (2023).
- [21] D. Aguillard and others (Muon g-2 Collaboration), *Phys. Rev. Lett.* **131**, 161802 (2023).
- [22] R. Pohl, A. Antognini, F. Nez, F. D. Amaro, F. Biraben, J. M. R. Cardoso, D. S. Covita, A. Dax, S. Dhawan, L. M. P. Fernandes, A. L. Gouvea, T. Graf, T. W. Hänsch, P. Indelicato, L. Julien, K. Kirch, A. Knecht, Y.-W. Liu, J. Marschall, J. Martino, C. M. B. Monteiro, F. Mulhauser, F. Nez, K. Schuhmann, C. Schwob, D. Taqqu, A. Voss, J. Vogelsang, and C. Weinheimer, *Nature (London)* **466**, 213 (2010).
- [23] N. Bezginov, T. Valdez, M. Horbatsch, A. Marsman, A. Vutha, and E. Hessels, *Science* **365**, 1007 (2019).

- [24] A. T. Bondy, D. C. Morton, and G. W. F. Drake, Phys. Rev. A **102**, 052807 (2020).
- [25] B. Henson, J. Ross, K. Thomas, C. Kuhn, D. Shin, S. Hodgman, Y.-H. Zhang, L.-Y. Tang, G. W. F. Drake, A. T. Bondy, A. Truscott, and K. G. H. Baldwin, Science **376**, 199 (2022).
- [26] A. T. Bondy and G. W. F. Drake, Atoms **11**, 41 (2023).
- [27] A. T. Bondy and G. W. F. Drake, Phys. Rev. A **108**, 032807 (2023).
- [28] M. González-Alonso, O. Naviliat-Cuncic, and N. Severijns, Prog. Part. Nucl. Phys. **104**, 165 (2019).
- [29] G. W. F. Drake and S. P. Goldman, Can. J. Phys. **77**, 835 (2000).
- [30] D. R. Hartree, in *Mathematical Proceedings of the Cambridge Philosophical Society*, Vol. 24 (Cambridge University Press, 1928) pp. 89–110.
- [31] E. Tiesinga, P. J. Mohr, D. B. Newell, and B. N. Taylor, J. Phys. Chem. Ref. Data **50** (2021).
- [32] A. R. Edmonds, *Angular Momentum in Quantum Mechanics*, 2nd ed. (Princeton University Press, Princeton, NJ, 1968).
- [33] M. Abramowitz and I. A. Stegun, *Handbook of Mathematical Functions with Formulas, Graphs, and Mathematical Tables*, Vol. 55 (US Government printing office, 1968).
- [34] G. W. F. Drake, in *Encyclopedia of Applied Physics*, Vol. 23, edited by G. L. Trigg (Wiley-VCH Verlag GmbH, New York, 1998) pp. 121–149.
- [35] E. L. Ince, *Ordinary Differential Equations* (Longmans, Green and Co., 1926) pp. 231–237.
- [36] B. Klahn and W. A. Bingel, Theor. Chim. Acta **44**, 27 (1977).

- [37] B. Klahn and W. A. Bingel, *Theor. Chim. Acta* **44**, 9 (1977).
- [38] G. W. F. Drake, Special Topics on Precision Measurement in Atomic Physics (2019), available at http://drake.sharcnet.ca/wiki/index.php/Lecture_Notes#WIPM_Lecture_Notes (accessed June 19, 2024).
- [39] G. W. F. Drake, Notes on solving the schrödinger equation in hylleraas coordinates for heliumlike atoms (2024), lecture notes. Available at http://drake.sharcnet.ca/wiki/index.php/Theory_Notes (accessed May 3, 2024).
- [40] H. A. Bethe and E. E. Salpeter, *Quantum Mechanics of One- and Two-electron Atoms* (Dover Publications, Mineola, NY, 2008).
- [41] I. Newton, *Philosophiae Naturalis Principia Mathematica* (Royal Society, London, 1687) translated to English as "The Mathematical Principles of Natural Philosophy".
- [42] L. L. Moffatt, *Radiative Decay Rates of Metastable Triplet Helium and Helium-like Ions*, Ph.D. thesis, University of Windsor, Canada, (2013) pp. 92–93.
- [43] G. W. F. Drake, in *Springer Handbook of Atomic, Molecular, and Optical Physics*, edited by G. W. F. Drake (Springer, 2023) pp. 199–216.
- [44] E. A. Hylleraas and B. Undheim, *Z. Phys.* **65**, 759 (1930).
- [45] J. MacDonald, *Phys. Rev.* **43**, 830 (1933).
- [46] G. W. F. Drake, M. M. Cassar, and R. A. Nistor, *Phys. Rev. A* **65**, 054501 (2002).
- [47] E. M. R. Petrimoulx, A. T. Bondy, E. A. Ene, L. A. Sati, and G. W. F. Drake, *Can. J. Phys.* (2024).
- [48] G. W. F. Drake, *Phys. Rev. Lett.* **59**, 1549 (1987).
- [49] G. W. F. Drake and A. Makowski, *J. Opt. Soc. Am. B* **5**, 2207 (1988).

[50] G. W. F. Drake and Z.-C. Yan, Phys. Rev. A **46**, 2378 (1992).

[51] E. Schulhoff, *Excitation and Ionization of ${}^6\text{Li}$ ions Following Beta-Decay of ${}^6\text{He}$.*, Master's thesis, University of Windsor, Canada, (2010) pp. 40–57.

[52] G. W. F. Drake, in *Long-Range Casimir Forces: Theory and Recent Experiments on Atomic Systems*, edited by F. S. Levin and D. A. Micha (Springer, 1993) pp. 107–217.

[53] B. Klahn and W. A. Bingel, Int. J. of Quantum Chem. **11**, 943 (1977).

[54] G. W. F. Drake, Q. Wu, and Z. Zhong, in *Modeling and Numerical Simulations I*, edited by M. Schlesinger (Springer, 2009) pp. 33–66.

[55] T. Kato, Commun. Pure Appl. Math. **10**, 151 (1957).

[56] Y. I. Kurokawa, H. Nakashima, and H. Nakatsuji, in *Adv. Quantum Chem.*, Vol. 73 (Elsevier, 2016) pp. 59–79.

[57] S. Bubin and L. Adamowicz, J. Chem. Phys. **136** (2012).

[58] C. Schwartz, Int. J. Mod. Phys. E **15**, 877 (2006).

[59] H. Nakashima and H. Nakatsuji, J. Chem. Phys. **127** (2007).

[60] D. Aznabaev, A. Bekbaev, and V. I. Korobov, Phys. Rev. A **98**, 012510 (2018).

[61] G. W. F. Drake, Phys. Rev. A **18**, 820 (1978).

[62] G. W. F. Drake, Program notes: Energy and wave function files (2024), lecture notes. Available at https://drake.sharcnet.ca/wiki/index.php/Program_Notes (accessed May 4, 2024).

[63] H. Margenau and G. M. Murphy, *The Mathematics of Physics and Chemistry* (D. Van Nostrand Company, 1956) pp. 382–383.

[64] C. Wu, Rev. Mod. Phys. **31**, 783 (1959).

- [65] K. S. Krane, *Introductory Nuclear Physics* (John Wiley & Sons, 1988) pp. 272–277.
- [66] H. Becquerel, Comptes rendus de l'Académie des sciences **122**, 420 (1896).
- [67] J. Chadwick, Verh. Phys. Gesell **16**, 3 (1914).
- [68] A. Franklin, Spontaneous Generations **4**, 71 (2010).
- [69] C. D. Ellis and W. A. Wooster, Proc. R. Soc. London Sect. A **117**, 109 (1927).
- [70] J. Chalmers, in *Mathematical Proceedings of the Cambridge Philosophical Society*, Vol. 28 (Cambridge University Press, 1932) pp. 328–337.
- [71] L. M. Brown, Phys. Today **31**, 23 (1978).
- [72] N. Bohr, Nature (London) **138**, 25 (1936).
- [73] J. Chadwick, Proc. R. Soc. London Sect. A **136**, 692 (1932).
- [74] E. Fermi, Z. Phys. **88**, 161 (1934).
- [75] F. L. Wilson, Am. J. Phys. **36**, 1150 (1968).
- [76] A. Pais, *Inward Bound: Of Matter and Forces in the Physical World* (Clarendon Press, 1986) p. 418.
- [77] G. Gamow and E. Teller, Phys. Rev. **49**, 895 (1936).
- [78] S. Weinberg, Phys. Rev. Lett. **19**, 1264 (1967).
- [79] S. Weinberg, Current Science **116**, 193 (2019).
- [80] C. Rubbia, Rev. Mod. Phys. **57**, 699 (1985).
- [81] H. A. Bethe, Phys. Rev. **55**, 434 (1939).
- [82] A. G. W. Cameron, Publ. Astron. Soc. Pac. **69**, 201 (1957).

[83] J. J. Gómez-Cadenas, J. Martín-Albo, J. Menéndez, M. Mezzetto, F. Monrabal, and M. Sorel, Riv. Nuovo Cimento **46**, 1 (2024).

[84] A. B. McDonald, Rev. Mod. Phys. **88**, 030502 (2016).

[85] T.-D. Lee and C.-N. Yang, Phys. Rev. **104**, 254 (1956).

[86] E. C. Sudarshan and R. Marshak, Phys. Rev. **109**, 1860 (1958).

[87] R. P. Feynman and M. Gell-Mann, Phys. Rev. **109**, 193 (1958).

[88] J. J. Sakurai, Nuovo Cimento **7**, 649 (1958).

[89] R. P. Feynman, “*Surely You’re Joking, Mr. Feynman!*”: *Adventures of a Curious Character* (W. W. Norton & Company, 1985).

[90] G. Johnson, The Jaguar and the Fox, *The Atlantic Monthly* (2000), available at <https://www.theatlantic.com/magazine/archive/2000/07/the-jaguar-and-the-fox/378264/> (accessed April 30, 2024).

[91] O. Kofoed-Hansen and C. Christensen, in *Beta Decay/Betazerfall*, edited by M. Fierz and W. Heisenberg (Springer, 1962) pp. 1–105.

[92] A. Brosi, A. Galonsky, B. Ketelle, and H. Willard, Nucl. Phys. **33**, 353 (1962).

[93] J. Allen, R. Burman, W. Herrmannsfeldt, P. Stähelin, and T. Braid, Phys. Rev. **116**, 134 (1959).

[94] C. Johnson, F. Pleasonton, and T. Carlson, Phys. Rev. **132**, 1149 (1963).

[95] V. A. Kostelecky, *CPT And Lorentz Symmetry-Proceedings Of The Fifth Meeting* (World Scientific, 2010).

[96] W. Greiner and B. Müller, *Gauge Theory of Weak Interactions*, 3rd ed. (Springer-Verlag Berlin Heidelberg, 2000).

- [97] X. Fléchard, E. Liénard, A. Méry, D. Rodríguez, G. Ban, D. Durand, F. Duval, M. Herbane, M. Labalme, F. Mauger, O. Naviliat-Cuncic, J. C. Thomas, and P. Velten, *Phys. Rev. Lett.* **101**, 212504 (2008).
- [98] P. Müller, Y. Bagdasarova, R. Hong, A. Leredde, K. G. Bailey, X. Fléchard, A. García, B. Graner, A. Knecht, O. Naviliat-Cuncic, and J. Wilcox, *Phys. Rev. Lett.* **129**, 182502 (2022).
- [99] J. Jackson, S. Treiman, and H. Wyld Jr, *Nucl. Phys.* **4**, 206 (1957).
- [100] M. Gonzalez-Alonso and O. Naviliat-Cuncic, *Phys. Rev. C* **94**, 035503 (2016).
- [101] V. Araujo-Escalona, D. Atanasov, X. Fléchard, P. Alfaurt, P. Ascher, B. Blank, L. Daudin, M. Gerboux, J. Giovinazzo, S. Grévy, and the ISOLDE Collaboration, *Phys. Rev. C* **101**, 055501 (2020).
- [102] A. D. Sakharov, *Pisma Zh. Eksp. Teor. Fiz.* **5**, 32 (1967).
- [103] G. Lüders, *Dan. Mat. Fys. Medd.* **28**, 1 (1954).
- [104] P. Herczeg, *Prog. Part. Nucl. Phys.* **46**, 413 (2001).
- [105] T. Bhattacharya, V. Cirigliano, S. D. Cohen, A. Filipuzzi, M. Gonzalez-Alonso, M. L. Graesser, R. Gupta, and H.-W. Lin, *Phys. Rev. D* **85**, 054512 (2012).
- [106] R. Barbieri and R. N. Mohapatra, *Phys. Rev. D* **39**, 1229 (1989).
- [107] V. Cirigliano, M. Gonzalez-Alonso, and M. L. Graesser, *J. High Energy Phys.* **2013** (2), 1.
- [108] S. Profumo, M. J. Ramsey-Musolf, and S. Tulin, *Phys. Rev. D* **75**, 075017 (2007).
- [109] N. Severijns, M. Beck, and O. Naviliat-Cuncic, *Rev. Mod. Phys.* **78**, 991 (2006).
- [110] X. Fléchard, P. Velten, E. Liénard, A. Méry, D. Rodríguez, G. Ban, D. Durand, F. Mauger, O. Naviliat-Cuncic, and J. Thomas, *J. Phys. G* **38**, 055101 (2011).

[111] C. Couratin, P. Velten, X. Fléchard, E. Liénard, G. Ban, A. Cassimi, P. Delahaye, D. Durand, D. Hennecart, F. Mauger, A. Méry, O. Naviliat-Cuncic, Z. Patyk, D. Rodríguez, K. Siegień-Iwaniuk, and J.-C. Thomas, Phys. Rev. Lett. **108**, 243201 (2012).

[112] C. Couratin, X. Fabian, B. Fabre, B. Pons, X. Fléchard, E. Liénard, G. Ban, M. Breitenfeldt, P. Delahaye, D. Durand, and F. Mauger, Phys. Rev. A **88**, 041403 (2013).

[113] X. Fabian, X. Fléchard, B. Pons, E. Liénard, G. Ban, M. Breitenfeldt, C. Couratin, P. Delahaye, D. Durand, P. Finlay, and F. Mauger, Phys. Rev. A **97**, 023402 (2018).

[114] T. Carlson, F. Pleasonton, and C. Johnson, Phys. Rev. **129**, 2220 (1963).

[115] R. Hong, A. Leredde, Y. Bagdasarova, X. Fléchard, A. García, A. Knecht, P. Müller, O. Naviliat-Cuncic, J. Pedersen, E. Smith, and J. Wilcox, Phys. Rev. A **96**, 053411 (2017).

[116] O. Aviv, S. Vaintraub, T. Hirsh, A. Dhal, M. L. Rappaport, D. Melnik, O. Heber, D. Schwalm, D. Zajfman, K. Blaum, and M. Hass, in *J. Phys. Conf. Ser.*, Vol. 337 (IOP Publishing, 2012) p. 012020.

[117] I. Mardor, O. Aviv, M. Avrigeanu, D. Berkovits, A. Dahan, T. Dickel, I. Eliyahu, M. Gai, I. Gavish-Segev, S. Halfon, M. Hass, T. Hirsh, B. Kaiser, D. Kijel, A. Kreisel, M. Mardor, M. Paul, J. Rodnizki, L. Sagiv, A. Shor, and M. Tessler, Eur. Phys. J. A **54**, 1 (2018).

[118] N. Scielzo, S. Freedman, B. Fujikawa, and P. Vetter, Phys. Rev. Lett. **93**, 102501 (2004).

[119] P. Vetter, J. Abo-Shaeer, S. Freedman, and R. Maruyama, Phys. Rev. C **77**, 035502 (2008).

[120] E. G. Adelberger, C. Ortiz, A. García, H. E. Swanson, M. Beck, O. Tengblad, M. J. G. Borge, I. Martel, H. Bichsel, and the ISOLDE Collaboration, Phys. Rev. Lett. **83**, 1299 (1999).

[121] P. Ascher, B. Blank, S. Grévy, G. Ban, E. Liénard, X. Fléchard, G. Quéméner, J. Giovinazzo, M. Gerbaux, V. Araujo-Escalona, P. Alfaurt, D. Atanasov, F. Cresto, L. Daudin, T. Kurtukian-Nieto, M. Pomorski, N. Severijns, S. Vanlangendonck, M. Versteegen, and D. Zakoucky, *WISARD: Weak-interaction studies with ^{32}Ar decay*, Tech. Rep. (University of Bordeaux, 2016).

[122] A. Gorelov, D. Melconian, W. P. Alford, D. Ashery, G. Ball, J. A. Behr, P. G. Bricault, J. M. D'Auria, J. Deutsch, J. Dilling, M. Dombsky, P. Dubé, J. Fingler, U. Giesen, F. Glück, S. Gu, O. Häusser, K. P. Jackson, B. K. Jennings, M. R. Pearson, T. J. Stocki, T. B. Swanson, and M. Trinczek, Phys. Rev. Lett. **94**, 142501 (2005).

[123] G. Li, R. Segel, N. D. Scielzo, P. F. Bertone, F. Buchinger, S. Caldwell, A. Chaudhuri, J. A. Clark, J. E. Crawford, C. M. Deibel, J. Greene, S. Gulick, D. Lascar, A. F. Levand, A. Pérez Galván, K. S. Sharma, J. Van Schelt, R. M. Yee, and B. J. Zabransky, Phys. Rev. Lett. **110**, 092502 (2013).

[124] M. G. Sternberg, R. Segel, N. D. Scielzo, G. Savard, J. A. Clark, P. F. Bertone, F. Buchinger, M. Burkey, S. Caldwell, A. Chaudhuri, J. E. Crawford, C. M. Deibel, J. Greene, S. Gulick, D. Lascar, A. F. Levand, G. Li, A. Pérez Galván, K. S. Sharma, J. Van Schelt, R. M. Yee, and B. J. Zabransky, Phys. Rev. Lett. **115**, 182501 (2015).

[125] M. T. Burkey, G. Savard, A. T. Gallant, N. D. Scielzo, J. A. Clark, T. Y. Hirsh, L. Varriano, G. H. Sargsyan, K. D. Launey, M. Brodeur, M. G. Sternberg, R. Segel, P. F. Bertone, F. Buchinger, S. Caldwell, A. Chaudhuri, J. E. Crawford, C. M. Deibel, J. Greene, S. Gulick, D. Lascar, A. F. Levand, G. Li, A. Pérez Galván, K. S. Sharma, J. Van Schelt, R. M. Yee, and B. J. Zabransky, Phys. Rev. Lett. **128**, 202502 (2022).

- [126] E. Liénard, G. Ban, C. Couratin, P. Delahaye, D. Durand, X. Fabian, B. Fabre, X. Fléchard, P. Finlay, F. Mauger, C. Rigollet, F. Duval, and T. Gravestock, *Hyperfine Interact.* **236**, 1 (2015).
- [127] F. Glück, S. Baeßler, J. Byrne, M. van der Grinten, F. Hartmann, W. Heil, I. Konorov, G. Petzoldt, Y. Sobolev, and O. Zimmer, *Eur. Phys. J. A* **23**, 135 (2005).
- [128] B. Collett *et al.*, *Rev. Sci. Instrum.* **88** (2017).
- [129] X. Fabian, F. Mauger, G. Quéméner, P. Velten, G. Ban, C. Couratin, P. Delahaye, D. Durand, B. Fabre, P. Finlay, D. Blanchard, and J. Guillot, in *TCP 2014: Proceedings of the 6th International Conference on Trapped Charged Particles and Fundamental Physics, held in Takamatsu, Japan, 1-5, December 2014* (IOP Publishing, 2017) pp. 165–173.
- [130] R. Hong, M. G. Sternberg, and A. Garcia, *Am. J. Phys.* **85**, 45 (2017).
- [131] L. Wauters and N. Vaeck, *Phys. Rev. C* **53**, 497 (1996).
- [132] E. E. Schulhoff and G. W. F. Drake, *Phys. Rev. A* **92**, 050701 (2015).
- [133] E. E. Schulhoff, *Calculated Charge State Distributions and Anisotropies following the β -Decay of ${}^6\text{He}$* , Ph.D. thesis, University of Windsor, Canada (2022).
- [134] A. M. Frolov and M. B. Ruiz, *Phys. Rev. A* **82**, 042511 (2010).
- [135] J. Chizma, G. Karl, and V. Novikov, *Phys. Rev. C* **58**, 3674 (1998).
- [136] J. Cooper and T. Åberg, *Nucl. Phys.* **298**, 239 (1978).
- [137] A. Saenz and P. Froelich, *Phys. Rev. C* **56**, 2132 (1997).
- [138] A. Winther, *Mat. Fys. Medd. Dan. Vid. Selsk.* **27** (1952).
- [139] T. A. Carlson, C. Nestor Jr, T. C. Tucker, and F. Malik, *Phys. Rev.* **169**, 27 (1968).

- [140] C. Froese, Can. J. Phys. **41**, 1895 (1963).
- [141] J. S. Sims and S. A. Hagstrom, J. Chem. Phys. **55**, 4699 (1971).
- [142] J. S. Sims and S. Hagstrom, Phys. Rev. A **4**, 908 (1971).
- [143] C. Winstead and P. Langhoff, J. Chem. Phys. **95**, 3107 (1991).
- [144] S. Goldman and G. W. F. Drake, Can. J. Phys. **61**, 198 (1983).
- [145] J. A. Samson, Z. He, L. Yin, and G. Haddad, J. Phys. B **27**, 887 (1994).
- [146] J. A. Samson, W. C. Stolte, Z.-X. He, J. N. Cutler, Y. Lu, and R. Bartlett, Phys. Rev. A **57**, 1906 (1998).
- [147] R. C. Forrey, Z.-C. Yan, H. Sadeghpour, and A. Dalgarno, Phys. Rev. Lett. **78**, 3662 (1997).
- [148] H. Friedrich, *Theoretical Atomic Physics*, Vol. 3 (Springer, 2017).
- [149] S. Carter and H. Kelly, Phys. Rev. A **24**, 170 (1981).
- [150] M. Sagurton, R. Bartlett, J. Samson, Z. He, and D. Morgan, Phys. Rev. A **52**, 2829 (1995).
- [151] P. Bergstrom, K. Hino, and J. Macek, Phys. Rev. A **51**, 3044 (1995).
- [152] J.-Z. Tang and I. Shimamura, Phys. Rev. A **52**, R3413 (1995).
- [153] A. Kheifets and I. Bray, Phys. Rev. A **54**, R995 (1996).
- [154] K. Meyer, C. Greene, and I. Bray, Phys. Rev. A **52**, 1334 (1995).
- [155] D. Proulx and R. Shakeshaft, Phys. Rev. A **48**, R875 (1993).
- [156] M. Pont and R. Shakeshaft, Phys. Rev. A **51**, R2676 (1995).
- [157] M. Pont, R. Shakeshaft, F. Maulbetsch, and J. Briggs, Phys. Rev. A **53**, 3671 (1996).

- [158] F. Maulbetsch and J. Briggs, J. Phys. B. **26**, 1679 (1993).
- [159] H. Sadeghpour, Can. J. Phys. **74**, 727 (1996).
- [160] B. McLaughlin, J. Phys. B. **46**, 075204 (2013).
- [161] M. McIntyre and M. Scott, Phys. Rev. A **89**, 043418 (2014).
- [162] U. Kleiman, M. Pindzola, and F. Robicheaux, Phys. Rev. A **72**, 022707 (2005).
- [163] A. Kheifets and I. Bray, Phys. Rev. A **58**, 4501 (1998).
- [164] H. Hart and L. Feng, J. Phys. B. **34**, L601 (2001).
- [165] R. G. Sachs, Phys. Today **35**, 46 (1982).
- [166] M. Goeppert Mayer, *Über Elementarakte mit zwei Quantensprünge*, Ph.D. thesis, University of Göttingen (1930).
- [167] P. A. M. Dirac, Proc. R. Soc. London Sect. A **113**, 621 (1927).
- [168] P. A. M. Dirac, Proc. R. Soc. London Sect. A **114**, 243 (1927).
- [169] P. A. M. Dirac, Proc. R. Soc. London Sect. A **114**, 710 (1927).
- [170] T. Pauly, A. T. Bondy, K. R. Hamilton, N. Douguet, X.-M. Tong, D. Chetty, and K. Bartschat, Phys. Rev. A **102**, 013116 (2020).
- [171] S. Meister, A. T. Bondy, K. Schnorr, S. Augustin, H. Lindenblatt, F. Trost, X. Xie, M. Braune, R. Treusch, B. Manschwetus, N. Schirmel, N. Douguet, T. Pfeifer, K. Bartschat, and R. Moshammer, Phys. Rev. A **102**, 062809 (2020).
- [172] S. Meister, A. T. Bondy, K. Schnorr, S. Augustin, H. Lindenblatt, F. Trost, X. Xie, M. Braune, B. Manschwetus, N. Schirmel, H. Redlin, N. Douguet, T. Pfeifer, K. Bartschat, and R. Moshammer, Eur. Phys. J. D **75**, 1 (2021).
- [173] D. Bharti, H. Srinivas, F. Shobeyri, A. T. Bondy, S. Saha, K. Hamilton, R. Moshammer, T. Pfeifer, K. Bartschat, and A. Harth, Phys. Rev. A **109**, 023110 (2024).

- [174] A. T. Bondy, S. Saha, J. del Valle, A. Harth, N. Douguet, K. Hamilton, and K. Bartschat, Phys. Rev. A **109**, 043113 (2024).
- [175] A. T. Bondy, J. C. del Valle, S. Saha, K. R. Hamilton, D. Bharti, A. Harth, and K. Bartschat, Eur. Phys. J. D **78**, 106 (2024).
- [176] W. Kaiser and C. Garrett, Phys. Rev. Lett. **7**, 229 (1961).
- [177] T. H. Maiman, Nature (London) **187**, 493 (1960).
- [178] A. Einstein, Z. Phys. **18**, 121 (1917).
- [179] W. E. Lamb and R. C. Rutherford, Phys. Rev. **72**, 241 (1947).
- [180] H. B. G. Casimir, Proc. K. Ned. Akad. Wet. **51**, 793 (1948).
- [181] G. W. F. Drake and D. C. Morton, Astrophys. J. Suppl. Ser. **170**, 251 (2007).
- [182] D. C. Morton, P. Moffatt, and G. W. F. Drake, Can. J. Phys. **89**, 129 (2011).
- [183] D. C. Morton, E. E. Schulhoff, and G. W. F. Drake, J. Phys. B **48**, 235001 (2015).
- [184] W. Y. Wong and D. Scott, Mon. Not. R. Astron. Soc. **375**, 1441 (2007).
- [185] G. W. F. Drake and A. Dalgarno, Astrophys. J. **152**, L121 (1968).
- [186] G. W. F. Drake, G. Victor, and A. Dalgarno, Phys. Rev. **180**, 25 (1969).
- [187] G. W. F. Drake, Phys. Rev. A **3**, 908 (1971).
- [188] Y. B. Zeldovich, V. G. Kurt, and R. Syunyaev, Zh. Eksp. Teor. Fiz. **55**, 278 (1968).
- [189] P. J. E. Peebles, Astrophys. J. **153**, 1 (1968).
- [190] W. Y. Wong, S. Seager, and D. Scott, Mon. Not. R. Astron. Soc. **367**, 1666 (2006).

- [191] L. Spitzer Jr and J. L. Greenstein, *Astrophys. J.* **114**, 407 (1951).
- [192] D. E. Osterbrock, *Astrophysics of Gaseous Nebulae* (W. H. Freeman & Co, San Francisco).
- [193] G. W. F. Drake, *Phys. Rev. A* **34**, 2871 (1986).
- [194] A. M. Boesgaard and G. Steigman, *Ann. Rev. Astron. and Astrophys.* **23**, 319 (1985).
- [195] R. S. Van Dyck Jr, C. E. Johnson, and H. A. Shugart, *Phys. Rev. A* **4**, 1327 (1971).
- [196] M. Prior and H. Shugart, *Phys. Rev. Lett.* **27**, 902 (1971).
- [197] H. Gould and R. Marrus, *Phys. Rev. A* **28**, 2001 (1983).
- [198] R. W. Dunford, H. G. Berry, K. O. Groeneveld, M. Hass, E. Bakke, M. L. A. Raphaelian, A. E. Livingston, and L. J. Curtis, *Phys. Rev. A* **38**, 5423 (1988).
- [199] R. W. Dunford, H. G. Berry, S. Cheng, E. P. Kanter, C. Kurtz, B. J. Zabransky, A. E. Livingston, and L. J. Curtis, *Phys. Rev. A* **48**, 1929 (1993).
- [200] R. Marrus, V. S. Vicente, P. Charles, J. P. Briand, F. Bosch, D. Liesen, and I. Varga, *Phys. Rev. Lett.* **56**, 1683 (1986).
- [201] A. Simionovici, B. B. Birkett, J. P. Briand, P. Charles, D. D. Dietrich, K. Finlayson, P. Indelicato, D. Liesen, and R. Marrus, *Phys. Rev. A* **48**, 1695 (1993).
- [202] P. H. Mokler and R. W. Dunford, *Phys. Scr.* **69**, C1 (2004).
- [203] A. V. Volotka, A. Surzhykov, V. M. Shabaev, and G. Plunien, *Phys. Rev. A* **83**, 062508 (2011).
- [204] D. Banas, A. Gumberidze, S. Trotsenko, A. V. Volotka, A. Surzhykov, H. F. Beyer, F. Bosch, A. Brauning-Demian, S. Fritzsche, S. Hagmann, C. Kozhuharov, A. Kumar, X. Ma, R. Mann, P. H. Mokler, D. Sierkowski,

U. Spillmann, S. Tashenov, Z. Stachura, A. Warczak, and T. Stohlker, Phys. Rev. A **87**, 062510 (2013).

[205] L. Safari, P. Amaro, J. P. Santos, and F. Fratini, Phys. Rev. A **90**, 014502 (2014).

[206] I. P. Grant, J. Phys. B **7**, 1458 (1974).

[207] U. D. Jentschura and C. M. Adhikari, Phys. Rev. A **97**, 062120 (2018).

[208] G. Breit and E. Teller, Astrophys. J. **91**, 215 (1940).

[209] A. Dalgarno and D. Bates, Mon. Not. R. Astron. Soc. **131**, 311 (1966).

[210] S. P. Goldman and G. W. F. Drake, Phys. Rev. A **24**, 183 (1981).

[211] A. Derevianko and W. Johnson, Phys. Rev. A **56**, 1288 (1997).

[212] O. Bely and P. Faucher, Astron. Astrophys. **1**, 37 (1969).

[213] H. Goldstein, *Classical Mechanics* (Pearson Education India) (2011) p. 22.

[214] Z. Fried and A. Martin, Nuovo Cimento **29**, 574 (1963).

[215] Z.-C. Yan and G. W. F. Drake, Phys. Rev. A **52**, R4316 (1995).

[216] A. I. Akhiezer and V. B. Berestetskii, *Quantum Electrodynamics* (Wiley Interscience, New York, 1965) pp. 484–498.

[217] G. W. F. Drake, J. G. Manalo, P.-P. Zhang, and K. G. H. Baldwin, Hyperfine Interact. **240**, 1 (2019).

[218] G. W. F. Drake, Phys. Rev. A **19**, 1387 (1979).

[219] M. Puchalski, K. Szalewicz, M. Lesiuk, and B. Jeziorski, Phys. Rev. A **101**, 022505 (2020).

[220] G. W. F. Drake and S. Goldman, in *Adv. At. Mol. Phys.*, Vol. 25 (Elsevier, 1989) pp. 393–416.

- [221] G. W. F. Drake, Phys. Scr. **1999**, 83 (1999).
- [222] G. W. F. Drake and S. Goldman, Phys. Rev. A **23**, 2093 (1981).
- [223] L. L. Foldy and S. A. Wouthuysen, Phys. Rev. **78**, 29 (1950).
- [224] K. Pachucki, Phys. Rev. A **69**, 052502 (2004).
- [225] M. Sami, *Nonrelativistic Operators for Relativistic Transition Rates*, Master's thesis, University of Windsor, Canada, (2019) pp. 28–32.
- [226] T. Hirsch, D. Cocks, and S. Hodgman, Phys. Rev. A **104**, 033317 (2021).
- [227] G. W. F. Drake, Can. J. Phys. **66**, 586 (1988).
- [228] K. Pachucki and M. Puchalski, Phys. Rev. A **99**, 041803 (2019).
- [229] G. W. F. Drake and Z.-C. Yan, Can. J. Phys. **86**, 45 (2008).
- [230] T. Zhang, Z.-C. Yan, and G. W. F. Drake, Phys. Rev. Lett. **77**, 1715 (1996).
- [231] K. Pachucki, Phys. Rev. A **74**, 022512 (2006).
- [232] K. Pachucki, Phys. Rev. A **74**, 062510 (2006).
- [233] V. Patkóš, V. A. Yerokhin, and K. Pachucki, Phys. Rev. A **103**, 042809 (2021).
- [234] R. Sanchez, W. Nörtershäuser, G. Ewald, D. Albers, J. Behr, P. Bricault, B. A. Bushaw, A. Dax, J. Dilling, M. Dombsky, G. W. F. Drake, P. Finlay, K. Minamisono, M. R. Pearson, M. Schumann, and J. Whalen, Phys. Rev. Lett. **96**, 033002 (2006).
- [235] M. Smith, M. Brodeur, T. Brunner, S. Ettenauer, A. Lapierre, R. Ringle, V. L. Ryjkov, F. Ames, P. Bricault, G. W. F. Drake, J. Dilling, and G. Uller, Phys. Rev. Lett. **101**, 202501 (2008).

[236] W. Nörtershäuser, D. Tiedemann, M. Žáková, Z. Andjelkovic, K. Blaum, M. L. Bissell, R. Cazan, G. W. F. Drake, C. Geppert, M. Kowalska, K. König, R. Neugart, R. Sanchez, L. Schweikhard, and D. Yordanov, *Phys. Rev. Lett.* **102**, 062503 (2009).

[237] M. Brodeur, T. Brunner, C. Champagne, S. Ettenauer, M. J. Smith, A. Lapierre, R. Ringle, V. L. Ryjkov, S. Bacca, P. Delheij, J. Dilling, G. W. F. Drake, A. Ekström, and F. R. Espinoza-Quinones, *Phys. Rev. Lett.* **108**, 052504 (2012).

[238] R. Dall, K. Baldwin, L. Byron, and A. Truscott, *Phys. Rev. Lett.* **100**, 023001 (2008).

[239] J. Fischer, *Ann. Phys. (Leipzig)* **531**, 1800304 (2019).

[240] P. M. Rourke, C. Gaiser, B. Gao, D. M. Ripa, M. R. Moldover, L. Pitre, and R. J. Underwood, *Metrologia* **56**, 032001 (2019).

[241] K. Piszczałkowski, M. Puchalski, J. Komasa, B. Jeziorski, and K. Szalewicz, *Phys. Rev. Lett.* **114**, 173004 (2015).

[242] M. Puchalski, K. Piszczałkowski, J. Komasa, B. Jeziorski, and K. Szalewicz, *Phys. Rev. A* **93**, 032515 (2016).

[243] A. G. Truscott, K. E. Strecker, W. I. McAlexander, G. B. Partridge, and R. G. Hulet, *Science* **291**, 2570 (2001).

[244] J. Mitroy and L.-Y. Tang, *Phys. Rev. A* **88**, 052515 (2013).

[245] K. Thomas, J. Ross, B. Henson, D. Shin, K. Baldwin, S. Hodgman, and A. Truscott, *Phys. Rev. Lett.* **125**, 013002 (2020).

[246] B. Henson, R. Khakimov, R. Dall, K. Baldwin, L.-Y. Tang, and A. Truscott, *Phys. Rev. Lett.* **115**, 043004 (2015).

[247] B. Henson, K. Thomas, Z. Mehdi, T. Burnett, J. Ross, S. Hodgman, and A. Truscott, *Opt. Express* **30**, 13252 (2022).

[248] J. G. Manalo, *The Variational Calculation of the 413 nm ^4He Tune-out Wavelength*, Master's thesis, University of Windsor, Canada, (2017) pp. 28–32.

[249] V. A. Yerokhin and K. Pachucki, Phys. Rev. A **81**, 022507 (2010).

[250] H. Araki, Prog. Theor. Phys. **17**, 619 (1957).

[251] J. Sucher, Phys. Rev. **109**, 1010 (1958).

[252] Z.-C. Yan and G. W. F. Drake, Phys. Rev. Lett. **91**, 113004 (2003).

[253] L. Bruch and F. Weinhold, J. Chem. Phys. **117**, 3243 (2002).

[254] K. Pachucki and V. A. Yerokhin, Phys. Rev. A **100**, 062510 (2019).

[255] Y.-S. Wang, S. Kar, and Y. K. Ho, Atoms **8**, 90 (2020).

[256] Y.-H. Zhang, F.-F. Wu, P.-P. Zhang, L.-Y. Tang, J.-Y. Zhang, K. Baldwin, and T.-Y. Shi, Phys. Rev. A **99**, 040502 (2019).

[257] I. Angeli and K. P. Marinova, At. Data Nucl. Data Tables **99**, 69 (2013).

[258] D. B. Newell and E. Tiesinga, NIST Spec. Publ. **330**, 1 (2019).

[259] G. R. Blumenthal, G. W. F. Drake, and W. H. Tucker, Astrophys. J. **172**, 205 (1972).

[260] G. W. F. Drake and R. Robbins, Astrophys. J. **171**, 55 (1972).

[261] S. Goldman and G. W. F. Drake, Phys. Rev. Lett. **68**, 1683 (1992).

[262] V. I. Korobov, Phys. Rev. A **100**, 012517 (2019).

[263] G. W. F. Drake, Phys. Rev. A **45**, 70 (1992).

[264] G. W. F. Drake, Phys. Scr. **2001**, 22 (2001).

[265] D. Faddeev and V. Faddeeva, Sov. J. Math. **15**, 531 (1981).

[266] G. H. Golub and H. A. Van der Vorst, J. Comp. Appl. Math. **123**, 35 (2000).

- [267] R. Martin, C. Reinsch, and J. Wilkinson, *Numer. Math.* **11**, 181 (1968).
- [268] R. S. Martin and J. Wilkinson, *Numer. Math.* **12**, 377 (1968).
- [269] T. Kirchner, *Atomic and Molecular Physics Lecture Notes* (2013), accessed July 4, 2024.
- [270] Y. Fukuda *et al.*, *Phys. Rev. Lett.* **81**, 1562 (1998).
- [271] Q. R. Ahmad *et al.*, *Phys. Rev. Lett.* **89**, 011301 (2002).
- [272] A. Y. Smirnov, *Nucl. Part. Phys. Proc.* **265**, 1 (2015).
- [273] J. J. Sakurai and J. Napolitano, *Modern Quantum Mechanics*, 3rd ed. (Cambridge University Press, 2017).

VITA AUCTORIS

NAME:	Aaron Thomas Bondy
PLACE OF BIRTH:	Windsor, Canada
EDUCATION:	St. Thomas of Villanova Secondary School, LaSalle, ON, 2011
	University of Windsor, B.Sc. Physics, Windsor, Ontario, 2016

Publications

12. "Double atomic electron emission following the beta decay of ${}^6\text{He}$ " A. T. Bondy and G. W. F. Drake, In press for 2024 issue of *Physics in Canada* issue.
11. "R-matrix with time-dependence calculations for three-sideband RABBITT in helium," A. T. Bondy, J. C. del Valle, S. Saha, K. R. Hamilton, D. Bharti, A. Harth, and K. Bartschat, *European Physics Journal D* **78** 106 (2024).
10. "High-order harmonic generation in helium: a comparison study," A. T. Bondy, S. Saha, J. C. del Valle, A. Harth, N. Douguet, K. R. Hamilton, and K. Bartschat, *Physical Review A* **109** 043113 (2024).
9. "Ground-state energy of H^- : a critical test of triple basis sets," E. Petrimoulx, A. T. Bondy, E. Ene, L. Sati, and G. W. F. Drake, *Canadian Journal of Physics* (2024).
8. "Multi-sideband interference structures by high-order photon-induced continuum-continuum transitions in helium," D. Bharti, H. Srinivas, F. Shobeiry, A. T. Bondy, S. Saha, K. R. Hamilton, R. Moshammer, T. Pfeifer, K. Bartschat, and A. Harth, *Physical Review A* **109** 023110 (2024).
7. "Algebraic relations from finite-nuclear-mass effects to test atomic transition rates," A. T. Bondy and G. W. F. Drake, *Physical Review A* **108**, 032807 (2023).
6. "Charge state distributions following the beta decay of ${}^6\text{He}$ to form ${}^6\text{Li}^+$," A. T. Bondy and G. W. F. Drake, *Atoms* **11**, 41 (2023).

5. “Precision measurement of the helium $2^3S_1 - 2^3P/3^3P$ tune-out frequency as a test of QED,” B. M. Henson, J. A. Ross, K. F. Thomas, C. N. Kuhn, D. K. Shin, S. S. Hodgman, Y.-H. Zhang, L.-Y. Tang, G. W. F. Drake, A. T. Bondy, A. G. Truscott, and K. G. H. Baldwin, *Science* **376**, 199-203(2022).
4. “Linear dichroism in few-photon ionization of laser-dressed helium,” Severin Meister, A. T. Bondy, K. Schnorr, S. Augustin, H. Lindenblatt, F. Trost, X. Xie, M. Braune, R. Treusch, B. Manschvetus, N. Schirmel, H. Redlin, N. Douguet, T. Pfeifer, K. Bartschat, and R. Moshammer, *European Physics Journal D* **75** 205 (2021).
3. “Photoelectron spectroscopy of laser-dressed atomic helium,” S. Meister, A. T. Bondy, K. Schnorr, S. Augustin, H. Lindenblatt, F. Trost, X. Xie, M. Braune, R. Treusch, B. Manschvetus, N. Schirmel, H. Redlin, N. Douguet, T. Pfeifer, K. Bartschat, and R. Moshammer, *Physical Review A* **102** 062809 (2020).
2. “Two-photon decay rates in heliumlike ions: Finite-nuclear-mass effects,” **Aaron T. Bondy**, D. C. Morton, and G. W. F. Drake, *Physical Review A* **102** 052807 (2020).
1. “Ellipticity dependence of excitation and ionization of argon atoms by short-pulse infrared radiation,” T. Pauly, A. T. Bondy, K. R. Hamilton, N. Douguet, X.-M. Tong, D. Chetty, and K. Bartschat, *Physical Review A* **102** 013116 (2020).

Invited Presentations

- “Developing a Formalism for the Beta Decay of Helium-6,” CM-AMO Seminar, University of Michigan, USA (2024).
- “Special Report: Charge-state distributions after beta decay of ${}^6\text{He}$ to form ${}^6\text{Li}^+$,” XXIII International Conference on Photonic, Electronic and Atomic Collisions (ICPEAC), Ottawa, Canada (2023).
- “Atomic physics searches for new physics: Beta decay of ${}^6\text{He}$,” Fundamental Science and Quantum Technologies using Atomic Systems, Gujarat, India (2020).

Contributed Oral Presentations

- “Algebraic relations arising from mass polarization in one-photon and two-photon transitions of heliumlike ions,” APS DAMOP Meeting, Spokane, USA (2023).
- “Relativistic corrections to helium two-photon decay rates,” Canadian Association of Physicists (CAP) Congress, Hamilton, Canada (2022).
- “A projection operator approach to charge-state distributions following the beta-decay of ${}^6\text{He}$,” Canadian Association of Physicists (CAP) Congress, Hamilton, Canada (2022).
- “Equivalent one-electron Breit-Pauli operators for relativistic corrections to two-photon decay rates in helium,” APS DAMOP Meeting, Orlando, USA (2022).
- “Two-photon decay of heliumlike ions: Finite-nuclear-mass effects,” Canadian Association of Physicists (CAP) Congress, held virtually (2021).
- “Two-photon decay rates in heliumlike ions: finite-nuclear-mass effects,” APS DAMOP Meeting, held virtually (2021).
- “Emergence of light-induced states in the few-photon ionization of atomic helium,” Canadian Association of Physics (CAP) Congress, held virtually (2021).
- “Double atomic electron emission following the beta decay of ${}^6\text{He}$,” Canadian Association of Physicists (CAP) Congress, held virtually (2021)
Won 1st place in DAMOPc graduate competition; 3rd place overall
- “Single vs. double electron emission following the beta decay of ${}^6\text{He}$,” APS DAMOP Meeting, held virtually (2020).
- “Electron emission and angular anisotropy following the beta decay of helium-6,” APS DAMOP Meeting, Milwaukee, USA (2019).

Poster Presentations

- “Charge-state distributions after beta decay of ${}^6\text{He}$ to form ${}^6\text{Li}^+$,” XXIII International Conference on Photonic, Electronic and Atomic Collisions (ICPEAC), Ottawa, Canada (2023).
- “A comparison study for high-order harmonic generation in helium,” XXIII International Conference on Photonic, Electronic and Atomic Collisions (ICPEAC), Ottawa, Canada (2023).
- “Relativistic corrections to two-photon decay rates in heliumlike ions,” The 27th International Conference on Atomic Physics (ICAP), Toronto, Canada (2022).
- “A projection operator approach to charge-state distributions following the beta-Decay of ${}^6\text{He}$,” APS DAMOP Meeting, Orlando, USA (2022).
- “Emergence of light-induced states in the few-photon ionization of atomic helium,” International Symposium on Correlation, Polarization and Ionization in Atomic and Molecular Collisions (vCOPIAMC), held virtually (2021).
- “Two-photon decay rates in heliumlike atoms: Finite-nuclear-mass effects,” 32nd International Conference on Photonic, Electronic and Atomic Collisions (ICPEAC), held virtually (2021).
- “Emergence of light-induced states in the few-photon ionization of atomic helium,” APS DAMOP Meeting, held virtually (2021).
- “Two-color few-photon ionization of helium: comparison of theory and experiment,” APS DAMOP Meeting, held virtually (2020).

National Scholarships

- NSERC Michael Smith Foreign Study Supplement (March–April 2024)
- NSERC CGS Doctoral Award (2022–2024)
- NSERC Michael Smith Foreign Study Supplement (January–July 2020)
- NSERC CGS Master’s Award (2019–2020)